THE UNIVERSITY *of* EDINBURGH

Orbital Interactions

Dominic James Pascoe

THE UNIVERSITY *of* EDINBURGH

Thesis presented for the degree of

Doctor of Philosophy

The University of Edinburgh

2018

Declaration

This work has been entirely composed by the author.

All work contained within has been undertaken by the author, except where indicated within the main body of this document.

This work has not been submitted for any other degree or professional qualification.

Signature:  23/10/2018

Dominic Pascoe

Table of Contents

Acknowledgements

First and foremost I would like to thank Dr Scott Cockroft for providing the academic and emotional support to complete my PhD. Throughout my PhD he has provided many words of wisdom I will cherish, for example, what not to Google and how to get gout (and a little bit of chemistry).

I would also like to thank Dr Kenny Ling, who has provided such valuable contributions to the completion of my PhD and made sure I had a great placement while at *Syngenta*.

All members of the Cockroft group have helped me through the last four years, providing a fun and relaxed environment to work in. Particularly I would like to thank Dr Stefan Borsley for his help in proof reading everything I ever write and for the supportive pub trips!

The Official Trumps League; Lord Trumpington, Shuffles, Minus 3, Zhengers and Chucky, must also be recognised as an important contributor to keeping me sane. I would also like to thank the Bangers (co-developed with Alex Elmi) that provided the best possible soundtrack to work. Thanks to those in the beginning, Dr Kamila Muchowska and Dr Tom Hubbard, who inspired me to pursue this PhD and help me settle into the Cockroft group.

Thank you to those outside the lab who have supported me through my PhD, Adam Michalchuk for helping me fend off seagulls and his guidance in using computational chemistry. Finally, thank you to my parents for their unwavering support throughout.

I thank *Syngenta* and the European Research Council (ERC) for funding.

Abstract

It is widely accepted that the sharing of electrons constitutes a bond. Conversely, molecular interactions that do not involve electron transfer, such as van der Waals forces and electrostatics are defined as “non-bonding” or “non-covalent” interactions. More recently computational and experimental observations have shown situations where the division between “bonding” and “non-bonding” interactions is blurred. One such class of interactions are known as σ-hole interactions.

Chapter 1 provides a literature review of investigations into the nature of σ-hole interactions, highlighting the individual contributing factors.

Chapter 2 provides a detailed analysis into the nature of chalcogen-bonding interactions. Synthetic molecular balances are employed for experimental measurements of conformational free energies in different solvents, facilitating a detailed examination of the energetics and associated solvent and substituent effects on chalcogen-bonding interactions. The chalcogen-bonding interactions examined were found to have surprisingly little solvent dependence. The independence of the conformational free energies on solvent polarity, polarisability and H-bond characteristics showed that electrostatic, solvophobic or dispersion forces were not dominant factors in accounting for the experimentally observed trends. A molecular orbital analysis provided a quantitative relationship between the experimental free energies and the molecular orbital energies, which was consistent with chalcogen-bonding interactions being dominated by an n→σ* orbital delocalisation.

Chapters 3 and **4** both use the molecular orbital modelling approach established in C**hapter 2** to investigate the potential partial covalency in H-bonding and carbonyl···carbonyl interactions. H-bonding is generally considered to be an electrostatically dominated interaction. However, computational results have suggested a partial covalent character in H-bonding. The molecular orbital analysis revealed an n→σ* electron delocalisation in all H-bonding systems evaluated. However, no quantitative correlation could be found with experimental free energies. Similarly, the nature of carbonyl···carbonyl interactions has been subject to debate,

with electrostatic or an n→π* electron delocalisation having been proposed as the dominant factors. The molecular orbital analysis employed here showed that n→π* delocalisation was exceptionally geometry dependent. Studies of literature systems reveal that n→π* delocalisation contributes to overall stability of a range of systems, with a quantitative link between molecular orbital energy and conformational free energies.

Lay Summary

The term “non-covalent interactions” refers to favourable interactions between atoms in the absence of a formal chemical bond. These interactions are crucial to life, dictating the function and behaviour of DNA and proteins within our cells. Non-covalent interactions have also been employed in many man-made systems, which rely on these interactions, for example in the catalytic synthesis of drug molecules. To fully exploit these interactions, it is important to understand why particular molecules stick together by determining the nature of the interaction.

Chalcogen atoms (oxygen, sulfur, selenium and tellurium) form favourable interactions with each other. These so-called chalcogen···chalcogen interactions have attracted increasing interest as their importance in many biologically relevant systems has been revealed. The first part of this thesis focuses on determining the nature of chalcogen···chalcogen interactions. These interactions were found to be strong in solution, but also, surprisingly, their strength did not vary in different solvents. Computational analysis revealed that these interactions demonstrate characteristics of both non-covalent interactions, and formally bonded structures.

The same computational approach that had been used to studying chalcogen interactions was subsequently applied to other classes of non-covalent interactions. Hydrogen bonds, one of the most common interactions, were examined, and revealed similar formally bonded characteristics. However, unlike for chalcogen···chalcogen interactions, the analysis could not fully explain their experimental behaviour in solution, indicating a more complex situation. Finally, the nature of interactions between carbonyls (carbon–oxygen groups within molecules), was investigated due to their importance in controlling protein function. The interaction between two carbonyl groups was shown to be very directionally dependent. This directional, or geometric, dependence was found to be very important in determining whether formal bonding characteristics were observed in interactions between carbonyls.

Abbreviations

A^-	Anion
Ae	Aerogen
ALMO	Absolutely Localised Molecular Orbital
AO	Atomic orbital
CCSD	Coupled Cluster calculation
Ch	Chalcogen
CSD	Cambridge Structural Database
d	Doublet (NMR analysis)
dd	Doublet of doublets (NMR analysis)
DCM	Dichloromethane
DFT	Density Functional Theory
DFT-D	Density Functional Theory – Dispersion corrected
DMEDA	1,2-Dimethylethylenediamine
DMSO	Dimethylsulfoxide
dt	Doublet of Triplets (NMR analysis)
EDA	Energy Decomposition Analysis
EI	Electrospray Ionisation
ESP	Electrostatic Potential
EtOAc	Ethyl acetate
EWG	Electron-withdrawing Group
fiSAPT	Functional group Intramolecular Symmetry Adapted Perturbation Theory
HF	Hartree Fock

LUMO	Lowest Unoccupied Molecular Orbital
HMBC	Heteronuclear Multiple Bond Correlation (NMR)
HOMO	Highest Occupied Molecular Orbital
HRMS	High Resolution Mass Spectrometry
IR	Infrared
IUPAC	International Union of Pure and Applied Chemistry
m	*meta*
m	Multiplet (NMR analysis)
MO	Molecular Orbital
MP2	Møller–Plesset perturbation theory, 2nd generation
NAO	Natural Atomic Orbital
NBO	Natural Bond Orbital
NHO	Natural Hybrid Orbital
NLMO	Natural Localised Molecular Orbital
NMR	Nuclear Magnetic Resonance
NOCV	Natural Orbitals for Chemical Valence
NOE	Nuclear Overhauser effect
NOESY	Nuclear Overhauser effect spectroscopy
p	*para*
Pn	Pnicogen (Pnictogen)
ppm	Parts per million
q	Quartet (NMR analysis)
QTAIM	Quantum Theory of Atoms in Molecules

s	Singlet (NMR analysis)
SAPT	Symmetry Adapted Perturbation Theory
Sol	Solvent
t	triplet (NMR analysis)
THF	Tetrahydrofuran
TLC	Thin Layer Chromatography
Tr	Tetrel
UV/Vis	Ultraviolet/Visible
VSEPR	Valence Shell Electron Pair Repulsion
XAS	X-ray Absorption Spectroscopy

Publications

The Origin of Chalcogen-Bonding Interactions, *J. Am. Chem. Soc.*, **2017**, 139, 15160-1516 (**Chapter 2**)

Geometric Sensitivity of n→π* Carbonyl Interactions, *in preparation* (**Chapter 4**)

Chapter 1
The Nature of σ-hole Interactions

Abstract

σ-Hole interactions encompass favourable interactions involving group 14, 15, 16, 17 and even group 18 elements. Whilst the use of these interactions, particularly halogen bonding, has become prevalent in a range of applications, the physiochemical origin of σ-hole interactions is still debated. Electrostatic and partially covalent models stemming from an n→σ* orbital delocalisation have both been proposed as governing σ-hole interactions. While computational or experimental approaches have been used to investigate their strength and behaviour, few studies have used a combined experimental and theoretical approach, and a rigorous definition of σ-hole interactions remains elusive. The literature presented here shows how a wide range of techniques, including spectroscopy and theoretical energy decomposition analyses, have been used to explore the properties, strength and nature of σ-hole interactions. The findings generally support n→σ* electron delocalisation as being stabilising factors in σ-hole complexes. A wider question about the appropriate use of theoretical bonding models (such as molecular orbitals) in the definition of non-covalent interactions is raised. Many of the experimental investigations demonstrate that a purely electrostatic model cannot account for the behaviour of σ-hole interactions. Therefore, the complementary pairing of theoretical bonding models and experimental observations is necessary to adequately define σ-hole interactions.

1.1 Introduction

σ-Holes have been defined as an area of lower potential that sits along the extension of a covalent σ-bond (blue regions in **Figure 1.1**).[1] Since these regions often have partial positive charged, then it has been proposed that favourable interactions can form with Lewis bases, including heteroatoms and π-systems.[2] Since first being coined in 2007,[1] σ-hole interactions have been observed in elements from group 14 (tetrel),[3] 15 (pnicogen),[4] 16 (chalcogen),[5] 17 (halogen)[6] and even 18 (aerogen).[7] σ-Hole interactions have been widely employed in medicinal chemistry,[8,9] catalysis,[10,11] anion recognition[12,13] and materials chemistry[14] among others.

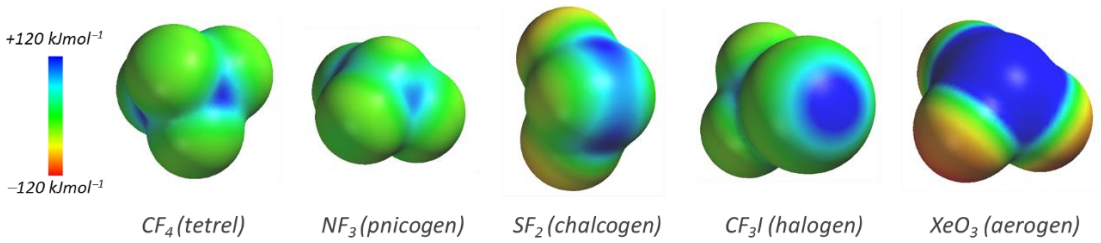

Figure 1.1 Electrostatic potentials (ESPs) demonstrating the positive σ-holes (blue) in groups 14–18 elements. Calculated using Spartan '14, DFT/B3LYP/6-311G*.

Understanding the fundamental nature of molecular interactions allows chemists to exploit their properties. Having a thorough definition of the nature of an interaction allows the prediction of chemical behaviour, and ultimately the ability to exploit and optimise such interactions to a given function. Such knowledge has helped in the development of bioactive molecules,[8] and an appreciation of their role in governing molecular structure and catalysis.[15] While the most complete description of chemistry lies within quantum mechanics, a range of qualitative terminologies and definitions have arisen to help define the factors that contribute to molecular interactions.

Electrostatic potentials (ESPs) are widely utilised for rationalising non-covalent interactions, such as hydrogen bonds (H-bonds),[16] due to it being a physically observable property. Partial positive electrostatic potentials can be seen over along the axis of C-X bonds (**Figure 1.1**), which led to term σ-hole being used to describe a region of low electron density, through which the positive nuclear charge could be

observed.[17–19] The Hellmann-Feynman theorem calculated the total energy based on a parameter using the derivative of the Hamiltonian using the same parameter (**Equation 1.1**).

$$\frac{dE_\lambda}{d\lambda} = \langle \psi_\lambda \left| \frac{d\hat{H}_\lambda}{d\lambda} \right| \psi_\lambda \rangle \qquad (\mathbf{1.1})$$

Where $\hat{H}_\lambda$ is the Hamiltonian depending on the parameter λ, $|\psi_\lambda\rangle$ is the eigenfunction of the Hamiltonian and E_λ is the energy.

The theorem states that once the distribution of electrons have been solved using the Schrödinger equation, all the forces can be calculated using classical electrostatics.[20] In relation to non-covalent interactions, this can be interpreted as all molecular interactions can be described using an electrostatic model.[21]

Molecular orbital theory is an important model that chemists have relied on when describing bond theory. Despite this, the terminology surrounding this definition is fuzzy,[22] particularly when referring to non-covalent interactions.[23] The energetic significance of orbital interactions (also known as electron delocalisation, polarisation, partial covalency, induction and donor-acceptor interactions) are hard to predict, due to the inability to physically observe individual molecular orbitals. However, orbital interactions have also been considered an important factor in σ-hole interactions. If an orbital-based theoretical description of the electron density is used, then the delocalisation of electrons from a lone pair on a Lewis base into the antibonding σ* orbital of the σ-hole (denoted n→σ* delocalisation) can be identified.[24,25]

Exchange repulsion (steric repulsion), which stems from the repulsion between two electrons, can also been used to explain the behaviour of molecular interactions.[26] Exchange repulsion takes place as two orbitals approach and begin to overlap. This overlap is forbidden according to the Pauli exclusion principle,[27] and therefore electrons are repelled, lowering the overall electron density in the inter or intramolecular space. As the electron density in the intermolecular space decreases, the positive nuclei become less shielded resulting in a repulsion between the two, increasing the overall energy of the system.

Finally, the significance of dispersion forces,[28] the attractive component of van der Waals interactions, has been demonstrated in a range of molecular interactions,

particularly between apolar groups where other interaction components such as electrostatics or polarisation are small.[29,30] Heavier elements can contribute a significant dispersive component to molecular interactions due to their increased polarisability. Of potential significance in σ-hole interactions, contacts between elements such as iodine and tellurium may have substantial dispersive contributions.

The nature of σ-hole interactions, and the relative contributions of abovementioned factors remains the subject of debate.[31] This chapter will discuss both the experimental and theoretical evidence relating to the nature of halogen, chalcogen, pnicogen, tetrel and aerogen bonds.

1.2 A note on nomenclature

A point of discussion is the clarity of nomenclature surrounding the investigation of molecular interactions, and whether any model beyond an electrostatic one is needed, such as molecular orbitals. As the Hellman-Feynman theorem states: molecular interactions can be described as a function of electrostatics as they can be explained as Coulombic interactions between electrons and nuclei once the electron distribution has been solved from the Schrödinger equation.[20] Therefore, an important question to ask is: are models needed to understand molecular interactions?

Some will argue that the introduction of models, such as molecular orbital theory, complicates the understanding of molecular interactions, particularly as many of these models have no physical, measurable parameter. Clark is quoted as saying "How many different contributions do we need to analyze a bond of a few kcal mol^{-1}?".[32] Others believe the introduction of theoretical models to describe molecular interactions are an important way of ensuring understanding and explaining experimental behaviour. One problem that is encountered by chemists is that the terminology used to describe different interaction components is not consistent. For example, electron delocalisation, charge transfer, orbital interactions, donor-acceptor interactions and induction may all be used to describe broadly the same phenomenon, in this review all these terms will be referred to as electron delocalisation.

1.3 Computational methods used

Computational predictions have become an important method to predict the behaviour and strength of molecular interactions. This section looks to summarise and compare the computational methodologies presented in the thesis.

1.3.2 Basis sets

Basis sets are the set of functionals used to create molecular orbitals. The use of basis sets can vary results greatly and choice of basis set can be very important for optimal accuracy. Many basis sets are available and ideally a comparative study using a range of basis sets would be used to find the best compared to a benchmarking set.

A way to improve the accuracy of basis sets it to add extra basis functions beyond what is minimally needed. A minimum basis set would contain one basis function for each atomic orbital. For example, a minimum basis set would include five basis functions for carbon, $1s^2 2s^2 2p^2$ (two *s*-orbitals and three *p*-orbitals). While computationally inexpensive, minimal basis sets do not allow atomic orbitals to get larger or smaller as other atoms approach, and therefore are not very accurate. Adding basis functions can improve accuracy by allowing atomic orbitals to change as other atoms interact with them. A double-ζ basis set (for example the Pople 6-31G and jun-cc-pvdz) gives two basis functions per atomic orbital (10 in the carbon example). Triple-, quadruple-, etc. ζ basis sets give three and four basis sets per atomic orbital. The larger the ζ value the greater flexibility atomic orbitals have for interactions, improving accuracy.[33]

In this thesis many of the calculations are performed using Pople basis sets.[34] Pople basis sets are presented to show how core and valence electrons are treated. For example, the common Pople basis set 6-31G shows that core electrons are calculated using six Gaussian-type orbitals and valence electrons are calculated first using three GTOs and then 1 GTO, hence this basis set is a double- ζ basis set.[35] Higher ζ-value basis sets are shown by the number of values after the hyphen, for example, 6-311G is a triple- ζ basis set.[36] The inclusion of polarisation (denoted by a *) and diffuse (denoted with a +) functions in these basis sets can increase the flexibility of atomic orbitals further. A polarisation function gives access to higher atomic orbitals on heavy

atoms, such as *d*-orbitals on carbon atoms (e.g. 6-31G*), the addition of polarisation functions on light elements gives access to *p*-orbitals to hydrogen atoms (e.g. 6-31G**). Diffuse functions keep electrons away from the nucleus and is essential when considering anions. All these functions can be combined to build larger basis sets, such as 6+31G**.

1.3.2 Energy Decomposition Analysis (EDA)

Energy decomposition analysis (EDA) methods are popular approaches that are applied to the understanding of molecular interactions. Many different decomposition analyses exist, which break down molecular interactions into their primary components. These components regularly include electrostatics, induction, dispersion and exchange, but can also include others such as orbital interactions. **Table 1.1** shows the difference and similarities in the components in different EDAs.

Table 1.1 The different components symmetry-adapted perturbation theory (SAPT), Kohn-Sham and Absolutely Localised Molecular Orbital (ALMO) are decomposed to.

Methodology	SAPT	Kohn-Sham	ALMO
Electrostatics	✓	✓	
Exchange	✓	✓	
Induction	✓		
Dispersion	✓		✓
Orbital Interactions		✓	
Polarisation			✓
Charge Transfer			✓

One of the most commonly used decomposition methods, and the most used in this thesis, is symmetry-adapted perturbation theory (SAPT) for intermolecular interactions. SAPT allows the decomposition of the individual energetic contributions

of the repulsive exchange term, and the attractive electrostatic, dispersion and induction terms (**Equation 1.2**).

$$E_{tot} = E_{elec} + E_{ind} + E_{disp} + E_{exch} \quad \textbf{(1.2)}$$

There are different levels of SAPT (SAPT(0), SAPT(2), SAPT(2+3) and DFT-SAPT as examples). The difference in calculated interactions energies using these different levels can be large and therefore it is important to understand the advantages and limitations of different SAPT methodologies. SAPT(0) is the simplest methodology, which is also the least accurate due to its simpler estimation of electron correlation, treating the two monomers at the Hartree-Fock (HF) level.[37] SAPT(0) breaks down the interaction energy into its components (**Equation 1.3**) by using second-order perturbations to the electrostatics, exchange and induction terms, the dispersion term is appended as a result of these.[37] The components are denoted as $E^{(vw)}$ where *v* is the order of the intermolecular potential and *w* is the order of the intramolecular electron correlation. From **Equation 1.3** it can be seen that interactions in SAPT(0) only considers intermolecular potentials beyond zeroth order, limiting its accuracy. A HF correction (δ_{HF}^2) is added to account for the polarisation beyond the first order. DFT-SAPT is broadly comparable to SAPT(0), although the monomer's wavefunctions are calculated using density functional theory rather than HF.

$$E_{SAPT0} = E_{elec}^{(10)} + E_{exch}^{(10)} + E_{ind,resp}^{(20)} + E_{exch-ind,resp}^{(20)} + E_{disp}^{(20)} + E_{exch-disp}^{(20)} + \delta_{HF}^2 \quad \textbf{(1.3)}$$

The higher order SAPT(2) methodology uses the same dispersion prediction as SAPT(0) although includes up to second order intramolecular electron correlation terms for electrostatic, exchange and induction terms (**Equation 1.4**), in comparison to SAPT(0), which is zeroth order with respect to intramolecular electron correlation terms. Higher order SAPT methodologies, such as SAPT(2+3) contains higher order perturbations, which ultimately improve accuracy, albeit for a much higher computational cost.[37]

$$E_{SAPT2} = E_{SAPT0} + E_{elec,resp}^{(12)} + E_{exch}^{(11)} + E_{exch}^{(12)} + E_{ind}^{(22)} + E_{exch+ind}^{(22)} \quad \textbf{(1.4)}$$

These differences can greatly change the accuracy of the prediction of interaction energies. SAPT methodologies have been shown to be very sensitive to basis set choice.[37] SAPT is limited to intermolecular interactions, and therefore must be altered to investigate intramolecular interactions. When considering intramolecular interactions, assignment of particles (protons and electrons) to each fragment is key to ensure that no charge is assigned to a fragment, which will overshadow any weak molecular interaction. Covalent interactions between each fragment must also be kept constant to allow the weak interactions to be determined. The intramolecular SAPT (iSAPT) technique has been developed and shown to be a simple way to overcome these challenges.[38] Functional group SAPT (fSAPT), which is an intermolecular SAPT technique studying the interactions between different functional groups,[39] can be combined with iSAPT. Functional group intramolecular SAPT (fiSAPT) uses the same levels of methodology for intramolecular interactions, which will be used in further **Chapters 3** and **4**.[39]

1.3.3 Natural Bond Orbital (NBO) and Molecular Orbital (MO) analysis

Natural bond orbital analyses have become prevalent in the study of molecular interactions as an energetic prediction of electron delocalisation between a donor and acceptor.[24,40] Natural bond orbitals use the optimal Lewis structure, which therefore provides a localised view of molecular orbitals based on electron density between one or two atom centres. Second order perturbations are calculated using **Equation 1.5** to give the energetic importance of electron delocalisations.

$$\Delta E^2 = q_i \frac{F(i,j)^2}{\varepsilon_i - \varepsilon_j} \qquad \textbf{(1.5)}$$

Where q_i represents the donor orbital occupancy, ε_i and ε_j are the orbital energies and F is the Fock matrix element, which estimates the single electron energy operator. Although no extensive comparison on the impact of basis set and theory level has been performed on the accuracy of NBO calculations, it has been shown that the inclusion of diffuse functions within the basis set can impact the predicted energetic importance of electron delocalisations.[41] However, the theory level and basis set used to minimise the geometry could impact on the predicted energetics of electron delocalisation as

bond distances and angles are changed, which is highlighted in **Chapter 4**. Therefore the theory level and basis set that has provided the most accurate predictions of geometry and conformational energy differences have been used across all chapters in this thesis.

Unlike NBO analysis, molecular orbital analyses presented in this thesis is not limited to a local centre and instead can delocalise over the entire molecule due to being built from wavefunctions rather than electron densities. The predicted energies of molecular orbitals can indicate the stabilisation of interactions.

The combination of both techniques can provide a very useful tool to look for quantitative and qualitative evidence for electron delocalisations in molecular interactions.

1.4 Halogen bonding

Halogen bonding is the most well-known and earliest identified σ-hole interaction. Halogen bonding was first noted over 200 years ago, when a change in colour was observed upon mixing ammonia and iodine by Colin in 1814.[42] Unbeknown to them at the time, they had formed the first halogen-bonded complex, $NH_3 \cdots I_2$. The structure of this complex was confirmed by Guthrie 50 years later.[43] Since then, hundreds of theoretical and experimental investigations in to halogen bonding have been conducted, and halogen bonding was the subject of Hassel's Nobel Prize lecture.[44] Halogen bonding has been employed in a wide variety of chemical processes, including organic synthesis,[45] medicinal chemistry[9] and crystal engineering.[46] Halogen bonding exhibits a high degree of directionality, and is therefore considered analogous to H-bonding.[47,48] A prominent investigation by Resnati and Metrangolo demonstrated that halogen bonding could be a viable alternative to H-bonding in supramolecular chemistry,[49] popularising the use of this interaction to this day (**Figure 1.2**).[6,50,51] However, the nature of the interaction still remains a subject of debate for chemists. IUPAC states that a halogen bond is: "*... denoted by the three dots in R–X···Y. R–X is the halogen bond donor, X is any halogen atom with an electrophilic region, and R is a group covalently bound to X. Y is the halogen bond acceptor and is typically a molecular entity possessing at least one nucleophilic region. The X···Y distance is less*

than van der Waals separations, the R–X···Y angle is around 180° and the R–X bond length is slightly elongated.".[52]

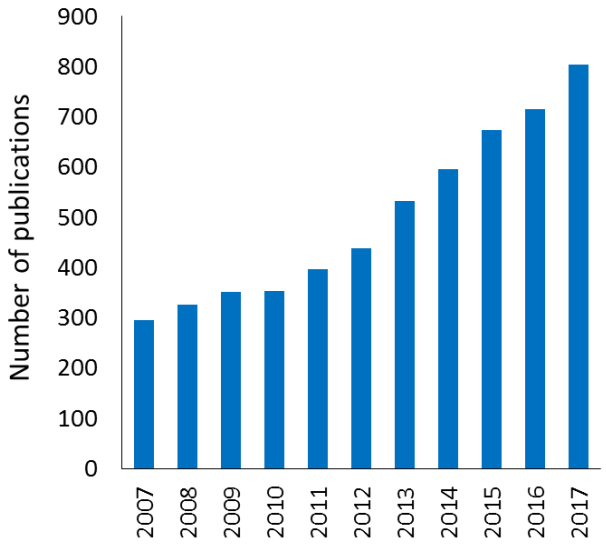

Figure 1.2 Number of publications featuring the key words "halogen bonding" from Thomson Reuters Web of Knowledge (02/2018).

The dominant literature rationalisations of halogen bonding propose that the interaction is either partially covalent, or primarily electrostatic. The proposed partial covalency of halogen bonding is attributed to electron delocalisation from the lone pair of a Lewis base into the antibonding σ-bond of the R-X bond, denoted an n→σ* delocalisation. This delocalisation stabilises the lone pair of the halogen bond acceptor (**Figure 1.3**).

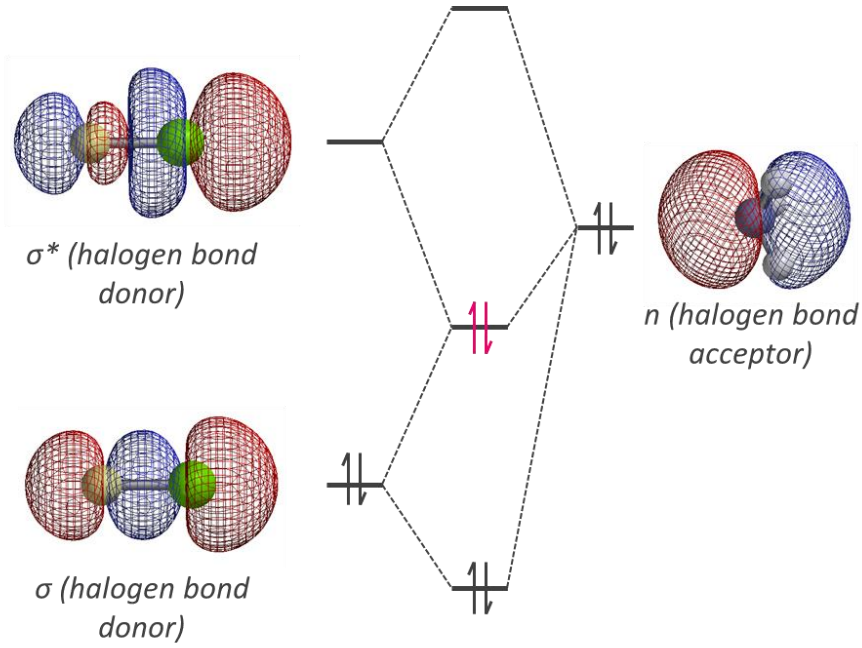

Figure 1.3 A simplified molecular orbital diagram, showing the combination of the lone pair of the halogen bond acceptor (right) in to the σ* of the halogen bond donor. Stabilised electrons are shown in pink. MOs calculated using Spartan '14, DFT/B3LYP/6-311G*.

Halogen bonding has been studied using numerous techniques including spectroscopy, X-ray crystallography and theoretical energy decomposition. The findings of different experimental and computational investigations of halogen bonding are discussed below.

1.4.1 σ-hole theory

Considering a simple electrostatic model, it is counterintuitive that interactions between two 'negative' atoms, such as chlorine and bromine, would form favourable interactions. Despite this, early crystal database searches for complexes involving halogens have demonstrated that halogens can interact with 'negative' nucleophilic species. Nucleophiles (Nu^-) generally interact with a halogen, X at an angle of 160–180° relative to the covalent σ-bond to another atom (black circle) (**Figure 1.4**).[53,54] In

contrast, electrophiles (E^+) were seen to interact with halogens at an angle of 90–120° relative to the covalent σ-bond (**Figure 1.4**).[53,54]

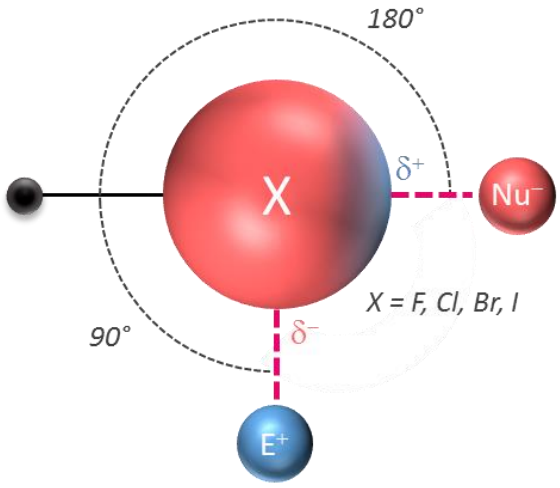

Figure 1.4 Schematic of interactions between electrophilic (E^+) and nucleophilic (Nu^-) species and a halogen (X = F, Cl, Br or I).

One of the most influential models employed in the investigation of the nature of halogen bonding is σ-hole theory (**Figures 1.1** and **1.4**). The ESPs of halogenated species were first investigated in 1992 by Brinck *et al.*,[19] which, surprisingly, revealed that covalent halogen atoms have areas of both negative and positive potential on their atomic surfaces, where the positive potential sits along the C–X bond axis (**Figure 1.5**). The electrostatic potential (*Vr*) at any point on the molecule (r) is given by **Equation 1.6**, where Z_A is the charge on nucleus A at point R_A and $\rho(r)$ is the electron density. An electrostatic potential calculated on a surface is denoted as $V_s(r)$, and in the case of σ-holes, $V_{s,max}(r)$ (the maximum positive potential) sits along the R–X bond, and is defined by a contour of its electron density of 0.001 au by Bader, resembling the van der Waals surface of the atom.[55]

$$V(r) = \sum_r \frac{Z_A}{|R_A - r|} - \int \frac{\rho(r')dr'}{|r' - r|} \qquad \textbf{(1.6)}$$

Such ESP surfaces provided a qualitative explanation for the observation that electrophiles could interact with the 'negative' ring surrounding the halogen, while

nucleophiles interact with the 'positive' hole (**Figure 1.5**). ESPs have subsequently been used to explain the intermolecular contacts observed in the crystal structures of halomethanes. However, it took 15 years until Clark *et al*. named such positive regions as σ-holes, due to its location along the σ-bond of the C–X bond.[1]

The size and magnitude of the positive potential increases down the halogen group; I > Br > Cl, with F not generally displaying a σ-hole (**Figure 1.5**, right), in accordance with the increase in electronegativity and decrease in polarizability. Nonetheless, fluorine has still been shown to take part in halogen bonding.[56,57] The inclusion of substituents can tune the size of the σ-hole even more, with electron-withdrawing groups increasing the size and magnitude of the positive hole, and electron-donating groups shrinking it.[58]

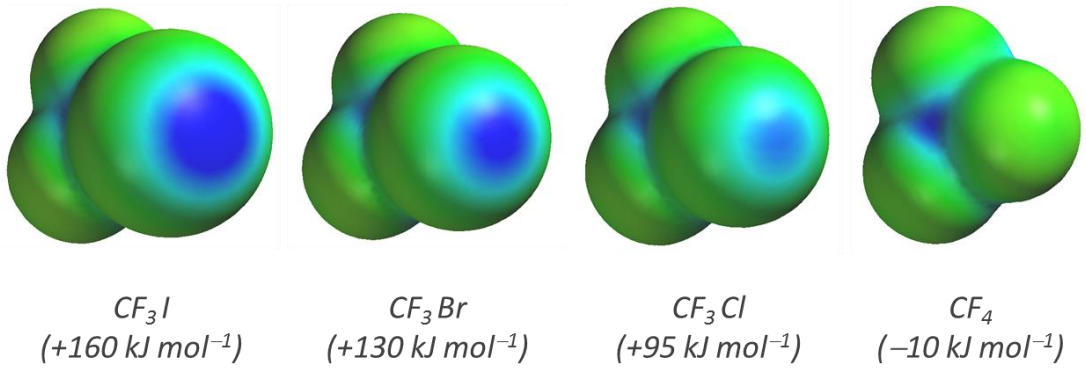

Figure 1.5 ESPs of CF_3X, with $V_{s,max}$ values shown below. Calculated using Spartan '14, DFT/B3LYP/6-311G*.

The σ-hole observed in the electrostatic potential of halogen-containing molecules can be explained by considering atomic orbitals (AOs). If we study, for example, the chlorine atom, its electronic structure is [Ne]$3s^2 3p_x^2 3p_y^2 3p_z^1$, where the *z* axis is in the direction of the R–X bond. The single electron in the $3p_z$ orbital sits predominantly in the R–X bond causing an electron-deficient region along the covalent bond, or a positive potential hole (**Figure 1.6**).[59]

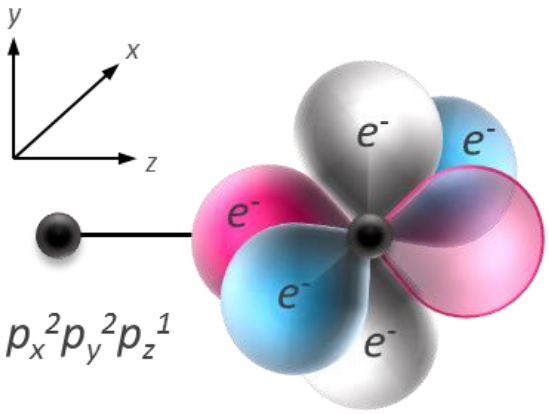

Figure 1.6 Diagram of molecular orbitals p_z (pink), p_x (blue) and p_y (white), electrons are represented by e^-. Filled lobes are shown as solid. The outer lobe of p_z is electron deficient (shown as transparent) and manifests as a σ-hole. Black dots represent the atoms in the molecule.

It is perhaps surprising that the σ-hole concept has taken so long to develop given that as the anisotropy of electron density on halogens has been known since the 1960s![60] The σ-hole explanation is in agreement with Feynman's original theory that all molecular interactions are electrostatically driven,[20] which has also gained the of several chemists more recently.[52,61,62] It has been proposed that some fluorinated and chlorinated molecules that lack positively charged σ-holes may still form favourable interactions with nucleophiles via σ-holes that have a negative charge, albeit less negative than the rest of the halogen surface.[56,63] The appearance of negative σ-holes still interacting with 'negative' halogen bond acceptors shows an electrostatic argument is a minimalistic view of halogen bonding.

A number of investigations have been used to show the correlation between the magnitude of the ESP over the σ-hole and the interaction energy.[64–69] In general, it has been well demonstrated qualitatively that the more positive a σ-hole the stronger the halogen bond. When using predicted interaction energies, both Politzer[64] and Hobza[69] have found surprisingly strong correlations between the interaction energy and electrostatic surface potential maxima, $V_{s,max}$ (**Figure 1.7**).

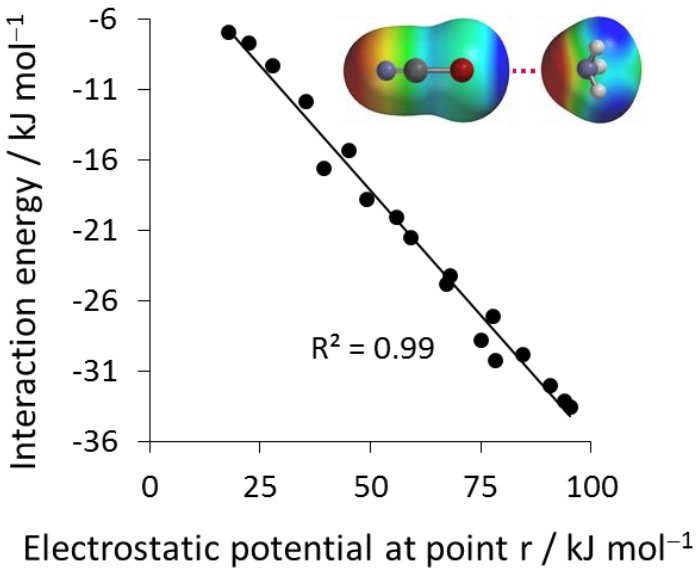

Figure 1.7 Predicted interaction energies of CN-Br···NH_3 versus the electrostatic potential at various positions (r) on the nitrogen, giving different interaction angles ranging from 100–180°. Adapted from reference 64.

Despite this apparent qualitative link between the electrostatic potential and predicted interaction energies, these results lack experimental verification.

1.4.2 Spectroscopic analysis of halogen bonding

Spectroscopy is a powerful experimental tool for studying molecular interactions and their associated solvent effects. In this regard, nuclear magnetic resonance (NMR),[70] ultraviolet/visible (UV),[71] infrared (IR)[72] and microwave spectroscopy[73] have all be used in determining characteristics of molecular interactions. Some of the earliest work by Benesi and Hildebrand used UV/vis spectroscopy to investigate the potential "charge transfer" in halogen bonding as first proposed by Mulliken in the 1950s and further discussed in relation to halogen bonding by Bent *et al*..[74] UV/vis spectroscopy has led to further investigations into the strength and properties of halogen bonding.[75] One of the more recent and significant contributions to the investigation of halogen bonding is by Hunter *et al*..[76] Hunter developed a system to predict the free energy of

H-bonding complexes using H-bond donor and acceptor abilities of the solute (α and β respectively) and the solvent (α_s and β_s) (**Equation 1.7**).[16,77]

$$\Delta G^{\circ}_{calc} = -(\alpha - \alpha_s) \times (\beta - \beta_s) + c \qquad (\mathbf{1.7})$$

These α and β parameters be calculated from ESPs or measured experimentally through titration, while *c* represents an empirically determined constant worth 6 kJ mol^{-1} that encodes the entropy cost of bimolecular association.[16] Thus, if the energetics of halogen bonding were dominated by electrostatics in the same way that hydrogen bonds often are, one might expect that the same model might work well for the prediction of halogen bond energies. Thus, UV/vis and NMR titrations were performed with either H-bond or halogen bond donors and acceptors in a range of solvents from apolar *n*-ocatane to polar methanol to compare the nature of these interactions and their associated solvent effects (**Figure 1.8**).

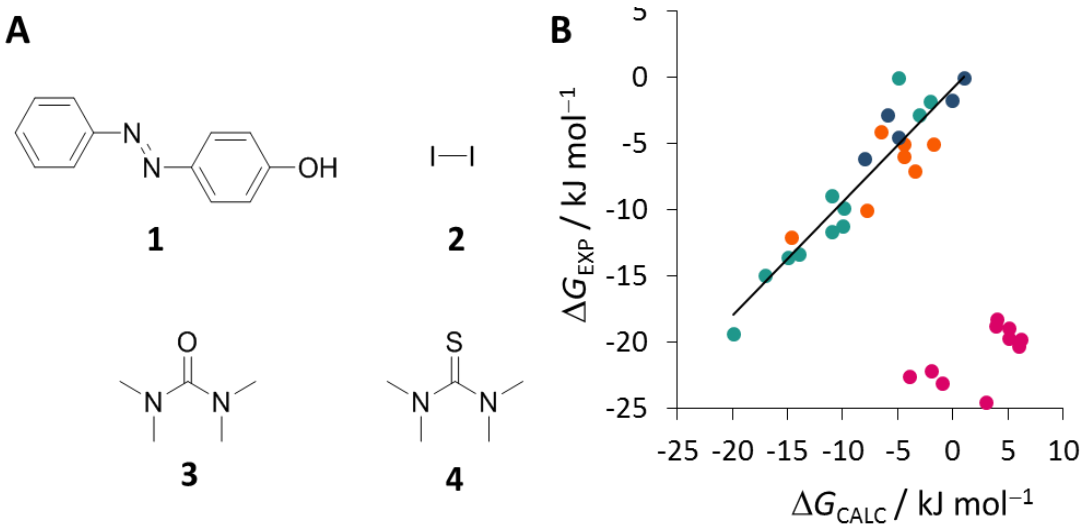

Figure 1.8 (A) Structures of the hydrogen (**1**) and halogen (**2**) bond donors and acceptors (**3** and **4**). (B) Plot of experimentally measured free energies across a range of solvents versus calculated free energies for complexes **1**:**3** (teal), **1**:**4** (orange), **2**:**3** (blue) and **2**:**4** (pink). Adapted from reference 78.

In general, H-bonded complexes displayed a good correlation with free energies predicted using **Equation 1.7**

(**Figure 1.8B**, teal and orange). For halogen bonding, the I_2···**3** complex correlated well too (**Figure 1.8B**, blue). However, complex I_2···**4** followed a very different trend, showing interactions in complex I_2···**4** were much stronger than could be predicted using **Equation 1.7**. The experimental association constants appeared to show a stark solvent independence (**Figure 1.8B**, pink), with only slight reductions in association constants moving from apolar (e.g. *n*-octane) to polar solvents (e.g. methanol), contrasting the large decreases seen in all other complexes. Interestingly, the UV/vis spectra for the two halogen bonding complexes appeared to be very different (**Figure 1.9**), with the spectrum for I_2···**4** being dominated by a charge transfer band at 330–340 nm, implying the governing factors for the two complexes may be quite different.

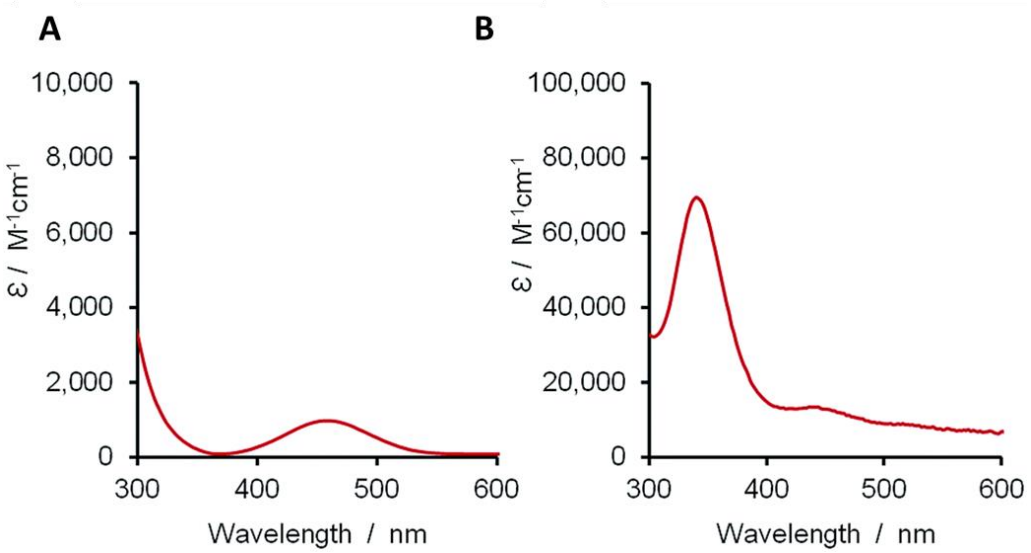

Figure 1.9 UV/Vis traces of (A) complex **2**:**3** and (B) complex **2**:**4**. Replicated from reference 78.

The absorption band (330–340 nm) and coefficient for the charge transfer (30000–55000 M^{-1} cm^{-1}) remained roughly the same in all solvents, confirming the solvent independence of the strong interaction. The same effects have been presented in theoretical work, with weaker halogen bonds behaving similarly to H-bonds (e.g.

complex I_2···**3**), whereas stronger halogen bonds appearing to be more covalent in nature (e.g. I_2···**4**).[78]

NMR has also become a gold standard in experimental investigations of non-covalent interactions. Studying chemical shift changes via NMR titrations in combination with a binding isotherm can reveal the energetic significance of interactions in solution.[79] Pioneers of halogen bonding Metrangolo and Resnati used NMR studies to observe potential lone pair (n) to R–X antibonding σ* orbital (**Figure 1.3**), denoted n→σ* interactions. The binding of halo-perfluoroalkanes and N, O and S-containing acceptors resulted in chemical shifts of up to 7 ppm in ^{15}N and ^{19}F NMR spectra. The addition of an electron-withdrawing group next to the halogen resulted in greater *s* character in the lone pair, n, and therefore a weaker interaction due to the lower electron delocalisation, consistent with n→σ* orbital delocalisation.[80] Further NMR studies confirmed the importance of this delocalisation in halogen bonding.[81]

Taylor and co-workers have performed notable NMR investigations into halogen bonding complexes. Sarwar *et al*. studied halogen bonding complexes with Lewis base acceptors by comparing experimentally determined binding constants with the electrostatic potentials of the halogen-bond donor.[82] Hammett substituent constants (σ_m) and ESPs were plotted against the binding constant, and gave good correlations (**Figure 1.10**), implying an electrostatically driven interaction. However, the small data set makes the correlation far from convincing, and Taylor more recent NMR binding studies contradict the original findings.[83]

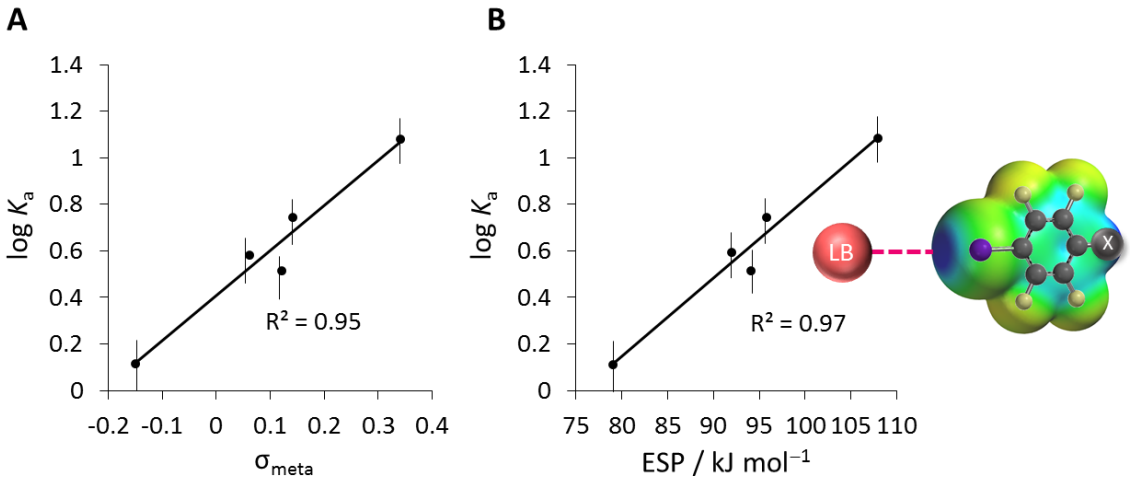

Figure 1.10 Plots of log of the binding constant, K_a, versus (A) σ_{meta} and (B) ESP calculated using DFT/B3LYP/6-31G**. Recreated from reference 82.

The more recent work also used Hunter's electrostatic interaction model to interrogate experimentally determined binding constants between both organic (perfluorinated iodoalkanes or arenes) and inorganic (I_2, IBr, ICN) halogen-bond donors, and oxygen- and nitrogen-containing acceptors. In agreement with Hunter's previous findings, no correlation between experimentally measured free energies and those predicted using Hunter's model was found (**Equation 1.7**). This work reinforces the idea that a purely electrostatic model of halogen bonding cannot satisfactorily explain the experimentally observed behaviour of halogen bonds.[83]

NMR spectroscopy can provide accurate, experimental binding energies, while also revealing the importance of solvent effects. Whilst the studies highlighted above provide an interesting insight into the energetics of halogen bonding, there remains a lack of definitive quantitative data from which the underlying physicochemical origin of halogen bonding can be determined.

One of the largest contributions to experimental measurements of halogen bonding comes from Legon who has used microwave spectroscopy to investigate the potential electron delocalisation accompanying these interactions.[84] Microwave spectroscopy can be used to investigate the electron distribution across complexes. Mulliken first proposed electron delocalisation occurring in molecular interactions in the 1950s. He classified the electron delocalisations as either a strong, inner type or a weak, outer

type interactions. An outer type interaction occurred when only a small electron delocalisation was seen, and was generally accompanied by a larger electrostatic attraction.[25] Whereas an inner type interaction was stronger with a large electron delocalisation, leaning towards interactions with greater 'bonding' character. Legon sought to discover which classification of electron delocalisation interactions halogen bonding belonged to. Upon studying the electron distribution of a large range of halogen-bonding complexes, Legon found only minimal electron delocalisation, and thus classified these interactions as being outer-type according to Mulliken.[84,85] Legon's microwave spectroscopy studies have provided a useful insight into halogen bonding and demonstrate that overarching electrostatic effects cause halogen bonds to be favourable. Since these microwave spectroscopy experiments were performed in the gas phase, no insight into solvent effects, or the significance of such interaction in solution could be determined.

Finally, vibrational spectroscopy, including IR and Raman spectroscopy, has been used to investigate halogen bonding.[86,87] Vibrational spectra can be measured experimentally and compared with predictions from theory. Cremer *et al*. used the stretching force constant (k^a) from computationally predicted IR vibrational spectroscopy, which is related to the experimentally measured intermonomer stretching force constants, k_σ to investigate the strength and nature of halogen bonding complexes.[88,89] IR spectra were combined with computational methods to show that halogen bonding appeared to be electrostatic when weak, and partially covalent when strong.[90] Cremer has since expanded the analysis to a much larger data set containing over 200 halogen bonding complexes. The results are in agreement with the proposal that strong halogen bonds can be considered as being partially covalent and that the origin of this partial covalency stems from n→σ* electron delocalisation.[87]

X-ray crystallography has been a key experimental tool for identifying and investigating non-covalent interactions. X-ray data provided some of the earliest indications of favourable interactions between halogens and Lewis bases. An early survey of the Cambridge Structural Database (CSD) found numerous halogen···N, O or S intermolecular contacts.[91] In this study, Lommerse *et al*. combined the experimental structures seen in the solid state with computational predictions of

interaction strength. He concluded that electrostatic effects were the predominant contributor to the interaction due to the calculated increase in interaction strength with the increasing electronegativity of the halogen-bond acceptor (S < N < O).

While crystallography allows us to identify the presence of interactions, other crystallographic techniques are required to probe their nature. Beer *et al*. used X-ray absorption spectroscopy to observe the electronic structure of [2]catenanes that exploit halogen bonds for anion recognition (**Figure 1.11**).[92]

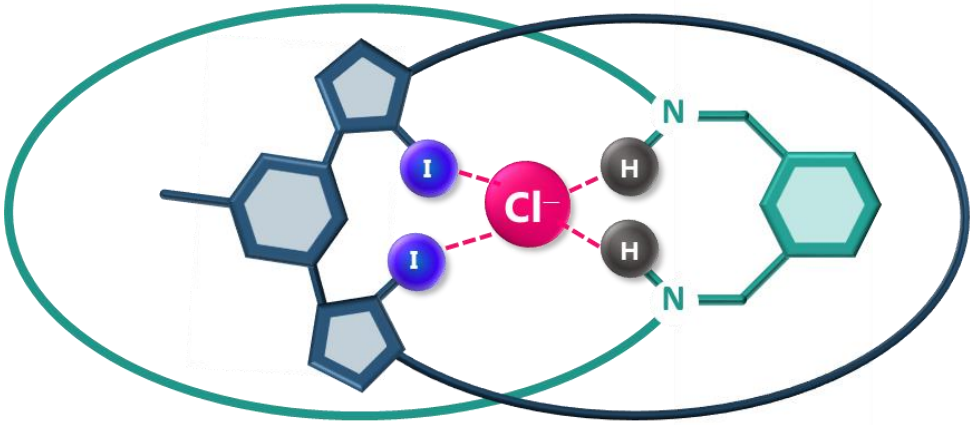

Figure 1.11 Schematic of the [2]catenane structure used to study halogen bonding. Adapted from reference 92.

While demonstrating the ability of the system to provide selectivity for anions, X-ray absorption spectroscopy (XAS), which allows the study of electronic structure, was used to investigate the halogen bonding interactions within the system. This approach has previously been used to examine interactions between chlorine and metals, and revealed electron delocalisation from the halogen atom into the empty *d*-orbitals of the metal.[93] Remarkably, the same type of analysis revealed that the 1*s* electrons of the chloride anion were delocalised into the empty anti-bonding R–X* orbital, $Cl_{1s} \rightarrow \sigma^*_{R-X}$ in their catenated system (**Figure 1.12**). Furthermore, the XAS technique allowed the level of covalency within the interaction to be directly observed,

as the intensity of the observed transitions is proportional to the amount of Cl_{3p} electrons delocalised into the acceptor orbitals.[94]

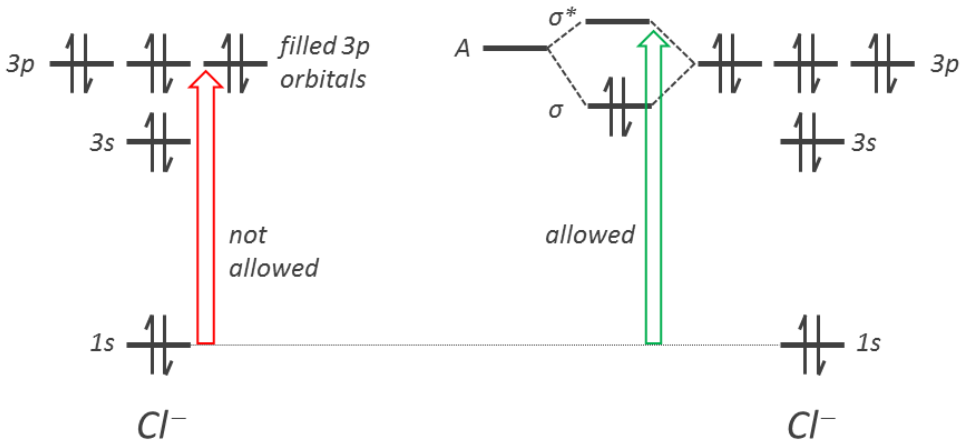

Figure 1.12 The allowed and not allowed transitions of Cl^- with an acceptor (A). Adapted from reference 94.

The experimental results clearly demonstrate the importance of electron delocalisation in halogen bonding. A single halogen bond results in a ~6% electron delocalisation from halide ion to acceptor, compared to H-bonding with less than 1% transfer. Interestingly, the addition of a second halogen bond acceptor approximately doubles the donation to ~11%, indicating an additive nature. This level of electron delocalisation is comparable to that seen in transition-metal complexes, where the covalency of ligand binding is widely accepted.[93] Other halogen-bonding complexes have been shown to behave in a similar fashion using XAS, lending further support to a partial covalent argument, arising from the same n→σ* electron delocalisation.[95]

Overall, spectroscopy has provided large amounts of experimental data investigating halogen bonds. However, different experimental methods and model systems present conflicting data interpretations; whilst UV/vis and XAS data[13] suggest that electron delocalisation is involved, this suggestion is countered by some NMR[82] and microwave spectroscopy data[84] that support a predominantly electrostatic interaction.

1.4.3 Energy decomposition analysis of halogen bonding

Hobza has been a major contributor in this area, analysing hundreds of halogen bonding complexes and coming to the conclusion energy contributions were electrostatic > induction > dispersion when a strong halogen bond was present (> 29.3 kJ mol^{-1}), while weaker halogen bonds seemed to be dominated most often by dispersion.[59] One of Hobza and co-workers' investigations used coupled cluster theory and the complete basis set to obtain the interaction energies of halomethane···formaldehyde dimers.[96] SAPT(0) analysis was used to further uncover the relative contributions to the halogen bonding interaction. The halogen bond donor propensities were found to be in the expected order, CH_3I > CH_3Br > CH_3Cl. Most interestingly, when it came to SAPT(0) analysis, both chloro- and bromomethane showed dispersion as the dominant component of the interaction (61% and 52% respectively of the total SAPT interaction energy when using large basis set aug-cc-pVQZ), while induction accounted for less than 10% of the binding energy in the dimers. However, the CH_3I···$O{=}CH_2$ interaction appears to be dominated by electrostatics (54%) (**Figure 1.13A**). Hobza's investigation using SAPT decomposition analysis would suggest electrostatics is the dominating force in halogen bonding. However, SAPT could not agree with the more accurate coupled cluster predicted interactions energies, revealing the potential inaccuracies of the SAPT calculation.

Hobza further tested their hypothesis of an electrostatically governed interaction, by substituting the protons with electron-withdrawing fluorines (CF_3X).[96] They found the interaction could be varied greatly depending on the number of fluorine substituents added (one, two or three) and all interactions became dominated by electrostatics as more fluorine atoms were added (**Figure 1.13B**). Hobza's further investigations have also used halogen-bonding directionality to confirm the electrostatic nature of halogen bonding.[97] It was found that the most favourable geometry was when the interatomic angle between donor an acceptor was 180°. Hobza claimed this was due to best alignment with the positive σ-hole, however, this interaction geometry would also support an n→σ* electron delocalisation model given the directionality needed for significant orbital overlap.

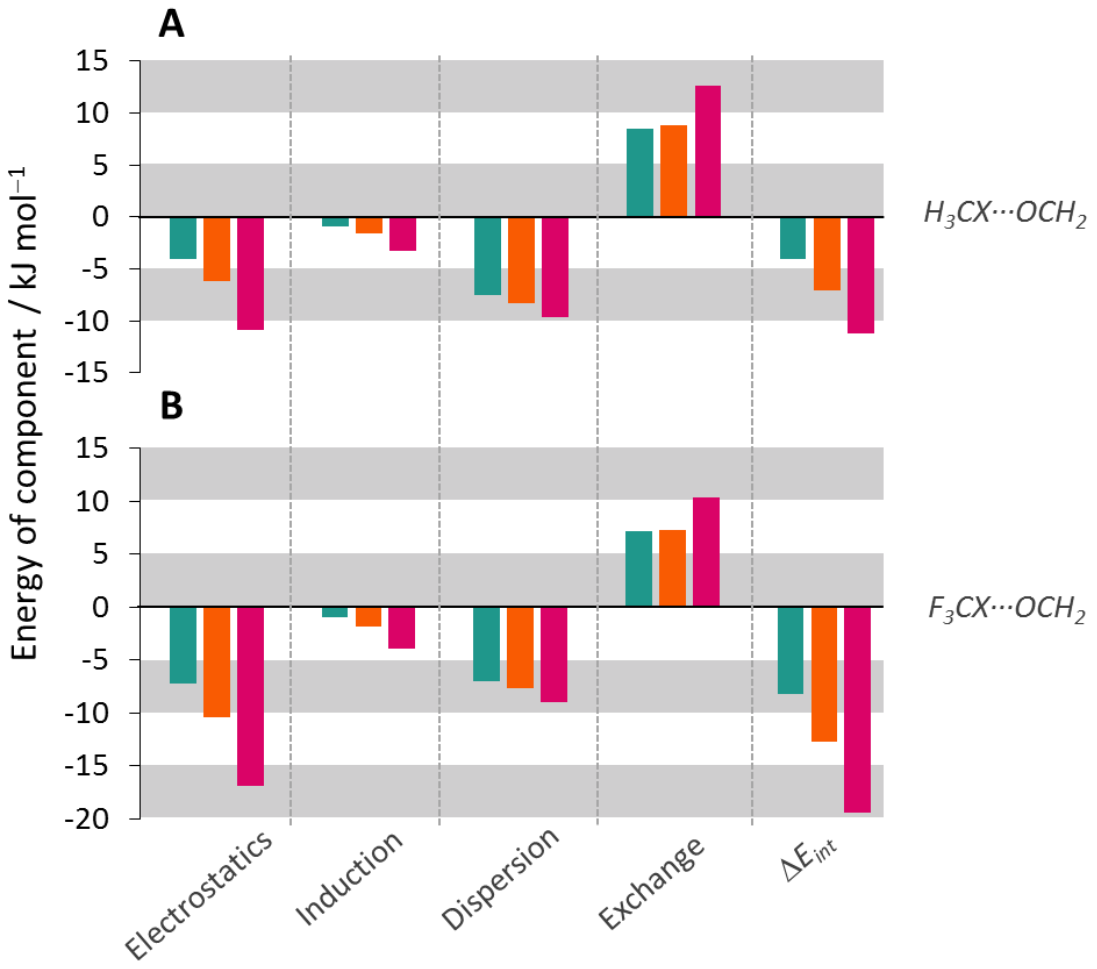

Figure 1.13 SAPT contribution energies for RX···OCH_2 (R = CH_3 (A) or CF_3,(B) X = Cl (teal), Br (orange) or I (pink)) in kJ mol^{-1}. Calculated using SAPT(0)/aug-cc-pVTZ. Values taken from reference 97.

Stone used a similar SAPT method based on density functional theory (DFT-SAPT) to Hobza for investigating the impact of varying the interaction angle between halogens and Lewis bases. Stone agreed with Hobza that electrostatics played a dominant role in the overall interaction energy, although the most favourable electrostatic interaction energy did not match the most favourable geometry.[98] Stone instead found that it was important to account for induction and dispersion in halogen-bonding interactions.

Others have used SAPT to investigate the importance of dispersion is halogen bonding.[99] Dispersion was found to play a much larger role in interactions between

two, more diffuse halogens such as bromine, when decomposed by SAPT. Whereas interactions involving less diffuse halogens like chlorine appear to have less of a dispersive component.[96,99,100]

An alternative energy decomposition method applied to halogen bonding is the Kohn-Sham molecular orbital method. Unlike SAPT, this decomposition divides the total interaction energy in to electrostatics ($\Delta V_{electro}$), exchange (or Pauli repulsion, ΔE_{exch}) and an orbital interaction contribution (ΔE_{oi}) (**Equation 1.8**).

$$\Delta E_{int} = \Delta V_{electro} + \Delta E_{exch} + \Delta E_{oi} \qquad \textbf{(1.8)}$$

The orbital interaction term accounts purely for the electron delocalisation, whether moving from an occupied to an unoccupied orbital, or orbital mixing from one fragment to another. Palusiak studied the interaction between CH_3X and formaldehyde,[101] which gives an interesting comparison to the same system Hobza studied using SAPT decomposition.[96] Contrary to Hobza's findings, Palusiak found that the orbital interaction is the largest contributor since favourable electrostatic contributions were usually outweighed by a repulsive exchange term that scaled with the favourability of the electrostatic term (**Figure 1.14**).

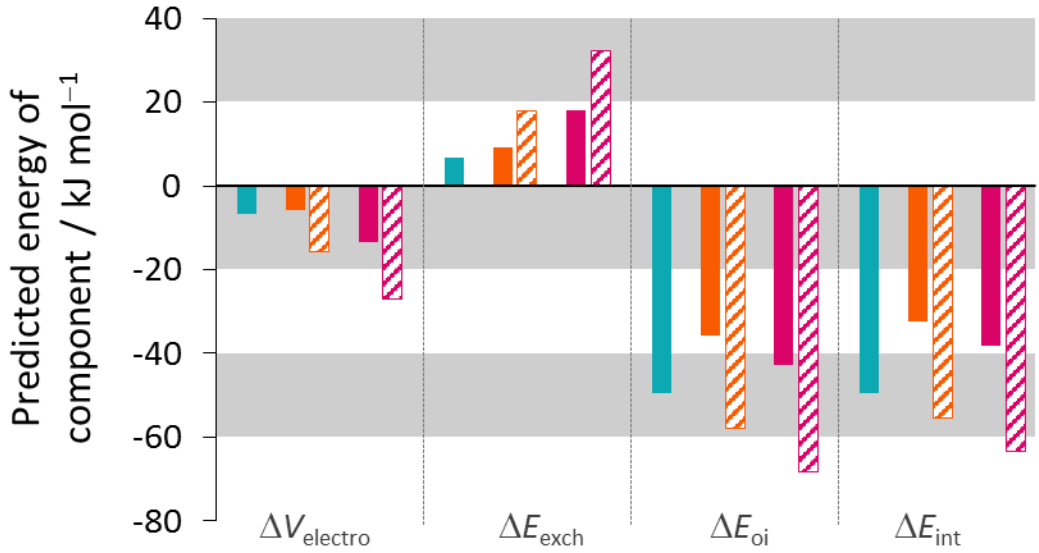

Figure 1.14 Energetic components of interactions RX···OCH_2 where X= Cl (teal), Br (orange) and I (pink) and R = CH_3 (solid) or CF_3 (dashed). Values taken from reference 101.

Palusiak proposed that this was due to a HOMO→LUMO electron delocalisation, which is consistent with the earlier discussed n→σ* interaction (**Figure 1.15**). Other studies performed using the Kohn-Sham decomposition method have supported the findings of a significant orbital interaction in halogen bonding,[102] including in Beer *et al.*'s [2]catenane halogen bond anion recognition system that was discussed earlier (**Figure 1.11**).[92]

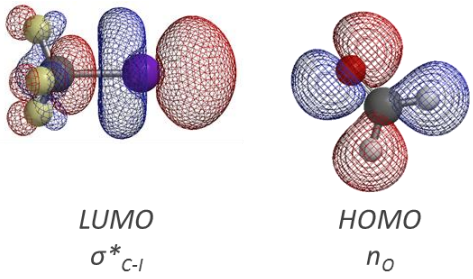

Figure 1.15 Molecular orbitals corresponding to the LUMO of the halogen bond donor and LUMO of the halogen bond acceptor. Molecular orbitals calculated using Spartan '14 DFT/B3LYP/6-311G*.

A very recent energy decomposition analysis developed by Head-Gordon *et al.* employs a molecular orbital approach.[103] The Absolutely Localised Molecular Orbital

energy decomposition analysis (ALMO-EDA) describes the interactions using the frozen energy of the complex (ΔE_{frz}), which is the energy change seen when bringing together two fragments that have been infinitely separated without relaxing their molecular orbitals. The energetics of polarisation (ΔE_{pol}), dispersion (ΔE_{disp}) and charge transfer (ΔE_{CT}) are also given (**Equation 1.9**).

$$\Delta E = \Delta E_{frz} + \Delta E_{pol} + \Delta E_{disp} + \Delta E_{CT} \qquad \textbf{(1.9)}$$

The decomposition suggested that charge transfer and polarisation dominated the interaction energy in $CX_3I\cdots Y^-$ complexes (where X = F, Cl, Br or I, Y = F, Cl or Br) (**Figure 1.16**). As expected, as the fragments were brought closer together the energy differences became larger, giving an increasingly unfavourable frozen energy term, mirroring a van der Waals energy profile.

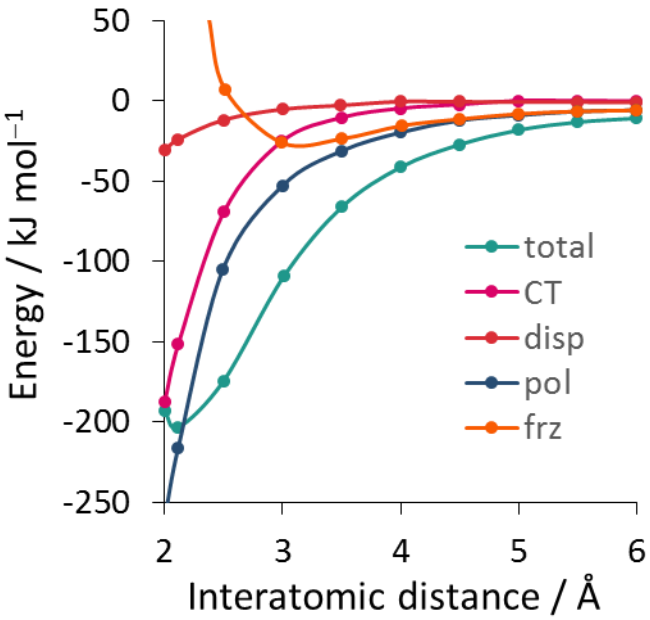

Figure 1.16 Total energy and component energies versus interatomic distance of $CF_3I\cdots F^-$ complex. Adapted from reference 103.

Energy decomposition analyses provide a useful means of rationalising the relative contributions to a molecular interaction. However, as has been highlighted by the above cases, a major limitation is that the major energetic contributors identified by a particular EDA approach may vary from method to method. For example, SAPT-based

analyses suggest that halogen bonding is electrostatic in nature, with significant additional contributions from dispersion. However, when other EDAs are used that include a specific orbital interaction term (such as Kohn-Sham) the energetic significance of electron delocalisation increases to the point where the nature of halogen bonding can be attributed to n→σ* delocalisation.

1.3.4 Natural Bond Orbital (NBO) and other computational methods for analysing halogen bonding

Although SAPT decomposition (*vide supra*) has been used in relation to halogen bonding, as noted previously, SAPT may struggle to account for the electron delocalisation term properly. Despite this, the technique has been used to estimate the influence of electron delocalisation and, at least qualitatively, show the occurrence of electron delocalisation within halogen bonding.

Instead, natural bond orbital (NBO) analysis has generally proved more useful in the study of electron delocalisation in halogen bonding, providing a means of estimating the energetic significance of electron delocalisation in molecular interactions.[40] NBOs are a theoretical construct that sits between an atomic and molecular orbital. Prediction of natural orbitals allows the electron density that sits between atoms to be predicted. It has been claimed that NBO (versus natural atomic orbitals (NAO)) gives the most accurate prediction of the Lewis structure.[24]

One NBO study investigated halogen bonding between pyridine and di- or interhalogens (halogens bonded to a non-halogen atom). The dimerization of such species can give rise to two conformations: a halogen···π interaction (**Figure 1.17A**) and a halogen bonding interaction, halogen···N (**Figure 1.17B**).[104]

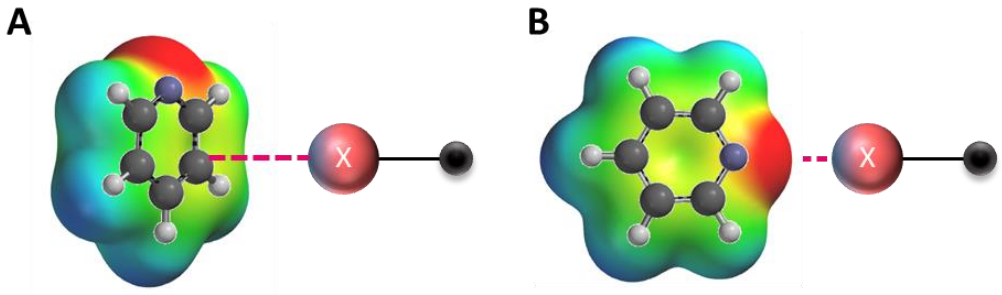

Figure 1.17 Schematic showing the possible binding modes of halogens and pyridine forming a (A) halogen···π or (B) halogen···N interaction. Black dots represent the rest of the molecule.

Where a halogen bond is formed, the halogen-halogen bond length increases, indictive of an antibonding orbital being filled, whilst the C–N bond in the pyridine shortens. These dimers were generally found to be the most stable, with interactions with halogen···π interactions being weaker. NBO analysis provides second order perturbation energies (ΔE^2) and stabilisation energies of the donor-acceptor interactions and can therefore be used to estimate the energetic contribution of electron delocalisation interactions. Wang *et al*. found that the orbital delocalisation from $n \rightarrow \sigma^*_{C\text{-}X}$ were very significant, with ΔE^2 values showing that electron delocalisation was worth an energetic contribution of ~200 kJ mol^{-1}.[104] Furthermore, SAPT(2) analysis showed that the induction component accounted for up to 63% of the interaction.

NBO analysis can also be used to predict the 'number' of electrons that are transferred or held between two atoms. A computational study of the interactions between halobromides and Lewis bases performed by Rosokha suggested that 0.028 e^- were transferred in the $CH_3Br\cdots OCN^-$ complex in dichloromethane (DCM) versus 0.32 e^- in $CH_3Br\cdots N_3^-$ in the gas phase.[105,106] In an extreme instance, the interatomic Br···N distance in $NO_2CBr_3\cdots N_3^-$ was found to be the same as the C–Br bond in the halogen bond donor. Such a remarkably short interatomic distance was ascribed to transfer of the entire electron, effectively forming a covalent bond. This predicted electron transfer correlated very well with the change in C–Br bond length on complexation.[106] Rosokha's investigations into halogen bonds agree with Wang's

findings that an electron delocalisation is an important energetic factor in halogen bonds.

Many other investigations have used simple systems to investigate halogen bonding by NBO analysis, all agreeing with the findings of Wang and Rosokha that an n→σ* electron delocalisation provides a large stabilisation in the formation of halogen bonds.[107] These findings have been supported further using another computational technique called the Quantum Theory in Atoms in Molecules (QMAIM). QTAIM, similar to NBO, allows the detection of bond critical points between atoms, which is defined as where the differential of the electron density at point r, $\nabla\rho(r)$, is equal to 0. This gives a bond critical point, which is the trajectory where the electron density is the highest. The electron density at the bond critical point can be calculated giving an indication how covalent an interaction is. AIM investigations of halogen bonding have largely supported the findings of NBO calculations, since the calculated electron densities at the bond critical point are indicative of a significant covalent character in halogen bonding.[108,109]

NBO and AIM analyses both suggest that electron delocalisation occurs, supporting early molecular orbital analyses of halogen bonding by Morokuma *et al*..[110] The literature agrees that n→σ* orbital interaction is the source of this delocalisation and that this substantially contributes to the stabilisation of halogen bonds. However, further links to experimental results are needed to provide quantitative evidence for the partial covalency of halogen bonding.

1.3.5 Halogen bonding conclusion

The nature and energetics of halogen bonding has been extensively investigated using both experimental and computational techniques. The results have presented a complicated picture, with results from experiment and theory differing in their definition, sometimes even on the same system! It is clear electrostatics, dispersion and partial covalency all contribute to the experimental behaviour. However, experimental results show a purely electrostatic model cannot explain the behaviour seen in either the solid or solution phase. The experimental results seen, particularly

from UV/Vis and X-ray spectroscopy, have indicated the importance of partial covalency in halogen bonding. What is clear is a purely computational or experimental study cannot alone provide an accurate definition. Instead, theory should be combined with experiment to look for quantitative evidence of the nature of halogen bonding. From the results presented in this section it appears a purely electrostatic model (for example using ESPs) cannot fully explain the experimental behaviour. This viewpoint is confirmed when combined with other experimental results such as XAS and computational analyses. In future discussions of halogen bonding an electron delocalisation model should be considered as an important contributor to the overall stability of halogen bond formation.

1.5 Chalcogen bonding

Interest in chalcogen bonding has risen significantly over the past decade and it has become established as an important class of σ-hole interaction. However, the nature of the interaction is still subject to debate. The chalcogens are group 16 elements: O, S, Se and Te. Chalcogen atoms may also possess σ-holes that increase in size going down the group (**Figure 1.18**).

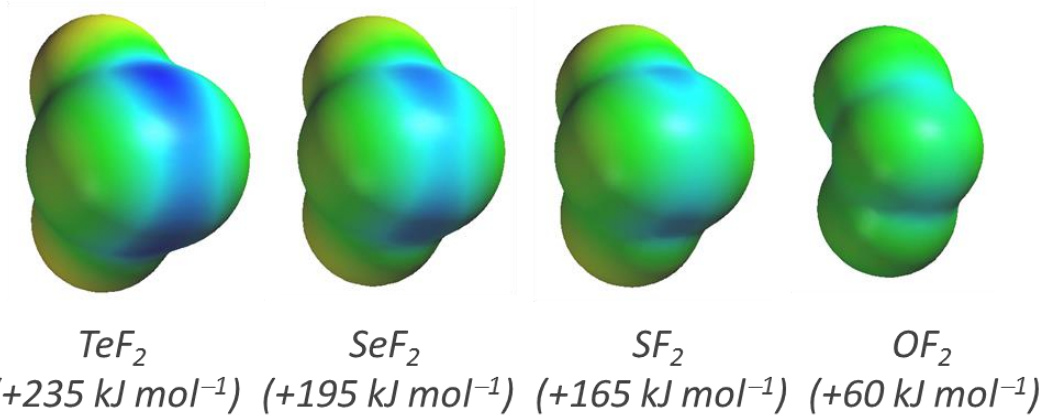

Figure 1.18 ESPs of ChF_2, with $V_{s,max}$ values shown below. Calculated using Spartan '14, DFT/B3LYP/3-21G.

Chalcogen bonding has found use in biological,[8] catalytic[111] and supramolecular chemistry,[5,12] but still there is no rigorous definition as to what constitutes a chalcogen bond. While chalcogen bonding has been widely accepted to be an electrostatically driven interaction since the introduction of σ-hole theory, experimental and computational results have so far been inconclusive on the nature of the interaction. Alongside the electrostatic explanation of chalcogen bonding, partial covalency has also been proposed as an important factor in driving chalcogen bonding. Partial covalency is generally considered to be due to the electron delocalisation from the lone pair (n) of a Lewis base in to the antibonding σ-bond of the chalcogen bond donor (σ*), as seen in halogen bonding (**Figure 1.3**).

This section of the thesis will focus on the investigations in to the nature of chalcogen bonding.

1.5.1 σ-hole theory in chalcogen bonding

Clarke, who first predicted this 'new' interaction in 2007, has been at the forefront of investigating the electrostatic nature of chalcogen bonding, along with Politzer.[112] He, and others, propose that a positive σ-hole, located along the σ-bonds (**Figure 1.18**), can interact with a Lewis base (**Figure 1.19**). Chalcogen bonding can explain trends seen in crystal structures surveys from 30–40 years ago, where disulfide crystals were seen to interact with both nucleophiles and electrophiles at different angles.[113,114] In contrast to halogen bonding, chalcogens possess two σ-holes (when sp^3 hybridised), meaning chalcogens can interact with two Lewis bases at the same time (**Figure 1.19**).

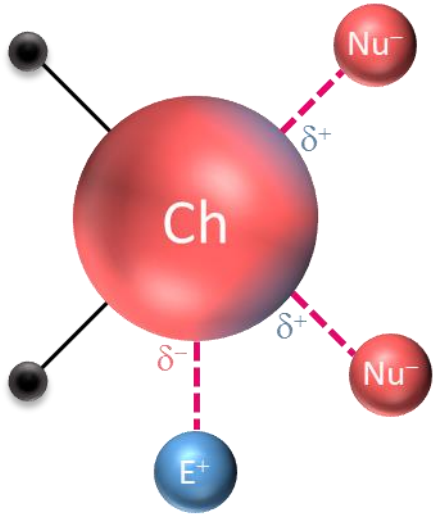

Figure 1.19 Schematic of interactions between electrophilic (E^+) and nucleophilic (Nu^-) species and a chalcogen (Ch = O, S, Se or Te). Black dots represent the rest of the molecule.

The origin of this positive potential can be described by the atomic orbitals. Considering the sulfur atom, which has an electronic structure of [Ne]$3s^2 3p_x^2 3p_z^1 3p_y^2$, two electron deficient 'holes' result from the *z* and *y* *p*-electrons taking part in a σ-bond (**Figure 1.20**).

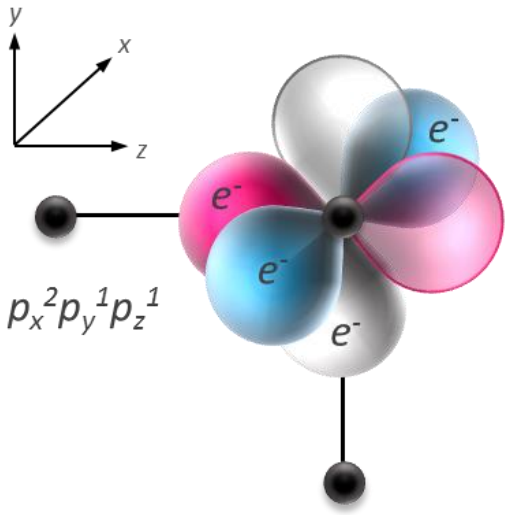

Figure 1.20 Diagram of molecular orbitals p_z (pink), p_x (blue) and p_y (white), electrons are represented by e^-. Filled lobes are shown as solid. The outer lobes of p_z and p_y are electron deficient (shown as transparent) and are manifested as σ-holes. Black dots represent the covalently bonded atoms in the molecule.

1.5.2 Spectroscopic analysis of chalcogen bonding

Some of the first investigations into chalcogen bonding interactions employed NMR spectroscopy. The chemotherapy agent, 5-aminoselenazofurin (**Figure 1.21B**), was examined by Goldstein *et al*., with a view to determining the origin of the interaction between selenium an oxygen.[115] Of particular interest was the impact of introducing an amino group, which increases the positive potential of the Se. The chemical shift differences seen in ^{77}Se NMR was significantly more shielded in the 5-amino variant (**Figure 1.21B**), demonstrating an increase in the tendency to adopt a conformation in which chalcogen contacts are present. The observed increase in chalcogen bonding propensity in relation to the electrostatic properties of the selenium centre led the authors to conclude that these intramolecular chalcogen interactions were dominated by electrostatics.

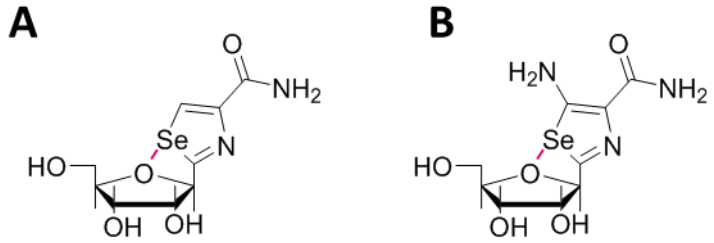

Figure 1.21 Structure of (A) selenazofurin and (B) 5-aminoelenazofurin.

Around the same time in the 1990s Iwaoka made significant contributions to the experimental study of chalcogen bonding. Iwaoka *et al*. used 2-selenobenzylamine derivatives (**Figure 1.22**) to study the nature of intramolecular interactions involving selenium over almost a decade.[116–118] A range of variable-temperature NMR techniques were employed including ^{1}H, ^{15}N and ^{77}Se spectroscopies to study conformational free energies in simple compounds shown in **Figure 1.22**. The conformational free energy differences between the states in which the chalcogen bond was formed *vs.* broken were determined to be ~40 kJ mol^{-1}, demonstrating the significance of such interactions in solution. A linear relationship between the conformational free energies and delocalisation energies predicted by NBO analysis indicated that an n→σ* electron delocalisation from the nitrogen lone pair to the σ* antibonding orbital of the Se–X bond was energetically significant. Similar orbital interactions between between Se and O have also been noted.[119,120]

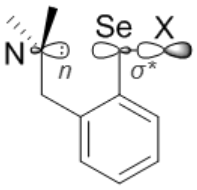

Figure 1.22 Structure of 2-selenobenzylamine derivatives used by Iwaoka and co-workers.

Iwaoka came to a similar conclusion as Barton using a structurally related system (**Figure 1.23**). Barton had first used X-ray crystallography to study the structures

containing O···Se contacts in selenoiminoquinones.[121] IR spectroscopy showed a change in the C=O stretch between when a chalcogen contact is formed compared to the conformation in which the O···Se contact was broken. They combined these results with valence shell electron pair repulsion (VSEPR) theory to explain the structure seen by X-ray crystallography. The electronic structure predicted by VSEPR qualitatively showed a 3-centre, 4-electron (3c-4e) bond, indicating the hypervalency of Se, and therefore the partial covalency of the chalcogen bond.

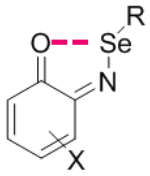

Figure 1.23 Structure of selenoiminoquinones used by Barton.

Other experimental chalcogen-bond investigations have also found evidence of partial covalency stemming from an n→σ* electron delocalisation.[122–124] More recently, Garrett *et al*. presented a study of chalcogen bonding in solution using benzotelluradiazoles with both charged and neutral Lewis bases.[125] UV/vis titrations enabled the binding of Lewis bases to the chalcogens to be measured. Despite the presence of two σ-holes on a single chalcogen, the data suggested that only a 1:1 binding complex was being formed. Moreover, when titrating against a neutral Lewis base (quinuclidine), the association constants varied only slightly across the (admittedly limited) range of solvents used. Furthermore, the binding was investigated using ^{1}H NMR, which demonstrated that the binding free energy of binding ranged between −7 kJ mol^{-1} and −29 kJ mol^{-1}. A linear relationship was observed between the log of the experimentally determined association constants and the calculated electrostatic potential maxima (located at the σ-hole in this case), $V_{s,max}$. This finding implied that there was an electrostatically dominated interaction with Cl^- (**Figure 1.24**), which contradicted Iwaoka's and Barton's suggestion of partial covalency being important. Indeed, it might be expected that electrostatic interactions might dominate

the interaction due to the charged nature of the system, highlighting the need for a neutral system to investigate chalcogen bonding.

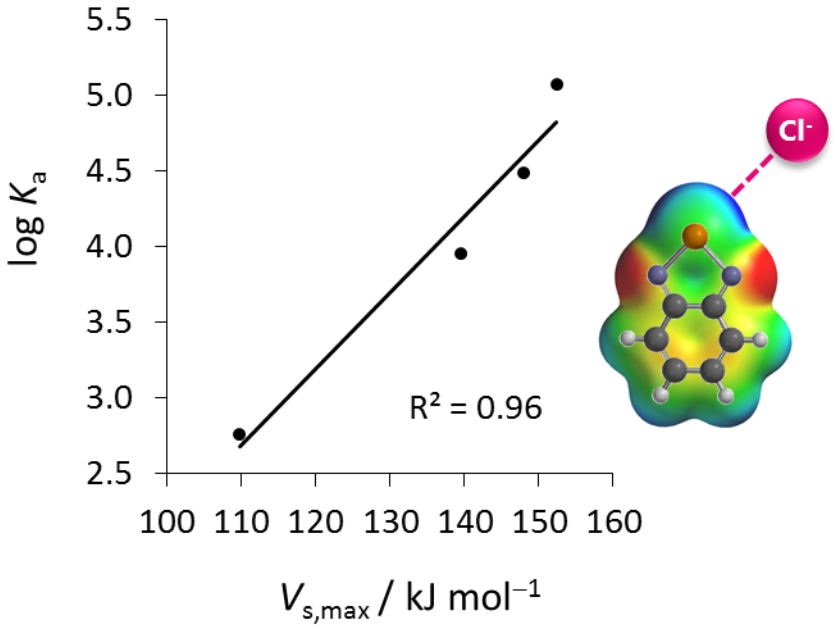

Figure 1.24 Plot of log K_a versus $V_{s,max}$ of the chalcogen bond donor. Adapted from reference 125.

1.5.3 Natural bond orbital, energy decomposition and other computational analysis of halogen bonding

Natural bond orbital (NBO), energy decomposition analysis (EDA) and the quantum theory of atoms in molecules (QTAIM) have all been used in determining the nature of molecular interactions between chalcogens. Bleiholder *et al*. performed a comprehensive computational analysis of chalcogen bonding complexes by employing symmetry adapted perturbation theory (SAPT) decomposition and NBO analysis (**Figure 1.25**).[126]

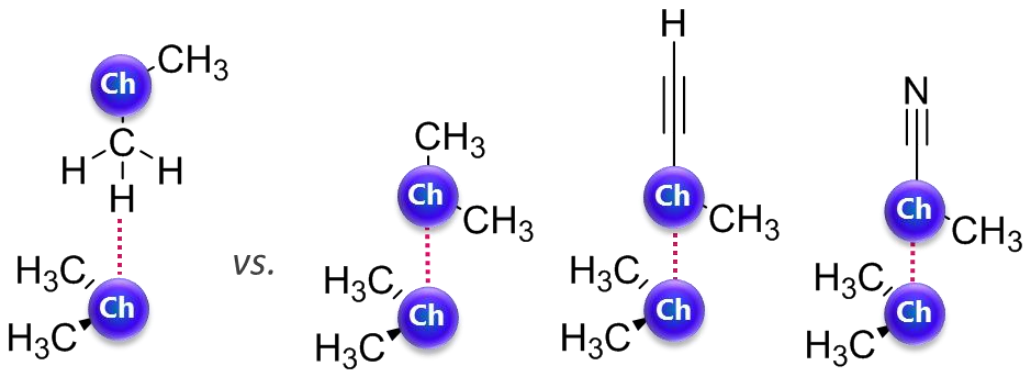

Figure 1.25 The structures of model complexes used by Bleiholder in conformations containing competing H-bonds (left) and chalcogen bonds (right). Ch corresponds to chalcogen atoms.

Detailed SAPT2002 analysis of homoatomic dimers showed that electrostatics and dispersion forces were the dominant contributors to interactions between two oxygen containing dimers, stemming from secondary CH···O interactions (**Figure 1.25**, left). However, electrostatics were found to be repulsive between heavier chalcogen atoms, particularly tellurium. The group later studied heteroatomic dimers, with varying methyl or cyano substituents to change the electronics of the system (**Figure 1.25**). Except for oxygen, chalcogen bonding was generally found to dominate over the competing H-bonding (**Figure 1.25**, left). Minimised structures showed the linear intermolecular assembly of chalcogen atoms, consistent with the directionality of an n→σ* delocalisation, and also consistent with experimental spectroscopic findings.[120,121] Furthermore, NBO analysis predicted increasing participation of orbital delocalisation for heavier chalcogen atoms. Although the authors point out the analysis of molecular orbitals using this method was only qualitative, the importance of an n→σ* interaction was clearly demonstrated.[127] Frontera *et al*. provided further analysis of similar model systems, with AIM showing a bond critical point in chalcogen bonding, again demonstrating the sharing of electrons and the formation of a partially covalent molecular interaction.[128]

Dispersion forces are also proposed to make substantial energetic contributions in chalcogen bonding. Bleiholder's SAPT(0) decomposition regularly showed that dispersion made a large contribution to the stability of chalcogen bonds. Interactions

involving heavier, disperse chalcogens such as selenium or tellurium were even suggested to be dominated by dispersion.[126] Such findings are unsurprising for a gas-phase analysis, where one would expect the interactions between two disperse elements to have a large contribution from van der Waal dispersion forces.

A theoretical investigation by de Vleeschouwer *et al*. using similar benzochalcodiazoles to those used by Garrett *et al*. (**Figure 1.24**) disagreed with the conclusions drawn from the experimental findings that electrostatics was the governing force.[125] It was found the interactions between benzochalcodiazoles and Lewis bases contained both an electrostatic and orbital component by using Natural Orbitals for Chemical Valence (NOCV) energy decomposition. De Vleeschouwer's NOCV analysis suggested that the n→σ* delocalisation was significant and that the interactions should therefore be treated with a partial covalent character.[129] Given Vleeschouwer *et al*. used the same system as Garrett *et al*. (discussed earlier, **Figure 1.24**) a combination with Garrett's experimental findings could give experimental validation of these predictions.

Contrasting to the other theoretical investigations presented in this section, Cremer *et al*. found evidence for an electrostatically dominated interaction in substituted chalcogens (CF_3-Ch, ChF_2) and ammonia or homoatomic chalcogen containing dimers,[130] supporting the results of Garrett, Politzer and co-workers.[112,125] The combination of SAPT(0) and QTAIM analyses of over 100 chalcogen-bond containing complexes in this case pointed towards an electrostatically controlled interaction.[130]

1.5.4 Chalcogen bonding conclusion

Despite numerous computational and experimental investigations, there is still no rigorous definition of chalcogen bonding. Indeed, IUPAC recently formed a panel tasked with defining chalcogen, tetrel and pnicogen bonds. The findings from both experimentalists and theoreticians would suggest a partial covalent model is suitable for describing chalcogen bonding. Experimental evidence of electrostatically driven chalcogen bonds are over-represented by charged systems. More collaboration between experimental evidence and computational analyses is needed to justify the

bonding models proposed in chalcogen bonding to further investigate the nature of the interaction.

1.6 Pnicogen bonding

Pnicogen (or pnictogen) bonding is a σ-hole interaction involving group 15 elements (N, P, As and Sb), which involves three σ-holes sitting along the three covalent σ-bonds connected to the pnicogen atom (**Figure 1.26**). The interaction was first described in 2007 by Politzer *et al*. who used σ-hole theory to rationalise them,[131] although the idea of favourable molecular interactions involving pnicogens (Pn···Pn interactions) were first proposed in the late 1970s.[132]

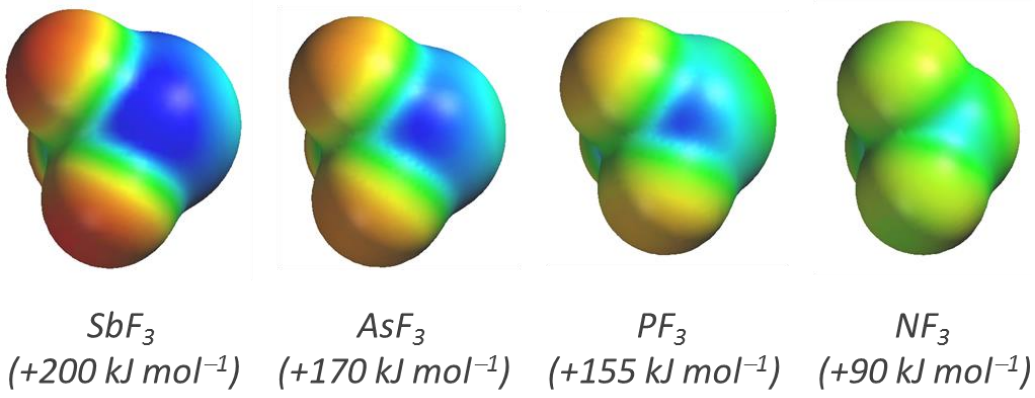

Figure 1.26 ESPs of PnF_3, with $V_{s,max}$ values shown below. Calculated using Spartan '14, DFT/B3LYP/3-21G.

As with the previously discussed σ-hole interactions, a debate continues surrounding the nature of the interaction, with both electrostatics and partial covalency involving an n→σ* electron delocalisation being frequently used to rationalise the favourability of pnicogen bonds.

1.6.1 σ-hole theory in pnicogen bonding

Politzer has proposed that pnicogen interactions arise from the interaction between the area of 'positive' potential, the σ-hole, and 'negative' potential on the Lewis base.[131] The σ-hole is due to electronic structure of the pnicogen element. For example, phosphorous has an electronic structure of [Ne]$3s^2 3p_x^1 3p_y^1 3p_z^1$, which means that the electrons in each *p*-orbital are involved in the formation of σ-bonds, leaving each *p*-orbital with a lobe having lower electron density, allowing the positive charge of the nucleus being seen (transparent lobes in **Figure 1.27**).

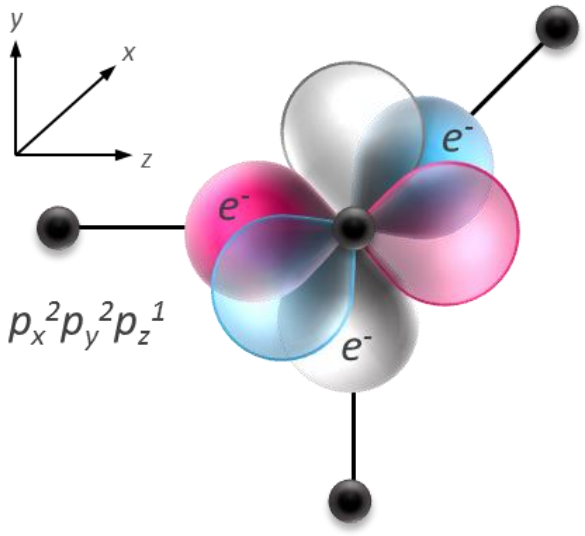

Figure 1.27 Diagram of molecular orbitals p_z (pink), p_x (blue) and p_y (white), electrons are represented by e^-. Filled lobes are shown as solid. The outer lobes of p_z, p_y and p_x are electron deficient (shown as transparent) and manifests as σ-holes. Black dots represent the atoms in the molecule.

Other, crystallographic studies have agreed with Politzer's suggestion of the dominance of electrostatic effects. For example, Zarić *et al*. performed a CSD search to look for close pnicogen···Lewis base contacts. The group used Politzer's electrostatic σ-hole theory to explain the linear geometry of Pn···Pn contacts observed in the solid state within a wide range of crystal structures.[133] While such crystallographic and theoretical studies provide a qualitative explanation for pnicogen

bonds, there remains a lack of quantitative, experimental evidence for the electrostatic nature of pnicogen bonding.

1.6.2 Computational studies of pnicogen bonding

Partial covalency in pnicogen bonds, specifically electron delocalisation from the Lewis base lone pair (n) to the antibonding σ* bond R–Pn (similar to **Figure 1.3**) has also been proposed. Studies into partial covalency in pnicogen bonding currently remain purely *in silico*, with a lack of experimental justification of the potential electron delocalisation in pnicogen bonds. However, several theoretical studies have pointed towards the occurrence of n→σ* electron delocalisation as described above.

Sundberg *et al*. presented a study in to intramolecular P···P pnicogen bonds using 1,2-(diphenylphosphino)-1,2-dicarba-closo-dodecaborane (**Figure 1.28**). Crystal structures show a close P···P contact,[134] which was also examined using NBO calculations. The calculations gave second-order perturbation energies of 8–12 kJ mol^{-1} for the delocalisation of one P lone pair into the antibonding σ* orbital of the adjacent C–P bond.[135] Molecular orbital diagrams similar to that depicted in **Figure 1.3** also supports the qualitative possibility of n→σ* electron delocalisation from the interaction angle and bond distances seen in the crystal structure.[136]

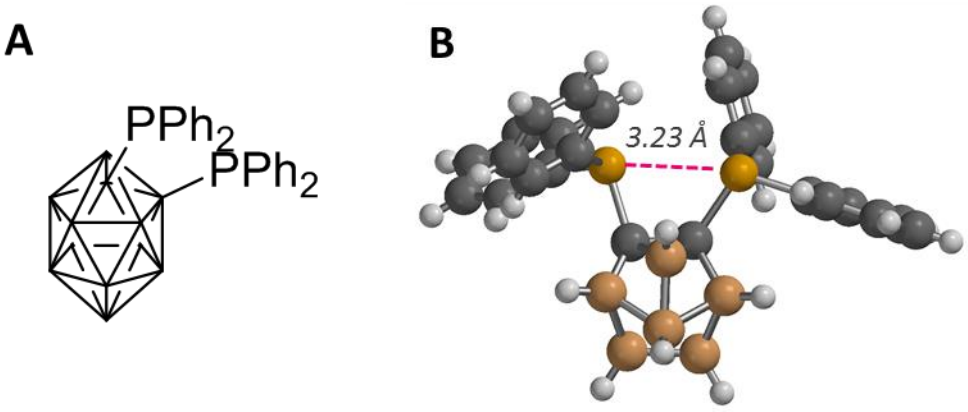

Figure 1.28 (A) Structure and (B) crystal structure of 1,2-(diphenylphosphino)-1,2-dicarba-closo-dodecaborane. Crystal structure taken from reference 136.

In agreement with Sundberg's analysis, Scheiner used NBO and SAPT decomposition to reveal that significant electron delocalisation accompanied the interaction between NH_3 and PH_3 with a stabilising energy of ~4 kJ mol^{-1}.[137] A minimisation showed a HP···N interaction angle of 168°, consistent with both the directionality of a putative orbital interaction or electrostatically driven interaction. SAPT decomposition performed on interactions between PH_3 homodimers suggested that inductive electron delocalisation was a more significant component than electrostatics (8.4 versus 7.5 kJ mol^{-1}, respectively). Conversely, SAPT analyses performed by Kirchner and others on similar homo and heteroatomic dimers disagreed with Scheiner, and instead indicated electrostatically dominated interactions.[4,138–140] NBO calculations also showed similar energetic significance of n→σ* delocalisation of around 5 kJ mol^{-1}.[141,142] Other NBO analyses of pnicogen bonds have supported an important contribution from an n→σ* delocalisation.[143,144]

Cremer *et al*. have also applied vibrational spectroscopy to analyse pnicogen bonding. A range of model homo- and hetero-pnicogen complexes were examined in which the force constant k^a was used as an indicator of pnicogen bond strength. A $2e^-$ stabilisation due to the n→σ* (as seen in **Figure 1.3**) was observed when the pnicogen contact is formed head on.[145] The importance of electron delocalisation was indicated by an increase in electron density being indicated by analysis of the bond critical point by atoms in molecule analysis, which shows an increase in electron density upon formation of a pnicogen-bonded dimer.[146] The work constituted a rare quantitative, experimental analysis of pnicogen bonding using experimental (force constant) measurements.

1.6.3 Conclusion on pnicogen bonding

Most evidence from investigations into pnicogen bonding leads to a conclusion that an n→σ* electron delocalisation is responsible for the favourable interaction involving group 15 elements. However, it is hard to quantitatively determine the nature of the interaction due to limited experimental evidence, highlighting the need for further experimental investigations in to pnicogen bonding, particularly examination of

solution-phase behaviour. Pnicogen bonding has the potential to open doors to exciting new areas of research, such as catalysis,[147] therefore the pursuit of a deeper understanding of these interactions will enable their properties to be exploited by chemists.

1.7 Tetrel bonding

Tetrel bonding is a σ-hole interaction involving group 14 elements (C, Si, Ge and Sn). Four σ-holes sit along the corresponding σ-bonds of an sp^3-hybridised tetrel centre (**Figure 1.29**) that may form favourable interactions with Lewis bases. The existence of tetrel bonding is surprising given that steric hindrance around a sp^3-hybridised tetrel atom. In some regards, such interactions can be considered as resembling the approach of an incoming nucleophile in the early stages of an S_N2 mechanism. Despite the relatively limited exploration of tetrel bonding relative to halogen or chalcogen bonding, tetrel bonding has been used in cage-complex chemistry,[148] biological systems[149] and synthetic chemistry.[150]

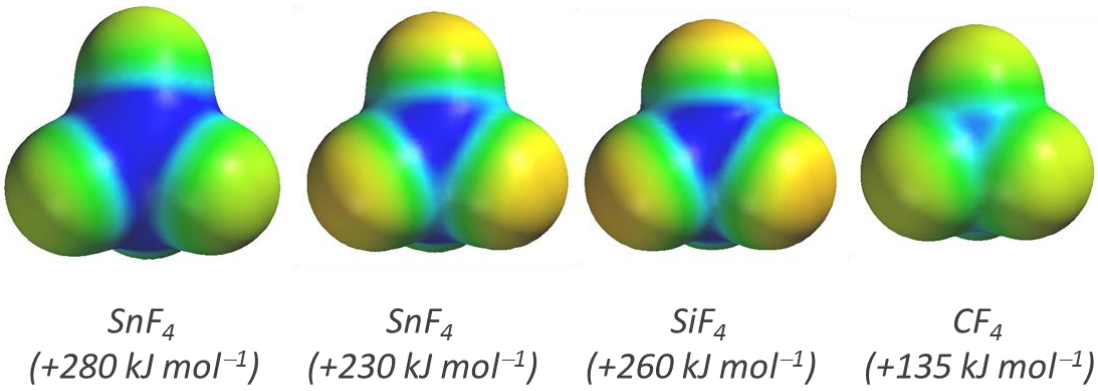

Figure 1.29 ESPs of TrF_4, with $V_{s,max}$ values shown below. Calculated using Spartan '14, DFT/B3LYP/3-21G.

1.7.1 σ-hole theory in tetrel bonding

Tetrel bonding was first described in electrostatic terms by Politzer 2009,[151] slightly later than his description of other σ-hole interactions. However, the term 'tetrel bond' was not coined until 2013 by Frontera.[3] As with other σ-hole interactions, the σ-hole increases in charge and intensity as the size of the tetrel element increases (**Figure 1.29**).

By predicting interacting energies between TrX_4 (where X = H, F or Cl and Tr is a tetrel element) and NH_3, Politzer qualitatively described tetrel bonding electrostatically.[152] Tetrel-containing monomers with the most positive σ-holes were predicted to form the strongest interactions. In a more quantitative investigation, they also found a strong correlation between the $V_{s,max}$ of the tetrel bond donor in $F_3PnX\cdots NCH$ complexes (where Pn is a pnicogen element and X is a halogen, **Figure 1.30**).[152] Frontera and co-workers added support to Politzer's proposal via a combined computational and CSD search in which the σ-hole model was used to rationalise the crystal packing in cycloalkanes.[153]

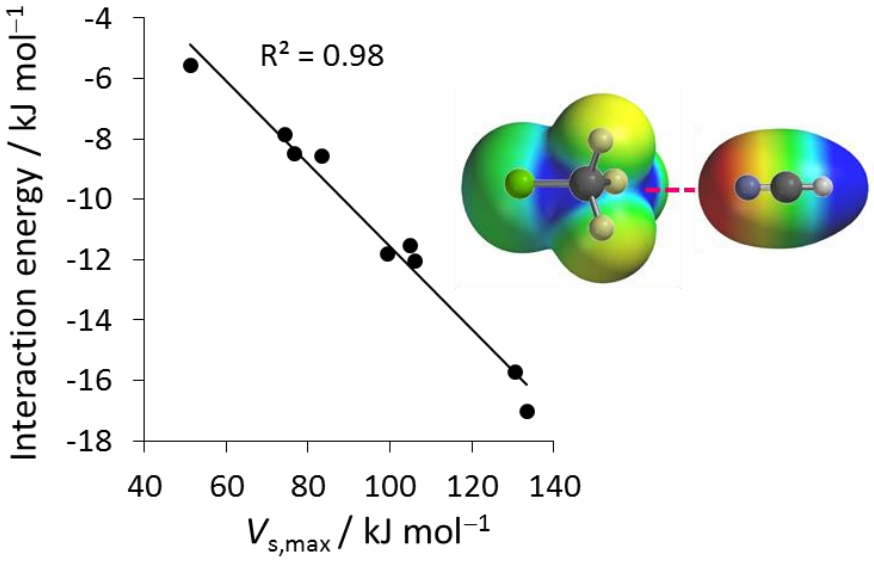

Figure 1.30 Plot of interaction energy versus $V_{s,max}$. Adapted from reference 152.

Scheiner *et al*. also found compelling evidence for electrostatically driven tetrel bonding interactions. They found that complexation of furanTrF_3 (**Figure 1.31A**) and PyTrF_3 (**Figure 1.31B**) (where Tr = Si or Ge) with NH_3 was dominated by electrostatics through energy decomposition analysis.[154] However, NBO analyses also showed a less significant n→σ* electron delocalisation occurring alongside the electrostatic interaction. Scheiner investigated the change in V_{max} when the tetrel bond donor was protonated (H^+-Py or H^+-furan). It was found the change in V_{max} between the charged and neutral tetrel donor correlated well with the change in predicted interaction strength between the protonated and neutral analogues of the tetrel bond donors for both silicon and germanium (**Figure 1.31C**, black and pink, respectively) implying an electrostatically governed interaction. However, the change in orbital delocalisation energies from NBO analysis in the charged and neutral forms also gave an excellent correlation with the same interaction energy difference (**Figure 1.31D**). Scheiner subsequently found that the electron density at the bond critical point did not correlate with predicted interaction energies, while second order perturbation energies from NBO calculations of the n→σ* delocalisation also correlated poorly. Similar findings were obtained when the both germanium and silicon centres were employed as the tetrel-bond donors.

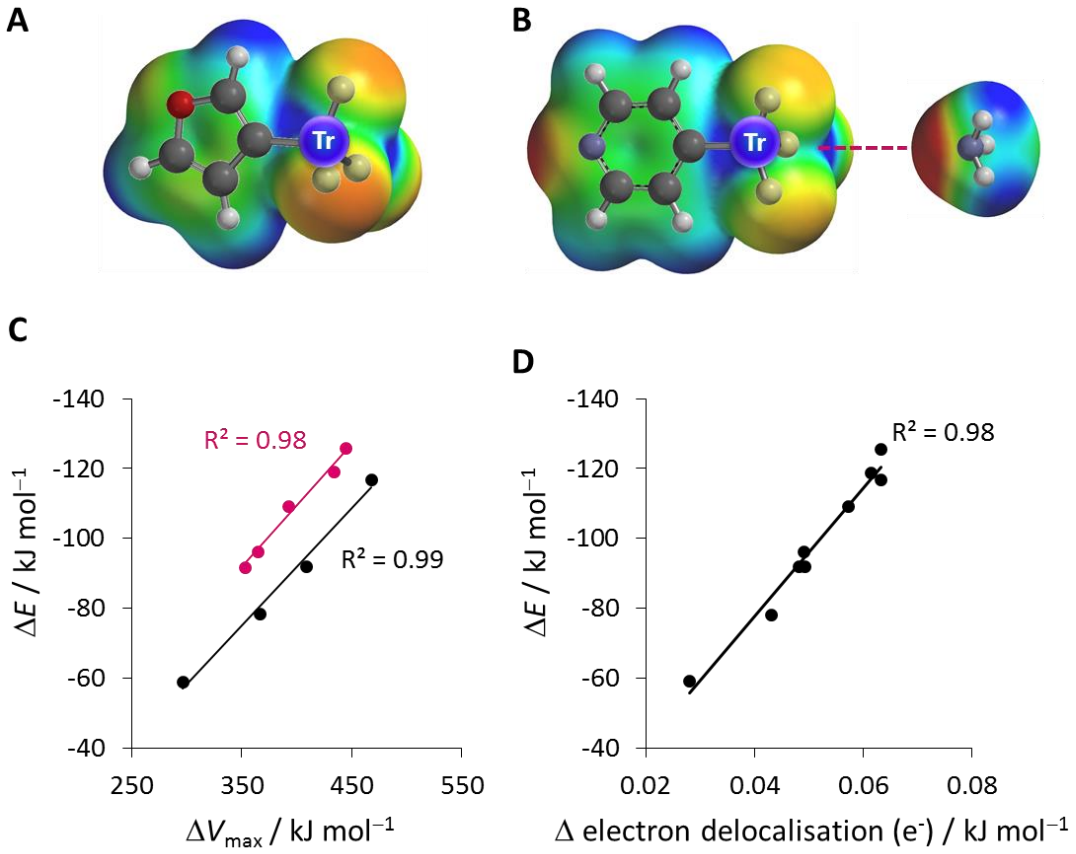

Figure 1.31 The structures of tetrel bond donors (A) furanTrF$_3$ and (B) PyTrF$_3$ where Tr = Si or Ge. (C) and (D) The predicted change in interaction strength (ΔE) between the protonated complexes H$^+$-PyTrF$_3$···NH$_3$ and H$^+$-furanTrF$_3$···NH$_3$ compared to the neutral analogues plotted against (C) the change in V_{max} of the tetrel bond donor between protonated complexes H$^+$-PyTrF$_3$···NH$_3$ or H$^+$-furanTrF$_3$···NH$_3$ compared to the neutral analogues (where Tr = Si (black) or Ge (pink)). (D) ΔE versus the change in the electron delocalisation of complexes H$^+$-PyTrF$_3$···NH$_3$ or H$^+$-furanTrF$_3$···NH$_3$ compared to the neutral analogues calculated from NBO analysis. Recreated from reference 154.

Similarly, an early NMR spectroscopic investigation of tetrel bonds in solution, examined the interaction of silanes with N lone pair donors. Complexation-induced chemical shifts were consistent with the nitrogen donor losing electron density, consistent with an electron delocalisation interaction.[155] Another study used valence bond theory to predict the level of electron delocalisation within H$_3$Pn···TrH$_3$X (Pn = N, P and As, X = F, Cl and Br). Electron delocalisation accounted for a large proportion

of the predicted tetrel bond strength. The use of a modified orbital valence bond theory gave comparable results to those predicted with DFT calculations, and confirmed the importance of n→σ* electron delocalisation in tetrel bonding.[156]

However, in all cases though it is important to emphasise that it is the combination of electrostatics and electron delocalisation make the pnicogen bonds favourable.[157] Therefore, the limited evidence obtained so far points towards an electrostatic interaction being the most likely driving force for this interaction.[158]

1.7.2 Conclusion on tetrel bonding

Tetrel bonding remains an under-exploited molecular interaction, and as such there is a paucity of experimental or theoretical data to give a clear indication of the nature. Nonetheless, it is still clear that these interactions have a very strong electrostatic character, which has been regularly been found to be the largest contributor to the interaction energy. However, most authors also noted that n→σ* delocalisation may occur and must not be discounted when considering tetrel bonds. With further correlation between experimental and theoretical studies, tetrel bonding could be understood further, hopefully enabling the improved design of new systems, and unlocking a range of potential applications.

1.8 Aerogen bonding

Interactions between group 18 elements (Xe, Kr and Ar) are known as aerogen bonds. Aerogen bonding was first noted only very recently,[7] due in part to the counterintuitive nature of noble gases being able to take part in interactions beyond van der Waals forces. However, Frontera has theoretically demonstrated that favourable interactions between aerogens and both neutral and anionic species are possible.[7] The majority of work on aerogen bonding has focussed on argon, xenon and krypton, which display very large, positive σ-holes (**Figure 1.32**). One may question if these interactions can be called σ-hole interactions given that the areas of positive potential do not sit along σ-bonds. Aerogen interactions have even been seen experimentally in the crystal state,[159–161] although the investigation of their underlying origins is limited.

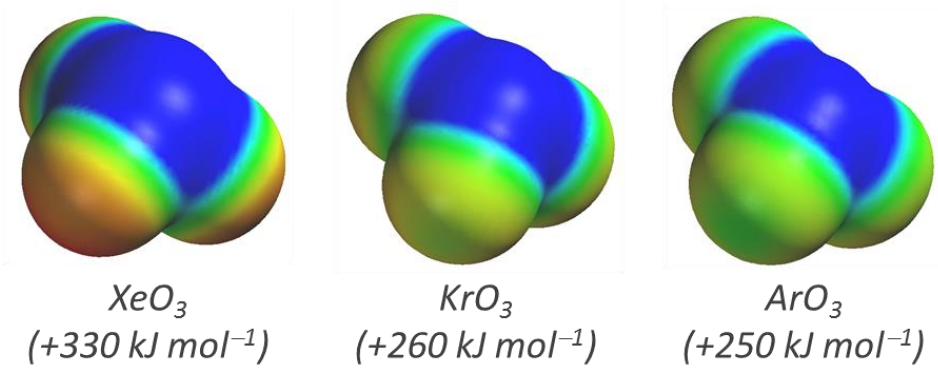

Figure 1.32 ESPs of AeO_3, with $V_{s,max}$ values shown below. Calculated using Spartan '14, DFT/B3LYP/3-21G.

The interactions between aerogens (Ae) and the hydroxy groups of 1,2-dihydroxybenzene derivatives has been investigated by varying substituents (**Figure 1.33**). The interaction of the hydroxyl groups with the aerogens were estimated to be worth up to 60 kJ mol^{-1} in gas phase calculations. Interactions involving Xe were significantly stronger than Kr and Ar and can be explained by the significantly more positive σ-hole seen on Xe. Consistent with an electrostatic interaction, a strong correlation between the predicted interaction energy and the $V_{s,min}$ of the aerogen bond acceptor was determined (**Figure 1.33**). The possibility of electron delocalisation was also evaluated using NBO calculations, but was found to make only a very small contribution relative to the electrostatic component.[162]

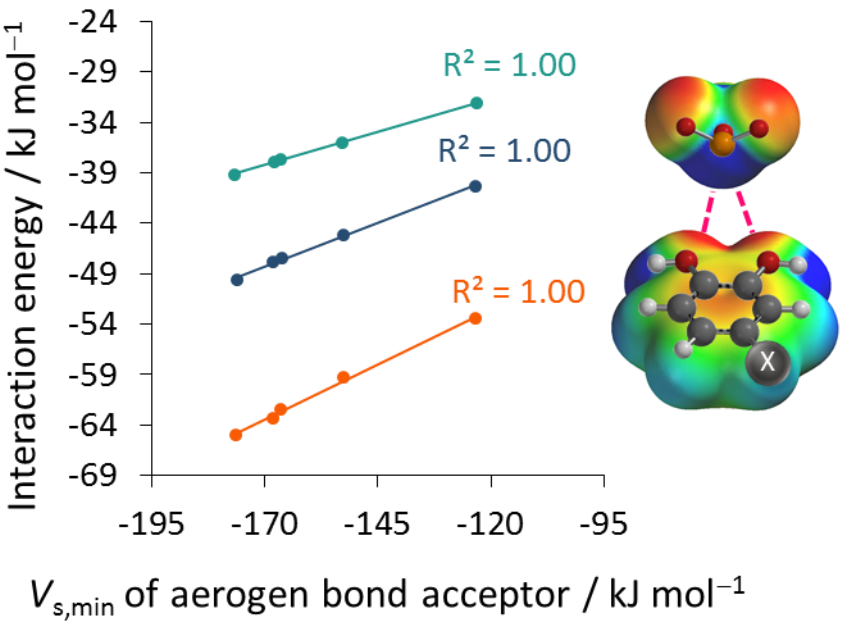

Figure 1.33 Plot of interaction energy versus the minimum electrostatic potential of the aerogen bond acceptor. Adapted from reference 162.

Computational evaluation of the interactions of Xe-containing salts revealed the existence of close N···Xe contacts. Furthermore, solid-state structures showed the geometry aligning the lone pair of N to the antibonding σ* Xe–C bond, as has been seen in other σ-hole interactions. NBO analysis of the X-ray structures also showed n→σ* electron delocalisation into both Xe–C and Xe–F σ* bonds.[163] A theoretical investigation of interactions between aerogen elements and hydrocarbons also concluded that orbital delocalisation was important. Atoms in molecules analysis revealed increased electron density of the bond critical point, confirming the existence of electron delocalisation interactions. NBO calculations indicated that n→σ* delocalisation accounted for the partial covalency seen in the interactions.[164]

1.8.3 Conclusion on aerogen bonding

It is hard to come to a rigorous definition on aerogen bonding due to the lack of investigations into its nature. While it is clear that aerogen bonding has significant covalent character from both experimental and theoretical study, the interactions remain relatively niche. Given the potential applications of aerogen bonding in crystal engineering, further understanding of the interaction could allow these unexpected interactions to become more widely used.

1.9 Conclusions and remarks

The nature of σ-holes proves to be complex at the best of times. Investigations into the nature of σ-hole interactions have made use of a wide range of experimental and computational techniques; from X-ray crystallography and NMR spectroscopy to energy decompositions and natural bond orbital analysis. The literature reviewed here demonstrates the need for a combined approach when defining non-covalent interactions, whilst recognising the limitations of some of these approaches, such as the inaccuracy of SAPT calculations to experimentally determined data and the over prediction of electron delocalisation energies by NBO analyses. Many investigations into σ-hole interactions reveal disagreement on the underlying phenomenon between experimentalists and theoreticians, despite the examinations often involving similar model systems. Even using the same computational techniques such as SAPT has resulted in conflicting opinions, highlighting the inaccuracies of some of these techniques and the differences that varying computational methods can have. Therefore, many of the energy decompositions results must be treated with caution. Ultimately, many investigations into σ-hole interactions lack the experimental justification of theoretical suggestions. Similarly, many experimental studies do not properly compare their data with theoretical bonding models. Greater collaboration between computational and experimental chemistry is necessary to advance our understanding of σ-hole interactions and molecular interactions in general.

Investigations into the nature of halogen bonding have been the most comprehensive among the various sub-classes of σ-hole interactions identified. Electrostatics, electron delocalisation, dispersion and exchange repulsion will all play

a part in the determining experimentally observed behaviour. However, experimental data shows that a strictly electrostatic model (that lacks electron delocalisation aspects) cannot fully account for experimental behaviour, as identified by Hunter's and Taylor's spectroscopic studies. Chalcogen bonding possesses many of the same characteristics as halogen bonds with original studies by Iwaoka providing convincing evidence of the importance of n→σ* electron delocalisation in the stabilisation of chalcogen bonds. Other σ-hole interactions remain underexplored, and as a result underexploited.

Overall, σ-hole interactions seem to have a partial covalent character arising from an n→σ* electron delocalisation from a lone pair of a Lewis base (n) to the antibonding (σ*) of the σ-hole bond donor, which governs the properties of these interactions. The literature presented here illustrates the importance of chemical models such as molecular orbital theory and electron delocalisation effects, which developed to help understand and simplify the identification and definitions of molecular interactions. It is hoped further experimental and computational investigations can progress to more rigorous definitions of σ-hole interactions, particularly those that are less well investigated, such as pnicogen, tetrel and aerogen bonding.

1.10 Thesis aims and outlook

This review has demonstrated the complicated nature of σ-hole interactions, and the need for further experimental and computational evidence to look for quantitative explanations of these interactions. One limitation of current studies is the paucity of correlation between experiment and theory. While halogen bonding has been extensively explored, both in its uses and nature, other σ-hole interactions remain comparatively unexplored. This thesis will present a fundamental study of the nature of molecular interactions, combining theory and experiment. To achieve this, experimental systems had to be designed to study the energetics of the interactions, as well as the associated substituent and solvent effects. Theoretical models can then be employed to explain the experimental behaviour seen. One limiting factor of many current studies of the nature of molecular interactions is the use of theoretically abstract models, which may lack physical meaning. It has therefore been important to

search for an accessible model to explain the experimental behaviour seen. This combined experimental and theoretical approach was first employed in the study of chalcogen bonding (**Chapter 2**). Subsequently, the same theoretical analysis will be used to explore electron delocalisation in hydrogen bonding (**Chapter 3**) and carbonyl···carbonyl interactions (**Chapter 4**), which are both the subject of current debate. Given the importance of molecular interactions in biological and chemical processes, it is hoped greater understanding of these interactions will be of immediate interest to the wider academic and industrial community.

1.11 References

1. Clark, T.; Hennemann, M.; Murray, J. S.; Politzer, P. Halogen Bonding: The σ-Hole. *J. Mol. Model.* **2007**, *13* (2), 291–296.
2. Alcock, N. W. Secondary Bonding to Nonmetallic Elements. *Adv. Inorg. Chem. Radiochem.* **1972**, *15*, 1–58.
3. Bauzá, A.; Mooibroek, T. J.; Frontera, A. Tetrel-Bonding Interaction: Rediscovered Supramolecular Force? *Angew. Chemie Int. Ed.* **2013**, *52* (47), 12317–12321.
4. Zahn, S.; Frank, R.; Hey-Hawkins, E.; Kirchner, B. Pnicogen Bonds: A New Molecular Linker? *Chem. - A Eur. J.* **2011**, *17* (22), 6034–6038.
5. Gleiter, R.; Haberhauer, G.; Werz, D. B.; Rominger, F.; Bleiholder, C. From Noncovalent Chalcogen–Chalcogen Interactions to Supramolecular Aggregates: Experiments and Calculations. *Chem. Rev.* **2018**, acs.chemrev.7b00449.
6. Cavallo, G.; Metrangolo, P.; Milani, R.; Pilati, T.; Priimagi, A.; Resnati, G.; Terraneo, G. The Halogen Bond. *Chem. Rev.* **2016**, *116* (4), 2478–2601.
7. Bauzá, A.; Frontera, A. Aerogen Bonding Interaction: A New Supramolecular Force? *Angew. Chemie Int. Ed.* **2015**, *54* (25), 7340–7343.
8. Beno, B. R.; Yeung, K.-S.; Bartberger, M. D.; Pennington, L. D.; Meanwell, N. A. A Survey of the Role of Noncovalent Sulfur Interactions in Drug Design. *J. Med. Chem.* **2015**, *58* (11), 4383–4438.
9. Wilcken, R.; Zimmermann, M. O.; Lange, A.; Joerger, A. C.; Boeckler, F. M. Principles and Applications of Halogen Bonding in Medicinal Chemistry and Chemical Biology. *J. Med. Chem.* **2013**, *56* (4), 1363–1388.
10. Neyyappadath, R. M.; Chisholm, R.; Greenhalgh, M. D.; Rodríguez-Escrich, C.; Pericàs, M. A.; Hähner, G.; Smith, A. D. Acylative Kinetic Resolution of Alcohols Using a Recyclable Polymer-Supported Isothiourea Catalyst in

Batch and Flow. *ACS Catal.* **2018**, *8* (2), 1067–1075.

11. Gliese, J.-P.; Jungbauer, S. H.; Huber, S. M. A Halogen-Bonding-Catalyzed Michael Addition Reaction. *Chem. Commun.* **2017**, *53* (88), 12052–12055.

12. Lim, J. Y. C.; Marques, I.; Thompson, A. L.; Christensen, K. E.; Félix, V.; Beer, P. D. Chalcogen Bonding Macrocycles and [2]Rotaxanes for Anion Recognition. *J. Am. Chem. Soc.* **2017**, *139* (8), 3122–3133.

13. Robinson, S. W.; Mustoe, C. L.; White, N. G.; Brown, A.; Thompson, A. L.; Kennepohl, P.; Beer, P. D. Evidence for Halogen Bond Covalency in Acyclic and Interlocked Halogen-Bonding Receptor Anion Recognition. *J. Am. Chem. Soc.* **2015**, *137* (1), 499–507.

14. Mahmudov, K. T.; Kopylovich, M. N.; Guedes da Silva, M. F. C.; Pombeiro, A. J. L. Chalcogen Bonding in Synthesis, Catalysis and Design of Materials. *Dalt. Trans.* **2017**, *46* (31), 10121–10138.

15. Neel, A. J.; Hilton, M. J.; Sigman, M. S.; Toste, F. D. Exploiting Non-Covalent π Interactions for Catalyst Design. *Nature* **2017**, *543* (7647), 637–646.

16. Hunter, C. A. Quantifying Intermolecular Interactions: Guidelines for the Molecular Recognition Toolbox. *Angew. Chemie Int. Ed.* **2004**, *43* (40), 5310–5324.

17. Mohajeri, A.; Pakiari, A. H.; Bagheri, N. Theoretical Studies on the Nature of Bonding in σ-Hole Complexes. *Chem. Phys. Lett.* **2009**, *467* (4–6), 393–397.

18. Politzer, P.; Murray, J. S.; Clark, T. Halogen Bonding: An Electrostatically-Driven Highly Directional Noncovalent Interaction. *Phys. Chem. Chem. Phys.* **2010**, *12* (28), 7748.

19. Brinck, T.; Murray, J. S.; Politzer, P. Surface Electrostatic Potentials of Halogenated Methanes as Indicators of Directional Intermolecular Interactions. *Int. J. Quantum Chem.* **1992**, *44* (S19), 57–64.

20. Feynman, R. P. Forces in Molecules. *Phys. Rev.* **1939**, *56* (4), 340–343.

21. Murray, J. S.; Politzer, P. Molecular Electrostatic Potentials and Noncovalent Interactions THE CENTURY OF NONCOVALENT BINDING. *WIREs Comput Mol Sci* **2017**, *7*.

22. Gonthier, J. F.; Steinmann, S. N.; Wodrich, M. D.; Corminboeuf, C. Quantification of "Fuzzy" Chemical Concepts: A Computational Perspective. *Chem. Soc. Rev.* **2012**, *41* (13), 4671.

23. Albright, T. A.; Burdett, J. K.; Whangbo, M.-H. *Orbital Interactions in Chemistry*; John Wiley & Sons, Inc.: Hoboken, NJ, USA, 2013.

24. Weinhold, F.; Landis, C. R. Chemistry Education: Research and Practice in Europe Natural Bond Orbitals and Extensions of Localized Bonding Concepts. *Educ. Res. Pr. Eur* **2001**, *2* (2), 91–104.

25. Mulliken, R. S. Structures of Complexes Formed by Halogen Molecules with Aromatic and with Oxygenated Solvents 1. *J. Am. Chem. Soc.* **1950**, *72* (1), 600–608.

26. Brdarski, S.; Karlström, G. Modeling of the Exchange Repulsion Energy. *J. Phys. Chem. A* **1998**, *102* (42), 8182–8192.

27. Pauli, W. Über Den Zusammenhang Des Abschlusses Der Elektronengruppen Im Atom Mit Der Komplexstruktur Der Spektren. *Zeitschrift für Phys.* **1925**, *31* (1), 765–783.

28. London, F. The General Theory of Molecular Forces. *Trans. Faraday Soc.* **1937**, *33*, 8b.

29. Yang, L.; Brazier, J. B.; Hubbard, T. A.; Rogers, D. M.; Cockroft, S. L. Can Dispersion Forces Govern Aromatic Stacking in an Organic Solvent? *Angew. Chemie Int. Ed.* **2016**, *55* (3), 912–916.

30. Schneider, H.-J. Dispersive Interactions in Solution Complexes. *Acc. Chem. Res.* **2015**, *48* (7), 1815–1822.

31. Brammer, L. Halogen Bonding, Chalcogen Bonding, Pnictogen Bonding, Tetrel Bonding: Origins, Current Status and Discussion. *Faraday Discuss.* **2017**, *203*, 485–507.

32. Clark, T. Halogen Bonds and σ-Holes. *Faraday Discuss.* **2017**, *203*, 9–27.

33. Papajak, E.; Zheng, J.; Xu, X.; Leverentz, H. R.; Truhlar, D. G. Perspectives on Basis Sets Beautiful: Seasonal Plantings of Diffuse Basis Functions. *J. Chem. Theory Comput.* **2011**, *7* (10), 3027–3034.

34. Hehre, W. J.; Stewart, R. F.; Pople, J. A. Self-Consistent Molecular-Orbital Methods. I. Use of Gaussian Expansions of Slater-Type Atomic Orbitals. *J. Chem. Phys.* **1969**, *51* (6), 2657–2664.

35. Ditchfield, R.; Hehre, W. J.; Pople, J. A. Self-Consistent Molecular-Orbital Methods. IX. An Extended Gaussian-Type Basis for Molecular-Orbital Studies of Organic Molecules. *J. Chem. Phys.* **1971**, *54* (2), 724–728.

36. Krishnan, R.; Binkley, J. S.; Seeger, R.; Pople, J. A. Self-consistent Molecular Orbital Methods. XX. A Basis Set for Correlated Wave Functions. *J. Chem. Phys.* **1980**, *72* (1), 650–654.

37. Parker, T. M.; Burns, L. A.; Parrish, R. M.; Ryno, A. G.; Sherrill, C. D. Levels of Symmetry Adapted Perturbation Theory (SAPT). I. Efficiency and Performance for Interaction Energies. *J. Chem. Phys.* **2014**, *140* (9), 094106.

38. Parrish, R. M.; Gonthier, J. F.; Corminbœuf, C.; Sherrill, C. D. Communication: Practical Intramolecular Symmetry Adapted Perturbation Theory via Hartree-Fock Embedding. *J. Chem. Phys.* **2015**, *143* (5), 051103.

39. Parrish, R. M.; Parker, T. M.; Sherrill, C. D. Chemical Assignment of Symmetry-Adapted Perturbation Theory Interaction Energy Components: The Functional-Group SAPT Partition. *J. Chem. Theory Comput.* **2014**, *10* (10),

4417–4431.

40. Reed, A. E.; Curtiss, L. A.; Weinhold, F. Intermolecular Interactions from a Natural Bond Orbital, Donor-Acceptor Viewpoint. *Chem. Rev.* **1988**, *88* (6), 899–926.

41. Goodman, L.; Sauers, R. R. Diffuse Functions in Natural Bond Orbital Analysis. *J. Comput. Chem.* **2007**, *28* (1), 269–275.

42. Colin, M. Sur l'iode. *Ann. Chim.* **1814**, *91*, 252–272.

43. Guthrie, F. XXVIII.—On the Iodide of Iodammonium. *J. Chem. Soc.* **1863**, *16* (0), 239–244.

44. Hassel, O. Structural Aspects of Interatomic Charge-Transfer Bonding. *Science (80-.).* **1970**, *170* (3957), 497–502.

45. Bulfield, D.; Huber, S. M. Halogen Bonding in Organic Synthesis and Organocatalysis. *Chem. - A Eur. J.* **2016**, *22* (41), 14434–14450.

46. Mukherjee, A.; Tothadi, S.; Desiraju, G. R. Halogen Bonds in Crystal Engineering: Like Hydrogen Bonds yet Different. *Acc. Chem. Res.* **2014**, *47* (8), 2514–2524.

47. Grabowski, S. J. Hydrogen and Halogen Bonds Are Ruled by the Same Mechanisms. *Phys. Chem. Chem. Phys.* **2013**, *15* (19), 7249.

48. Crabtree, R. H. Hypervalency, Secondary Bonding and Hydrogen Bonding: Siblings under the Skin. *Chem. Soc. Rev.* **2017**, *46* (6), 1720–1729.

49. Corradi, E.; Meille, S. V.; Messina, M. T.; Metrangolo, P.; Resnati, G. Halogen Bonding versus Hydrogen Bonding in Driving Self-Assembly Processes. *Angew. Chemie Int. Ed.* **2000**, *39* (10), 1782–1786.

50. Gilday, L. C.; Robinson, S. W.; Barendt, T. A.; Langton, M. J.; Mullaney, B. R.; Beer, P. D. Halogen Bonding in Supramolecular Chemistry. *Chem. Rev.* **2015**, *115* (15), 7118–7195.

51. Metrangolo, P.; Meyer, F.; Pilati, T.; Resnati, G.; Terraneo, G. Halogen Bonding in Supramolecular Chemistry. *Angew. Chemie Int. Ed.* **2008**, *47* (33), 6114–6127.

52. Desiraju, G. R.; Ho, P. S.; Kloo, L.; Legon, A. C.; Marquardt, R.; Metrangolo, P.; Politzer, P.; Resnati, G.; Rissanen, K. Definition of the Halogen Bond (IUPAC Recommendations 2013). *Pure Appl. Chem.* **2013**, *85* (8).

53. Ramasubbu, N.; Parthasarathy, R.; Murray-Rust, P. Angular Preferences of Intermolecular Forces around Halogen Centers: Preferred Directions of Approach of Electrophiles and Nucleophiles around Carbon-Halogen Bond. *J. Am. Chem. Soc.* **1986**, *108* (15), 4308–4314.

54. Auffinger, P.; Hays, F. A.; Westhof, E.; Ho, P. S. Halogen Bonds in Biological Molecules. *Proc. Natl. Acad. Sci.* **2004**, *101* (48), 16789–16794.

55. Bader, R. F. W.; Carroll, M. T.; Cheeseman, J. R.; Chang, C. Properties of

Atoms in Molecules: Atomic Volumes. *J. Am. Chem. Soc.* **1987**, *109* (26), 7968–7979.

56. Metrangolo, P.; Murray, J. S.; Pilati, T.; Politzer, P.; Resnati, G.; Terraneo, G. Fluorine-Centered Halogen Bonding: A Factor in Recognition Phenomena and Reactivity. *Cryst. Growth Des.* **2011**, *11* (9), 4238–4246.

57. Metrangolo, P.; Murray, J. S.; Pilati, T.; Politzer, P.; Resnati, G.; Terraneo, G. The Fluorine Atom as a Halogen Bond Donor, Viz. a Positive Site. *CrystEngComm* **2011**, *13* (22), 6593.

58. Bauzá, A.; Quiñonero, D.; Frontera, A.; Deyà, P. M. Substituent Effects in Halogen Bonding Complexes between Aromatic Donors and Acceptors: A Comprehensive Ab Initio Study. *Phys. Chem. Chem. Phys.* **2011**, *13* (45), 20371.

59. Kolář, M. H.; Hobza, P. Computer Modeling of Halogen Bonds and Other σ-Hole Interactions. *Chem. Rev.* **2016**, *116* (9), 5155–5187.

60. Donohue, J.; Goodman, S. H.; IUCr. Interatomic Distances in Solid Chlorine. *Acta Crystallogr.* **1965**, *18* (3), 568–569.

61. Clark, T. σ-Holes. *Wiley Interdiscip. Rev. Comput. Mol. Sci.* **2013**, *3* (1), 13–20.

62. Clark, T.; Politzer, P.; Murray, J. S. Correct Electrostatic Treatment of Noncovalent Interactions: The Importance of Polarization. *Wiley Interdiscip. Rev. Comput. Mol. Sci.* **2015**, *5* (2), 169–177.

63. Kolář, M. H.; Carloni, P.; Hobza, P. Statistical Analysis of σ-Holes: A Novel Complementary View on Halogen Bonding. *Phys. Chem. Chem. Phys.* **2014**, *16* (36), 19111–19114.

64. Shields, Z. P.; Murray, J. S.; Politzer, P. Directional Tendencies of Halogen and Hydrogen Bonds. *Int. J. Quantum Chem.* **2010**, *110* (15), 2823–2832.

65. Politzer, P.; Murray, J. S. Halogen Bonding: An Interim Discussion. *ChemPhysChem* **2013**, *14* (2), 278–294.

66. Riley, K. E.; Murray, J. S.; Fanfrlík, J.; Řezáč, J.; Solá, R. J.; Concha, M. C.; Ramos, F. M.; Politzer, P. Halogen Bond Tunability I: The Effects of Aromatic Fluorine Substitution on the Strengths of Halogen-Bonding Interactions Involving Chlorine, Bromine, and Iodine. *J. Mol. Model.* **2011**, *17* (12), 3309–3318.

67. Riley, K. E.; Murray, J. S.; Politzer, P.; Concha, M. C.; Hobza, P. Br···O Complexes as Probes of Factors Affecting Halogen Bonding: Interactions of Bromobenzenes and Bromopyrimidines with Acetone. *J. Chem. Theory Comput.* **2009**, *5* (1), 155–163.

68. Esrafili, M. D.; Juyban, P. CNXeCl and CNXeBr Species as Halogen Bond Donors: A Quantum Chemical Study on the Structure, Properties, and Nature of Halogen···nitrogen Interactions. *J. Mol. Model.* **2014**, *20* (4), 2203.

69. Kolář, M.; Hostaš, J.; Hobza, P. The Strength and Directionality of a Halogen Bond Are Co-Determined by the Magnitude and Size of the σ-Hole. *Phys. Chem. Chem. Phys.* **2014**, *16* (21), 9987–9996.

70. Beweries, T.; Brammer, L.; Jasim, N. A.; McGrady, J. E.; Perutz, R. N.; Whitwood, A. C. Energetics of Halogen Bonding of Group 10 Metal Fluoride Complexes. *J. Am. Chem. Soc.* **2011**, *133* (36), 14338–14348.

71. Tolstoy, P. M.; Koeppe, B.; Denisov, G. S.; Limbach, H.-H. Combined NMR and UV/Vis Spectroscopy in the Solution State: Study of the Geometries of Strong OHO Hydrogen Bonds of Phenols with Carboxylic Acids. *Angew. Chemie Int. Ed.* **2009**, *48* (31), 5745–5747.

72. Hobza, P.; Muller-Dethlefs, K. *Non-Covalent Interactions*; Theoretical and Computational Chemistry Series; Royal Society of Chemistry: Cambridge, 2009.

73. Møllendal, H.; Samdal, S.; Guillemin, J.-C. Microwave Spectrum and Intramolecular Hydrogen Bonding of 2-Isocyanoethanol (HOCH 2 CH 2 N≡C). *J. Phys. Chem. A* **2014**, *118* (17), 3120–3127.

74. Bent, H. A. Structural Chemistry of Donor-Acceptor Interactions. *Chem. Rev.* **1968**, *68* (5), 587–648.

75. Rosokha, S. V.; Neretin, I. S.; Rosokha, T. Y.; Hecht, J.; Kochi, J. K. Charge-Transfer Character of Halogen Bonding: Molecular Structures and Electronic Spectroscopy of Carbon Tetrabromide and Bromoform Complexes with Organic σ- and π-Donors. *Heteroat. Chem.* **2006**, *17* (5), 449–459.

76. Robertson, C. C.; Perutz, R. N.; Brammer, L.; Hunter, C. A. A Solvent-Resistant Halogen Bond. *Chem. Sci.* **2014**, *5* (11), 4179–4183.

77. Abraham, M. H.; Platts, J. A. Hydrogen Bond Structural Group Constants. *J. Org. Chem.* **2001**, *66* (10), 3484–3491.

78. Zou, J.-W.; Huang, M.; Hu, G.-X.; Jiang, Y.-J. Toward a Uniform Description of Hydrogen Bonds and Halogen Bonds: Correlations of Interaction Energies with Various Geometric, Electronic and Topological Parameters. *RSC Adv.* **2017**, *7* (17), 10295–10305.

79. Thordarson, P. Determining Association Constants from Titration Experiments in Supramolecular Chemistry. *Chem. Soc. Rev.* **2011**, *40* (3), 1305–1323.

80. Messina, M. T.; Metrangolo, P.; Panzeri, W.; Ragg, E.; Resnati, G. Perfluorocarbon-Hydrocarbon Self-Assembly. Part 3. Liquid Phase Interactions between Perfluoroalkylhalides and Heteroatom Containing Hydrocarbons. *Tetrahedron Lett.* **1998**, *39* (49), 9069–9072.

81. Cardillo, P.; Corradi, E.; Lunghi, A.; Valdo Meille, S.; Teresa Messina, M.; Metrangolo, P.; Resnati, G. The N···I Intermolecular Interaction as a General Protocol for the Formation of Perfluorocarbon–Hydrocarbon Supramolecular Architectures 1. *Tetrahedron* **2000**, *56* (30), 5535–5550.

82. Sarwar, M. G.; Dragisic, B.; Salsberg, L. J.; Gouliaras, C.; Taylor, M. S. Thermodynamics of Halogen Bonding in Solution: Substituent, Structural, and Solvent Effects. *J. Am. Chem. Soc.* **2010**, *132* (5), 1646–1653.

83. Chudzinski, M. G.; Taylor, M. S. Correlations between Computation and Experimental Thermodynamics of Halogen Bonding. *J. Org. Chem.* **2012**, *77* (7), 3483–3491.

84. Legon, A. C. The Halogen Bond: An Interim Perspective. *Phys. Chem. Chem. Phys.* **2010**, *12* (28), 7736.

85. Legon, A. C. Prereactive Complexes of Dihalogens XY with Lewis Bases B in the Gas Phase: A Systematic Case for the Halogen Analogue B···XY of the Hydrogen Bond B···HX. *Angew. Chemie Int. Ed.* **1999**, *38* (18), 2686–2714.

86. Ellington, T. L.; Reves, P. L.; Simms, B. L.; Wilson, J. L.; Watkins, D. L.; Tschumper, G. S.; Hammer, N. I. Quantifying the Effects of Halogen Bonding by Haloaromatic Donors on the Acceptor Pyrimidine. *ChemPhysChem* **2017**, *18* (10), 1267–1273.

87. Oliveira, V.; Kraka, E.; Cremer, D. Quantitative Assessment of Halogen Bonding Utilizing Vibrational Spectroscopy. *Inorg. Chem.* **2017**, *56* (1), 488–502.

88. Konkoli, Z.; Cremer, D. A New Way of Analyzing Vibrational Spectra. I. Derivation of Adiabatic Internal Modes. *Int. J. Quantum Chem.* **1998**, *67* (1), 1–9.

89. Zou, W.; Kalescky, R.; Kraka, E.; Cremer, D. Relating Normal Vibrational Modes to Local Vibrational Modes with the Help of an Adiabatic Connection Scheme. *J. Chem. Phys.* **2012**, *137* (8), 084114.

90. Oliveira, V.; Kraka, E.; Cremer, D. The Intrinsic Strength of the Halogen Bond: Electrostatic and Covalent Contributions Described by Coupled Cluster Theory. *Phys. Chem. Chem. Phys.* **2016**, *18* (48), 33031–33046.

91. Lommerse, J. P. M.; Stone, A. J.; Taylor, R.; Allen, F. H. The Nature and Geometry of Intermolecular Interactions between Halogens and Oxygen or Nitrogen. *J. Am. Chem. Soc.* **1996**, *118* (13), 3108–3116.

92. Robinson, S. W.; Mustoe, C. L.; White, N. G.; Brown, A.; Thompson, A. L.; Kennepohl, P.; Beer, P. D. Evidence for Halogen Bond Covalency in Acyclic and Interlocked Halogen-Bonding Receptor Anion Recognition. *J. Am. Chem. Soc.* **2015**, *137* (1), 499–507.

93. Shadle, S. E.; Hedman, B.; Hodgson, K. O.; Solomon, E. I. Ligand K-Edge X-Ray Absorption Spectroscopy as a Probe of Ligand-Metal Bonding: Charge Donation and Covalency in Copper-Chloride Systems. *Inorg. Chem.* **1994**, *33* (19), 4235–4244.

94. Delgado-Jaime, M. U.; Conrad, J. C.; Fogg, D. E.; Kennepohl, P. X-Ray Absorption Methods for the Determination of Ru–Cl Bond Covalency in Olefin Metathesis Catalysts: On the Normalization of Chlorine K-Edges in

Ruthenium Complexes. *Inorganica Chim. Acta* **2006**, *359* (9), 3042–3047.

95. Mustoe, C. L.; Gunabalasingam, M.; Yu, D.; Patrick, B. O.; Kennepohl, P. Probing Covalency in Halogen Bonds through Donor K-Edge X-Ray Absorption Spectroscopy: Polyhalides as Coordination Complexes. *Faraday Discuss.* **2017**, *203*, 79–91.

96. Riley, K. E.; Hobza, P. Investigations into the Nature of Halogen Bonding Including Symmetry Adapted Perturbation Theory Analyses. *J. Chem. Theory Comput.* **2008**, *4* (2), 232–242.

97. Riley, K. E.; Tran, K.-A. Strength, Character, and Directionality of Halogen Bonds Involving Cationic Halogen Bond Donors. *Faraday Discuss.* **2017**, *203*, 47–60.

98. Stone, A. J. Are Halogen Bonded Structures Electrostatically Driven? *J. Am. Chem. Soc.* **2013**, *135* (18), 7005–7009.

99. Riley, K. E.; Hobza, P. The Relative Roles of Electrostatics and Dispersion in the Stabilization of Halogen Bonds. *Phys. Chem. Chem. Phys.* **2013**, *15* (41), 17742.

100. Hwang, J.; Dial, B. E.; Li, P.; Kozik, M. E.; Smith, M. D.; Shimizu, K. D. How Important Are Dispersion Interactions to the Strength of Aromatic Stacking Interactions in Solution? *Chem. Sci.* **2015**, *6* (7), 4358–4364.

101. Palusiak, M. On the Nature of Halogen Bond – The Kohn–Sham Molecular Orbital Approach. *J. Mol. Struct. THEOCHEM* **2010**, *945* (1–3), 89–92.

102. Wolters, L. P.; Bickelhaupt, F. M. Halogen Bonding versus Hydrogen Bonding: A Molecular Orbital Perspective. *ChemistryOpen* **2012**, *1* (2), 96–105.

103. Thirman, J.; Engelage, E.; Huber, S. M.; Head-Gordon, M. Characterizing the Interplay of Pauli Repulsion, Electrostatics, Dispersion and Charge Transfer in Halogen Bonding with Energy Decomposition Analysis. *Phys. Chem. Chem. Phys.* **2018**, *20* (2), 905–915.

104. Wang, Z.; Zheng, B.; Yu, X.; Li, X.; Yi, P. Structure, Properties, and Nature of the Pyridine-XY (X, Y=F, Cl, Br) Complexes: An Ab Initio Study. *J. Chem. Phys.* **2010**, *132* (16), 164104.

105. Rosokha, S. V.; Stern, C. L.; Ritzert, J. T. Experimental and Computational Probes of the Nature of Halogen Bonding: Complexes of Bromine-Containing Molecules with Bromide Anions. *Chem. - A Eur. J.* **2013**, *19* (27), 8774–8788.

106. Rosokha, S. V; Stern, C. L.; Swartz, A.; Stewart, R. Halogen Bonding of Electrophilic Bromocarbons with Pseudohalide Anions. *Phys. Chem. Chem. Phys.* **2014**, *16* (25), 12968–12979.

107. Smith, D. A.; Brammer, L.; Hunter, C. A.; Perutz, R. N. Metal Hydrides Form Halogen Bonds: Measurement of Energetics of Binding. *J. Am. Chem. Soc.* **2014**, *136* (4), 1288–1291.

108. Jabłoński, M.; Palusiak, M. Nature of a Hydride–Halogen Bond. A SAPT-, QTAIM-, and NBO-Based Study. *J. Phys. Chem. A* **2012**, *116* (9), 2322–2332.

109. Burling, F. T.; Goldstein, B. M. Computational Studies of Nonbonded Sulfur-Oxygen and Selenium-Oxygen Interactions in the Thiazole and Selenazole Nucleosides. *J. Am. Chem. Soc.* **1992**, *114* (7), 2313–2320.

110. Umeyama, H.; Morokuma, K.; Yamabe, S. Molecular Orbital Studies of Electron Donor-Acceptor Complexes. 4. Energy Decomposition Analysis of Halo-Complexes: Ammonia-Fluorine, -Chlorine, -Chlorine Fluoride, Methanamine-Chlorine Fluoride, Formaldehyde-Fluorine, Hydrogen Fluoride-Chlorine Fluoride,. *J. Am. Chem. Soc.* **1977**, *99* (2), 330–343.

111. Benz, S.; López-Andarias, J.; Mareda, J.; Sakai, N.; Matile, S. Catalysis with Chalcogen Bonds. *Angew. Chemie Int. Ed.* **2017**, *56* (3), 812–815.

112. Murray, J. S.; Lane, P.; Clark, T.; Politzer, P. σ-Hole Bonding: Molecules Containing Group VI Atoms. *J. Mol. Model.* **2007**, *13* (10), 1033–1038.

113. Rosenfield, R. E.; Parthasarathy, R.; Dunitz, J. D. Directional Preferences of Nonbonded Atomic Contacts with Divalent Sulfur. 1. Electrophiles and Nucleophiles. *J. Am. Chem. Soc.* **1977**, *99* (14), 4860–4862.

114. Row, T. N. G.; Parthasarathy, R. Directional Preferences of Nonbonded Atomic Contacts with Divalent Sulfur in Terms of Its Orbital Orientations. 2. Sulfur.Cntdot..Cntdot..Cntdot.Sulfur Interactions and Nonspherical Shape of Sulfur in Crystals. *J. Am. Chem. Soc.* **1981**, *103* (2), 477–479.

115. Goldstein, B. M.; Kennedy, S. D.; Hennen, W. J. Selenium-77 NMR and Crystallographic Studies of Selenazofurin and Its 5-Amino Derivative. *J. Am. Chem. Soc.* **1990**, *112* (23), 8265–8268.

116. Iwaoka, M.; Tomoda, S. Structural Characterization of Areneselenenyl Chloride Stabilized by the Stereoelectronic Effect of an Intramolecular Nitrogen Atom. *J. Org. Chem* **1995**, *60*, 5299–5302.

117. Iwaoka, M.; Tomoda, S. Nature of the Intramolecular Se···N Nonbonded Interaction of 2-Selenobenzylamine Derivatives. An Experimental Evaluation by 1 H, 77 Se, and 15 N NMR Spectroscopy. *J. Am. Chem. Soc.* **1996**, *118* (34), 8077–8084.

118. Iwaoka, M.; Komatsu, H.; Katsuda, T.; Tomoda, S. Quantitative Evaluation of Weak Nonbonded Se···F Interactions and Their Remarkable Nature as Orbital Interactions. *J. Am. Chem. Soc.* **2002**, *124* (9), 1902–1909.

119. Iwaoka, M.; Komatsu, H.; Katsuda, T.; Tomoda, S. Nature of Nonbonded Se···O Interactions Characterized by 17 O NMR Spectroscopy and NBO and AIM Analyses. *J. Am. Chem. Soc.* **2004**, *126* (16), 5309–5317.

120. Iwaoka, M.; Katsuda, T.; Komatsu, H.; Tomoda, S. Experimental and Theoretical Studies on the Nature of Weak Nonbonded Interactions between Divalent Selenium and Halogen Atoms. *J. Org. Chem.* **2005**, *70* (1), 321–327.

121. Barton, D. H. R.; Hall, M. B.; Lin, Z.; Parekh, S. I.; Reibenspies, J. Unusual

Attractive Interactions between Selenium and Oxygen in Selenoiminoquinones. *J. Am. Chem. Soc.* **1993**, *115* (12), 5056–5059.

122. Biot, N.; Bonifazi, D. Programming Recognition Arrays through Double Chalcogen-Bonding Interactions. *Chem. - A Eur. J.* **2017**.

123. Nuzzo, S.; Twamley, B.; Platts, J. A.; Baker, R. J. Pseudohalide Tectons within the Coordination Sphere of the Uranyl Ion: Experimental and Theoretical Study of C–H···O, C–H···S, and Chalcogenide Noncovalent Interactions. *Inorg. Chem.* **2018**, *57* (7), 3699–3712.

124. Tsubomoto, Y.; Hayashi, S.; Nakanishi, W.; Mapp, L. K.; Coles, S. J. High-Resolution X-Ray Diffraction Determination of the Electron Density of 1-(8-PhSC 10 H 6)SS(C 10 H 6 SPh-8′)-1′ with the QTAIM Approach: Evidence for S 4 σ(4c–6e) at the Naphthalene Peri -Positions. *RSC Adv.* **2018**, *8* (18), 9651–9660.

125. Garrett, G. E.; Gibson, G. L.; Straus, R. N.; Seferos, D. S.; Taylor, M. S. Chalcogen Bonding in Solution: Interactions of Benzotelluradiazoles with Anionic and Uncharged Lewis Bases. *J. Am. Chem. Soc.* **2015**, *137* (12), 4126–4133.

126. Bleiholder, C.; Werz, D. B.; Köppel, H.; Gleiter, R. Theoretical Investigations on Chalcogen−Chalcogen Interactions: What Makes These Nonbonded Interactions Bonding? *J. Am. Chem. Soc.* **2006**, *128* (8), 2666–2674.

127. Bleiholder, C.; Gleiter, R.; Werz, D. B.; Köppel, H. Theoretical Investigations on Heteronuclear Chalcogen−Chalcogen Interactions: On the Nature of Weak Bonds between Chalcogen Centers. *Inorg. Chem.* **2007**, *46* (6), 2249–2260.

128. Bauzá, A.; Quiñonero, D.; Deyà, P. M.; Frontera, A. Halogen Bonding Versuschalcogen and Pnicogen Bonding: A Combined Cambridge Structural Database and Theoretical Study. *CrystEngComm* **2013**, *15* (16), 3137–3144.

129. De Vleeschouwer, F.; Denayer, M.; Pinter, B.; Geerlings, P.; De Proft, F. Characterization of Chalcogen Bonding Interactions via an In-Depth Conceptual Quantum Chemical Analysis. *J. Comput. Chem.* **2018**, *39* (10), 557–572.

130. Oliveira, V.; Cremer, D.; Kraka, E. The Many Facets of Chalcogen Bonding: Described by Vibrational Spectroscopy. *J. Phys. Chem. A* **2017**, *121* (36), 6845–6862.

131. Murray, J. S.; Lane, P.; Politzer, P. A Predicted New Type of Directional Noncovalent Interaction. *Int. J. Quantum Chem.* **2007**, *107* (12), 2286–2292.

132. Hill, W. E.; Silva-Trivino, L. M. Preparation and Characterization of Di(Tertiary Phosphines) with Electronegative Substituents. 1. Symmetrical Derivatives. *Inorg. Chem.* **1978**, *17* (9), 2495–2498.

133. Politzer, P.; Murray, J.; Janjić, G.; Zarić, S. σ-Hole Interactions of Covalently-Bonded Nitrogen, Phosphorus and Arsenic: A Survey of Crystal Structures. *Crystals* **2014**, *4* (4), 12–31.

134. Zhang, D.-P.; Dou, J.-M.; Li, D.-C.; Wang, D.-Q. 1,2-Bis(Diphenylphosphino)-1,2-Dicarba- Closo -Dodecaborane. *Acta Crystallogr. Sect. E Struct. Reports Online* **2006**, *62* (2), o418–o419.

135. Sundberg, M. R.; Uggla, R.; Viñas, C.; Teixidor, F.; Paavola, S.; Kivekäs, R. Nature of Intramolecular Interactions in Hypercoordinate C-Substituted 1,2-Dicarba-Closo-Dodecaboranes with Short P···P Distances. *Inorg. Chem. Commun.* **2007**, *10* (6), 713–716.

136. Guan, L.; Mo, Y. Electron Transfer in Pnicogen Bonds. *J. Phys. Chem. A* **2014**, *118* (39), 8911–8921.

137. Scheiner, S. A New Noncovalent Force: Comparison of P···N Interaction with Hydrogen and Halogen Bonds. *J. Chem. Phys.* **2011**, *134* (9), 094315.

138. Del Bene, J. E.; Alkorta, I.; Sanchez-Sanz, G.; Elguero, J. Structures, Energies, Bonding, and NMR Properties of Pnicogen Complexes H 2 XP:NXH 2 (X = H, CH 3 , NH 2 , OH, F, Cl). *J. Phys. Chem. A* **2011**, *115* (46), 13724–13731.

139. Del Bene, J. E.; Alkorta, I.; Elguero, J. Properties of Complexes H 2 C=(X)P:PXH 2 , for X = F, Cl, OH, CN, NC, CCH, H, CH 3 , and BH 2 : P···P Pnicogen Bonding at σ-Holes and π-Holes. *J. Phys. Chem. A* **2013**, *117* (45), 11592–11604.

140. Del Bene, J. E.; Alkorta, I.; Elguero, J. Characterizing Complexes with Pnicogen Bonds Involving Sp 2 Hybridized Phosphorus Atoms: (H 2 C=PX) 2 with X = F, Cl, OH, CN, NC, CCH, H, CH 3 , and BH 2. *J. Phys. Chem. A* **2013**, *117* (31), 6893–6903.

141. Scheiner, S. The Pnicogen Bond: Its Relation to Hydrogen, Halogen, and Other Noncovalent Bonds. *Acc. Chem. Res.* **2013**, *46* (2), 280–288.

142. Scheiner, S. On the Properties of X···N Noncovalent Interactions for First-, Second-, and Third-Row X Atoms. *J. Chem. Phys.* **2011**, *134* (16), 164313.

143. Esrafili, M. D.; Mohammadian-Sabet, F.; Vessally, E. An Ab Initio Study on the Nature of σ-Hole Interactions in Pnicogen-Bonded Complexes with Carbene as an Electron Donor. *Mol. Phys.* **2016**, *114* (14), 2115–2122.

144. Bauzá, A.; Mooibroek, T. J.; Frontera, A. σ-Hole Opposite to a Lone Pair: Unconventional Pnicogen Bonding Interactions between ZF 3 (Z=N, P, As, and Sb) Compounds and Several Donors. *ChemPhysChem* **2016**, *17* (11), 1608–1614.

145. Setiawan, D.; Kraka, E.; Cremer, D. Strength of the Pnicogen Bond in Complexes Involving Group Va Elements N, P, and As. *J. Phys. Chem. A* **2015**, *119* (9), 1642–1656.

146. Eskandari, K.; Mahmoodabadi, N. Pnicogen Bonds: A Theoretical Study Based on the Laplacian of Electron Density. *J. Phys. Chem. A* **2013**, *117* (48), 13018–13024.

147. Schmauck, J.; Breugst, M. The Potential of Pnicogen Bonding for Catalysis –

a Computational Study. *Org. Biomol. Chem.* **2017**, *15* (38), 8037–8045.

148. Taylor, P. G.; Bassindale, A. R.; El Aziz, Y.; Pourny, M.; Stevenson, R.; Hursthouse, M. B.; Coles, S. J. Further Studies of Fluoride Ion Entrapment in Octasilsesquioxane Cages; X-Ray Crystal Structure Studies and Factors That Affect Their Formation. *Dalt. Trans.* **2012**, *41* (7), 2048–2059.

149. García-LLinás, X.; Bauzá, A.; Seth, S. K.; Frontera, A. Importance of R–CF 3 ⋯O Tetrel Bonding Interactions in Biological Systems. *J. Phys. Chem. A* **2017**, *121* (28), 5371–5376.

150. Liu, M.; Li, Q.; Cheng, J.; Li, W.; Li, H.-B. Tetrel Bond of Pseudohalide Anions with XH 3 F (X = C, Si, Ge, and Sn) and Its Role in S N 2 Reaction. *J. Chem. Phys.* **2016**, *145* (22), 224310.

151. Murray, J. S.; Lane, P.; Politzer, P. Expansion of the σ-Hole Concept. *J. Mol. Model.* **2009**, *15* (6), 723–729.

152. Bundhun, A.; Ramasami, P.; Murray, J. S.; Politzer, P. Trends in σ-Hole Strengths and Interactions of F3MX Molecules (M = C, Si, Ge and X = F, Cl, Br, I). *J. Mol. Model.* **2013**, *19* (7), 2739–2746.

153. Bauzá, A.; Mooibroek, T. J.; Frontera, A. Tetrel Bonding Interactions. *Chem. Rec.* **2016**, *16* (1), 473–487.

154. Liu, M.; Li, Q.; Scheiner, S. Comparison of Tetrel Bonds in Neutral and Protonated Complexes of PyridineTF 3 and FuranTF 3 (T = C, Si, and Ge) with NH 3. *Phys. Chem. Chem. Phys.* **2017**, *19* (7), 5550–5559.

155. Chandrasekaran, A.; Day, R. O.; Holmes, R. R. A New Class of Silatranes: Structure and Dynamic NMR Behavior 1. *J. Am. Chem. Soc.* **2000**, *122* (6), 1066–1072.

156. Laconsay, C. J.; Galbraith, J. M. A Valence Bond Theory Treatment of Tetrel Bonding Interactions. *Comput. Theor. Chem.* **2017**, *1116*, 202–206.

157. Liu, M.; Li, Q.; Li, W.; Cheng, J. Tetrel Bonds between PySiX3 and Some Nitrogenated Bases: Hybridization, Substitution, and Cooperativity. *J. Mol. Graph. Model.* **2016**, *65*, 35–42.

158. Scheiner, S. Systematic Elucidation of Factors That Influence the Strength of Tetrel Bonds. *J. Phys. Chem. A* **2017**, *121* (29), 5561–5568.

159. Frontera, A.; Bauzá, A. Concurrent Aerogen Bonding and Lone Pair/Anion–π Interactions in the Stability of Organoxenon Derivatives: A Combined CSD and Ab Initio Study. *Phys. Chem. Chem. Phys.* **2017**, *19* (44), 30063–30068.

160. Bauzá, A.; Frontera, A. π-Hole Aerogen Bonding Interactions. *Phys. Chem. Chem. Phys.* **2015**, *17* (38), 24748–24753.

161. Haner, J.; Schrobilgen, G. J. The Chemistry of Xenon(IV). *Chem. Rev.* **2015**, *115* (2), 1255–1295.

162. Esrafili, M. D.; Sadr-Mousavi, A. A Computational Study on the Strength and

Nature of Bifurcated Aerogen Bonds. *Chem. Phys. Lett.* **2018**, *698*, 1–6.

163. Koppe, K.; Haner, J.; Mercier, H. P. A.; Frohn, H.-J.; Schrobilgen, G. J. Xenon(IV)–Carbon Bond of [C 6 F 5 XeF 2] + ; Structural Characterization and Bonding of [C 6 F 5 XeF 2][BF 4], [C 6 F 5 XeF 2][BF 4]·2HF, and [C 6 F 5 XeF 2][BF 4]· n NCCH 3 (n = 1, 2); and the Fluorinating Properties of [C 6 F 5 XeF 2][BF 4]. *Inorg. Chem.* **2014**, *53* (21), 11640–11661.

164. Esrafili, M. D.; Mohammadian-Sabet, F.; Solimannejad, M. Single-Electron Aerogen Bonds: Do They Exist? *Chem. Phys. Lett.* **2016**, *659*, 196–202.

Chapter 2
Chalcogen-Bonding Interactions

Abstract

Favourable molecular interactions between group 16 elements have been implicated in catalysis, biological processes, and materials and medicinal chemistry. Such interactions have since become known as chalcogen bonds by analogy to hydrogen and halogen bonds. Although the prevalence and applications of chalcogen-bonding interactions continues to develop, debate still surrounds the energetic significance and physicochemical origins of this class of σ-hole interaction. Here, synthetic molecular balances were used to perform a quantitative experimental investigation of chalcogen-bonding interactions. Over 160 experimental conformational free energies were measured in 13 different solvents to examine the energetics of O···S, O···Se, S···S, O···HC, and S···HC contacts and the associated substituent and solvent effects. The strongest chalcogen-bonding interactions were found to be at least as strong as conventional H-bonds, but unlike H-bonds, surprisingly independent of the solvent. The independence of the conformational free energies on solvent polarity, polarizability, and H-bonding characteristics showed that electrostatic, solvophobic, and van der Waals dispersion forces did not account for the observed experimental trends. Instead, a quantitative relationship between the experimental conformational free energies and computed molecular orbital energies was consistent with the chalcogen-bonding interactions being dominated by n→σ* orbital delocalization between a lone pair (n) of a (thio)amide donor and the antibonding σ* orbital of an acceptor thiophene or selenophene. Interestingly, stabilization was manifested through the same acceptor molecular orbital irrespective of whether a direct chalcogen···chalcogen or chalcogen···H–C contact was made. Our results underline the importance of often-overlooked orbital delocalisation effects in conformational control and molecular recognition phenomena.

Publication: The Origin of Chalcogen-Bonding Interactions, *J. Am. Chem. Soc.*, **2017**, 139, 15160-1516

2.1 Introduction

It is perhaps counter-intuitive that favourable interactions between group 16 elements (oxygen, sulfur, selenium and tellurium) should exist, however, close contacts between these elements are commonly observed in crystal structures.[1,2] These σ-hole interactions were coined 'chalcogen interactions' by Clark *et al.* in 2007, and have been discussed extensively in **Chapter 1**. Despite the prevalence of chalcogen interactions, having been invoked in catalysis,[3–5] synthesis,[6,7] and materials,[8,9] biological,[10] medicinal[1,11] and supramolecular chemistry[12,13] (**Figure 2.1**), the precise physiochemical origins of the interaction remains a subject of debate (as highlighted in **Chapter 1**).

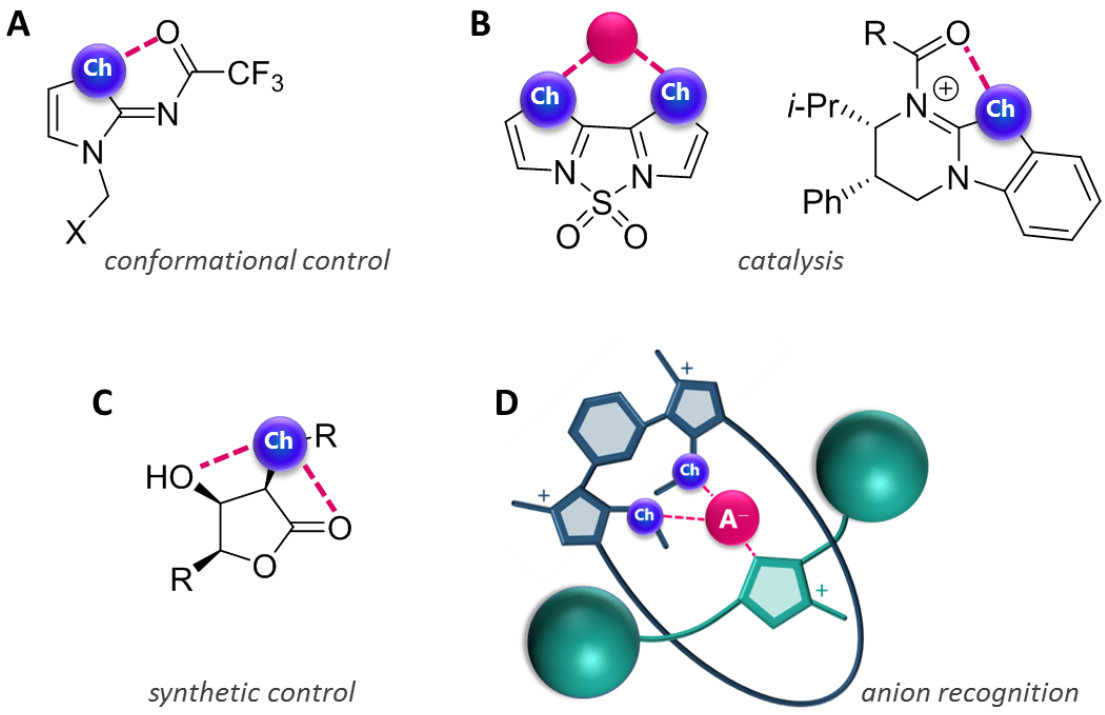

Figure 2.1 Applications of chalcogen bonding. (A) Conformational control in medicinal and agrochemistry,[1] (B) catalysis,[3,14] where the pink dot represents a substrate (C) synthetic chemistry[7] and (D) supramolecular anion recognition.[12]

2.2 Aims of the project

Previously, that the ability of foldamers to improve uptake of molecules, for example peptides, through the lipid bilayer of cells has been demonstrated.[15] Using H-bonds, molecular structure can be changed between a folded and an unfolded state. In the example in **Figure 2.2** the hydrophilic substituents are able to fold away from the lipid bilayer and form intramolecular H-bonds, increasing lipophilicity. When outside the bilayer, the foldamer can unfold to form favourable intermolecular H-bonds with the surrounding aqueous solvent.

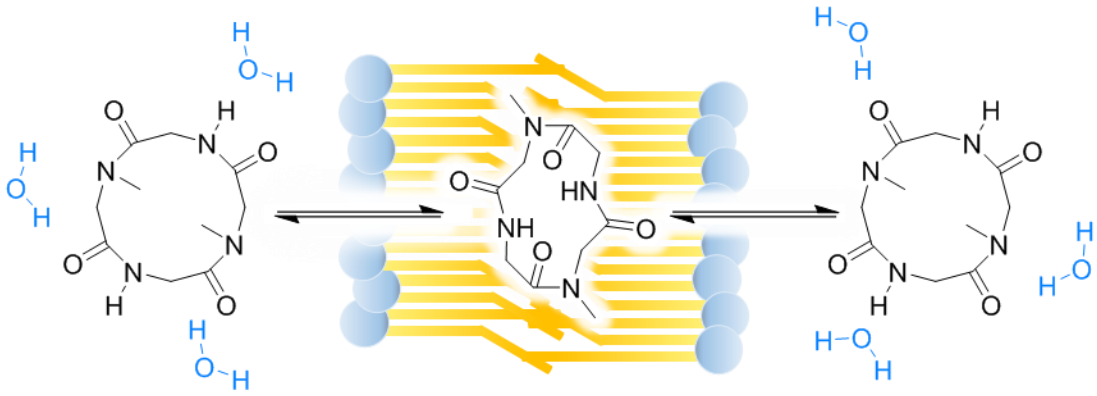

Figure 2.2 Structure of a foldamer in an aqueous environment (left and right) and in the lipid bilayer (middle). Upon folding the lipophilicity of the molecule increases, improving transport across the membrane.

Initial experimental measurements at *Syngenta* showed that chalcogen interactions could significantly impact the lipophilicity of molecules. Molecules with the motifs such as those shown in **Figure 2.3** were found to have much higher lipophilicity than calculated. It was proposed that the formation of an intramolecular chalcogen bond within the membrane could be one potential explanation for the higher than expected lipophilicity (**Figure 2.3**).

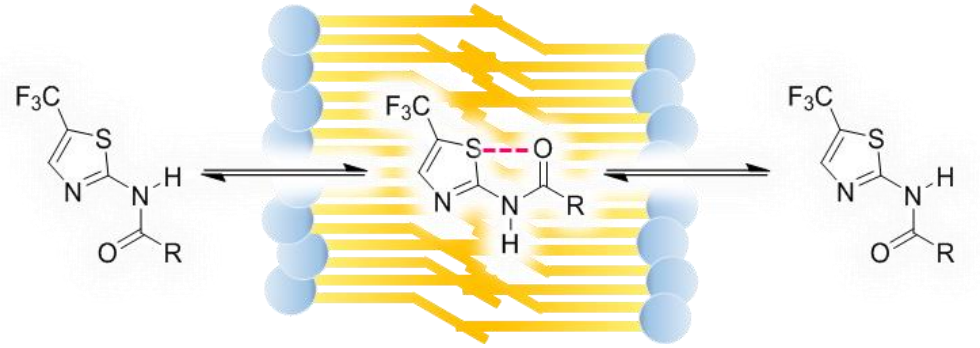

Figure 2.3 Structural motif supplied by *Syngenta*. Upon formation of an interaction between the sulfur and oxygen atoms, the lipophilicity of the molecule might be expected to increase, therefore improving uptake into cells.

The original aim of the project was to investigate the possibility of developing an 'adaptomer' system; one that can change its physical properties depending on its surrounding environment. The use of adaptomer systems could have a clear benefit in developing new agrochemicals, ensuring optimal physical parameters could be met at all stages of formulation and delivery (**Figure 2.4**). However, in order to develop such an adaptive system, it is important to first understand the nature of the relevant interactions, and their behaviour in solution, crucially in different solvents, and thus enable the rational design of new adaptomer systems.

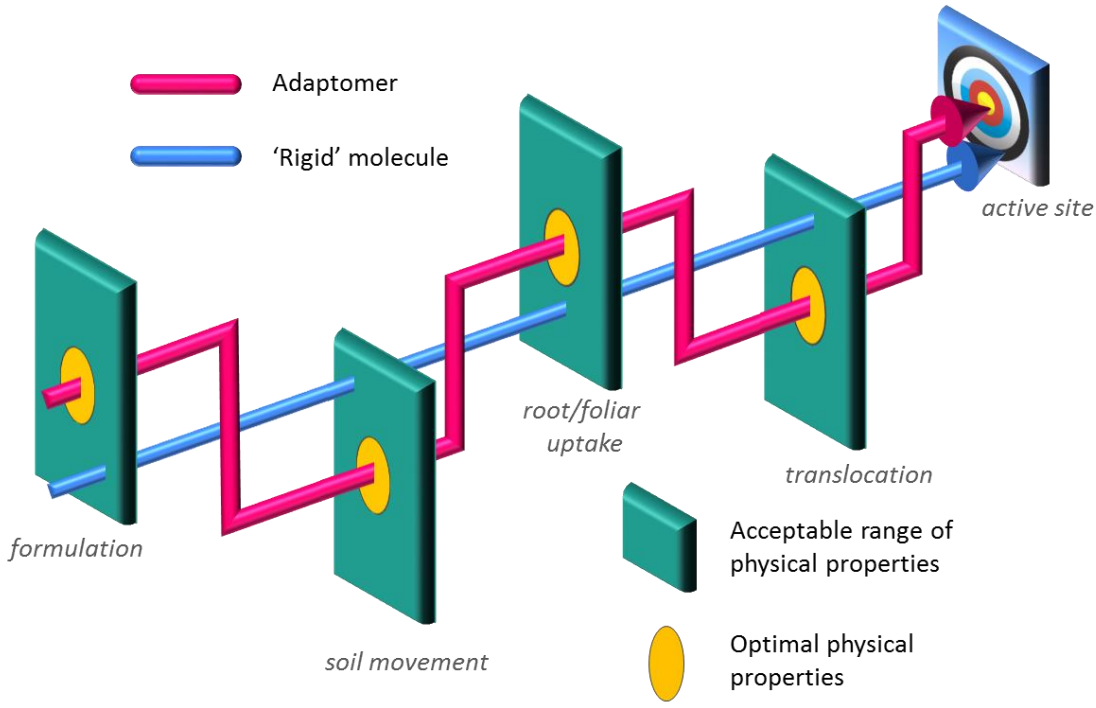

Figure 2.4 Schematic showing the proposed adaptomer concept. At each station the molecule would be able to change its physical properties to meet the optimal physical property required at that stage of formulation and delivery.

To understand the chalcogen interaction, and specifically to understand how it might behave in an adaptomer system, it was necessary to design an experimental system that mimics the chalcogen bonding motif used. Through varying the substituents on the motif supplied by *Syngenta*, the electronics of the system could be varied and the impact on the conformation free energy could be seen. As expected, substituent effects could have a large impact on the size and magnitude of the σ-hole, and therefore could impact the ability of an adaptomer (**Figure 2.5**).

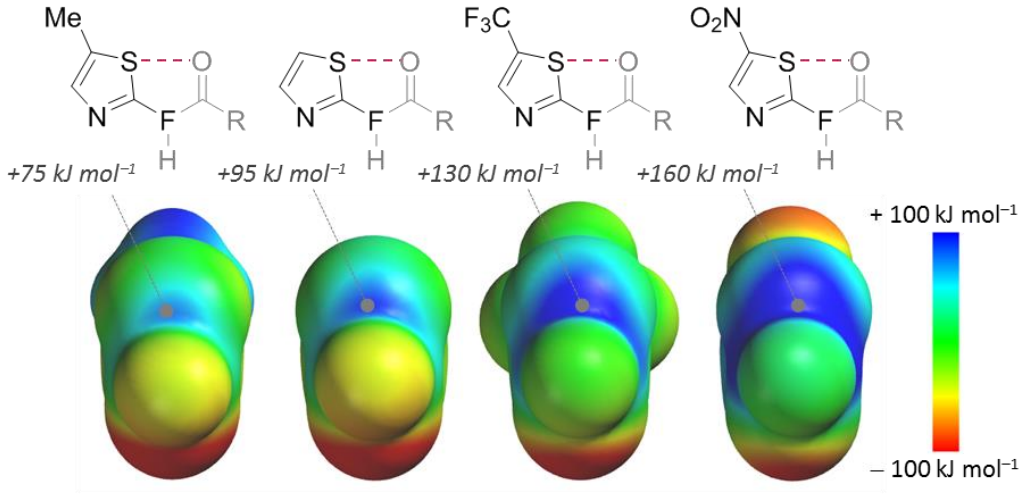

Figure 2.5 Structures of substituted derivatives of the motif supplied from *Syngenta*, where the amide group has been replaced with a fluorine cap to enable the σ-hole to be seen. The corresponding ESP diagrams highlight the magnitude of positive potential at the σ-hole. ESPs calculated using Spartan '14 DFT/B3LYP/6-311G*.

This chapter focuses on exploring the behaviour of chalcogen bonding in solution. Associated substituent and solvent effects have been studied to identify the energetic significance of these interactions in solution. Ultimately, a quantitative explanation for the nature of chalcogen-bonding interactions using a combined experimental and computational approach is proposed.

2.3 Molecular balances

Synthetic model compounds known as molecular torsion balances can be used for measuring and characterising non-covalent interactions.[16] Molecular balances typically contain a rotatable bond that allows the system to exist in two slowly exchanging conformers, the concentrations of which can be measured, for example by NMR spectroscopy. One of the conformers will contain the interaction of interest and the other that does not. Molecular balances were first demonstrated in 1990 by Oki using 1,9-disubstituted triptycenes to investigate weak interactions with arenes (**Figure 2.6A**).[17] Similar triptycene molecular balances have been used to study the interactions between oxygen and arene systems.[18,19] Wilcox designed his archetypical

molecular balance in 1994, again to investigate interactions with arene systems (**Figure 2.6B**).[20] Wilcox's system has become well known for studying molecular interactions, having been used to investigate interactions between alkyl and perfluoroalkyl chains,[21,22] and interactions with amide groups.[23,24] Other molecular balances have been developed by Gellman,[25,26] Motherwell,[27–29] Cockroft[30–33] and Shimizu[34,35] (**Figure 2.6C, D, E** and **F**) for investigating weak molecular interactions.

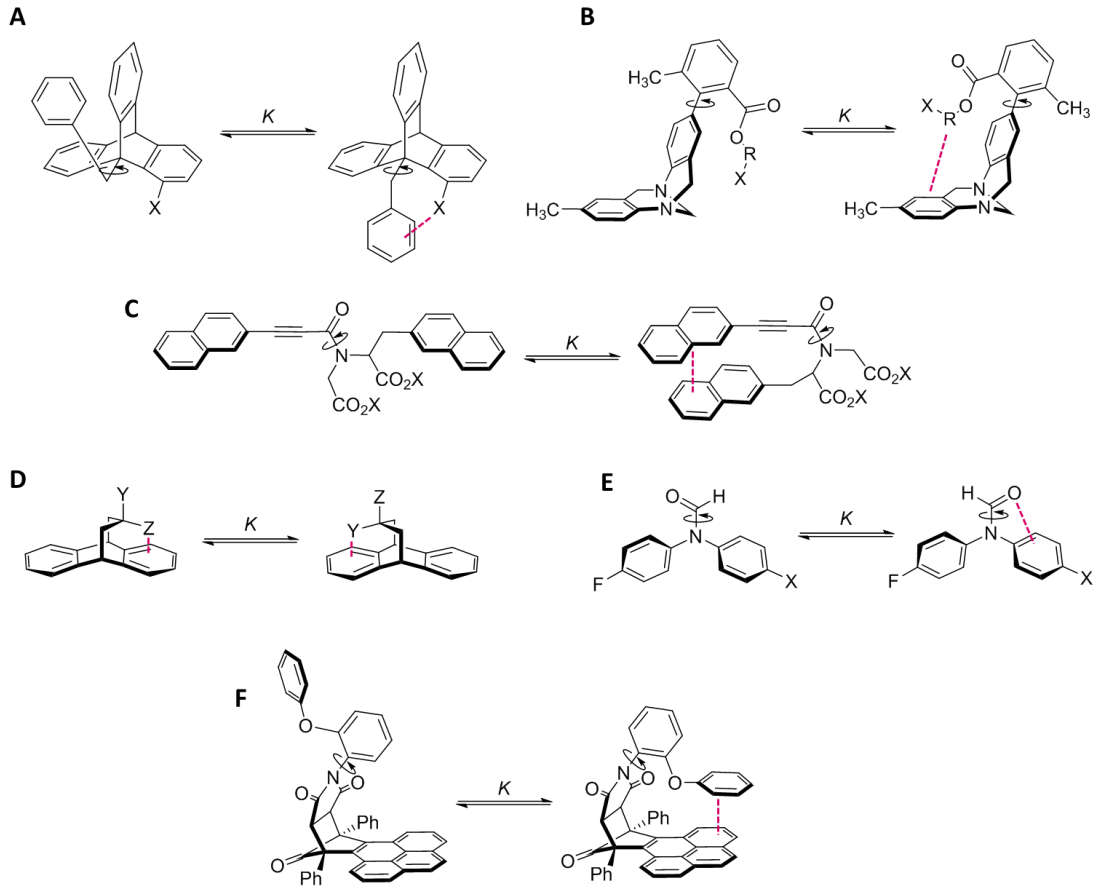

Figure 2.6 Structures of molecular balances designed by (A) Oki, (B) Wilcox, (C) Gellman, (D) Motherwell, (E) Cockroft and (F) Shimizu.

The conformational free energy differences between the two conformers are typically measured using NMR spectroscopy, and the ratio of the conformer integrals gives the conformational equilibrium, *K*. Using **Equation 2.1** the conformational free energy can be determined, where *R* is the gas constant and *T* is the temperature.

$$\Delta G = -RTlnK \qquad (\mathbf{2.1})$$

These systems also provide relatively easy access to the study of substituent effects and solvent effects.

2.3.1 Molecular balance design

For this investigation, a synthetic molecular balance based on the general design of those previously used in the Cockroft group (**Figure 2.6E**) was initially to investigate chalcogen-bonding interactions.

Due to the delocalisation of the lone pair of the nitrogen into the C-N bond (**Figure 2.8**), this bond has double-bond character. This character results in a slowly rotating formyl group, which allows both the *cis* and *trans* conformers to be observed on the NMR timescale. The inclusion of a fluorine tag on the phenyl ring allowed ^{19}F NMR to be used, therefore eliminating the need for often expensive deuterated solvents to investigate solvent effects.

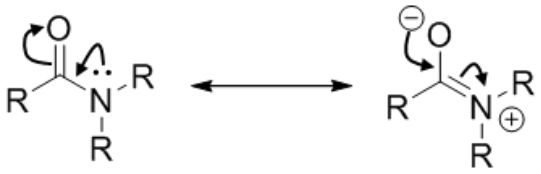

Figure 2.8 Delocalisation of the nitrogen lone pair in amides to give a double-bond characteristic. This allows the formyl group on molecular balances in **Figure 2.7** to rotate slowly on the NMR timescale.

A series of molecular balances were subsequently used to investigate O···S, O···Se (formamide balances, **Figure 2.9A** and **C**) and S···S (thioformide balances, **Figure 2.9D**) contacts. A series of β-thiophene molecular balances were also intended to act as controls in which no chalcogen···chalcogen contact could be formed, but instead allowing a chalcogen···H-C contact (**Figure 2.9B** and **E**).

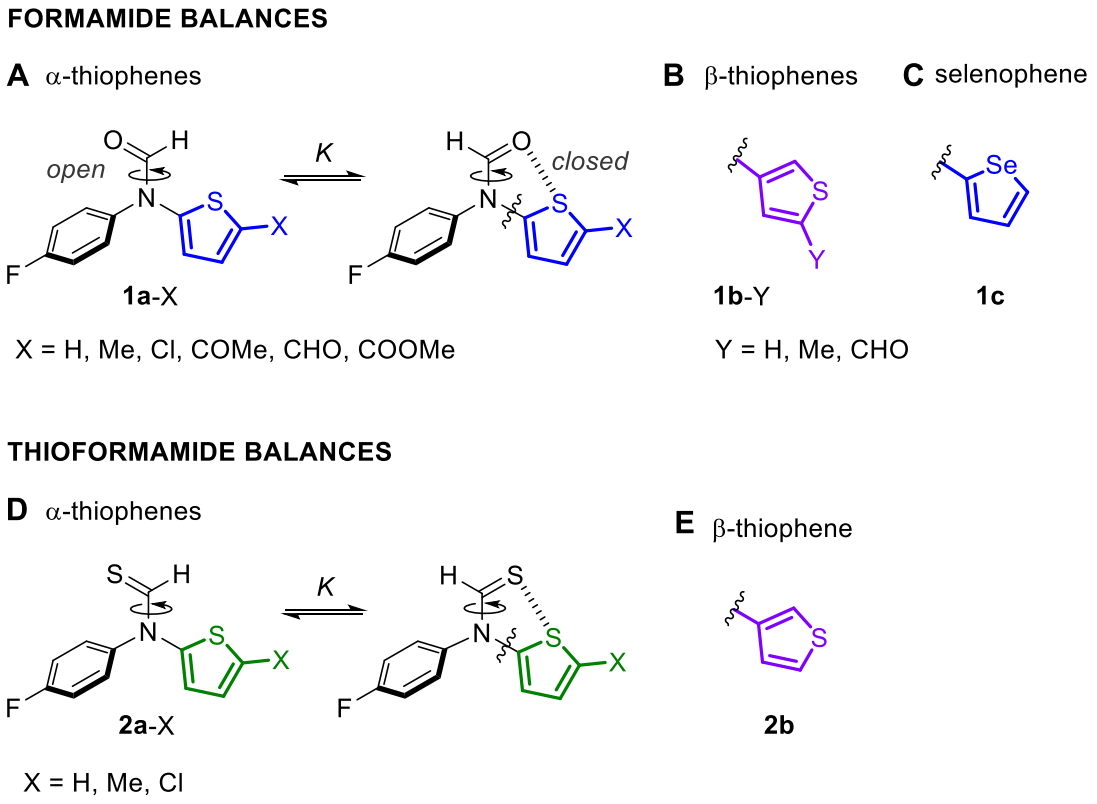

Figure 2.9 Molecular balances used in this investigation to study chalcogen bonding interactions.

To confirm that the system would provide the expected contacts, geometry optimisation calculations were performed (which will be discussed in greater detail later). The space-filling models showed that the amide and chalcogen-containing ring not only sat planar to one another, but also indicated overlap of the chalcogen van der Waal radii (**Figure 2.10A**). A non-covalent interaction (NCI) plot was used to investigate the potential interactions within the system.[36] A favourable interaction was suggested to be present between the chalcogens, confirming the suitability of this system for the study of chalcogen-bonding (**Figure 2.10B**).

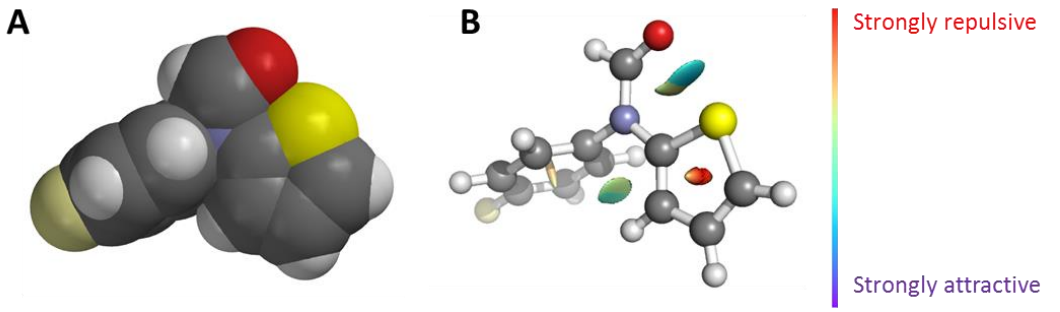

Figure 2.10 (A) Minimised space-filling model of molecular balance **1a**-H showing the close contact between sulfur and oxygen calculated using Spartan '14 DFT/B3LYP/6-311G*. (B) Non-covalent interaction (NCI) plot of molecular balance **1a**-H calculated using Gaussian '09 DFT/B3LYP/6-311G* and NCIplot and visualised using PyMol.

2.4 Synthesis of molecular balances

The molecular balance based around slow rotation of a formamide group has previously been employed within the Cockroft group to study a range of interactions, such as H-bonding, arene interactions and their associated substituent and solvent effects.[30–33] The simple synthesis of formamide-based molecular balances (often 2 steps) provides a clear advantage over other systems, such as the Wilcox balance (>8 steps). The synthetic ease with which formamide balances can be prepared enables facile scale-up to allow sufficient amounts of each balance to be prepared for large numbers of experimental measurements. The formamide balances are generally prepared through a Cu(I)-catalysed Goldberg-Ullmann coupling, which tolerates a good range of substituents (**Figure 2.11**), enabling the synthesis of diverse structures. Here, a range of bromothiophenes were used for the coupling step, giving the desired products in moderate yields.

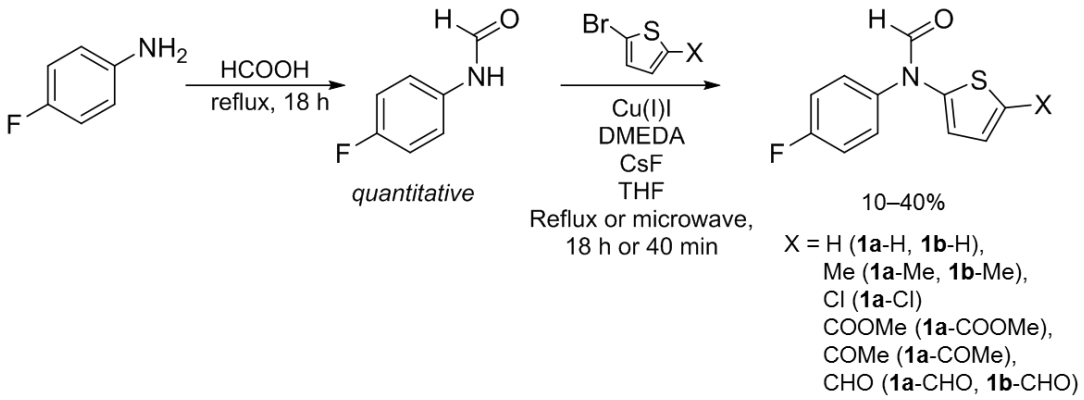

Figure 2.11 Synthesis of formamide molecular balance series used in this study, using either thermal or microwave conditions.

The conversion of the amide to a thioamide proved straightforward when using Lawesson's reagent, overall giving good yields across a range of electronically diverse substituents (**Figure 2.12**).

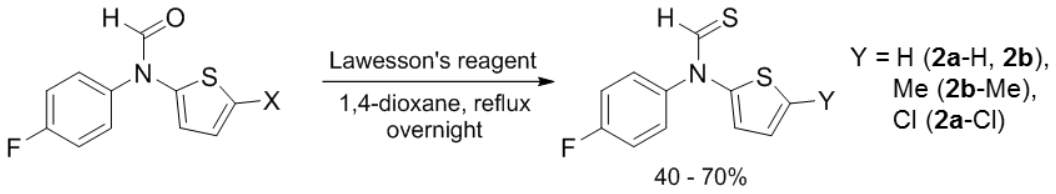

Figure 2.12 Synthesis of thioformamide molecular balances from corresponding formamide molecular balances.

For the selenium-based balance **1c**, selenophene was brominated and used immediately without any further purification in a Goldberg-Ullmann coupling to give the desired balance in a yield of 4% over two steps. This synthesis could not be further optimised, therefore limiting the amount of material that could be obtained, and limiting the number of solvents that could be examined (*vide infra*) (**Figure 2.13**).

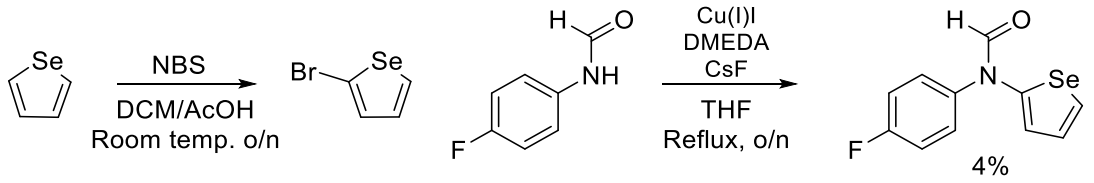

Figure 2.13 Synthesis of molecular balance **1c**.

2.5 Results and discussion

2.5.1 Determination of conformational free energies

Having synthesised a range of balances, the conformational free energies, ΔG, could be determined experimentally by using ^{19}F NMR spectroscopy to measure the ratio of the two conformers. Due to the slow rotation of the amide bond, two distinct peaks were observed in both the ^{19}F and ^{1}H NMR spectra, one for the open conformer, and one for the closed conformer (**Figure 2.14**).

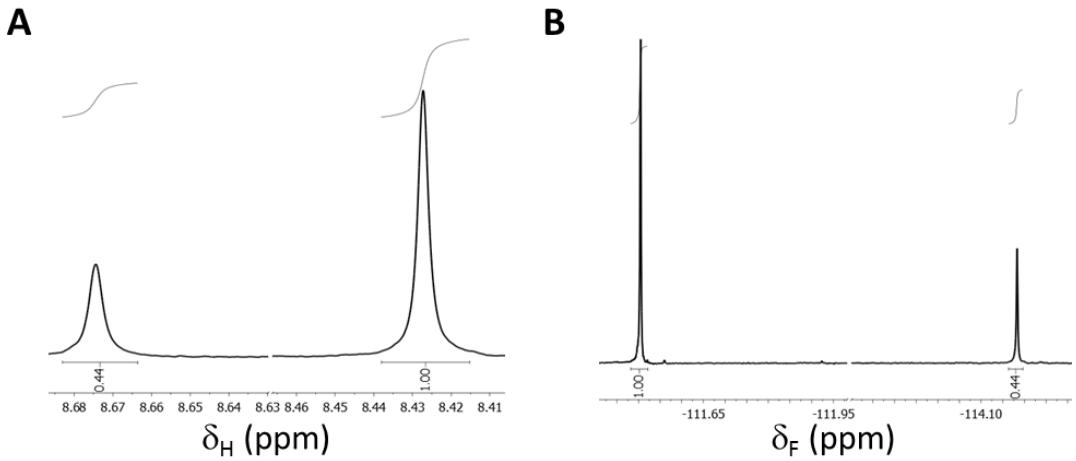

Figure 2.14 Partial NMR spectra of molecular balance **1a**-H showing the two conformers observed (A) ^{1}H NMR spectroscopy ($CDCl_3$, 500.1 MHz, 298 K) of the formamide resonance and (B) $^{19}F\{^{1}H\}$ NMR spectroscopy ($CDCl_3$, 376.5 MHz, 298 K) of the fluorine tag.

While the ratio of the two confirmers can be easily measured from the integrals of the peaks, it is not immediately clear which peak corresponds to which conformer, and

2D NMR must be employed to assign the peaks. First, the minimised structures of the molecular balances show that the formyl H and the 4-fluorophenyl ring are positioned close in space in the closed conformer (**Figure 2.15**). Using Nuclear Overhauser Effect spectroscopy (NOESY), protons that are close in space can be identified.

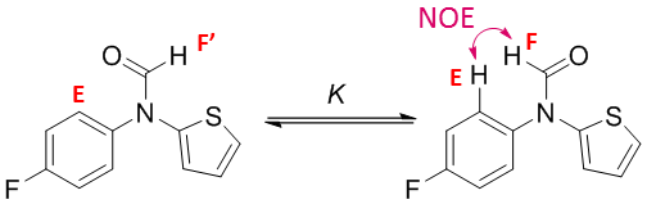

Figure 2.15 Structure of molecular balance **1a**-H showing where an NOE will be present in the closed conformer.

A clear cross peak was observed between protons **E** and **F** in one conformer that is not present in the other (**Figure 2.16**). This cross peak and corresponding signal for proton **F** therefore must represent the closed conformer.

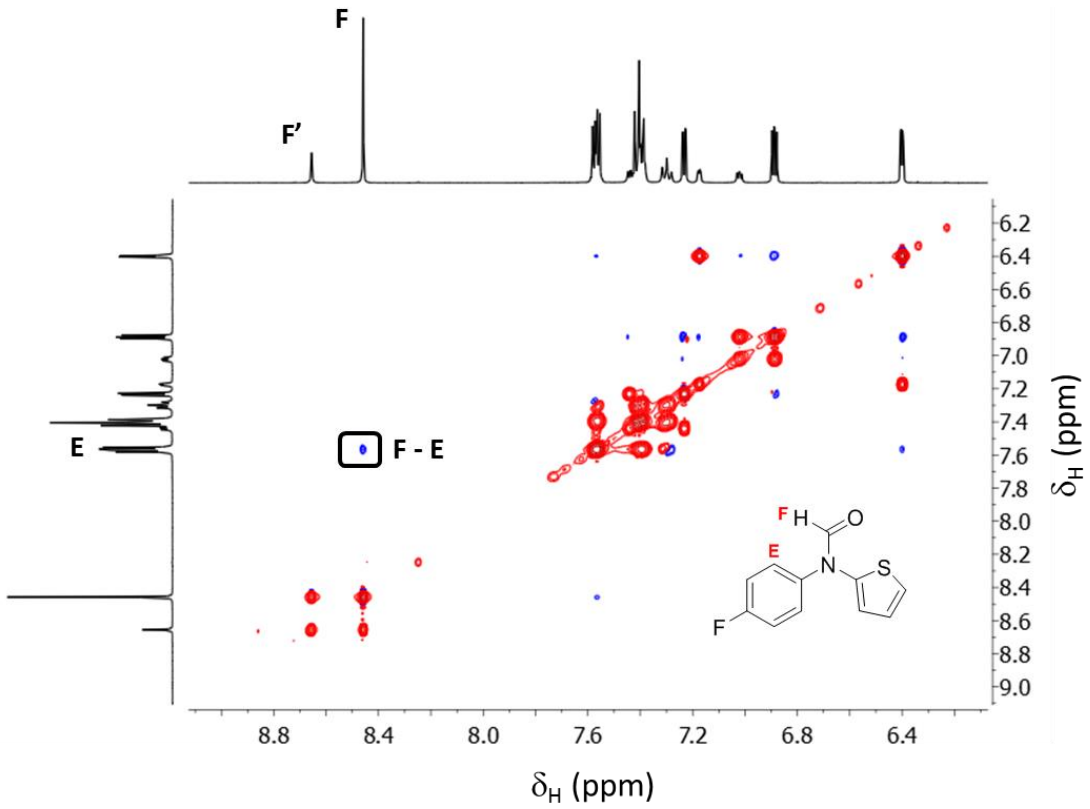

Figure 2.16 Partial ^{1}H-^{1}H NOESY NMR spectrum (DMSO-d_6, 500.1 MHz, mixing time = 400 ms 298 K) of molecular balance **1a**-H highlighting the cross peak corresponding the NOE seen between protons F and E.

Heteronuclear multiple bond correlation (HMBC) spectra can also confirm the correct assignment of conformers. A cross peak is observed between proton **F** and carbon **6** in the closed conformer, and proton **F** and carbon **8** in the open conformer. This is due to the 'W-effect' in NMR spectroscopy, where a planar 'W' shape will give a longer range cross coupling peak with atoms *trans* to itself (**Figure 2.17**).[37]

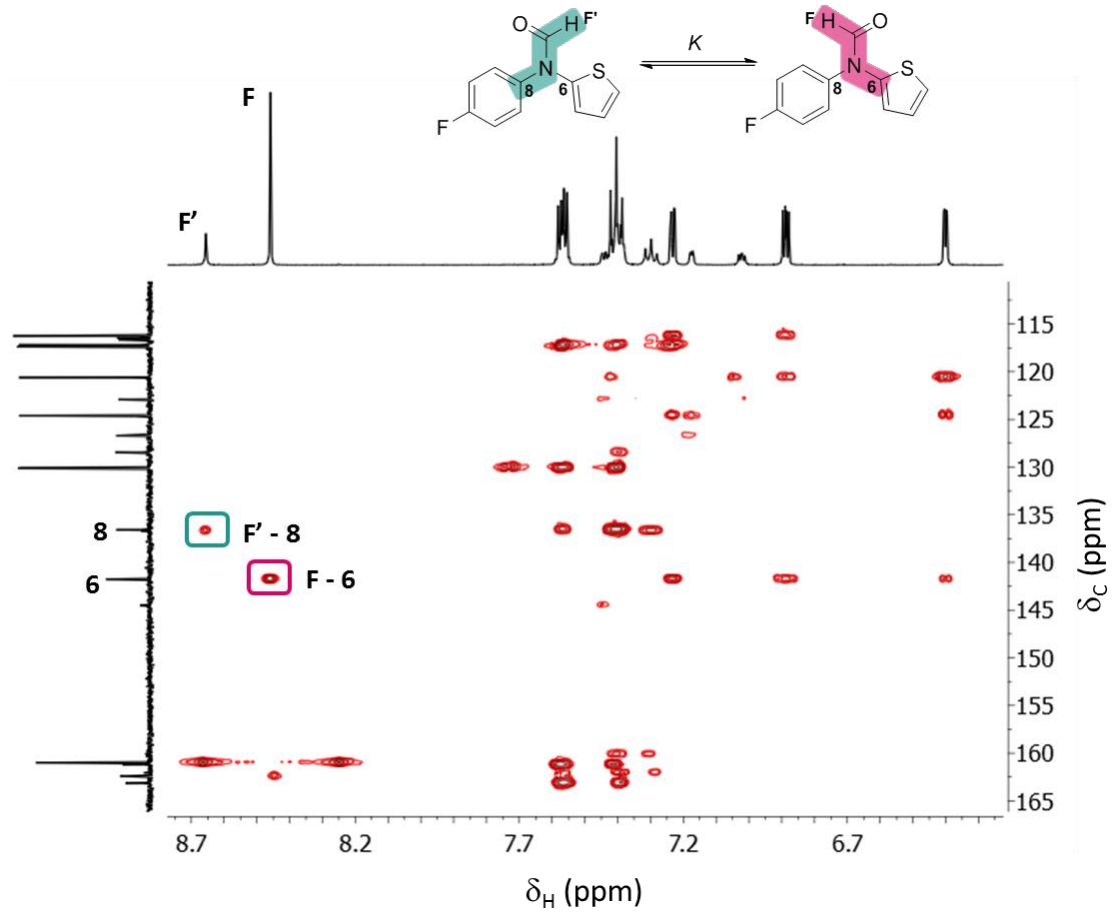

Figure 2.17 HMBC spectrum (DMSO-d_6, 500.1 MHz, 298 K) of molecular balance **1a**-H highlighting the cross peaks corresponding to the coupling seen between proton **F** and carbon **6** and the open conformer proton **F'** and carbon **8**.

Both 2D NMR techniques were applied to the assignment of conformers in all molecular balances in both $CDCl_3$ and DMSO-d_6. Crucially, the order of the peaks did not change in these solvents, i.e. the open confirmer always appeared more upfield of the closed conformer in ^{19}F NMR spectra. Thus, the assignment in other solvents could be made purely based on the relative chemical shifts of the observed resonances.

2.5.2 Experimental results

The ratio between the two conformers gives the value of the equilibrium constant governing the rotation between the two conformers, *K*. Once *K* has been measured, the conformational free energy can be calculated using **Equation 2.1** where *R* is the gas constant (8.314 J mol^{-1}), *T* is the temperature (in all cases presented in this study *T* = 298 K unless otherwise stated) and *K* is the equilibrium constant:

$$\Delta G = -RTlnK \qquad (\mathbf{2.1})$$

The conformational free energies of all molecular balances shown in **Figure 2.19** were measured across a range of solvents. Since the equilibrium is defined as *K* = [open]/[closed] in this investigation, values of ΔG <0 correspond to the closed conformer being the dominant conformer. Conformational ratios were found to be independent of concentration (**Figure 2.18**), indicating that no intermolecular interactions were influencing the system at the ~3 mM concentration used to measure the conformational free energies.

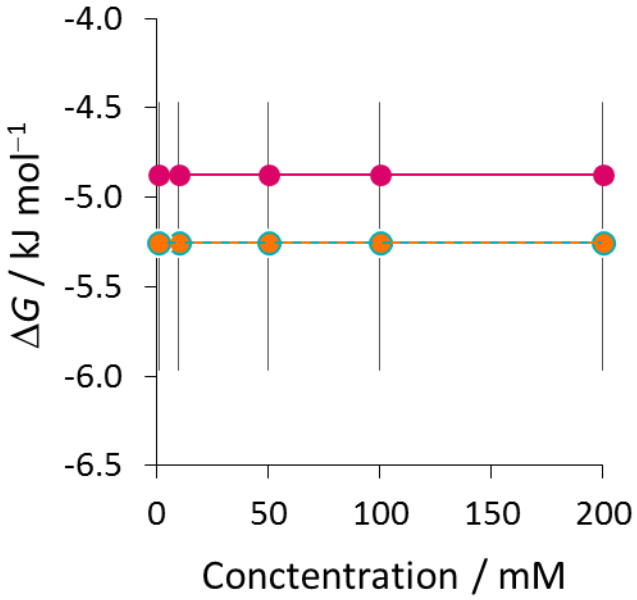

Figure 2.18 Experimental conformational free energy differences of molecular balance **1a**-Cl measured by $^{19}F\{^{1}H\}$ NMR spectroscopy (376.5 MHz, 298 K) at varying concentrations between 1 and 200 mM in $CDCl_3$ (pink), benzene-d_6 (teal) and DMSO-d_6 (orange).

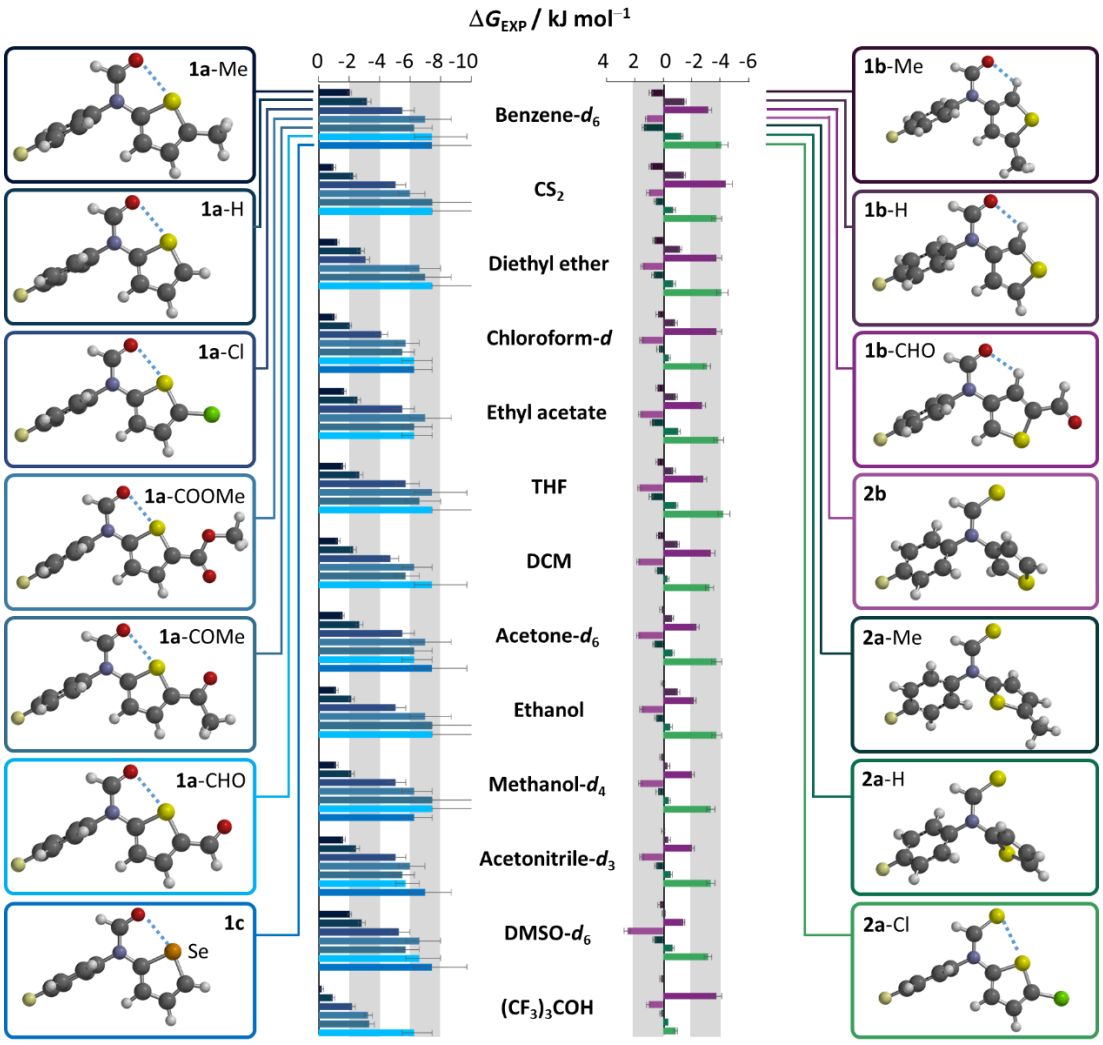

Figure 2.19 Experimental conformational free energies (ΔG_{EXP}) of the molecular balances shown measured in 13 different solvents using $^{19}F\{^{1}H\}$ NMR spectroscopy (376.5 MHz, 298 K). Corresponding minimised geometries of molecular balances in the closed conformer are shown. Colours correspond to those used in **Figure 2.9** representing the different series. Geometry optimisations were performed using Spartan '14 DFT/B3LYP/6-311G*.

Both the computed geometries and experimentally measured conformational free energies showed that all of the examined O···S and O···Se contacts were favourable (series **1a** and **1c**, **Figure 2.19**). However, the S···S contacts only became favourable upon addition of an electron-withdrawing group (EWG) (**2a**-Cl), with the other two molecular balances preferring the open conformer (**2a**-Me and **2a**-H).

2.5.3 Evaluation of solvent-mediated electrostatic and solvophobic effects

When considering molecular interactions in solution, it is important to consider the influence of the solvent, which may exert both electrostatic and solvophobic effects.[30,38–40] Forming an interaction between a two functional groups in solution, requires desolvation of both groups (**Figure 2.20**).

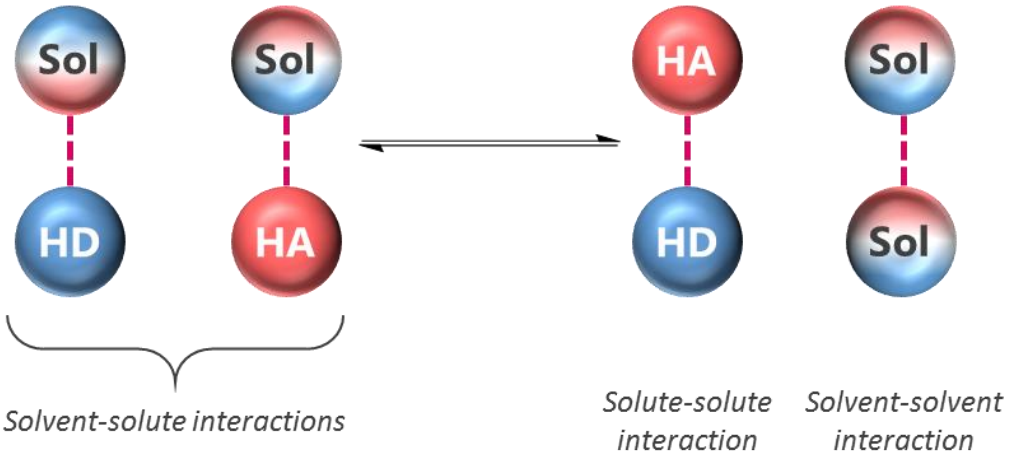

Figure 2.20 Schematic of solvation/desolvation of interacting partners resulting in solvent solute interactions (left) and solute-solute and solvent-solvent interactions (right).

In electrostatically driven interactions, particularly in hydrogen bonding, as the H-bond donor and acceptor abilities of the solvent (α_s and β_s respectively) increase, then solute-solvent interactions may be increasingly outcompete intra- or inter-molecular solute-solute interactions (**Figure 2.21**).[41]

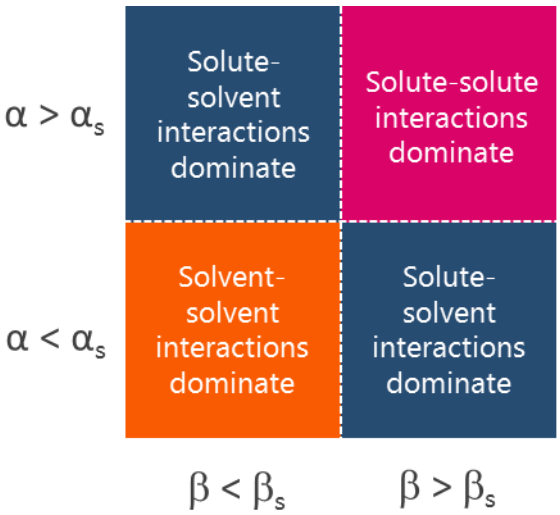

Figure 2.21 Scheme showing which interactions dominate depending on the magnitude of the H-bond donor or acceptor ability of the solvent (α_s or β_s respectively) or the solute (α or β). Adapted from reference 39.

As a result, previous studies of H-bonds and other electrostatic interactions have found that conformational free energies can vary substantially as the solvent is changed.[31,33] Strikingly, minimal solvent dependence is observed in the conformational free energy differences of the molecular balances presented in **Figure 2.9**. While few studies have investigated solvent effects in σ-hole interactions, several investigators have found weaker solvents effects compared to other interactions such as H-bonds (discussed in **Chapter 1**).[42–45] For example, the solvent independence observed in the present investigation of chalcogen bonding is in agreement with Hunter's report of "solvent resistant halogen bonds".[42]

Even when considering the data obtained in solvents with extreme α_s and β_s values, such as methanol-d_4 (α_s = 2.7[41]) or dimethylsulfoxide-d_6 (DMSO-d_6, β_s = 8.9[41]), the conformational preference of the molecular balances remain unchanged even compared to apolar solvents such as benzene-d_6 and CS_2. In fact, the only significant change in conformational preference was seen when the exceptionally strong H-bond donor perfluoro-*tert*-butanol was used, which resulted in around a 2 kJ mol^{-1} shift toward the open conformer, presumably due to favourable solvation of the formyl oxygen atom. The independence of the equilibrium position in the chalcogen-bonding

balances to the H-bonding abilities of the solvent suggests that a traditional electrostatic argument, such as is frequently applied to H-bonding, cannot be applied to chalcogen bonding.

A poor correlation was observed between the experimentally determined conformational free energy difference and the calculated electrostatic potential maxima $V_{s,max}$ located over the σ-hole of the thiophene fragments in the balances containing chalcogen···chalcogen contacts (R^2 = 0.60) (**Figure 2.22**). Such an observation is contrary to previous correlations seen in chalcogen bonding, and other σ-hole interactions,[45–47] further undermining an electrostatic model for the origin of the chalcogen bonds in our system.

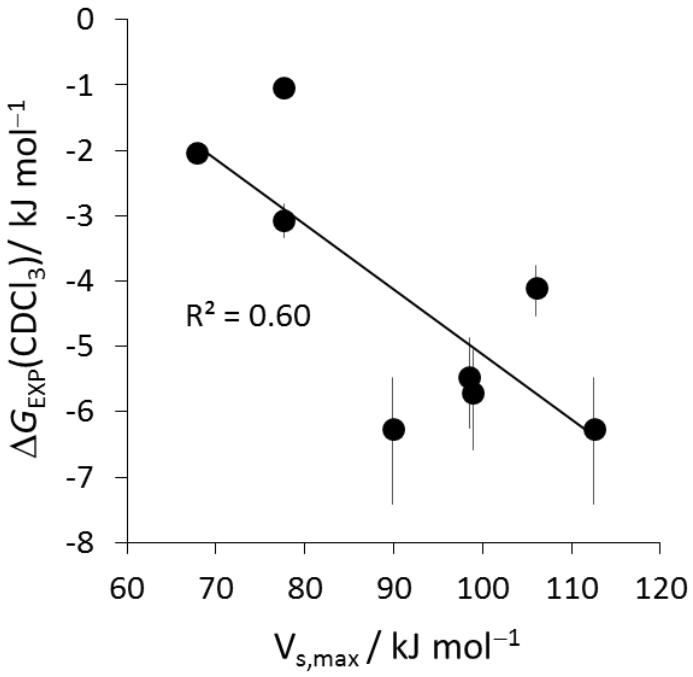

Figure 2.22 Plot of experimental conformational free energy difference of the balances from series **1** (**Figure 2.18**) measured by $^{19}F\{^1H\}$ NMR spectroscopy ($CDCl_3$, 376.5 MHz, 298 K) versus $V_{s,max}$ values of the corresponding substituted thiophene fragments. $V_{s,max}$ calculated using Spartan '14 DFT/B3LYP/6-311G*.

Similarly, while interactions such as aromatic stacking have been shown to be influenced by solvophobic effects,[48] the lack of solvent dependence observed in the present system demonstrates very different behaviour for chalcogen bonds. Given the conformational independence of the balances towards solvent polarity and H-bond ability, it can be concluded that electrostatic or solvophobic effects do not make major contributions to the experimental trends observed in the present chalcogen-bonded system.

2.5.4 Evaluation of van der Waals dispersion contributions

Having ruled out electrostatic or solvophobic effects governing the observed interaction trends, the contribution of dispersion forces were next considered. The bulk polarisability of the solvent determines the extent of solvent competition or attenuation of dispersion forces between functional groups.[22,49] If dispersion is a driving force for the chalcogen-bonding interactions, solvents with low bulk polarisability, such as methanol-d_4, should favour the closed conformer, allowing polarisable elements sulfur and selenium to come in to contact. Conversely, solvents with high bulk polarisability, such as CS_2 would favour the open conformer to allow polarisable atoms to come into contact with the solvent. As has been shown in the experimentally determined results, there is very little difference between conformational free energies in solvents with either high or low bulk polarizabilities, indicating that the interaction trends are not driven by van der Waals dispersion forces.

Computational predictions of the conformational energy differences were used to further investigate the role of dispersion in chalcogen-bonding interactions. To predict these computed ΔE values (ΔE_{CALC}) were used. Each molecular balance was optimised in both the open and closed conformer. The calculated minimised structures determined using different functionals (**Figure 2.26A, B** and **C**) all appeared to give a similar structure as seen by X-ray crystallography (**Figure 2.26D**).

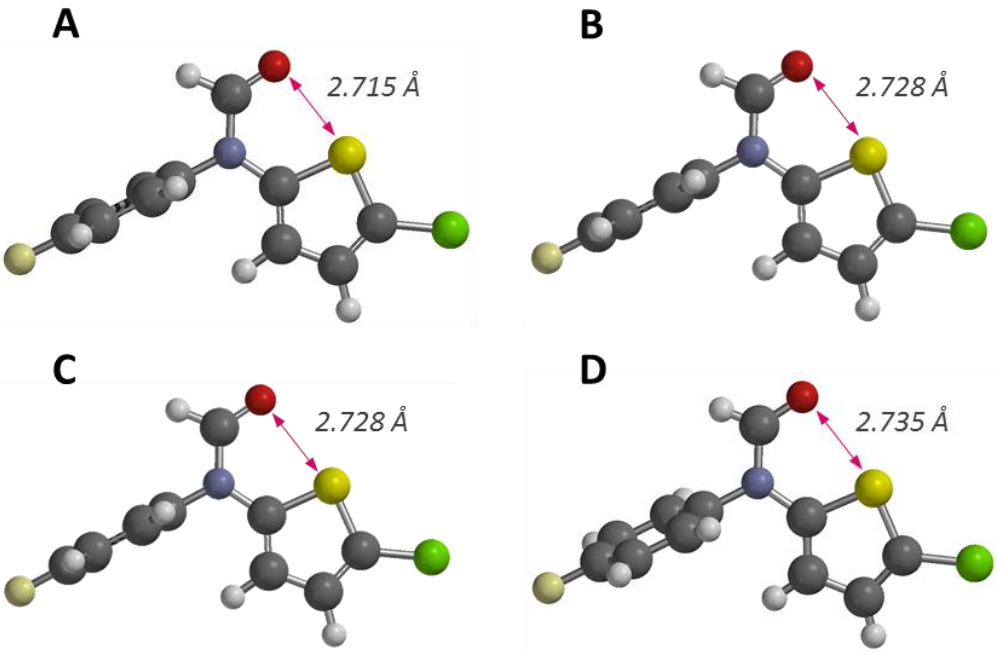

Figure 2.26 Minimised geometries of molecular balance using the (A) B3LYP, (B) M06-2X and (C) ωB97X-D functionals compared (D) the X-ray crystal structure of molecular balance **1a**-Cl. All geometry optimisations performed using Spartan '14 using 6-311G* basis set.

The predicted ΔE_{CALC} energy was then calculated simply by taking the difference in total energy between the two conformers using methods that either did, or did not, take dispersion into account (DFT vs. DFT-D). The hybrid DFT B3LYP functional has been used in computational chemistry for over 20 years and has become well-used for its short computational time with moderate results.[50,51] Crucially, for this investigation B3LYP does not include a dispersion correction. A very strong correlation between calculated ΔE_{CALC} values and experimentally measured ΔG values was seen when using the 6-311G* basis set. As expected for gas phase calculations, the absolute energy differences were not accurately predicted, but the trend was well predicted ($R^2 = 0.94$) (**Figure 2.23**). Thus, DFT/B3LYP/6-311G* appeared to provide a good model for predicting the trend of the conformer distribution of the chalcogen-bonding molecular balances.

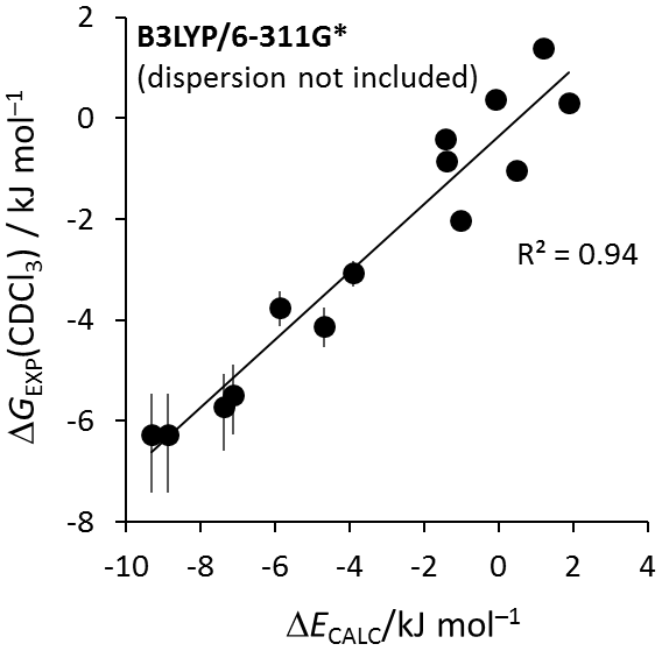

Figure 2.23 Experimental conformational free energies of the balances (**Figure 2.18**) measured by $^{19}F\{^{1}H\}$ NMR spectroscopy ($CDCl_3$, 376.5 MHz, 298 K) *versus* predicted ΔE_{CALC} values calculated using Spartan '14 DFT/B3LYP/6-311G*.

M06-2X is a more recent functional that has been shown to have used in studying non-covalent interactions.[52–54] Compared to the B3LYP functional, M06-2X is slightly more computationally expensive, but contains a dispersion correction. If intramolecular dispersion forces between polarisable chalcogen atoms contribute significantly to the experimentally observed conformational preferences, then the dispersion correction would be expected to improve the correlation with the experimental results. However, the plot between such dispersion-corrected ΔE_{CALC} values and the experimental ΔG values obtained in $CDCl_3$ correlated less well than the standard B3LYP energies (R^2 = 0.88 *versus* 0.94) (**Figure 2.24**).

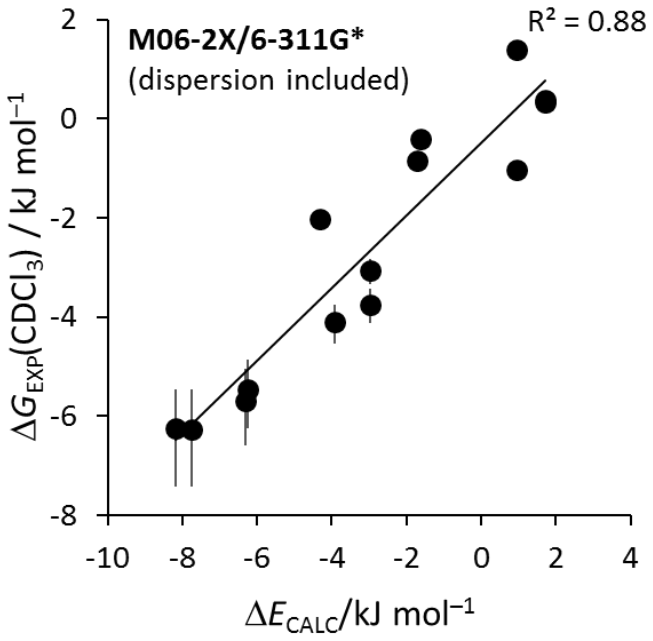

Figure 2.24 Experimental conformational free energies of the balances (**Figure 2.18**) measured by $^{19}F\{^{1}H\}$ NMR spectroscopy ($CDCl_3$, 376.5 MHz, 298 K) *versus* predicted ΔE_{CALC} values calculated using Spartan '14 DFT/M06-2X/6-311G*.

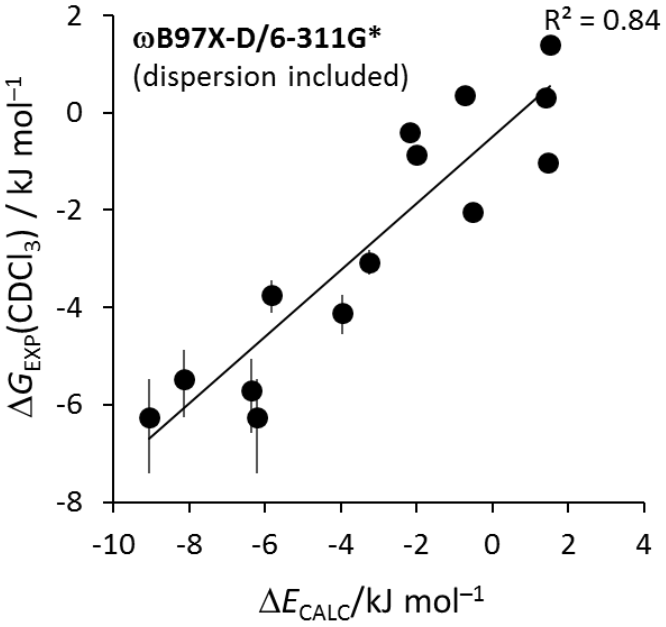

Figure 2.25 Experimental conformational free energies of the balances (**Figure 2.18**) measured by $^{19}F\{^{1}H\}$ NMR spectroscopy ($CDCl_3$, 376.5 MHz, 298 K) versus predicted ΔE_{CALC} values calculated using Spartan '14 DFT/ωB97X-D/6-311G*.

Finally, the long-range correlation ωB97X-D function was also used to predict Δ*E*s. As with M06-2X calculations, ωB97X-D has been used to evaluate non-covalent interactions and contains a dispersion correction term.[55–57] Again, the correlation showed a poorer correlation against the experimental values (R^2 = 0.84) than the equivalent energies determined using the non-dispersion-corrected B3LYP functional (**Figure 2.25**).

Overall, plotting the experimentally-determined conformational energies against two dispersion-corrected computational methods yielded no improvement in the correlation compared to the equivalent B3LYP values that *did not* include dispersion considerations. These correlations, coupled with the lack of variance in the experimentally-determined conformational energies of the balances in response to changes in solvent bulk polarisibility, indicate that the influence of van der Waals dispersion forces in these chalcogen-bonding interactions is negligible.

2.5.5 Evaluation of orbital delocalisation contributions

Electron delocalisation is an important aspect in bond theory, with polarisation along σ-bonds, resonance involving π-bonds or hyperconjugation between σ- and π-bonds being familiar concepts to chemists.[58] Despite this, electron delocalisation has been for the most part overlooked in non-covalent interactions. Nonetheless, n→π* interactions have been suggested to stabilise interactions between carbonyls in proteins (which will be discussed further in **Chapter 4**).[59–63] As discussed in **Chapter 1**, a number of spectroscopic and computational investigations have suggested the importance of electron delocalisation in σ-hole interactions.[64–71] In particular, putative electron delocalisation has been identified by NBO analysis from which second-order perturbation energies (ΔE^2) can be used as a predictor of the energetic significance of these delocalisations.[72]

NBO calculations were performed on the molecular balances show in **Figure 2.9**. First, geometry optimisations were performed in Spartan ’14 using B3LYP/6-311G* before using Gaussian ’09 to generate an NBO input, which was then used an input for NBO 6.0 visualisation and the determination of second-order perturbation energies.

n→σ* electron delocalisation was was seen to occur from both of the (thio)amide lone pairs into the antibonding σ* orbital of the chalcogen-C bond, or the C-H and C-C bond in the β-thiophene molecular balances (**Figure 2.27**).

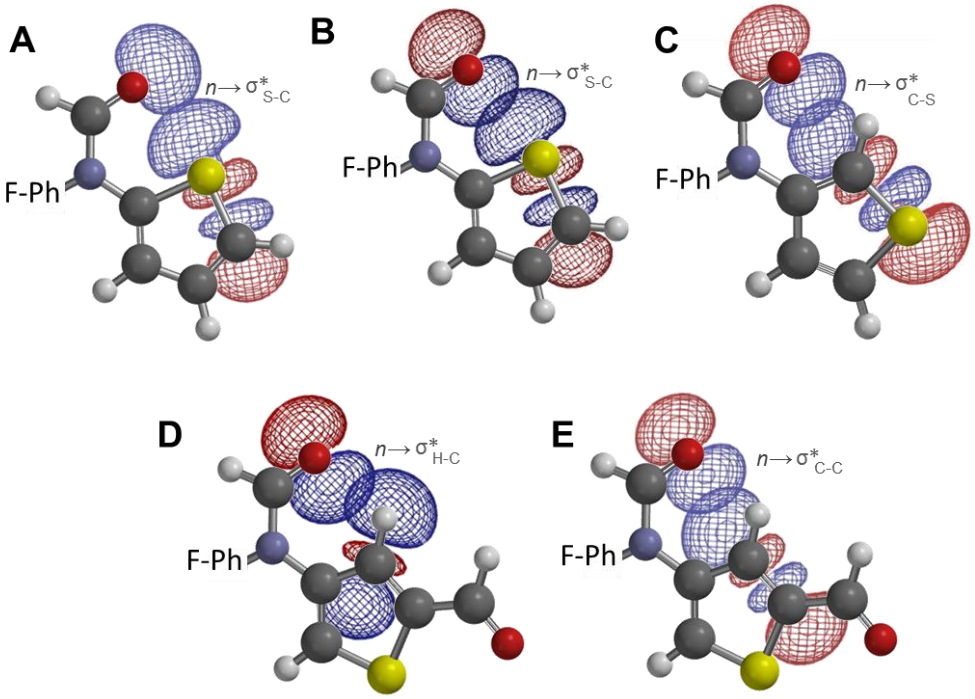

Figure 2.27 Visualisation of NBO interactions between (A) n(1)→σ*$_{S-C}$ (B) n(2)→σ*$_{S-C}$ in molecular balance **1a**-H. (C) n(2)→σ*$_{C-S}$ for molecular balance **1b**-H. (D) n(2)→σ*$_{H-C}$ and (E) n(2)→σ*$_{C-C}$ for molecular balance **1b**-CHO. NBO outputs were calculated using NBO 6.0.

The computation provided qualitative evidence that electron delocalisation might make a significant contribution to chalcogen interactions. In some cases the second-order perturbation energies, estimated such interaction to be worth up ~25 kJ mol^{-1} (**Figure 2.28**). However, when these second-order perturbation energies were compared to the experimentally determined conformational free energy differences, only a weak correlation was observed (**Figure 2.28**). Furthermore, as an abstract theoretical construct, sitting somewhere between an atomic orbital and a molecular

orbital, NBOs do not provide an easily understood model for rationalising molecular interactions (**Figure 2.29**).

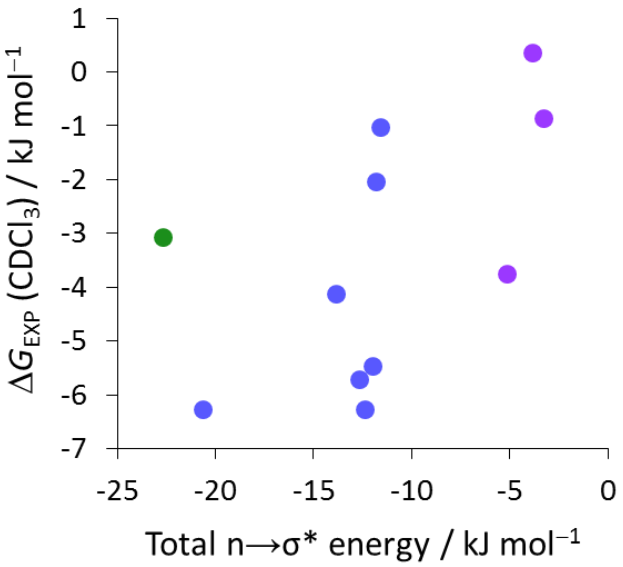

Figure 2.28 Experimental conformational free energies of the balances (**Figure 2.18**) measured by $^{19}F\{^{1}H\}$ NMR spectroscopy ($CDCl_3$, 376.5 MHz, 298 K) versus second order perturbation energies. Colours correspond to those seen in **Figure 2.9**. Second order perturbation energies calculated using NBO 6.0.

Molecular orbital theory has been an important model in bond theory and therefore provides a more accessible method than NBOs to study non-covalent interactions. Thus, we employed molecular orbitals (MOs) to examine the possible origins of chalcogen-bonding interactions occurring in our molecular balances. To simplify the analysis a simplified version of the molecular balances was used in the MO calculations (**Figure 2.30**).

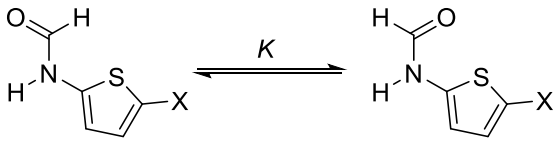

Figure 2.30 Structures of simplified molecular balances used for the molecular orbital analysis.

To ensure that the geometries of the simplified balances maintained the same chalcogen bonding geometries, complete molecular balances were geometry minimised using either B3LYP/6-311G*, M06-2X/6-311G* or ωB97X-D/6-311G* before the 4-fluorophenyl moiety was removed and replaced with a proton with a N-H bond length of 1.012 Å. A single-point energy calculation was then performed using the same functional and basis set as the initial geometry optimisation. It was important that the energetic trends of the simplified molecular balances were governed by similar factors as the full molecular balances, and therefore ΔE values of both the full and simple system were plotted against each other (**Figure 2.31**). Reasonable correlations were seen between the ΔE values determined for each balance series **1a** (**Figure 2.31**, blue), **1b** (**Figure 2.31**, purple) and **2a** (**Figure 2.31**, green), and their simplified analogues confirming the validity of the simplified balances for further study of the molecular orbitals involved in chalcogen-bonding interactions. The correlation of full and simplified molecular balances from series **2a** (**Figure 2.31**, green) was not as good as the others, which could be rationalised by the potential difference in delocalisation seen in amides and thioamides.

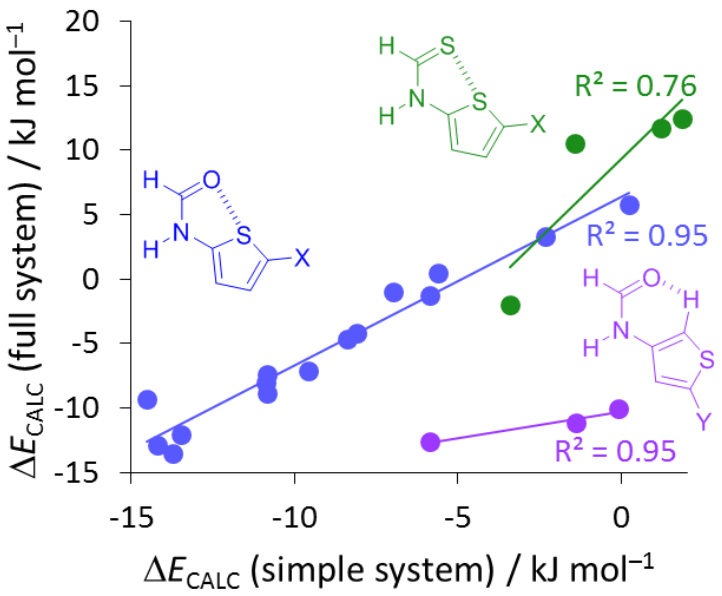

Figure 2.31 Calculated ΔE values for the full molecular balance system versus the simple molecular balance system. ΔE_{CALC} values calculated using Spartan '14 DFT/B3LYP/6-311G*.

The use of the molecular balance fragments greatly simplified the assignment of pairs of molecular orbitals between the two conformers (**Figure 2.32**). Specifically, the simplified balances that lacked the fluorophenyl moiety removed additional molecular orbital splitting arising from the canonical resonance form of electrons in the aromatic that was not involved in chalcogen bonding. Once all molecular orbitals from the HOMO to HOMO{-9} had been paired, molecular orbital energies in the closed and open conformer could be plotted (**Figure 2.33**).

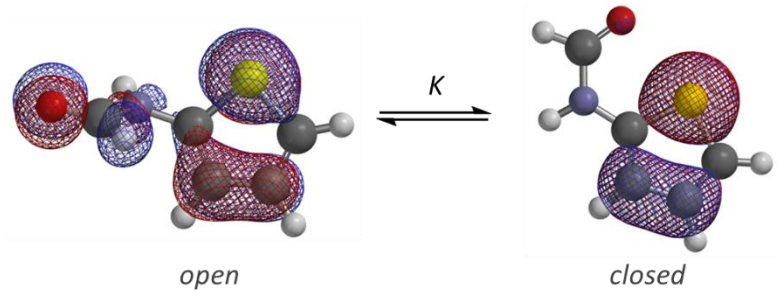

Figure 2.32 Visually matched molecular orbitals for the open (left) and closed (right) conformer of the HOMO of the simplified molecular balance of **1a**-H.

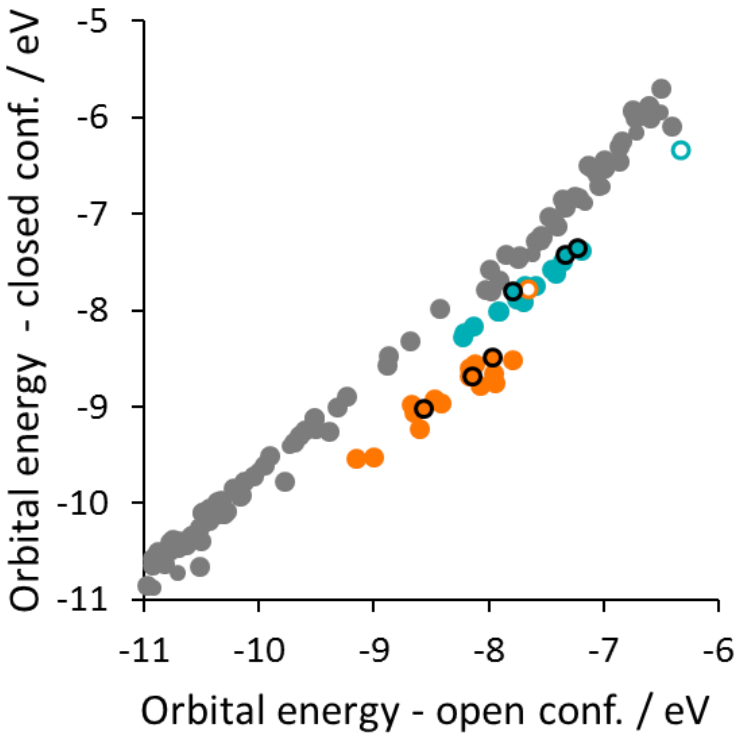

Figure 2.33 Correlation of all molecular orbital energies from HOMO to HOMO{-9} in the open *versus* closed conformers of simplified molecular balances. Points below the grey line are stabilised in the closed conformer by either a through-bond, resonance (orange) or n→σ* electron delocalisation (teal). molecular orbital energies calculated using Spartan '14 DFT/B3LYP/6-311G*.

Three separate series were revealed. The grey data set contained the majority of the molecular orbital pairs, where the difference in energy between the two conformers

remained largely the same. The graph is plotted in such a way that any points that are below the grey data set are lower in energy and therefore more stable in the closed conformer. Two classes of orbital pairs that fell below the grey background data were identified (orange and teal data sets, **Figure 2.33**). The orange series revealed stabilised orbitals in which through-bond, resonance delocalisation of the lone pair (lying above and below the (thio)amide) into the π system of the co-planar aromatic (seleno)thiophene in the closed conformation (**Figure 2.34A**). The teal series revealed stabilising delocalisation of the other, orthogonal lone pair into the σ C-chalcogen bond in the closed conformation (**Figure 2.34B**).

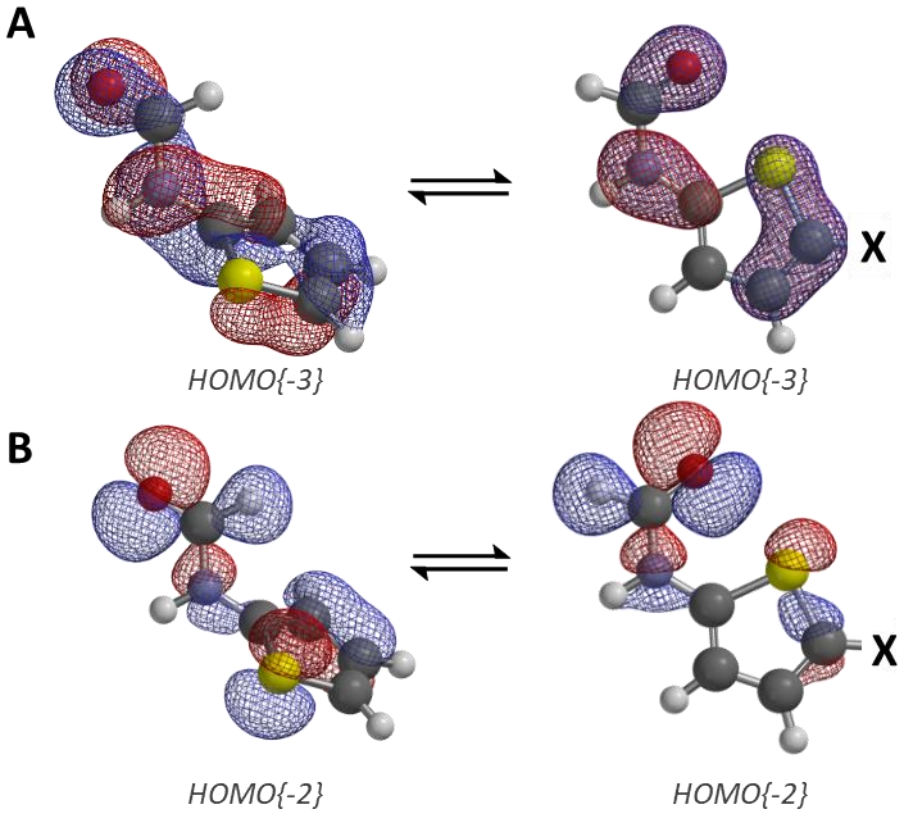

Figure 2.34 Molecular orbitals corresponding to the (A) orange and (B) teal points in **Figure 2.33** in the open (left) and closed (right).

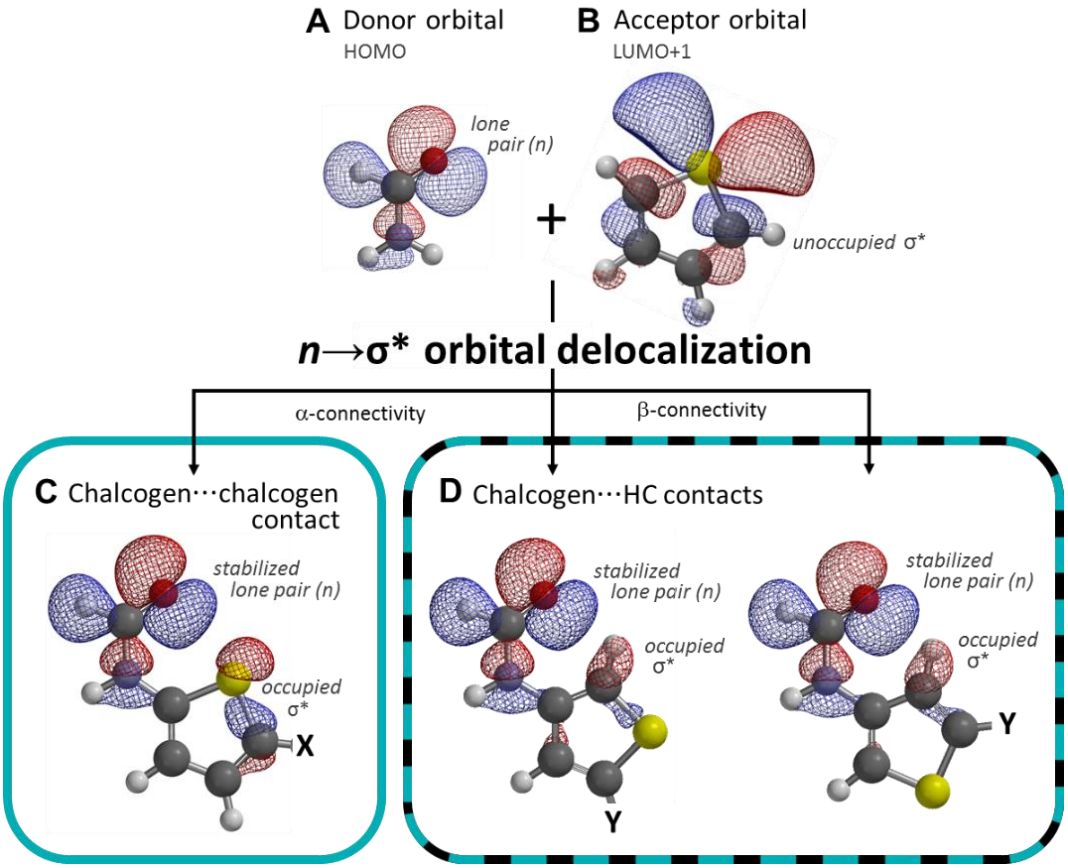

Figure 2.35 Molecular orbital decomposition of molecular orbitals corresponding to teal points seen in **Figure 2.33** and depicted in **Figure 2.34B**. Hypothetical combination of molecular orbitals (A) and (B) in three different orientations to give molecular orbitals (C) and (D).

To identify the underlying components of the teal series of molecular orbitals, we further decomposed the fragments into the amide and thiophene fragments (**Figure 2.35**). This decomposition analysis revealed that teal-coloured molecular orbital was formed from a combination of one of the occupied formyl lone pair orbitals (**Figure 2.35A**) with the unoccupied antibonding orbital of the chalcogen-C σ-bond (**Figure 2.35B**). These two molecular orbitals gave a 'recipe' for the hypothetical combination to form the overall molecular orbital seen in the molecular balances (**Figure 2.35C** and **D**). The thiophene molecular orbital is proposed to be the σ* chalcogen-C antibonding orbital, as has been found in numerous NBO investigations, including the one performed as part of the present work (**Figure 2.28**). Such delocalisation of electron density into the σ* antibonding orbital would be expected to

be associated with an increase in the chalcogen-C bond length. Unfortunately, the molecular balances could only be crystallised in one conformer, preventing experimental comparison of the chalcogen-C bond length in both conformers. However, bond lengths could be obtained from computationally minimised structures of the balances. The chalcogen-C bond was indeed found to be elongated in the molecular balances where a chalcogen···chalcogen contact was formed compared to the unfolded conformations (**Figure 2.36**, blue).

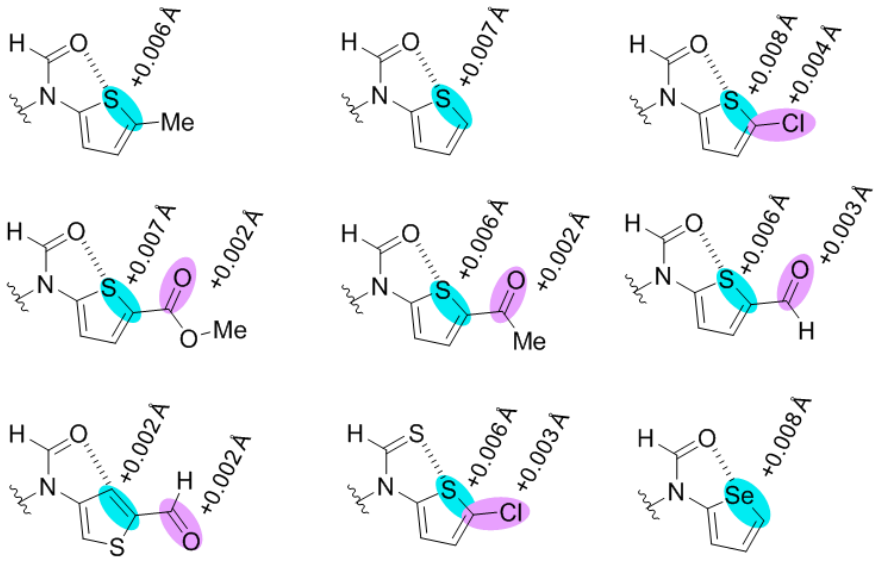

Figure 2.36 Calculated change in bond lengths in full molecular balances with chalcogen···chalcogen contacts. Blue bonds show the change in Ch-C bonds and purple show the elongation of electron-withdrawing groups. Calculated using Spartan '14 DFT/B3LYP/6-311G*.

In addition to the elongation of the chalocgen-C bonds, the bonds to electron-withdrawing substituents on the molecular balances were also elongated (**Figure 2.36**, purple). While no correlation between the magnitude of the increase and conformational free energies could be determined, the increased bond lengths provided qualitative evidence for the presence of an n→σ* electron delocalisation due to the filling of an antibonding molecular orbital, weakening the bond and increasing the bond length.

The most surprising find from the molecular orbital analysis was the occurance of similar orbital delocalisation effects in the β-thiophene molecular balances (**Figure 2.36B** and **E**), even though no chalcogen···chalcogen contact was present. The molecular orbital energies of these 'control' compounds (teal with black outline) even fitted on the same correlation as those with chalcogen···chalcogen contacts (teal) on the molecular orbital plot (**Figure 2.33**). When developing another 'recipe' for these β-thiophene molecular balances, it was found the same two fragment molecular orbitals were combined, with the only difference being that the thiophene fragment was rotated to accommodate the different bond connectivity (**Figure 2.35D**). Finally, molecular balance **1b**-CHO even gave the same bond length characteristics, with the C-chalcogen bond lengthening despite the lack of a direct chalcogen-chalcogen contact (**Figure 2.36**).

Thus far, only qualitative evidence for n→σ* delocalisation driving chalcogen bonding in these molecular balances has been considered. However, it is important to try and find a quantitative explanation for the experimental behaviour. Having determined that electrostatic, dispersion and solvophobic effects could not account for the observed behaviour, a correlation against molecular orbital properties was sought. A remarkable correlation with R^2 = 0.99 was seen between the experimental conformational free energy differences and the energies of the molecular orbitals hosting n→σ* delocalisation **(Figure 2.33**, teal and **Figure 2.34B**). The selenophene balance **1c** (**Figure 2.37**), was found to be an outlier, with the conformational energy being more favourable than predicted from this orbital energy alone. It is also important to remember that the through-bond resonance molecular orbital also provided stabilisation in chalcogen-bonding interactions (**Figure 2.33**, orange and **Figure 2.34A**). However, no correlation was observed when the energies of these resonantly delocalised molecular orbitals were plotted against the experimentally determined conformational free energies (**Figure 2.38**).

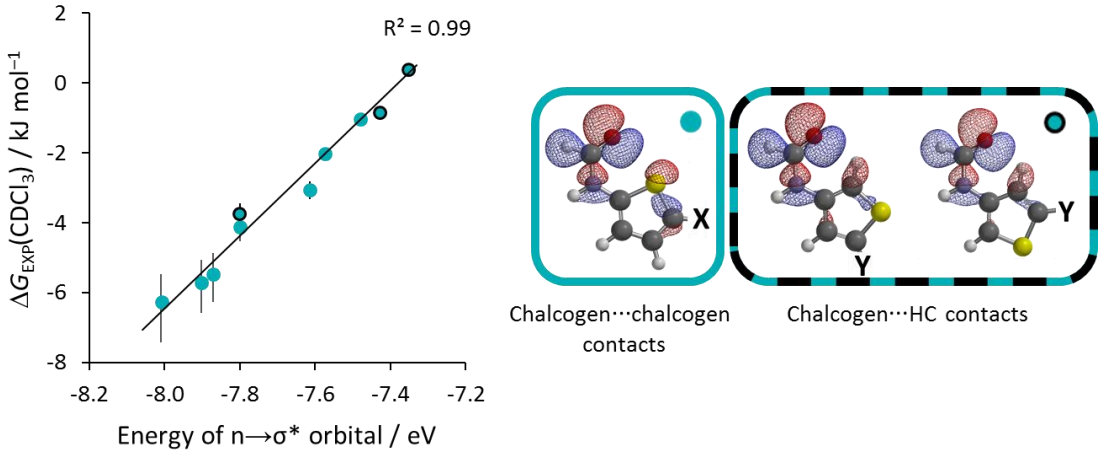

Figure 2.37 Correlation between molecular orbital energy containing n→σ* electron delocalisation *versus* conformational free energies measured by $^{19}F\{^{1}H\}$ NMR spectroscopy ($CDCl_3$, 376.5 MHz, 298 K) (**Figure 2.18**). Molecular orbital energies calculated using Spartan '14 DFT/B3LYP/6-311G*.

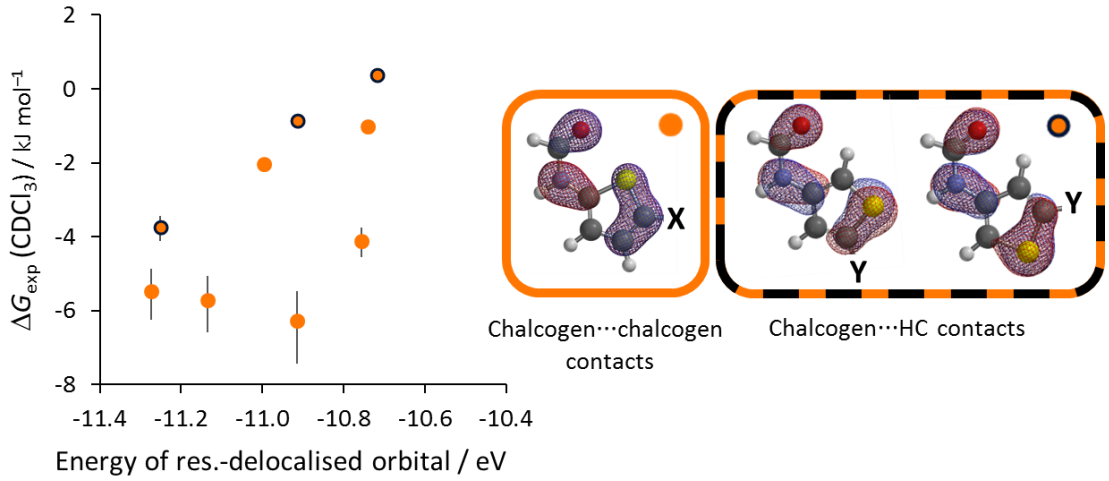

Figure 2.38 Plot of molecular orbital energies containing a through-bond resonance versus conformational free energies measured by $^{19}F\{^{1}H\}$ NMR spectroscopy ($CDCl_3$, 376.5 MHz, 298 K) (**Figure 2.18**). Molecular orbital energies calculated using Spartan '14 DFT/B3LYP/6-311G*.

Thus, a quantitative relationship between n→σ* delocalisation and the experimentally determined chalcogen bond-driven conformational free energies was

established. This quantitative evidence for the nature of chalcogen-bonding interactions suggests that while other factors certainly contribute to the solution-phase experimental behaviour of chalcogen bonds (most notably the through-bond resonance delocalisation), n→σ* electron delocalisation is the major factor determining the interaction trends that were observed.

Even more surprisingly, the conformational free energies of the β-thiophene series **1b** and **2b** (which lacked chalcogen···chalcogen contacts) not only showed a qualitative correlation with the energies of orbitals containing n→σ* electron delocalisation, but the data also fitted along the same correlation as the molecular balances containing chalcogen···chalcogen contacts (**Figure 2.37**, black outline). It would be reasonable to think that, given the orbital-derived nature of these chalcogen-bonding interactions, that a chalcogen bond could be formed at either end of the chalcogen-C bond, thus accounting for the observed behaviour. Another potentially interesting explanation is the potential of this series to form tetrel bonds through a σ hole on the carbon, although further molecular balances would be needed to investigate this.

To ensure that the energies of the n→σ* molecular orbital were the only ones that correlated with the experimental results, a number of other molecular orbital energies were also plotted against conformational free energies. Interestingly, the HOMO (**Figure 2.39A**) showed a good correlation with experimentally determined free energies, with series **1a** and **1b** forming separate correlations. The molecular orbital appears to be a canonical form of the formyl group. Despite this, the HOMO molecular orbital didn't provide any further stabilisation in the closed versus the open conformer, appearing as part of the background molecular orbitals in **Figure 2.33**. However, good correlations were not observed with any other molecular orbitals (**Figure 2.39B** and **C**).

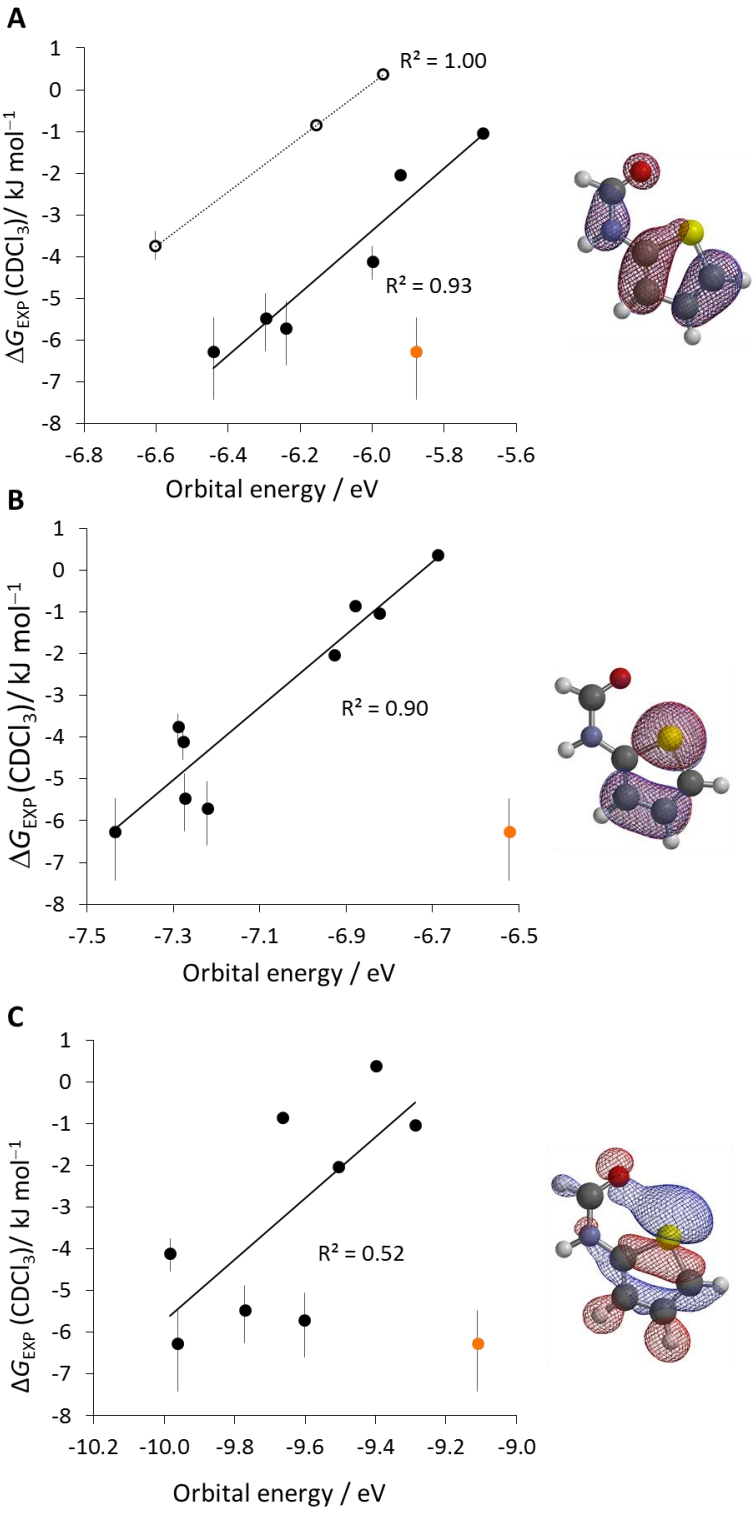

Figure 2.39 Correlations of (A) HOMO, (B) HOMO{-1} and (C) HOMO{-4} versus conformational free energies measured by $^{19}F\{^{1}H\}$ NMR spectroscopy ($CDCl_3$, 376.5 MHz, 298 K) (**Figure 2.18**). Molecular orbital energies calculated using Spartan '14 DFT/B3LYP/6-311G*.

2.6 Conclusions and outlook

A quantitative explanation for the occurrence of favourable chalcogen bonding interactions has been provided. Extensive solvent screening found a surprising independence of the interaction to solvent H-bond abilities and polarity, revealing that chalcogen bonding was not purely governed by electrostatics. This conclusion was further supported by the lack of correlation between ESPs and experimental free energies. Dispersion forces were likewise found to not be pivotal to chalcogen bonding in solution, not only due to the independence of the interaction from the bulk solvent polarisability, but also supported by computations that showed no improvement in conformational energy correlations when a dispersion correction was added. Finally, electron delocalisation was found to have a controlling influence on chalcogen bonding interactions. Following from previous NBO-based investigations, a molecular orbital study confirmed the presence of n→σ* electron delocalisation. The energy of the molecular orbital containing an n→σ* electron delocalisation correlated very well with the experimental conformational free energies, thereby providing a quantitative explanation for chalcogen bonding interactions.[73]

While this study into the fundamental physiochemical origin of chalcogen bonding, the initial investigation was to search for a suitable adaptomer system. Unfortunately, due to the stability of chalcogen bonds in all solvents these interactions would not be suitable for use in an adaptomer system as the system would be unable to change its physical properties as it moved from an aqueous environment to the lipid bilayer. Even though the molecular balances used in this study were not soluble in water, it is reasonable to assume that the same behaviour would be seen in aqueous solvents.

2.6.1 Future work

Future work may explore is the nature of the interactions occurring in the β-thiophene. In this chapter, I proposed that chalcogen bonding that can take place at either end of the acceptor σ-bond. However, it may also be possible to that either a CH···O hydrogen bond, or perhaps more interestingly, a tetrel bond might be forming between the carbon of the thiophene ring and the carbonyl group. Indeed, a very recent study into

chalcogen···H-C interactions suggest that instead of either a chalcogen or tetrel bond being formed, an internal H-bond could be responsible for the behaviour of the β-thiophene molecular balances.[74]

Finally, as discussed earlier in this chapter, chalcogen bonds may be exploited more widely within chemistry for a range of applications. Of particular note, chalcogen bonding has been implicated to be key to the activity of certain catalysts.[3,8] Preliminary molecular orbital and NBO analyses have revealed n→σ* electron delocalisation occurring in isothiourea-based catalysts developed by Prof. Andy Smith at the University of St. Andrews (**Figure 2.40**).[5,14,75] These calculations share striking similarities with the equivalent calculations performed on the molecular balances presented in this thesis (**Figure 2.34**). An NBO-deletion analysis (where the interaction of interest is removed and the energetic impact is seen) implies that the chalcogen bond in the isothiourea catalysts stabilise the catalytically active conformation by ~7 kJ mol^{-1}.

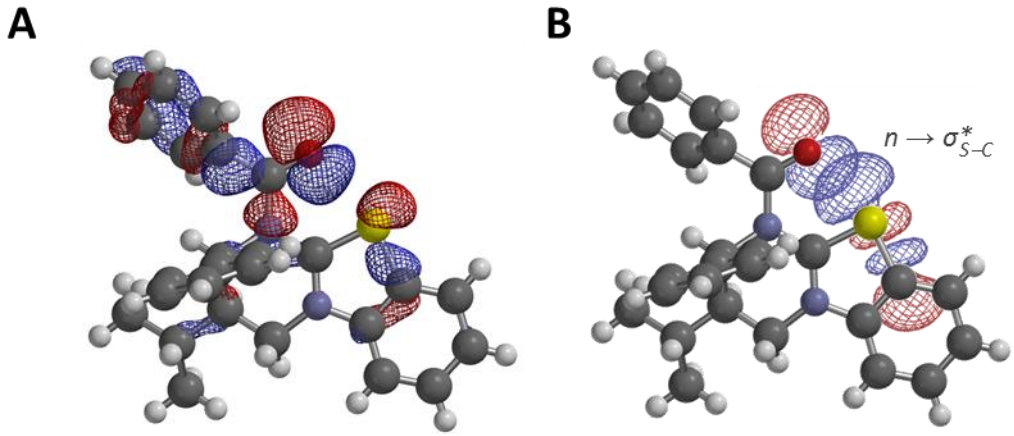

Figure 2.40 (A) Molecular orbital containing an n→σ* electron delocalisation in an isothiourea catalyst, calculated using Spartan '14 DFT/B3LYP/6-311G*. (B) NBO of n→σ*$_{S-C}$ in an isothiourea catalyst, calculated using NBO 6.0.

However, singling-out one particular interaction as being responsible for the performance of a particular catalyst is difficult as several other secondary interactions likely contribute to stabilising a particular conformation, as can be seen in the NCI plot

shown in **Figure 2.41**. Thus, future work will examine whether kinetic data can be correlated with chalcogen bond properties to identify whether such interactions contribute to the performance of isothiourea catalysts.

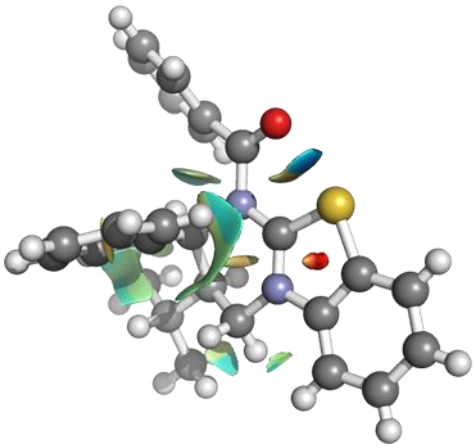

Figure 2.41 An isothiourea catalyst showing intramolecular non-covalent interactions calculated using NCI plot.

2.7 References

1. Beno, B. R.; Yeung, K.-S.; Bartberger, M. D.; Pennington, L. D.; Meanwell, N. A. A Survey of the Role of Noncovalent Sulfur Interactions in Drug Design. *J. Med. Chem.* **2015**, *58* (11), 4383–4438.

2. Bauzá, A.; Quiñonero, D.; Deyà, P. M.; Frontera, A. Halogen Bonding Versuschalcogen and Pnicogen Bonding: A Combined Cambridge Structural Database and Theoretical Study. *CrystEngComm* **2013**, *15* (16), 3137–3144.

3. Benz, S.; López-Andarias, J.; Mareda, J.; Sakai, N.; Matile, S. Catalysis with Chalcogen Bonds. *Angew. Chem. Int. Ed.* **2017**, *56* (3), 812–815.

4. Benz, S.; Poblador-Bahamonde, A. I.; Low-Ders, N.; Matile, S. Catalysis with Pnictogen, Chalcogen, and Halogen Bonds. *Angew. Chem. Int. Ed.* **2018,** *57* (19), 5408–5412.

5. Greenhalgh, M. D.; Smith, S. M.; Walden, D. M.; Taylor, J. E.; Brice, Z.; Robinson, E. R. T.; Fallan, C.; Cordes, D. B.; Slawin, A. M. Z.; Richardson, H. C.; et al. A C=O···Isothiouronium Interaction Dictates Enantiodiscrimination in Acylative Kinetic Resolutions of Tertiary Heterocyclic Alcohols. *Angew. Chem. Int. Ed.* **2018**, *57* (12), 3200–3206.

6. Cox, P. A.; Leach, A. G.; Campbell, A. D.; Lloyd-Jones, G. C. Protodeboronation of Heteroaromatic, Vinyl, and Cyclopropyl Boronic Acids: pH–

Rate Profiles, Autocatalysis, and Disproportionation. *J. Am. Chem. Soc.* **2016**, *138* (29), 9145–9157.

7. Shiina, I.; Nakata, K.; Ono, K.; Onda, Y.-S.; Itagaki, M. Kinetic Resolution of Racemic α-Arylalkanoic Acids with Achiral Alcohols via the Asymmetric Esterification Using Carboxylic Anhydrides and Acyl-Transfer Catalysts. *J. Am. Chem. Soc.* **2010**, *132* (33), 11629–11641.

8. Mahmudov, K. T.; Kopylovich, M. N.; Guedes da Silva, M. F. C.; Pombeiro, A. J. L. Chalcogen Bonding in Synthesis, Catalysis and Design of Materials. *Dalt. Trans.* **2017**, *46* (31), 10121–10138.

9. Werz, D. B.; Gleiter, R.; Rominger, F. Nanotube Formation Favored by Chalcogen−Chalcogen Interactions. *J. Am. Chem. Soc.* **2002**, *124* (36), 10638–10639.

10. Fick, R. J.; Kroner, G. M.; Nepal, B.; Magnani, R.; Horowitz, S.; Houtz, R. L.; Scheiner, S.; Trievel, R. C. Sulfur–Oxygen Chalcogen Bonding Mediates AdoMet Recognition in the Lysine Methyltransferase SET7/9. *ACS Chem. Biol.* **2016**, *11* (3), 748–754.

11. Reid, R. C.; Yau, M.-K.; Singh, R.; Lim, J.; Fairlie, D. P. Stereoelectronic Effects Dictate Molecular Conformation and Biological Function of Heterocyclic Amides. *J. Am. Chem. Soc.* **2014**, *136* (34), 11914–11917.

12. Lim, J. Y. C.; Marques, I.; Thompson, A. L.; Christensen, K. E.; Félix, V.; Beer, P. D. Chalcogen Bonding Macrocycles and [2]Rotaxanes for Anion Recognition. *J. Am. Chem. Soc.* **2017**, *139* (8), 3122–3133.

13. Gleiter, R.; Haberhauer, G.; Werz, D. B.; Rominger, F.; Bleiholder, C. From Noncovalent Chalcogen–Chalcogen Interactions to Supramolecular Aggregates: Experiments and Calculations. *Chem. Rev.* **2018**, *118* (4), 2010–2041..

14. Neyyappadath, R. M.; Chisholm, R.; Greenhalgh, M. D.; Rodríguez-Escrich, C.; Pericàs, M. A.; Hähner, G.; Smith, A. D. Acylative Kinetic Resolution of Alcohols Using a Recyclable Polymer-Supported Isothiourea Catalyst in Batch and Flow. *ACS Catal.* **2018**, *8* (2), 1067–1075.

15. White, T. R.; Renzelman, C. M.; Rand, A. C.; Rezai, T.; McEwen, C. M.; Gelev, V. M.; Turner, R. A.; Linington, R. G.; Leung, S. S. F.; Kalgutkar, A. S.; et al. On-Resin N-Methylation of Cyclic Peptides for Discovery of Orally Bioavailable Scaffolds. *Nat. Chem. Biol.* **2011**, *7* (11), 810–817.

16. Mati, I. K.; Cockroft, S. L. Molecular Balances for Quantifying Non-Covalent Interactions. *Chem. Soc. Rev.* **2010**, *39* (11), 4195.

17. Oki, M. 1,9-Disubstituted Triptycenes: An Excellent Probe for Weak Molecular Interactions. *Acc. Chem. Res.* **1990**, *23* (11), 351–356.

18. Gung, B. W.; Xue, X.; Reich, H. J. Off-Center Oxygen-Arene Interactions in Solution: A Quantitative Study. *J. Org. Chem.* **2005**, *70* (18), 7232–7237.

19. Gung, B. W.; Zou, Y.; Xu, Z.; Amicangelo, J. C.; Irwin, D. G.; Ma, S.; Zhou, H.-C. Quantitative Study of Interactions between Oxygen Lone Pair and Aromatic

Rings: Substituent Effect and the Importance of Closeness of Contact. *J. Org. Chem.* **2008**, *73* (2), 689–693.

20. Paliwal, S.; Geib, S.; Wilcox, C. S. Molecular Torsion Balance for Weak Molecular Recognition Forces. Effects of "Tilted-T" Edge-to-Face Aromatic Interactions on Conformational Selection and Solid-State Structure. *J. Am. Chem. Soc.* **1994**, *116* (10), 4497–4498.

21. Yang, L.; Adam, C.; Nichol, G. S.; Cockroft, S. L. How Much Do van Der Waals Dispersion Forces Contribute to Molecular Recognition in Solution? *Nat. Chem.* **2013**, *5* (12), 1006–1010.

22. Adam, C.; Yang, L.; Cockroft, S. L. Partitioning Solvophobic and Dispersion Forces in Alkyl and Perfluoroalkyl Cohesion. *Angew. Chem. Int. Ed.* **2015**, *54* (4), 1164–1167.

23. Hof, F.; Scofield, D. M.; Schweizer, W. B.; Diederich, F. A Weak Attractive Interaction between Organic Fluorine and an Amide Group. *Angew. Chem. Int. Ed.* **2004**, *43* (38), 5056–5059.

24. Fischer, F. R.; Wood, P. A.; Allen, F. H.; Diederich, F. Orthogonal Dipolar Interactions between Amide Carbonyl Groups. *Proc. Natl. Acad. Sci.* **2008**, *105* (45), 17290–17294.

25. Gardner, R. R.; Christianson, L. A.; Gellman, S. H. Quantitative Analysis of Hydrophobically Induced Folding in a Minimal Model System. *J. Am. Chem. Soc.* **1997**, *119* (21), 5041–5042.

26. McKay, S. L.; Haptonstall, B.; Gellman, S. H. Beyond the Hydrophobic Effect: Attractions Involving Heteroaromatic Rings in Aqueous Solution 1. *J. Am. Chem. Soc.* **2001**, *123* (6), 1244–1245.

27. Aliev, A. E.; Moïse, J.; Motherwell, W. B.; Nič, M.; Courtier-Murias, D.; Tocher, D. A. Probing Weak Non-Covalent Interactions in Solution and Solid States with Designed Molecules. *Phys. Chem. Chem. Phys.* **2009**, *11* (1), 97–100.

28. Pavlakos, I.; Arif, T.; Aliev, A. E.; Motherwell, W. B.; Tizzard, G. J.; Coles, S. J. Noncovalent Lone Pair···(No-Π!)-Heteroarene Interactions: The Janus-Faced Hydroxy Group. *Angew. Chem. Int. Ed.* **2015**, *54* (28), 8169–8174.

29. Motherwell, W. B.; Moreno, R. B.; Pavlakos, I.; Arendorf, J. R. T.; Arif, T.; Tizzard, G. J.; Coles, S. J.; Aliev, A. E. Noncovalent Interactions of π Systems with Sulfur: The Atomic Chameleon of Molecular Recognition. *Angew. Chem. Int. Ed.* **2018**, *57* (5), 1193–1198.

30. Mati, I. K.; Adam, C.; Cockroft, S. L. Seeing through Solvent Effects Using Molecular Balances. *Chem. Sci.* **2013**, *4* (10), 3965.

31. Muchowska, K. B.; Adam, C.; Mati, I. K.; Cockroft, S. L. Electrostatic Modulation of Aromatic Rings via Explicit Solvation of Substituents. *J. Am. Chem. Soc.* **2013**, *135* (27), 9976–9979.

32. Hubbard, T. A.; Brown, A. J.; Bell, I. A. W.; Cockroft, S. L. The Limit of Intramolecular H-Bonding. *J. Am. Chem. Soc.* **2016**, *138* (46), 15114–15117.

33. Dominelli-Whiteley, N.; Brown, J. J.; Muchowska, K. B.; Mati, I. K.; Adam, C.; Hubbard, T. A.; Elmi, A.; Brown, A. J.; Bell, I. A. W.; Cockroft, S. L. Strong Short-Range Cooperativity in Hydrogen-Bond Chains. *Angew. Chem. Int. Ed.* **2017**, *56* (26), 7658–7662.

34. Carroll, W. R.; Pellechia, P.; Shimizu, K. D. A Rigid Molecular Balance for Measuring Face-to-Face Arene−Arene Interactions. *Org. Lett.* **2008**, *10* (16), 3547–3550.

35. Hwang, J.; Li, P.; Smith, M. D.; Shimizu, K. D. Distance-Dependent Attractive and Repulsive Interactions of Bulky Alkyl Groups. *Angew. Chem. Int. Ed.* **2016**, *55* (28), 8086–8089.

36. Contreras-García, J.; Johnson, E. R.; Keinan, S.; Chaudret, R.; Piquemal, J.-P.; Beratan, D. N.; Yang, W. NCIPLOT: A Program for Plotting Noncovalent Interaction Regions. *J. Chem. Theory Comput.* **2011**, *7* (3), 625–632.

37. Claridge, T. D. W. *High-Resolution NMR Techniques in Organic Chemistry*; Pergamon, 1999.

38. Cockroft, S. L.; Hunter, C. A. Desolvation Tips the Balance: Solvent Effects on Aromatic Interactions. *Chem. Commun.* **2006**, 3806− 3808.

39. Cockroft, S. L.; Hunter, C. A. Desolvation and Substituent Effects in Edge-to-Face Aromatic Interactions. *Chem. Commun.* **2009**, 3961− 3963.

40. Emenike, B. U.; Bey, S. N.; Bigelow, B. C.; Chakravartula, S. V. S. Quantitative Model for Rationalizing Solvent Effect in Noncovalent CH–Aryl Interactions. *Chem. Sci.* **2016**, *7* (2), 1401–1407.

41. Hunter, C. A. Quantifying Intermolecular Interactions: Guidelines for the Molecular Recognition Toolbox. *Angew. Chem. Int. Ed.* **2004**, *43* (40), 5310–5324.

42. Robertson, C. C.; Perutz, R. N.; Brammer, L.; Hunter, C. A. A Solvent-Resistant Halogen Bond. *Chem. Sci.* **2014**, *5* (11), 4179–4183.

43. Robertson, C. C.; Wright, J. S.; Carrington, E. J.; Perutz, R. N.; Hunter, C. A.; Brammer, L. Hydrogen Bonding vs. Halogen Bonding: The Solvent Decides. *Chem. Sci.* **2017**, *8* (8), 5392–5398.

44. Garrett, G. E.; Gibson, G. L.; Straus, R. N.; Seferos, D. S.; Taylor, M. S. Chalcogen Bonding in Solution: Interactions of Benzotelluradiazoles with Anionic and Uncharged Lewis Bases. *J. Am. Chem. Soc.* **2015**, *137* (12), 4126–4133.

45. Sarwar, M. G.; Dragisic, B.; Salsberg, L. J.; Gouliaras, C.; Taylor, M. S. Thermodynamics of Halogen Bonding in Solution: Substituent, Structural, and Solvent Effects. *J. Am. Chem. Soc.* **2010**, *132* (5), 1646–1653.

46. Shields, Z. P.; Murray, J. S.; Politzer, P. Directional Tendencies of Halogen and Hydrogen Bonds. *Int. J. Quantum Chem.* **2010**, *110* (15), 2823–2832.

47. Riley, K. E.; Murray, J. S.; Fanfrlík, J.; Řezáč, J.; Solá, R. J.; Concha, M. C.; Ramos, F. M.; Politzer, P. Halogen Bond Tunability I: The Effects of Aromatic Fluorine Substitution on the Strengths of Halogen-Bonding Interactions Involving

Chlorine, Bromine, and Iodine. *J. Mol. Model.* **2011**, *17* (12), 3309–3318.

48. Yang, L.; Adam, C.; Cockroft, S. L. Quantifying Solvophobic Effects in Nonpolar Cohesive Interactions. *J. Am. Chem. Soc.* **2015**, *137* (32), 10084–10087.

49. Yang, L.; Brazier, J. B.; Hubbard, T. A.; Rogers, D. M.; Cockroft, S. L. Can Dispersion Forces Govern Aromatic Stacking in an Organic Solvent? *Angew. Chem. Int. Ed.* **2016**, *55* (3), 912–916.

50. Kim, K.; Jordan, K. D. Comparison of Density Functional and MP2 Calculations on the Water Monomer and Dimer. *J. Phys. Chem.* **1994**, *98* (40), 10089–10094.

51. Tirado-Rives, J.; Jorgensen, W. L. Performance of B3LYP Density Functional Methods for a Large Set of Organic Molecules. *J. Chem. Theory Comput.* **2008**, *4* (2), 297–306.

52. Hohenstein, E. G.; Chill, S. T.; Sherrill, C. D. Assessment of the Performance of the M05−2X and M06−2X Exchange-Correlation Functionals for Noncovalent Interactions in Biomolecules. *J. Chem. Theory Comput.* **2008**, *4* (12), 1996–2000.

53. Corminboeuf, C. Minimizing Density Functional Failures for Non-Covalent Interactions Beyond van Der Waals Complexes. *Acc. Chem. Res.* **2014**, *47* (11), 3217–3224.

54. Mardirossian, N.; Head-Gordon, M. How Accurate Are the Minnesota Density Functionals for Noncovalent Interactions, Isomerization Energies, Thermochemistry, and Barrier Heights Involving Molecules Composed of Main-Group Elements? *J. Chem. Theory Comput.* **2016**, *12* (9), 4303–4325.

55. Kozuch, S.; Martin, J. M. L. Halogen Bonds: Benchmarks and Theoretical Analysis. *J. Chem. Theory Comput.* **2013**, *9* (4), 1918–1931.

56. Saikia, N.; Deka, R. C. Density Functional Study on Noncovalent Functionalization of Pyrazinamide Chemotherapeutic with Graphene and Its Prototypes. *New J. Chem.* **2014**, *38* (3), 1116.

57. Jheng, J.-F.; Lai, Y.-Y.; Wu, J.-S.; Chao, Y.-H.; Wang, C.-L.; Hsu, C.-S. Influences of the Non-Covalent Interaction Strength on Reaching High Solid-State Order and Device Performance of a Low Bandgap Polymer with Axisymmetrical Structural Units. *Adv. Mater.* **2013**, *25* (17), 2445–2451.

58. Schleyer, P. von R. Introduction: DelocalizationPi and Sigma. *Chem. Rev.* **2005**, *105* (10), 3433–3435.

59. Choudhary, A.; Gandla, D.; Krow, G. R.; Raines, R. T. Nature of Amide Carbonyl−Carbonyl Interactions in Proteins. *J. Am. Chem. Soc.* **2009**, *131* (21), 7244–7246.

60. Bartlett, G. J.; Choudhary, A.; Raines, R. T.; Woolfson, D. N. N→π* Interactions in Proteins. *Nat. Chem. Biol.* **2010**, *6* (8), 615–620.

61. Newberry, R. W.; VanVeller, B.; Guzei, I. A.; Raines, R. T. N →π* Interactions of Amides and Thioamides: Implications for Protein Stability. *J. Am.*

Chem. Soc. **2013**, *135* (21), 7843–7846.

62. Bartlett, G. J.; Newberry, R. W.; VanVeller, B.; Raines, R. T.; Woolfson, D. N. Interplay of Hydrogen Bonds and N →π* Interactions in Proteins. *J. Am. Chem. Soc.* **2013**, *135* (49), 18682–18688.

63. Newberry, R. W.; Orke, S. J.; Raines, R. T. N →π* Interactions Are Competitive with Hydrogen Bonds. *Org. Lett.* **2016**, *18* (15), 3614–3617.

64. Iwaoka, M.; Tomoda, S. Structural Characterization of Areneselenenyl Chloride Stabilized by the Stereoelectronic Effect of an Intramolecular Nitrogen Atom. *J. Org. Chem* **1995**, *60*, 5299–5302.

65. Iwaoka, M.; Tomoda, S. Nature of the Intramolecular Se···N Nonbonded Interaction of 2-Selenobenzylamine Derivatives. An Experimental Evaluation by 1 H, 77 Se, and 15 N NMR Spectroscopy. *J. Am. Chem. Soc.* **1996**, *118* (34), 8077–8084.

66. Iwaoka, M.; Komatsu, H.; Katsuda, T.; Tomoda, S. Quantitative Evaluation of Weak Nonbonded Se···F Interactions and Their Remarkable Nature as Orbital Interactions. *J. Am. Chem. Soc.* **2002**, *124* (9), 1902–1909.

67. Iwaoka, M.; Komatsu, H.; Katsuda, T.; Tomoda, S. Nature of Nonbonded Se···O Interactions Characterized by 17 O NMR Spectroscopy and NBO and AIM Analyses. *J. Am. Chem. Soc.* **2004**, *126* (16), 5309–5317.

68. Iwaoka, M.; Katsuda, T.; Komatsu, H.; Tomoda, S. Experimental and Theoretical Studies on the Nature of Weak Nonbonded Interactions between Divalent Selenium and Halogen Atoms. *J. Org. Chem.* **2005**, *70* (1), 321–327.

69. Barton, D. H. R.; Hall, M. B.; Lin, Z.; Parekh, S. I.; Reibenspies, J. Unusual Attractive Interactions between Selenium and Oxygen in Selenoiminoquinones. *J. Am. Chem. Soc.* **1993**, *115* (12), 5056–5059.

70. Bleiholder, C.; Werz, D. B.; Köppel, H.; Gleiter, R. Theoretical Investigations on Chalcogen−Chalcogen Interactions: What Makes These Nonbonded Interactions Bonding? *J. Am. Chem. Soc.* **2006**, *128* (8), 2666–2674.

71. Bleiholder, C.; Gleiter, R.; Werz, D. B.; Köppel, H. Theoretical Investigations on Heteronuclear Chalcogen−Chalcogen Interactions: On the Nature of Weak Bonds between Chalcogen Centers. *Inorg. Chem.* **2007**, *46* (6), 2249–2260.

72. Weinhold, F.; Landis, C. R. Chemistry Education: Research and Practice in Europe Natural Bond Orbitals and Extensions of Localized Bonding Concepts. *Educ. Res. Pr. Eur* **2001**, *2* (2), 91–104.

73. Pascoe, D. J.; Ling, K. B.; Cockroft, S. L. The Origin of Chalcogen-Bonding Interactions. *J. Am. Chem. Soc.* **2017**, *139* (42), 15160–15167.

74. Nuzzo, S.; Twamley, B.; Platts, J. A.; Baker, R. J. Pseudohalide Tectons within the Coordination Sphere of the Uranyl Ion: Experimental and Theoretical Study of C–H···O, C–H···S, and Chalcogenide Noncovalent Interactions. *Inorg. Chem.* **2018**, *57* (7), 3699–3712.

75. West, T. H.; Walden, D. M.; Taylor, J. E.; Brueckner, A. C.; Johnston, R. C.; Cheong, P. H.-Y.; Lloyd-Jones, G. C.; Smith, A. D. Catalytic Enantioselective [2,3]-Rearrangements of Allylic Ammonium Ylides: A Mechanistic and Computational Study. *J. Am. Chem. Soc.* **2017**, *139* (12), 4366–4375.

Chapter 3
Orbital Delocalisation in H-Bonds

Abstract

Hydrogen bonds are important across many chemical and biological processes including DNA structure and medicinal chemistry. The nature of the interaction has largely been attributed to electrostatic attraction between a positive area of potential on an H-bond donor and a negative area of potential on an H-bond acceptor. More recently, some computational approaches have proposed that n→σ* electron delocalisation may be important in H-bonds. A molecular orbital analysis and energy decomposition found that electrostatics, and not orbital interactions dominated H-bonds between an amine donor and an amide acceptor. When the same technique was applied to a H-bond chain used to investigate cooperativity in H-bonds it was found that molecular orbital energies followed the experimental trends seen, therefore demonstrating n→σ* electron delocalisation can be important in determining some H-bond systems experimentally.

Acknowledgements: All synthesis and experimental data for this chapter was obtained by Nicole Meredith and Nicholas Dominelli Whitely.

3.1 Introduction

Hydrogen-bonding underpins life itself, being seen in protein structure and DNA base pairing.[1] Furthermore, hydrogen-bonding has been found to be important in a range of synthetic systems, including in molecular recognition, catalysis[2] and medicinal chemistry.[3] The importance of hydrogen bonding has driven extensive studies and investigations into the nature of the interaction. Despite "bonding" still appearing in the name of these interactions, H-bonding is widely considered to be an electrostatically-driven interaction between a hydrogen atom with a positive electrostatic potential and an acceptor with a negative potential (**Figure 3.1**). However, have been some suggestions that H-bonding may in fact contain an n→σ* electron delocalisation component, similar to what has been described in halogen bonding (**Chapter 1**) and chalcogen bonding (**Chapters 1** and **2**).[4–9]

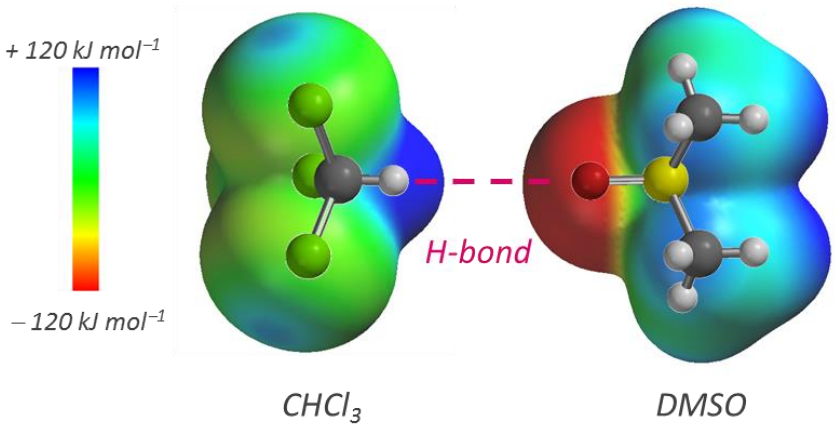

Figure 3.1 Electrostatic potentials of an H-bond donor ($CHCl_3$) and an H-bond acceptor (DMSO) forming an H-bond between the positive potential H and the negative potential acceptor. Calculated using Spartan '14 DFT/B3LYP/6-311G*.

The nature of H-bonding has been debated since Pauling first investigated[10] chemical bonding, noting that "*an atom of hydrogen is attracted by rather strong forces to two atoms, instead of only one, so that it may be considered a bond between them. This is called the hydrogen bond*". For strong H-bonds, for example NH···O or OH···O, this definition is in alignment. Such strong H-bonds are short, spectroscopically detectable and energetically favourable interactions, which for many

chemists at the time constituted a bond.[11] However, the classification of weaker interactions such as C-H···O and O-H···arene as H-bonds presents more of a grey area, since they are associated with far less convincing spectroscopic data according to classic H-bonding defintions.[11] Pauling's definition of an H-bond was maintained until the 1960s, with these weaker interactions not being accepted as falling under the H-bonding definition until later.[12,13] Pimentel and McClellan suggested an alternative definition of an H-bond: there must be some evidence of a bond, and the interaction must involve a hydrogen that is already bonded to another atom.[14] Crucially, this definition does not take into account the nature of any other atoms involved, such as electronegativity. Under Pimentel and McClellan's definition, bonds such as CH···O=C are defined as an H-bond, but not according to Pauling's definition.

The contentious issue of defining a H-bond has even resulted in the IUPAC definition being changed multiple times, coming to its current state in 2011: "*The forces involved in the formation of a hydrogen bond include those of an electrostatic origin, those arising from charge transfer between the donor and acceptor leading to partial covalent bond formation between H and Y, and those originating from dispersion*".[15] The murky area surrounding the definition of hydrogen bonding leads to important questions about the energetic significance of either electrostatic or partial covalency contributions in H-bonding. Can understanding the relative energetic contributions lead to a clear definition of the nature of H-bonding?

3.2 The nature of H-bonding

3.2.1 Electrostatic component of H-bonding

Traditionally, H-bonds have been considered an electrostatic interaction. In fact, previous IUPAC definitions have stated as much: "*A form of association between an electronegative atom and a hydrogen atom attached to a second, relatively electronegative atom. It is best considered as an electrostatic interaction, heightened by the small size of hydrogen, which permits proximity of the interacting dipoles or charges.*".[16]

Electrostatic properties can be used to predict the behaviour of H-bonds in solution. Abraham first devised[17] an empirical scale by which H-bond donor (α_2^H) and acceptor (β_2^H) abilities can be ranked. Quantitative structure activity relationships of large volumes of experimental titration data revealed that a large range of association constants for hydrogen bonding interactions, *K*, could be described by a simple equation (**Equation 3.1**):

$$logK = c_1\alpha_2^H\beta_2^H + c_1 \qquad \textbf{(3.1)}$$

Where c_1 and c_2 are constants that depend on the solvent. A similar α/β scale was subsequently (re)defined by Hunter to account for the solvent competition in Abraham's from CCl_4. Hunter showed that the experimental values of α_2^H and β_2^H correlated well with the predicted maximum electrostatic potential (E_{max}) and the minimum electrostatic potential (E_{min}), respectively.[18] Using the equations from correlations, Hunter defined his α/β scale as:

$$\alpha = \frac{E_{max}}{52\ kJ\ mol^{-1}} = 4.1(\alpha_2^H + 0.33) \qquad \textbf{(3.2)}$$

$$\beta = \frac{-E_{min}}{52\ kJ\ mol^{-1}} = 10.3(\beta_2^H + 0.06) \qquad \textbf{(3.3)}$$

Where 52 kJ mol^{-1} was used as a normalisation constant from the slope of the fits between Abraham's experimental α_2^H and β_2^H values and electrostatic potentials.

On Hunter's scale, α and β are directly linked to calculated electrostatic potentials (ESPs).[18–21] The α and β parameters have since been used to predict H-bond strength and correlate well to experimentally H-bond interaction strengths, giving experimental evidence of the electrostatic nature of H-bonding.[22,23]

Theoretical decompositions have been used to study the physiochemical origin of H-bonds. An early decomposition was used by Morokuma and Kitaura to evaluate the attractive polarisation, electrostatics and charge transfer, and the repulsive exchange components of a hydrogen bond.[24] The nature was found to be very dependent on the geometry of the H-bonding complex, with very short intermolecular distances having large contributions from electrostatics, polarisation and charge transfer. When the intermolecular distance was increased, only electrostatics forces were significant.[25]

3.2.2 Partial covalency of H-bonding

Linus Pauling's original definition suggests H-bonding can be considered a traditional bonding interaction, and therefore displays a significant covalent character. Resonance assisted H-bonds are considered evidence for covalent character in H-bonds, where H-bond strength is enhanced due to the electron delocalisation of π-electrons (**Figure 3.2**).[26,27]

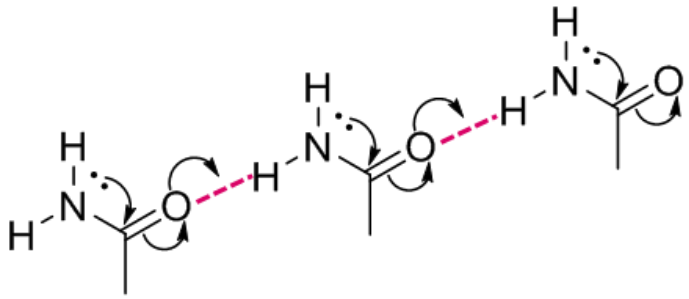

Figure 3.2 Resonance assisted H-bonds enhancing the strength of H-bonds in amides.

Other investigations into the partial covalency of H-bonding have been limited to theoretical or crystallographic studies. It has been proposed that an electron delocalisation from the lone pair of the H-bond acceptor into the antibonding σ* orbital of the H-bond donor (much like previously discussed σ-hole interactions in **Chapters 1** and **2**) contributes significantly to the stability of an H-bond, particularly for strong H-bonds.[5,28,29] n→σ* electron delocalisation can be qualitatively demonstrated by examining molecular geometries in the solid state. In systems containing weak H-bonds the D-H···A interaction angle was between 90–180°, whereas very strong H-bonds interactions appeared far more linear (175-180°). These findings are consistent with the linear geometry dependence of an electron delocalisation in strong H-bonds.[30] Natural bond orbital analysis complements such structural observations, and suggests that n→σ* delocalisation in H-bonds can have a large energetic contribution.[31,32] Similarly, Quantum Theory of Atoms in Molecules (QTAIM) has also been used to demonstrate the partial covalent character of H-bonds, showing the presence of electron density at the bond critical point.[33,34]

3.3 Aims

The exact physiochemical origin of H-bonding can be complicated and appears to change depending on the strength, geometru and nature of the surrounding atoms. The aim of this investigation is to provide a theoretical analysis on the nature of H-bonding in molecular balances previously examined within the Cockroft group. This chapter will focus on applying the techniques used in **Chapter 2** to H-bond systems, as well as using energy decomposition to search for a quantitative definition of NH···O=C and OH···O=C H-bonds. Furthermore, a cooperative H-bond network will be analysed to see if unexpected trends seen in a previous investigation can be explained using a partially covalent model.

3.4 Results and discussion

3.4.1 Amide/amine H-bond donors

H-bonds between amides are of great importance for biological processes, particularly in determining protein structure. This investigation seeks to correlate NBO theory, MO theory and energy decomposition data with experimentally determined conformational free energy differences to probe the physicochemical nature of these H-bonds. The molecular balances used to study H-bonding between amides are similar to others used in the Cockroft group,[23,35–37] including those used for the investigation of chalcogen bonding in **Chapter 2** (**Figure 3.4**).

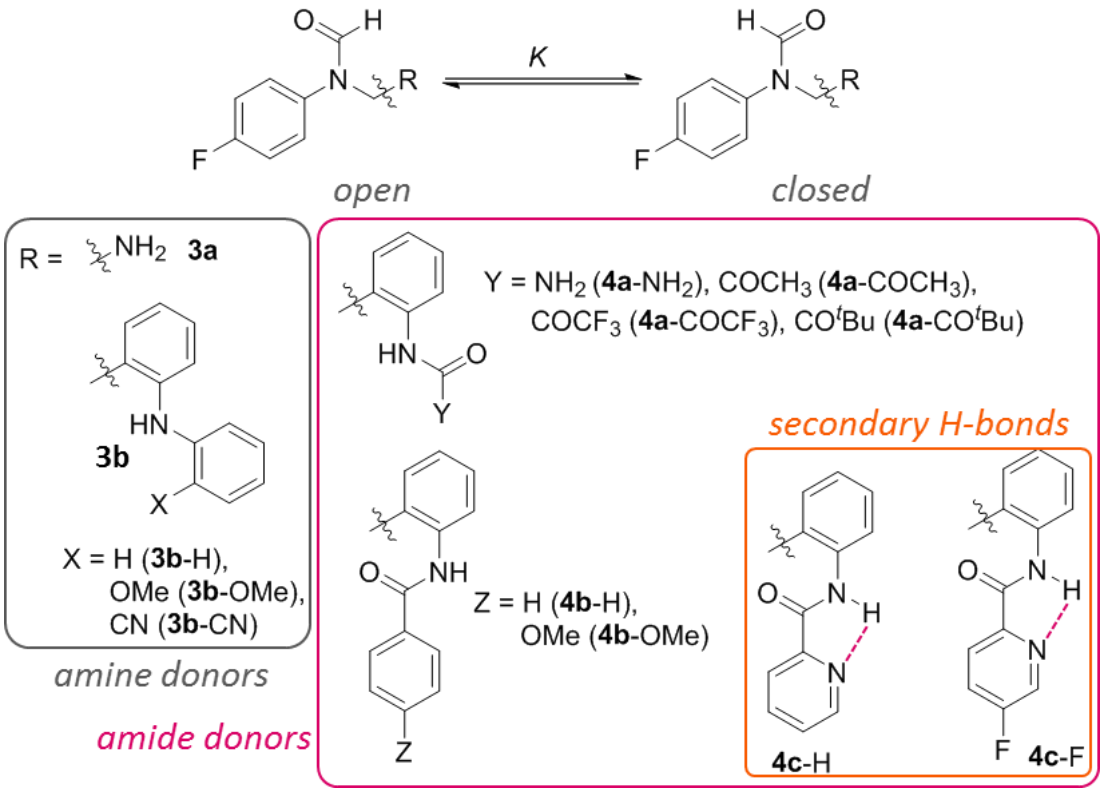

Figure 3.4 Molecular balances used in this study containing H-bonds between an amide acceptor and an amine (grey box, **series 3**) or amide (pink box, **series 4**) donor. Other molecular balances also have the potential to form secondary H-bonds (orange box).

Intramolecular H-bonds can be formed between the N-H donor and formyl oxygen acceptor in the closed conformer in these molecular balances (**Figure 3.5**).

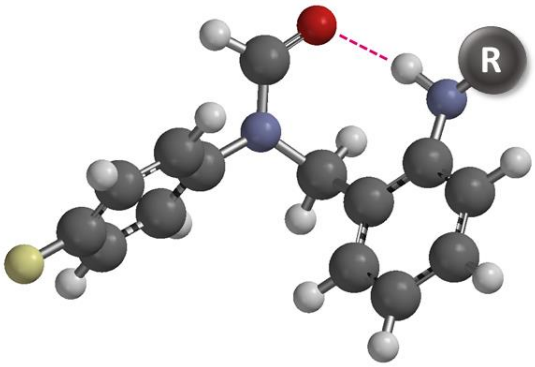

Figure 3.5 Optimised general geometry of molecular balances used in this study showing the formation of an H-bond in the closed conformer. Calculated using Spartan '14 DFT/B3LYP/6-311G*.

The conformational free energies indicated that the H-bonded conformer was strongly favoured in apolar solvents, such as $CDCl_3$ (< −10 kJ mol^{-1}) and significantly lower in polar solvents, such as methanol-d_4 and DMSO-d_6 (between −3 and −6 kJ mol^{-1}). These results appear to be consistent with an electrostatic competition solvation model. Solvents with high H-bond donor and acceptor properties outcompete the solute···solute interactions to give less favourable conformational free energies, and those with low H-bond donor and acceptor abilities gave more favourable conformational free energies (see **Chapter 2**, **Figure 2.21**). The experimental values can be fitted to a solvation model (**Equation 3.4**)

$$\Delta G_{CALC} = \Delta\alpha\beta_s + \Delta\beta\alpha_s + \Delta E \qquad \textbf{(3.4)}$$

Where α_s and β_s are the H-bond donor and acceptor abilities of the solvent respectively and $\Delta\alpha$ and $\Delta\beta$ are the change in the H-bond donor and acceptor abilities of the solute, respectively. ΔE represents the solvent independent part of the interaction. Upon calculating conformational free energies across a range of solvents with varying α and β values using **Equation 3.4** it gave a strong, linear correlation with experimentally determined conformational free energies and a y = x fit (**Figure 3.6**). The linear correlation is indicative of an electrostatically controlled interaction.

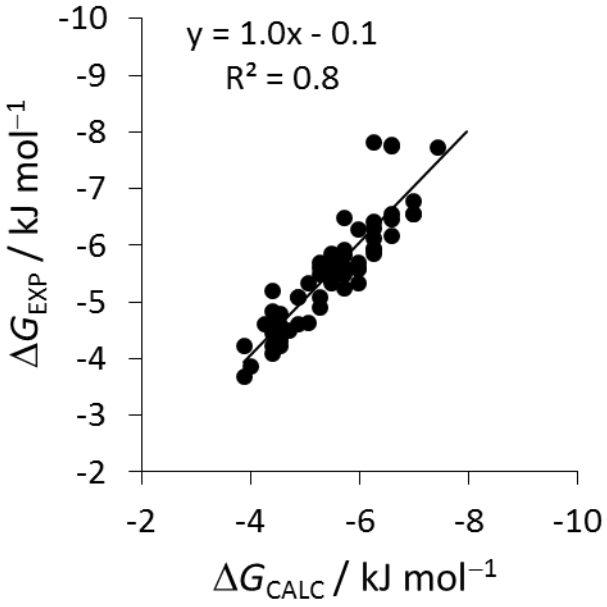

Figure 3.6 Correlation between experimentally determined conformational free energies (ΔG_{EXP}) and calculation conformational free energies from **Equation 3.2** (ΔG_{CALC}).

From **Equation 3.4**, the values of $\Delta\alpha$, $\Delta\beta$ and ΔE can be dissected. Given the solvent dependence of H-bonds,[38] the dissected solvent independent ΔE term is useful for comparisons with theoretical parameters, which are most readily calculated in the gas phase. Electrostatic potentials have been used in the study of molecular interactions and have been shown to be predictors of H-bond strength.[18,19] Thus, the derived ΔE values were plotted against electrostatic potentials taken along the NH axis of the H-bond donor (**Figure 3.7A** and **B**). The resulting high-quality correlation verified the validity and physical significance of the dissected ΔE values (**Figure 3.7C**). Therefore, ΔE values will be used in subsequent analyses of the intramolecular H-bonds hosted within the molecular balances shown in **Figure 3.4**.

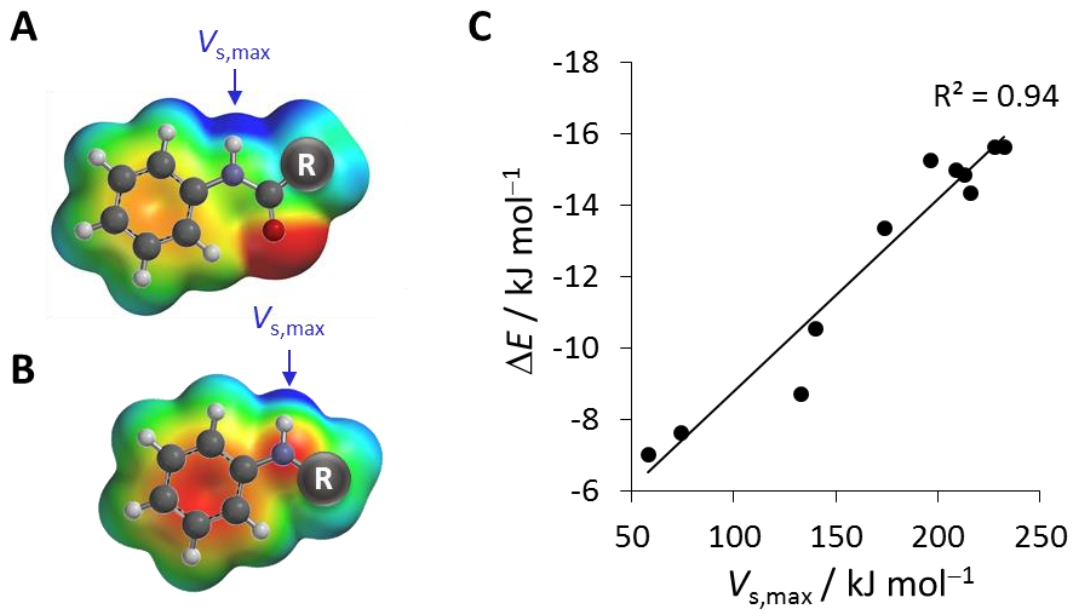

Figure 3.7 Plot of the maximum ESP value ($V_{s,max}$) along the N-H bond of the (A) amide and (B) amine H-bond donor versus (C) the solvent independent term ΔE, calculated from **Equation 3.2**

Despite the implication of an electrostatic interaction based on the observed solvent effects, evidence for potential partial covalency in these H-bonds was investigated. Natural bond orbital (NBO) analysis was used to look for the presence of this electron delocalisation. Where a H-bond was present, a delocalisation was seen by NBO from both lone pairs of the formyl oxygen in to the antibonding σ* N-H molecular orbital (**Figure 3.9**).

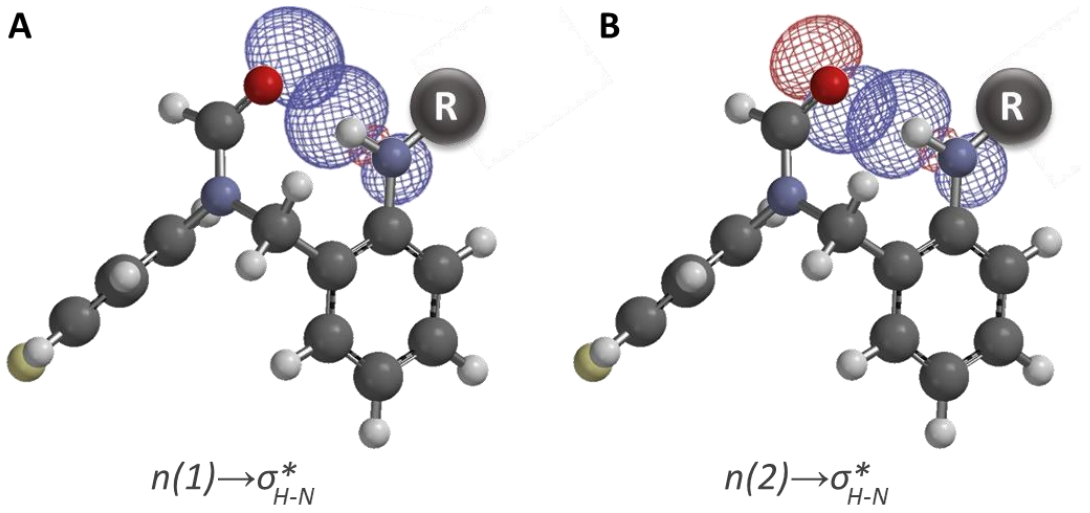

Figure 3.8 NBO interaction diagrams showing an (A) $n(1)\rightarrow\sigma^*_{H\text{-}N}$ and (B) $n(2)\rightarrow\sigma^*_{H\text{-}N}$ electron delocalisation.

NBO calculations can predict the energetic contribution of electron delocalisation between a Lewis acid donor and an acceptor natural bond orbital by the application of second order perturbation theory, as described in **Chapter 1**.

The combined second order perturbation energies (ΔE^2) for n→σ* delocalisation from both formyl lone pair orbitals into the NH group were shown to be important, and in some cases worth up to 60 kJ mol^{-1} in the gas phase (**Figure 3.10**). Experimental data showed that the presence of a second, competing intramolecular H-bond, e.g. between the NH group and an adjacent pyridine N (**Figure 3.8**) decreases the preference for the folded conformation. Consistent with this observation, NBO analyses of such secondary H-bonds between pyridine and the N-H were shown to be contain the similar n→σ* electron delocalisation effects from the N lone pair of the pyridine to the antibonding σ* of the N-H bond, although much weaker worth up to 10 kJ mol^{-1}.

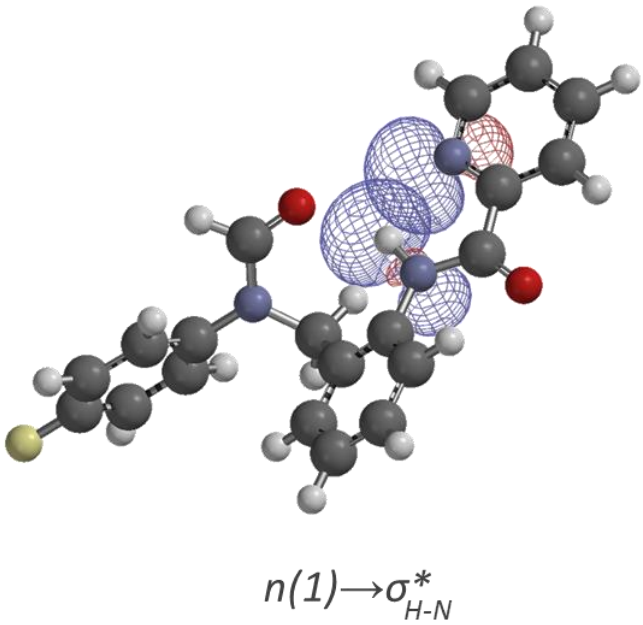

Figure 3.9 NBO interaction diagram showing the n(1)→σ*$_{H\text{-}N}$ of secondary H-bonds.

While the NBO analysis can indicate the qualitative occurrence of electron delocalisation, the energetic reliability of NBO calculations appears to be low. The correlation given between experimental conformational free energies and the sum of all second order perturbation energy values (ΔE^2) for n→σ* electron delocalisations from the formyl lone pair to the N-H antibonding σ* orbital in H-bonds is very poor (**Figure 3.10**).

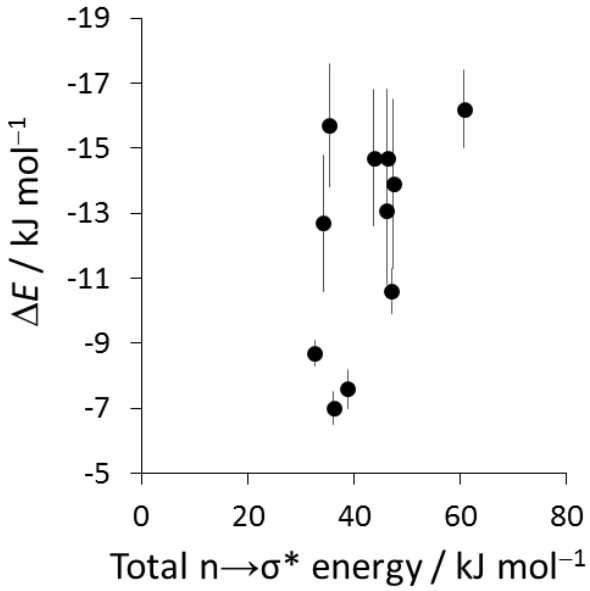

Figure 3.10 Experimentally determined solvent-independent ΔE values dissected using **Equation 3.2** *versus* the sum of all second order perturbation energies containing an n→σ* electron delocalisation from the formyl lone pair to the antibonding σ* orbital of the N-H bond. Calculated using NBO 6.0.

Molecular orbitals, as seen in **Chapter 2**, may provide a clearer, more physically meaningful description of the H-bonds in this system compared to using NBOs. Using the same technique of matching molecular orbitals of simplified molecular balances in the open and closed conformer, allowed creation of a molecular orbital plot. As seen for chalcogen bonds in **Chapter 2** (**Figure 2.33**), two subsets of data fell below the grey line, indicating greater stabilisation of these molecular orbitals in the closed conformer compared to the open (**Figure 3.11**).

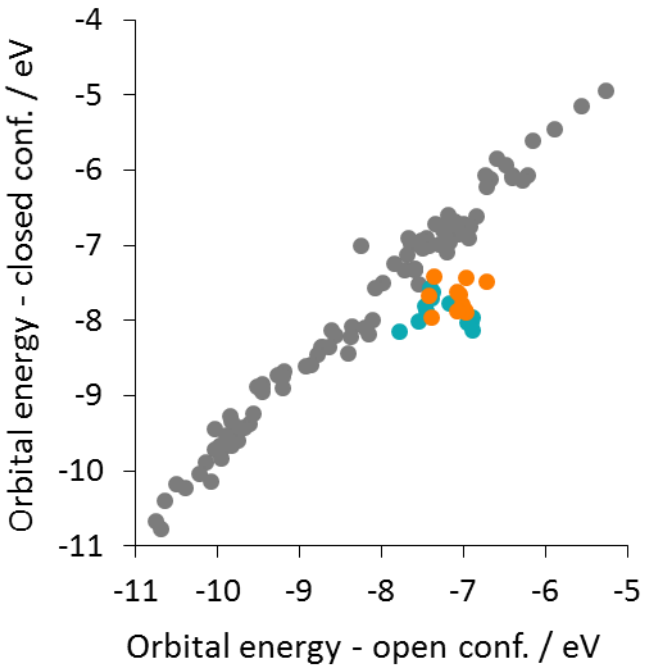

Figure 3.11 Molecular orbital energies in the closed versus the open conformer. Grey points are molecular orbital energies that consistently change between conformers and represent the background behaviour. Orange points correspond to an n→σ* electron delocalisation from one lone pair of the formyl oxygen and teal points correspond to an n→σ* electron delocalisation from the other lone pair of the formyl oxygen.

The orange points corresponded to the stabilisation of one formamide lone pair orbital via delocalisation into the antibonding σ* N-H bond (**Figure 3.12A**), while the teal points corresponded to the equivalent delocalisation of the orthogonal lone pair orbital (**Figure 3.12B**). However, no correlation was observed between either of the molecular orbital energies containing an n→σ* delocalisation and the experimental conformational free energy (**Figure 3.13**). Therefore, the MO evidence indicates that partial covalency may be occurring, but that the experimental conformational preferences are not dominated by orbital interactions.

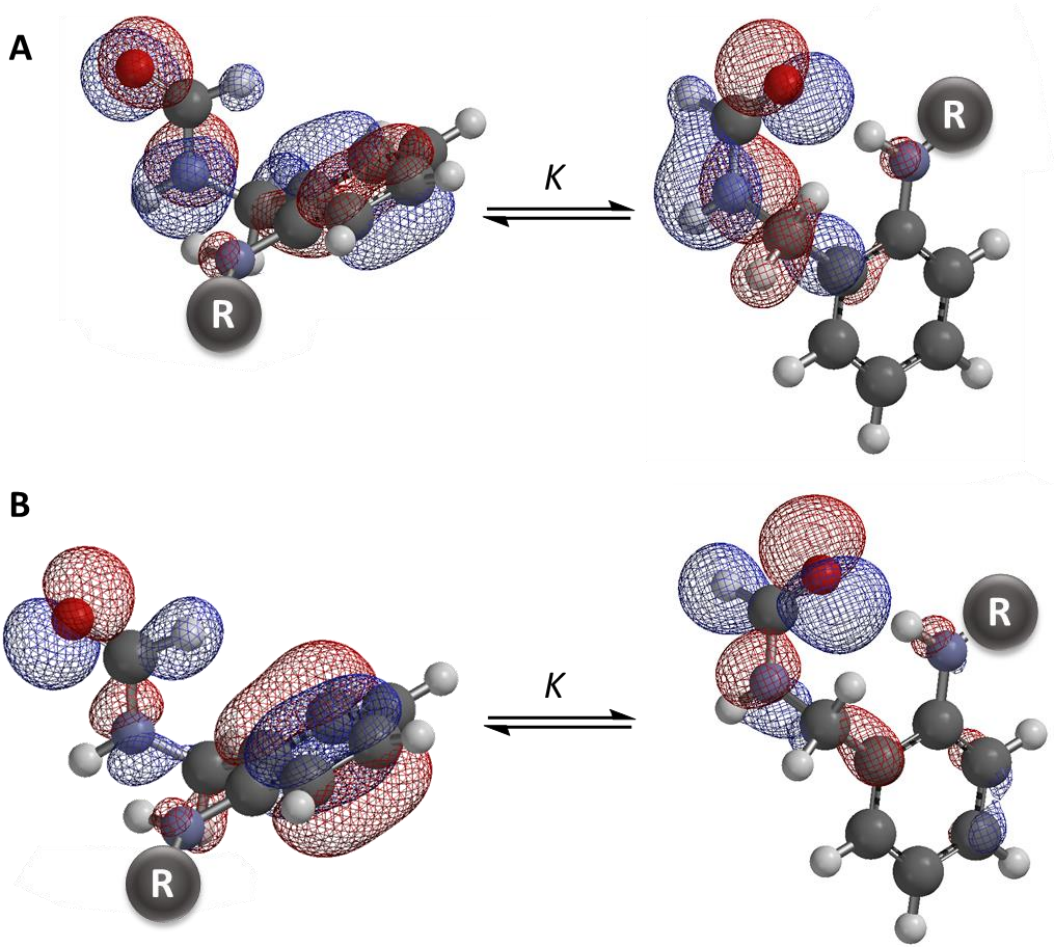

Figure 3.12 Molecular orbital diagrams corresponding to (A) orange points and (B) teal points in the open (left) and closed (right) conformers in **Figure 3.9**.

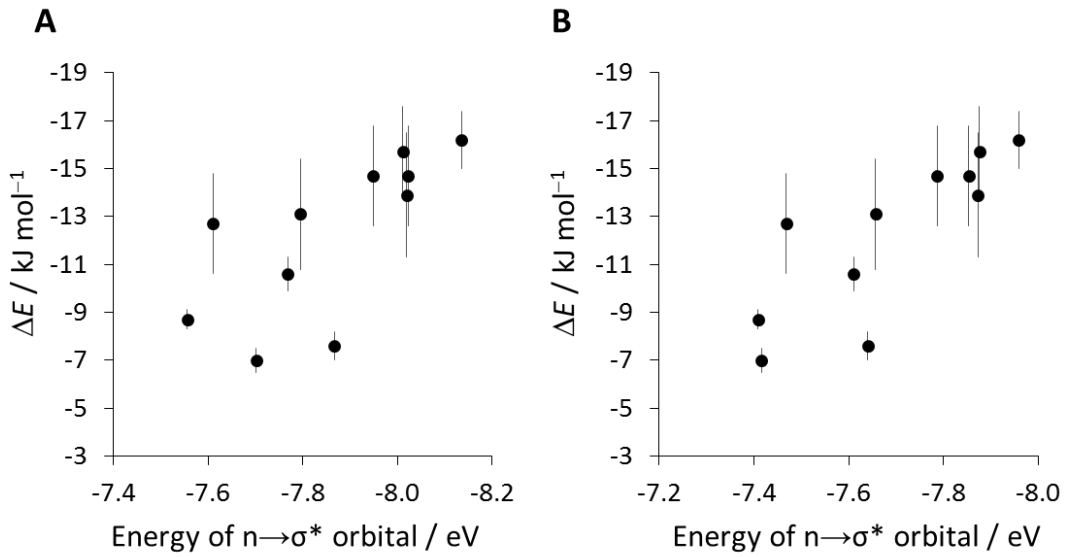

Figure 3.13 Experimentally determined solvent-independent ΔE values calculated from **Equation 3.4** versus molecular orbital energies containing an n→σ* electron delocalisation. (A) corresponds to **Figure 3.12A** and (B) corresponds to **Figure 3.12B** molecular orbitals.

The interactions were further evaluated though an energy decomposition using fiSAPT (functional group intramolecular symmetry adapted perturbation theory) to probe relative contributions of electrostatics, induction, dispersion and exchange-repulsion to H-bonding between carbonyls and amides/amines. Unlike the examples reported in **Chapter 1**, which studies the intermolecular interactions using two, non-covalently linked fragments, the study of intramolecular interactions using three fragments, two of which are covalently linked by the third, is difficult using SAPT. Instead, an intramolecular approach must be used, and therefore the fiSAPT method introduced at the beginning of **Chapter 1** was used. Unfortunately, this technique is limited to the simpler SAPT(0) methodology by the PSI4 software, which uses a simpler prediction of electron correlation and therefore less accurate than higher order methodologies.

The fiSAPT decomposition of H-bond-containing molecular balances is shown in **Figure 3.14**. In all cases the interaction is dominated by the electrostatic component (**Figure 3.14A**). Mirroring the finding from the earlier correlation of ΔE with calculated ESPs (**Figure 3.7C**), a good correlation is seen between the electrostatic

component and ΔE values (**Figure 3.15A**), further supporting the conclusion that these H-bonding interactions are electrostatically driven. Unfortunately, no quantitative link between the ΔE values and the predicted total SAPT interaction energy was seen, demonstrating the limitations to the SAPT0 fiSAPT method (**Figure 3.15B**).

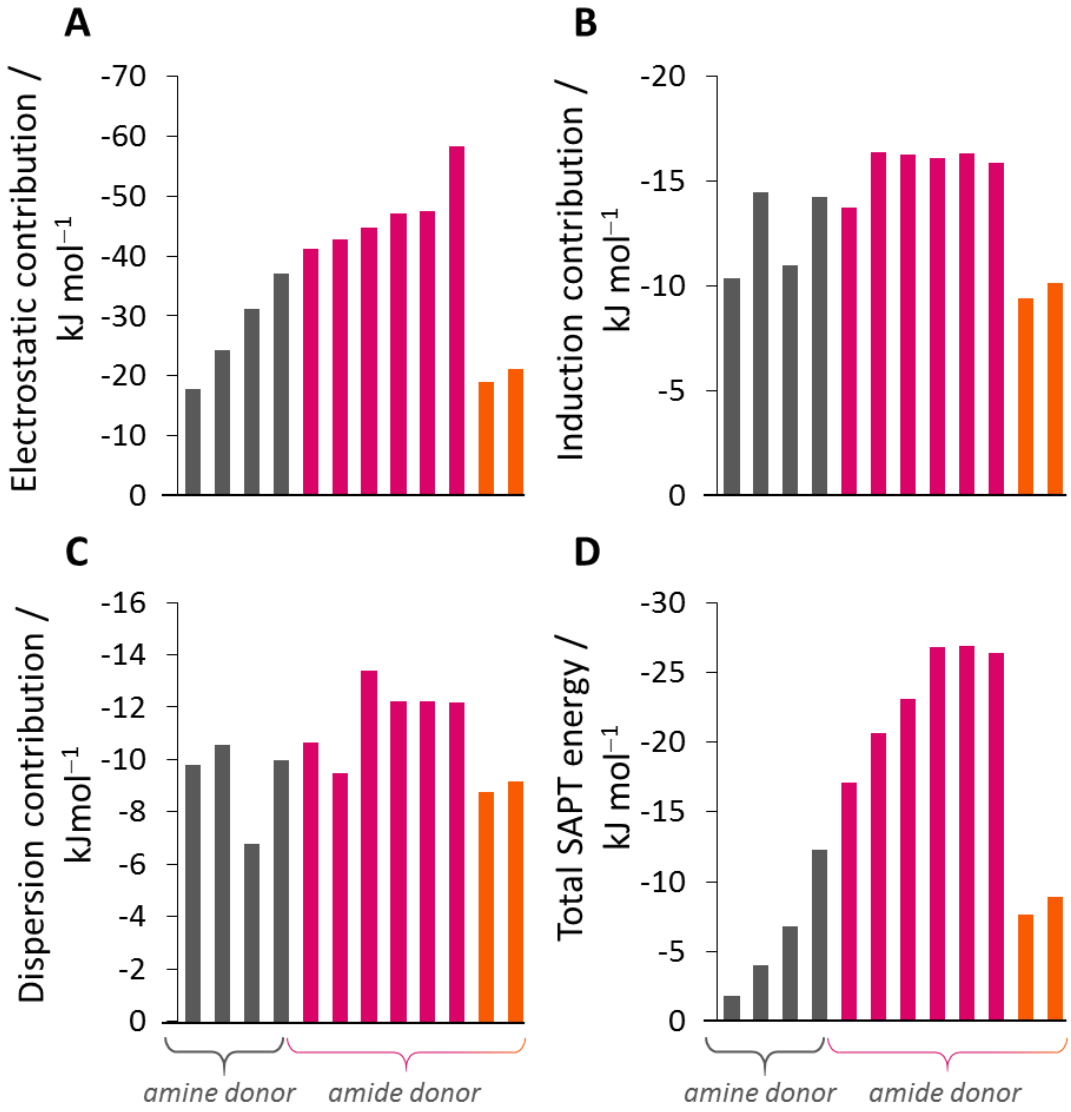

Figure 3.14 The (A) electrostatic, (B) induction and (C) dispersion components of intramolecular H-bonds between amides/amines predicted by fiSAPT. (D) the total SAPT interaction energy predicted by fiSAPT. fiSAPT calculations performed using PSI4/SAPT0/6-311G*. Colours correspond to those seen in **Figure 3.4**.

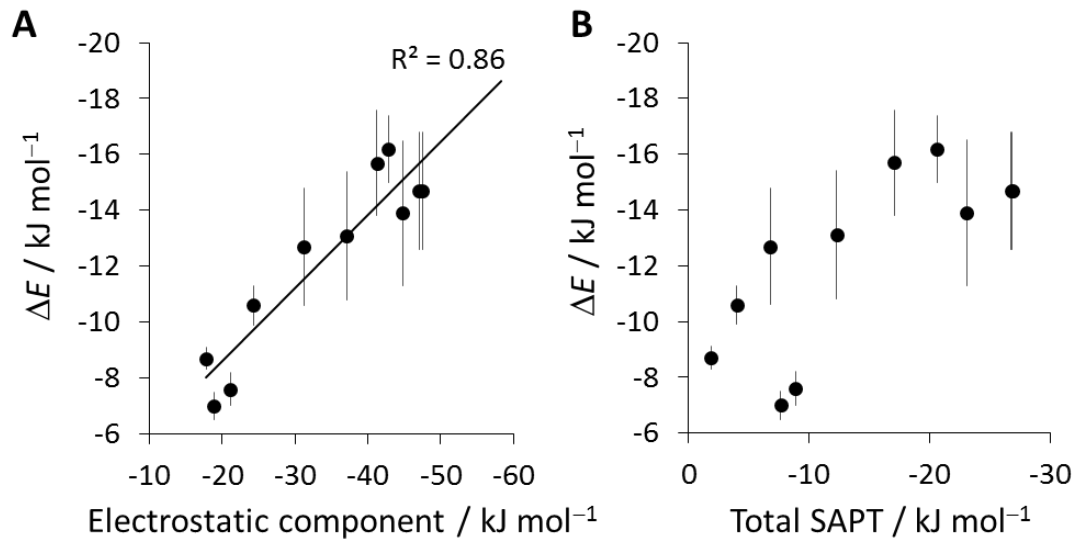

Figure 3.15 Solvent independent ΔE values calculated from **Equation 3.4** versus the predicted (A) electrostatic component predicted by fiSAPT and (B) the total SAPT interaction.

In conclusion, H-bonds between amine and amide donors to amide acceptors in these molecular balances appear to be electrostatic in nature. An electrostatic competition solvation model can be used to accurately predict the experimental behaviour of these interactions.[18] NBO and MO analysis did provide some evidence of n→σ* electron delocalisation, but neither the second-order perturbation energies from NBO calculations, nor molecular orbital energies provided a strong correlation with experimental free energies. The fiSAPT analysis provided a qualitative confirmation of the electrostatic nature of these interactions, with the electrostatic component being significantly dominant in all molecular balances. However, it is important, to recognise the limitations of the experimental system. The CH_2 linker present in these molecular balances provides some degrees of freedom and conformational flexibility, which may allow alternative conformations to be populated as well as introducing an entropic penalty for forming the desired interaction. These limitations may present extra challenges in dissecting out the strength and nature of the H-bonds in these molecular balances.

3.3.2 OH···O=C H-bonds and cooperativity

As highlighted in the introduction to this chapter, H-bonds may differ in their physiochemical origin depending on their strength. Weaker H-bonds are largely considered to be electrostatic in nature while computations can suggest stronger H-bonds have covalent character.[9] H-bonds between amides and amines examined in the previous section appear to be electrostatic, but can this electrostatic model be applied to other H-bonding systems?

H-bond chains are present in a number of chemical and biological systems and processes.[41,42] The origins of cooperativity[43] in H-bond chains has been proposed to differ depending on the system. Weaker interactions along urea chains were theoretically determined to fall under a classic electrostatic definition, whereas H-bond chains along enol-containing molecules displayed a much stronger predicted interaction energies (over three times that of chains of urea) and was therefore suggested to have more covalent character.[44] A recent experimental molecular balance study has shown that energetic cooperativity in H-bond chains can double the strength of a terminal H-bond, but surprisingly, the cooperative effect was found not to extend beyond two H-bonds (**Figure 3.16**).[36]

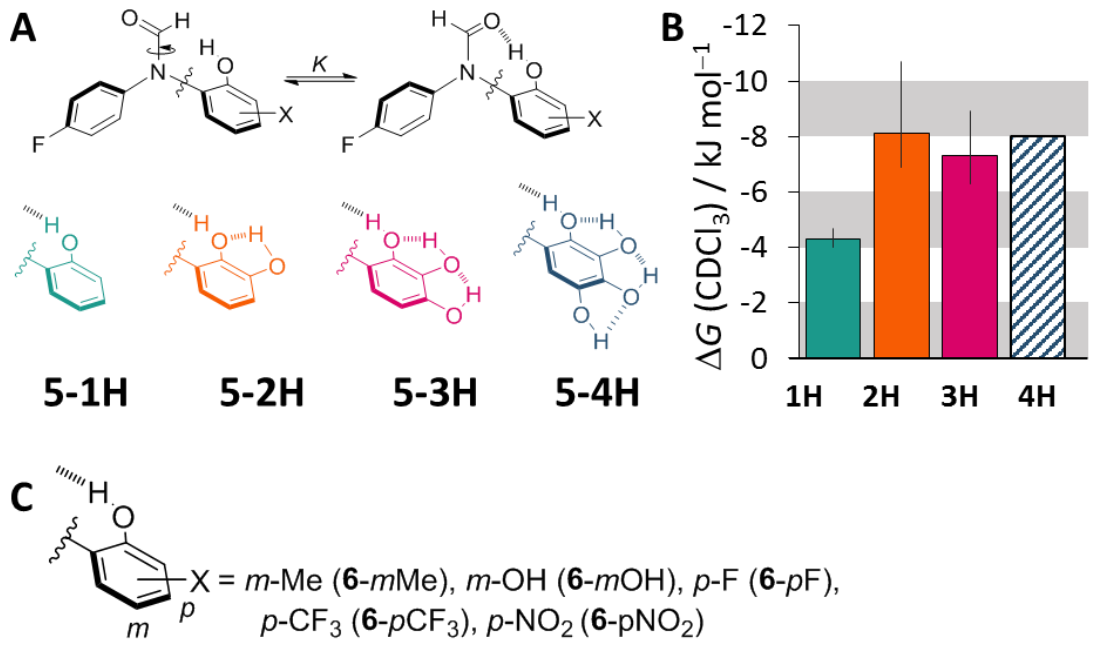

Figure 3.16 (A) and (C) Molecular balances used in this study. (B) Previous experimentally determined ΔG values measured by ^{19}F NMR spectroscopy ($CDCl_3$, 500.1 MHz, 298 K) demonstrating the limit of H-bond cooperativity does not extend beyond two H-bonds. Data for molecular balance **5**-4H was calculated from a correlation of calculated DFT conformational energies with experimental data for all of the balances shown.[36]

The conformational free energies of a balance (**Figure 3.16A**) in the original experimental study were measured in a limited number of solvents ($CDCl_3$ and CD_3CN).[36] Therefore an expanded solvent screen was subsequently conducted to gain a more detailed understanding of the experimental of behaviour these molecular balances.

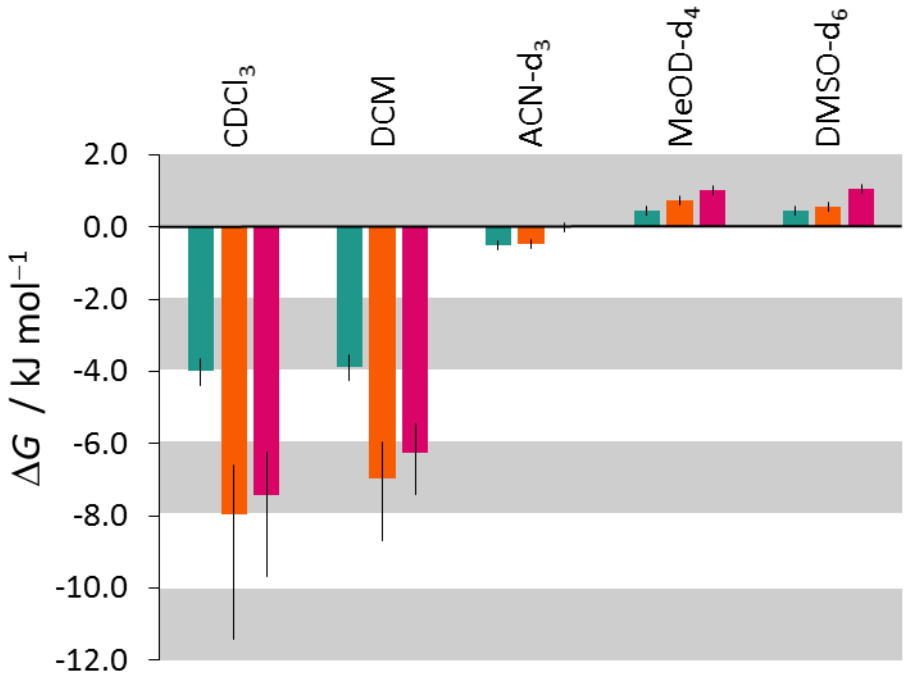

Figure 3.17 Experimental conformational free energy differences, ΔG measured by ^{19}F NMR spectroscopy (500.1 MHz, 298 K) in a range of solvents for molecular balances **5**-1H (teal), **5**-2H (orange) and **5**-3H (pink).

The expected favourable folding was seen in apolar solvents (e.g. $CDCl_3$), but the intramolecular H-bond was outcompeted in polar solvents (e.g. DMSO-d_6) (**Figure 3.17**). As was also employed in the first section of this chapter, the empirical solvation model shown in **Equation 3.4** was employed to see if a simple electrostatic model could account for the experimental conformational energies of the balance in a range of solvents.[23]

$$\Delta G_{calc} = \Delta\alpha\beta_s + \Delta\beta\alpha_s + \Delta E \qquad (\mathbf{3.4})$$

However, in contrast to the earlier dataset for the amine/amide H-bond system, the modelled free energies only showed a moderate correlation with experimental conformational free energies (**Figure 3.18**). This result implied that this simple electrostatic model could not fully account for the experimental behaviour of these OH···O=C H-bonds. It is therefore possible that these H-bonds could contain a significant covalent character, which might be better explained through an orbital analysis. Due to the limited correlations between experimentally determined and

calculated conformational free energies using Equation 3.4, the solvent independent ΔE term will not be used to represent experimental results. Instead, ΔG values measured in $CDCl_3$ will be used due to the apolar, non-competitive nature of chloroform as a solvent.

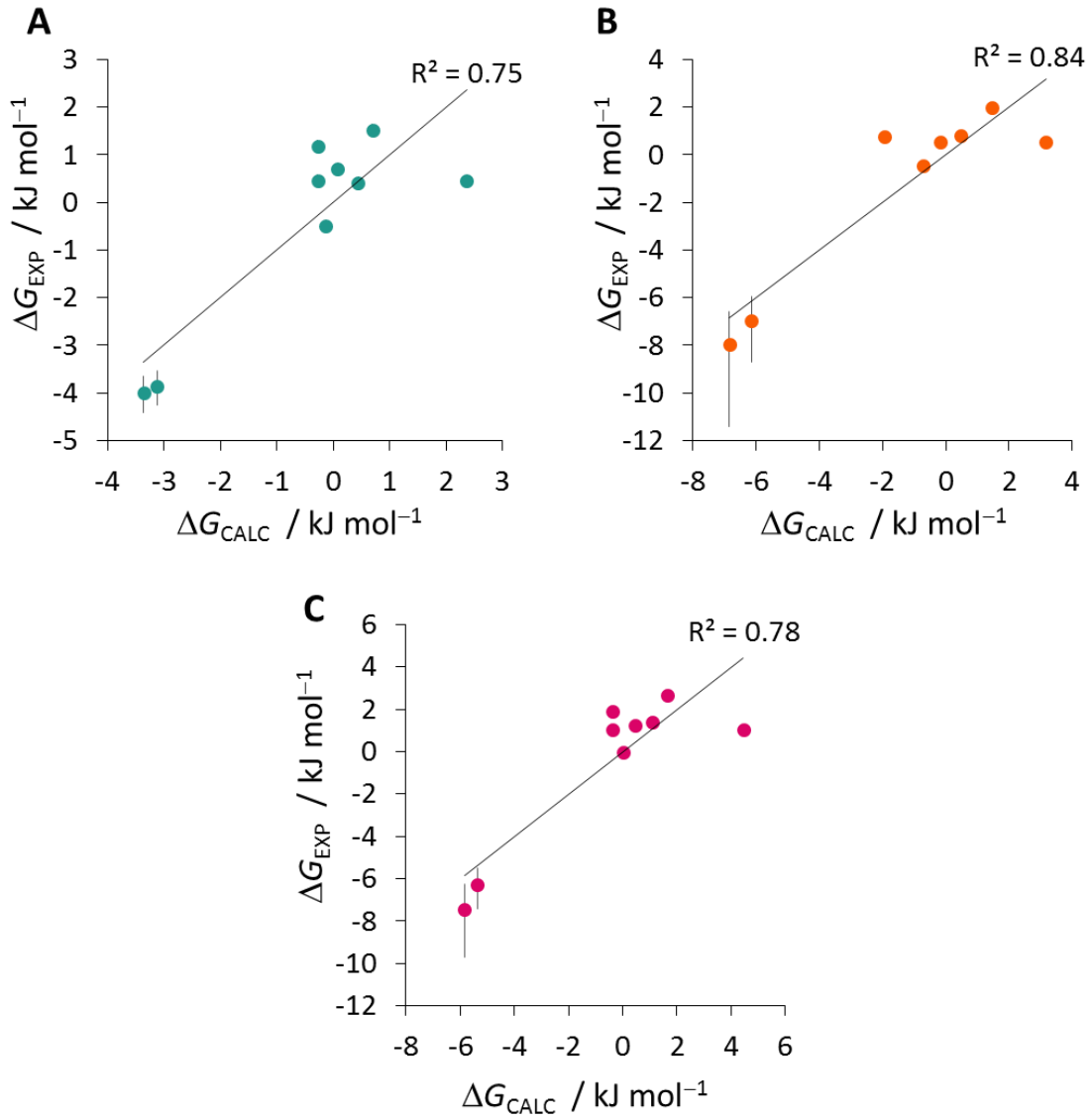

Figure 3.18 Experimental conformational free energy differences, ΔG_{EXP} measured by ^{19}F NMR spectroscopy ($CDCl_3$, 500.1 MHz, 298 K) in a range of solvents versus calculated ΔG values using an electrostatic competition solvation model for (A) **5**-1H, (B) **5**-2H and (C) **5**-3H molecular balances.

The same computational analyses were employed for the phenol-derived balances as for earlier the amine/amide system (see **Section 3.4.1**). First, NBO analysis was used to evaluate potential electron delocalisation, which found that both lone pair orbitals of the formyl oxygen were delocalised into the antibonding σ* O-H bond (**Figure 3.19A** and **B**). Additional electron delocalisation from OH oxygen lone pairs into the antibonding O-H σ* could be seen on further H-bonds in the chain (**Figure 3.19C** and **D**) in molecular balances **5**-2H and **5**-3H. Second order perturbation energies were generally higher than in the H-bonds seen in the amine/amide system (c.f. **Section 3.4.1**), with predicted energies between 45 to 75 kJ mol^{-1}. However, no correlation was observed between calculated second-order perturbation energies and experimental conformational free energies (**Figure 3.20**).

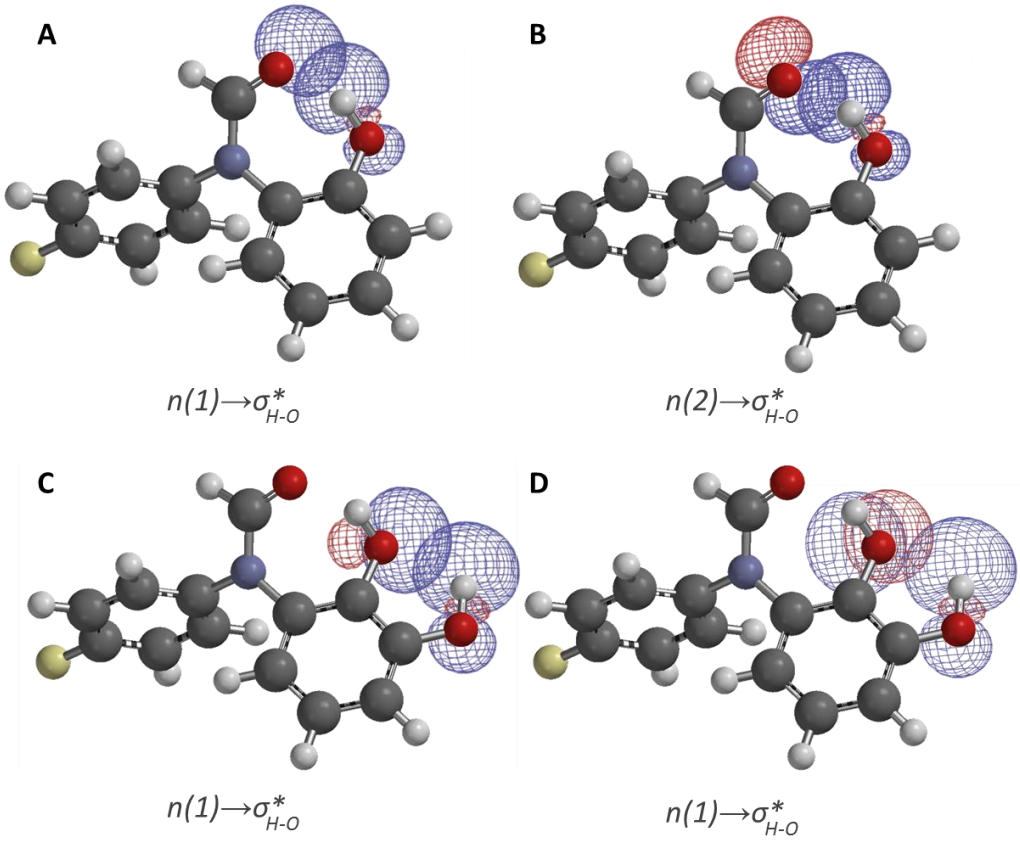

Figure 3.19 NBO interaction diagrams for (A) n(1)→σ*O-H (B) n(2)→σ*O-H seen in molecular balances containing one or more H-bond. NBO interactions for (C) n(1)→σ*O-H and (D) n(2)→σ*O-H were also present in molecular balances containing two or more H-bonds.

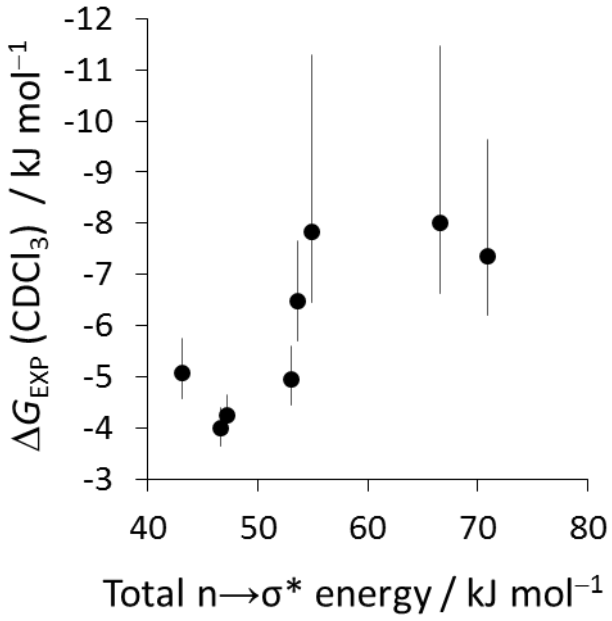

Figure 3.20 Experimental ΔG values measured by ^{19}F NMR spectroscopy ($CDCl_3$, 500.1 MHz, 298 K) versus the sum of second order perturbation energies of n→σ* electron delocalisation. Calculated using NBO 6.0.

Again as was the case for the amine/amide balances earlier, molecular orbitals were calculated on a simplified molecular balances, visually matched between the open and closed conformer, and plotted (**Figure 3.21**).

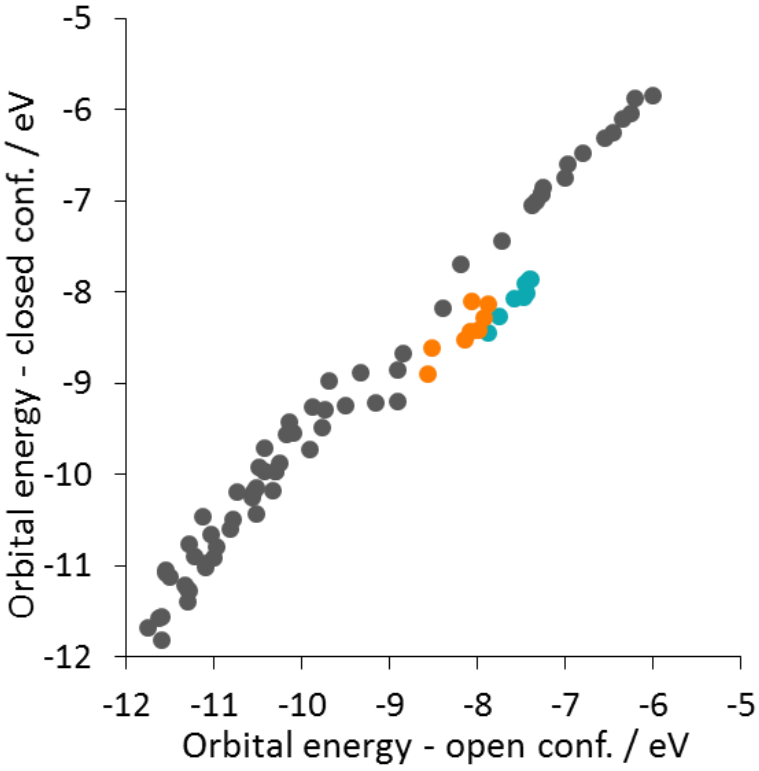

Figure 3.21 Molecular orbital energies in the closed *versus* the open conformer. Grey points are molecular orbital energies that consistently change between conformers. Orange points correspond to a through-bond resonance delocalisation and teal points correspond to an n→σ* electron delocalisation.

Two subsets of molecular orbitals fall below the grey line (as seen in chalcogen bonding in **Chapter 2**, **Figure 2.33**), implying that these orbitals are stabilised in the closed conformer compared to the open conformer. Upon examining the molecular orbitals, the orange points appeared to correspond to a through-bond delocalisation of a formyl lone pair into the aromatic ring due to increase in the planarity of the system on going from the open to the closed conformer (**Figure 3.21**). The second set of data below the grey line (teal points) correspond to stabilisation of the other lone pair. In combination with the NBO analysis, this molecular orbital analysis suggests that this second class of stabilisation may stem from an n→σ* electron delocalisation from the lone pair into the antibonding σ* O-H orbital (**Figure 3.22**).

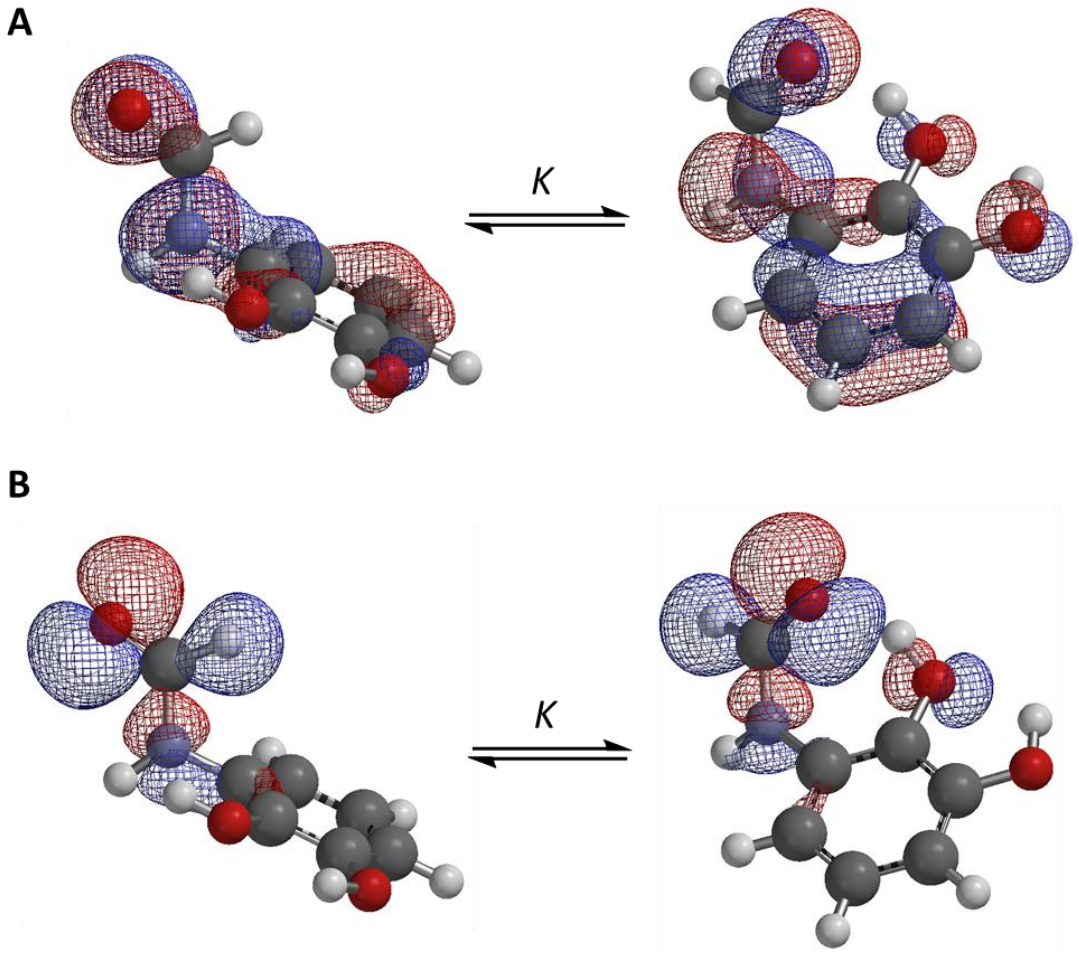

Figure 3.22 Molecular orbital diagrams corresponding to (A) orange and (B) teal points in **Figure 3.21**.

The orbital delocalisation is supported by the good correlation between the molecular orbital energies and the experimentally determined conformational free energies (R^2 = 0.89) for the molecular balances that contain one H-bond (**Figure 3.23**). The outliers were those with more than one H-bond (2H, 3H and the theoretical 4H molecular balances).

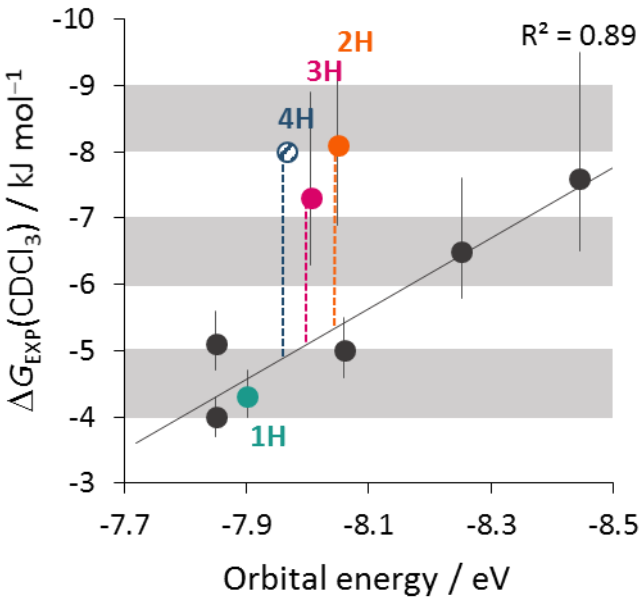

Figure 3.23 Experimental conformational free energy differences, ΔG_{EXP} measured by ^{19}F NMR spectroscopy ($CDCl_3$, 500.1 MHz, 298 K) versus molecular orbital energies containing an n→σ* electron delocalisation. MO energies calculated using Spartan '14 DFT/B3LYP/6-311G*.

Although the molecular orbital energies of molecular balances that form H-bond chains (**5**-2H, **5**-3H and **5**-4H) do not correlate well with the simple 1H-bond balances (**5**-1H, series **6**), intriguingly, the 2H, 3H and 4H all have similar n→σ * molecular orbital energies. This is in keeping with the observed experimental behaviour, where only the first H-bond of a H-bonding chain results in a more favourable conformational free energy. The results may be accounted for through a combination of electrostatics and possibly n→σ* electron delocalisation being involved in the formation of the terminal H-bond (CH···O=C), while the additional H-bond chain (non-correlating **5**-2H, **5**-3H and **5**-4H data, **Figure 3.23**) stabilises the interaction through a predominantly electrostatic contribution.

A fiSAPT analysis was performed to further evaluate the nature of the individual contributions within the system. fiSAPT showed that the CH···O=C interaction between the terminal H-bond was electrostatically, and not orbital dominated (**Figure 3.24A**). The trend in conformational free energy followed the

electron-withdrawing capability, with molecular balance **6**-*m*OH having the smallest electrostatic contribution and molecular balance **6**-*p*NO_2 having the largest. The induction component proved smaller, worth around half of the electrostatic component (**Figure 3.24B**), but significantly larger than the dispersion component (**Figure 3.24C**).

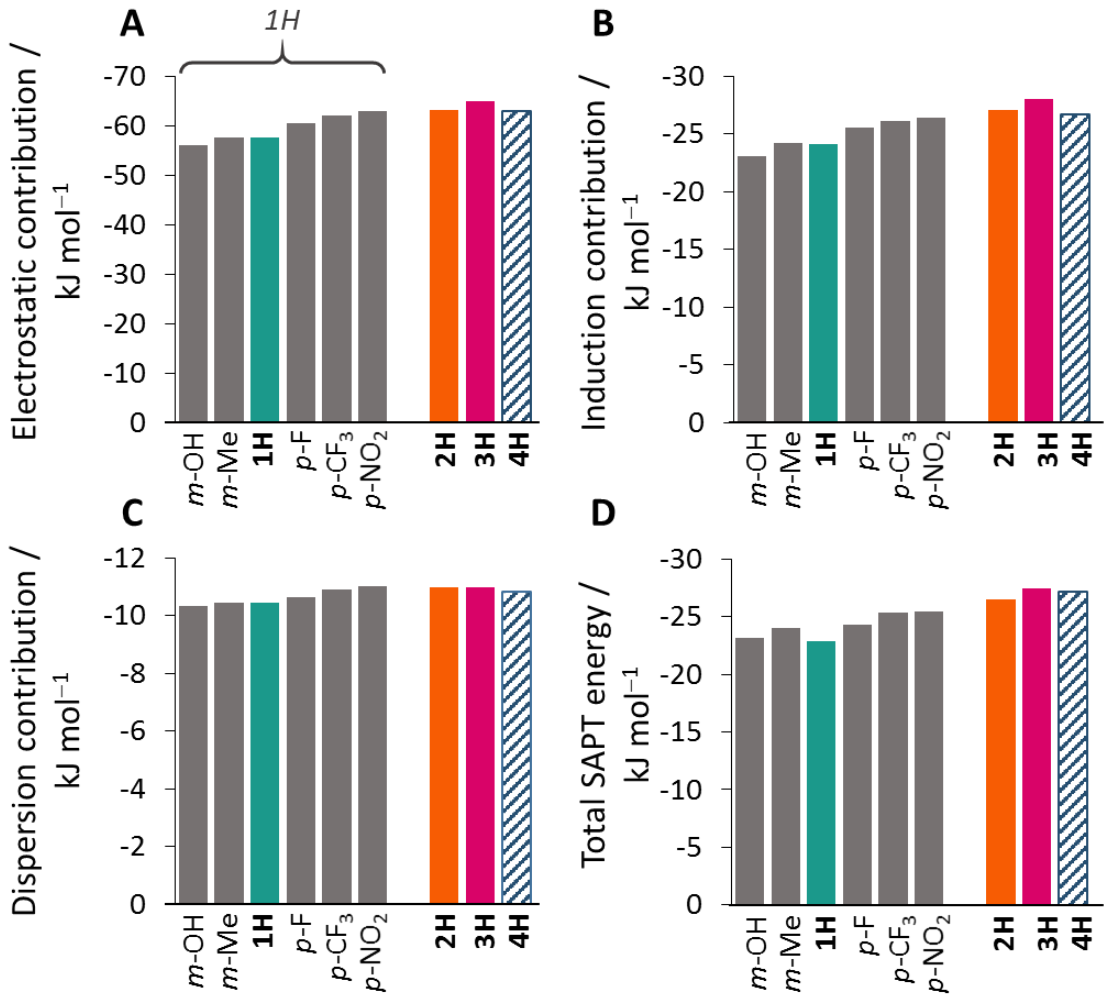

Figure 3.24 (A) Electrostatic, (B) induction and (C) dispersion components of the intramolecular H-bond. (D) The total predicted SAPT energies of the intramolecular H-bond. Calculated using PSI4 SAPT0/6-311G*.

The addition of further H-bonds to the chains as contained in molecular balances **5**-2H and **5**-3H were seen to be electrostatically dominated, although the benefit of each extra H-bond diminishes sequentially (**Figure 3.25**).

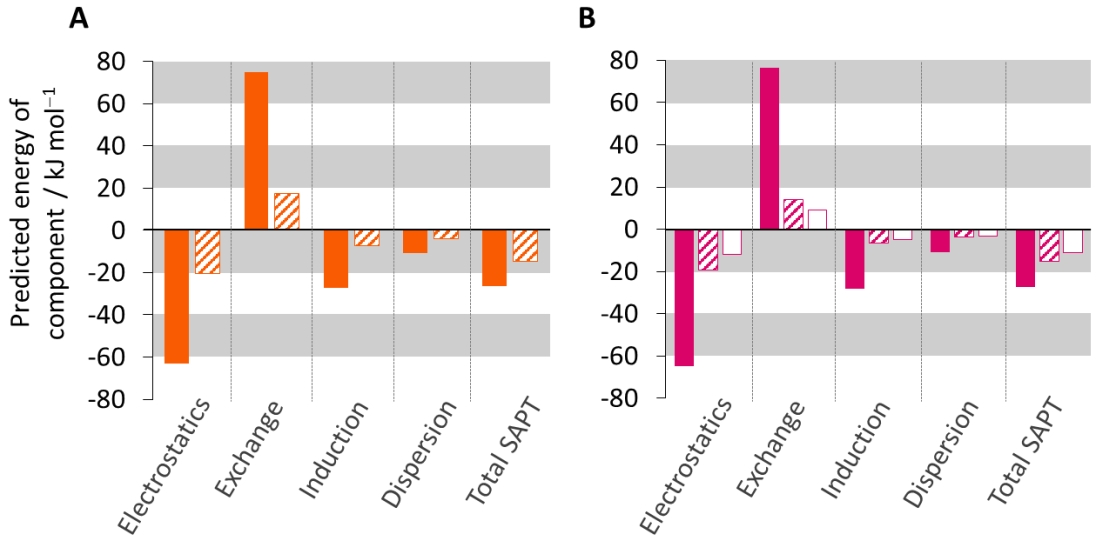

Figure 3.25 fiSAPT energetic contributions for the first (solid), second (dashed) and third (hollow) H-bonds in molecular balances (A) **5**-2H (orange) and (B) **5**-3H (pink).

The results point towards a complicated physiochemical origin in this H-bonding system, with potential contributions from orbital delocalisation, but with electrostatic behaviour generally dominating the major trends.

3.5 Conclusions and outlook

Two different H-bonding systems have been investigated computationally to try to establish their physiochemical origin. Previously obtained experimental results implied an electrostatic interaction, as has been the precedent on the nature of H-bonding. The first system, investigating H-bonding between amines and amides, was found to be dominated by electrostatics from a fiSAPT investigation. The lack of correlations between NBO second-order perturbation energies or molecular orbital energies implies that electron delocalisation does not play a major role in determining the experimental behaviour of these systems. In the second system, investigating the

interaction between an amide and OH functional groups, showed that a fully electrostatic model was unable to fully account for the experimental behaviour. Experimentally determined conformational energies could not be predicted using an electrostatic solvent competition model. Electron delocalisation was found to potentially impact the conformational stabilisation in this system. A moderate correlation was seen between molecular orbital energies containing an n→σ* electron delocalisation, but only for a subset of the data. A fiSAPT decomposition, however, showed the dominance of electrostatics, although the induction component was still significant.

Based on the computational examination of the two experimental systems presented here, H-bonding in solution certainly has a significant electrostatic component. However, there are some suggestions that it may be important to consider electron delocalisation in some special cases. The experimental data analysed here is, however limited. The molecular balance technique is unable to measure particularly weak or particularly strong interactions, and flexibility in the system may affect the conformational distribution, meaning that entropic contributions might complicate the results. Furthermore, solvent competition can make the evaluation of hydrogen-bond strengths particularly difficult in solution. In the future, new systems capable of measuring stronger H-bonds in solution should be designed, which may demonstrate higher levels of covalency than the systems investigated here.

3.6 References

1. Watson, J. D.; Crick, F. H. C. Molecular Structure of Nucleic Acids: A Structure for Deoxyribose Nucleic Acid. *Nature* **1953**, *171* (4356), 737–738.

2. Jeffrey, J. L.; Terrett, J. A.; MacMillan, D. W. C. O-H Hydrogen Bonding Promotes H-Atom Transfer from C-H Bonds for C-Alkylation of Alcohols. *Science (80).* **2015**, *349* (6255), 1532–1536.

3. Kuhn, B.; Mohr, P.; Stahl, M. Intramolecular Hydrogen Bonding in Medicinal Chemistry. *J. Med. Chem.* **2010**, *53* (6), 2601–2611.

4. Stone, A. J. Natural Bond Orbitals and the Nature of the Hydrogen Bond. *J. Phys. Chem. A* **2017**, *121* (7), 1531–1534.

5. Reed, A. E.; Curtiss, L. A.; Weinhold, F. Intermolecular Interactions from a

Natural Bond Orbital, Donor-Acceptor Viewpoint. *Chem. Rev.* **1988**, *88* (6), 899–926.

6. Bartlett, G. J.; Newberry, R. W.; VanVeller, B.; Raines, R. T.; Woolfson, D. N. Interplay of Hydrogen Bonds and N →π* Interactions in Proteins. *J. Am. Chem. Soc.* **2013**, *135* (49), 18682–18688.

7. Crabtree, R. H. Hypervalency, Secondary Bonding and Hydrogen Bonding: Siblings under the Skin. *Chem. Soc. Rev.* **2017**, *46* (6), 1720–1729.

8. Grabowski, S. J. Hydrogen and Halogen Bonds Are Ruled by the Same Mechanisms. *Phys. Chem. Chem. Phys.* **2013**, *15* (19), 7249.

9. Grabowski, S. J. What Is the Covalency of Hydrogen Bonding? *Chem. Rev.* **2011**, *111* (4), 2597–2625.

10. Pauling, L. The Nature of the Chemical Bond. Application of Results Obtained from the Quantum Mechanics and from a Theory of Paramagnetic Susceptibility to the Structure of Molecules. *J. Am. Chem. Soc.* **1931**, *53* (4), 1367–1400.

11. Desiraju, G. R. A Bond by Any Other Name. *Angew. Chem. Int. Ed.* **2011**, *50* (1), 52–59.

12. June Sutor, D. The C–H···O Hydrogen Bond in Crystals. *Nature* **1962**, *195* (4836), 68–69.

13. Taylor, R.; Kennard, O. Crystallographic Evidence for the Existence of CH···O, CH···N and CH···Cl Hydrogen Bonds. *J. Am. Chem. Soc.* **1982**, *104* (19), 5063–5070.

14. Pimentel, G. C.; McClellan, A. L. *The Hydrogen Bond*; W. H. Freeman: San Francisco, 1960.

15. Arunan, E.; Desiraju, G. R.; Klein, R. A.; Sadlej, J.; Scheiner, S.; Alkorta, I.; Clary, D. C.; Crabtree, R. H.; Dannenberg, J. J.; Hobza, P.; et al. Definition of the Hydrogen Bond (IUPAC Recommendations 2011). *Pure Appl. Chem.* **2011**, *83* (8), 1637–1641.

16. McNaught, A. D.; Wilkinson, A. *IUPAC Compendium of Chemical Terminology, 2nd Ed.*; Blackwell Scientific Publications: Oxford, **1997**.

17. Abraham, M. H.; Platts, J. A. Hydrogen Bond Structural Group Constants. *J. Org. Chem.* **2001**, *66* (10), 3484–3491.

18. Hunter, C. A. Quantifying Intermolecular Interactions: Guidelines for the Molecular Recognition Toolbox. *Angew. Chem. Int. Ed.* **2004**, *43* (40), 5310–5324.

19. Calero, C. S.; Farwer, J.; Gardiner, E. J.; Hunter, C. A.; Mackey, M.; Scuderi, S.; Thompson, S.; Vinter, J. G. Footprinting Molecular Electrostatic Potential Surfaces for Calculation of Solvation Energies. *Phys. Chem. Chem. Phys.* **2013**, *15* (41), 18262.

20. Graton, J.; Le Questel, J.-Y.; Maxwell, P.; Popelier, P. Hydrogen-Bond

Accepting Properties of New Heteroaromatic Ring Chemical Motifs: A Theoretical Study. *J. Chem. Inf. Model.* **2016**, *56* (2), 322–334.

21. Platts, J. A. Theoretical Prediction of Hydrogen Bond Donor Capacity. *Phys. Chem. Chem. Phys.* **2000**, *2* (5), 973–980.

22. Besseau, F.; Graton, J.; Berthelot, M. A Theoretical Evaluation of the pKHB and ΔH⊖HB Hydrogen-Bond Scales of Nitrogen Bases. *Chem. Eur. J.* **2008**, *14* (34), 10656–10669.

23. Mati, I. K.; Adam, C.; Cockroft, S. L. Seeing through Solvent Effects Using Molecular Balances. *Chem. Sci.* **2013**, *4* (10), 3965.

24. Kitaura, K.; Morokuma, K. A New Energy Decomposition Scheme for Molecular Interactions within the Hartree-Fock Approximation. *Int. J. Quantum Chem.* **1976**, *10* (2), 325–340.

25. Umeyama, H.; Morokuma, K. The Origin of Hydrogen Bonding. An Energy Decomposition Study. *J. Am. Chem. Soc.* **1977**, *99* (5), 1316–1332.

26. Gilli, P.; Bertolasi, V.; Ferretti, V.; Gilli, G. Evidence for Resonance-Assisted Hydrogen Bonding. 4. Covalent Nature of the Strong Homonuclear Hydrogen Bond. Study of the O-H--O System by Crystal Structure Correlation Methods. *J. Am. Chem. Soc.* **1994**, *116* (3), 909–915.

27. Grabowski, S. J. Hydrogen Bonds Assisted by π-Electron Delocalization – the Influence of External Intermolecular Interactions on Dimer of Formic Acid. *J. Phys. Org. Chem.* **2008**, *21* (7–8), 694–702.

28. Weinhold, F. Nature of H-Bonding in Clusters, Liquids, and Enzymes: An Ab Initio, Natural Bond Orbital Perspective. *J. Mol. Struct. THEOCHEM* **1997**, *398–399*, 181–197.

29. Chen, J.; McAllister, M. A.; Lee, J. K.; Houk, K. N. Short, Strong Hydrogen Bonds in the Gas Phase and in Solution: Theoretical Exploration of P K a Matching and Environmental Effects on the Strengths of Hydrogen Bonds and Their Potential Roles in Enzymatic Catalysis. *J. Org. Chem.* **1998**, *63* (14), 4611–4619.

30. Desiraju, G.; Steiner, T. *The Weak Hydrogen Bond*; Oxford University Press, **2001**.

31. Alabugin, I. V; Manoharan, M.; Peabody, S.; Weinhold, F. Electronic Basis of Improper Hydrogen Bonding: A Subtle Balance of Hyperconjugation and Rehybridization. *J. Am. Chem. Soc.* **2003**, *125* (19), 5973–5987.

32. Reed, A. E.; Curtiss, L. A.; Weinhold, F. Intermolecular Interactions from a Natural Bond Orbital, Donor-Acceptor Viewpoint. *Chem. Rev.* **1988**, *88* (6), 899–926.

33. Pacios, L. F.; Gálvez, O.; Gómez, P. C. Variation of Geometries and Electron Properties along Proton Transfer in Strong Hydrogen-Bond Complexes. *J. Chem. Phys.* **2005**, *122* (21), 214307.

34. Afonin, A. V; Vashchenko, A. V; Sigalov, M. V. Estimating the Energy of

Intramolecular Hydrogen Bonds from 1 H NMR and QTAIM Calculations. *Org. Biomol. Chem.* **2016**, *14* (47), 11199–11211.

35. Muchowska, K. B.; Adam, C.; Mati, I. K.; Cockroft, S. L. Electrostatic Modulation of Aromatic Rings via Explicit Solvation of Substituents. *J. Am. Chem. Soc.* **2013**, *135* (27), 9976–9979.

36. Dominelli-Whiteley, N.; Brown, J. J.; Muchowska, K. B.; Mati, I. K.; Adam, C.; Hubbard, T. A.; Elmi, A.; Brown, A. J.; Bell, I. A. W.; Cockroft, S. L. Strong Short-Range Cooperativity in Hydrogen-Bond Chains. *Angew. Chem. Int. Ed.* **2017**, *56* (26), 7658–7662.

37. Pascoe, D. J.; Ling, K. B.; Cockroft, S. L. The Origin of Chalcogen-Bonding Interactions. *J. Am. Chem. Soc.* **2017**, *139* (42), 15160–15167.

38. Demarque, D. P.; Merten, C. Intra- versus Intermolecular Hydrogen Bonding: Solvent-Dependent Conformational Preferences of a Common Supramolecular Binding Motif from 1 H NMR and Vibrational Circular Dichroism Spectra. *Chem. Eur. J.* **2017**, *23* (71), 17915–17922.

39. Parrish, R. M.; Gonthier, J. F.; Corminbœuf, C.; Sherrill, C. D. Communication: Practical Intramolecular Symmetry Adapted Perturbation Theory via Hartree-Fock Embedding. *J. Chem. Phys.* **2015**, *143* (5), 51103.

40. Parrish, R. M.; Parker, T. M.; Sherrill, C. D. Chemical Assignment of Symmetry-Adapted Perturbation Theory Interaction Energy Components: The Functional-Group SAPT Partition. *J. Chem. Theory Comput.* **2014**, *10* (10), 4417–4431.

41. Boyken, S. E.; Chen, Z.; Groves, B.; Langan, R. A.; Oberdorfer, G.; Ford, A.; Gilmore, J. M.; Xu, C.; DiMaio, F.; Pereira, J. H.; et al. De Novo Design of Protein Homo-Oligomers with Modular Hydrogen-Bond Network-Mediated Specificity. *Science (80-.).* **2016**, *352* (6286), 680–687.

42. Shokri, A.; Wang, Y.; O'Doherty, G. A.; Wang, X.-B.; Kass, S. R. Hydrogen-Bond Networks: Strengths of Different Types of Hydrogen Bonds and An Alternative to the Low Barrier Hydrogen-Bond Proposal. *J. Am. Chem. Soc.* **2013**, *135* (47), 17919–17924.

43. Williams, D. H. An Analysis of the Origins of a Cooperative Binding Energy of Dimerization. *Science (80-.).* **1998**, *280* (5364), 711–714.

44. Dannenberg, J. J.; Haskamp, L.; Masunov, A. Are Hydrogen Bonds Covalent or Electrostatic? A Molecular Orbital Comparison of Molecules in Electric Fields and H-Bonding Environments. *J. Phys. Chem. A* **1999**, *103* (35), 7083–7086.

Chapter 4
Geometric Sensitivity of n→π* Carbonyl Interactions

Abstract

Interactions between carbonyl groups have been shown to be important in protein structure. The physiochemical origin of carbonyl···carbonyl interactions is the subject of debate, with literature suggesting either electrostatics or n→π* electron delocalisation being the main contributors. The molecular orbital analysis presented here shows that n→π* electron delocalisation may only occur in some systems, while an electrostatic nature appears more important in other cases. Carbonyl···carbonyl interactions appear to be geometry dependent, with a change in interaction distance and angle altering the nature of the interaction.

Acknowledgements: Dr Kamila Muchowska obtained all experimental data in this chapter.

4.1 Introduction

Interactions between carbonyl groups (C=O) are important in defining biomolecular structure.[1–3] H-bonding has long been recognised as an important factor in protein structure and function,[4] whereas the important interactions between amide carbonyl groups have been recognised within the last 20 years.[1,5–7] So-called π-holes have been proposed by analogy to σ-hole interactions, to help rationalise the energetics and occurrence of carbonyl interactions. Like σ-hole interactions, π-holes are characterised by an area of positive potential where nucleophilic species can interact.[8,9] Unlike σ-bonding interactions, where a region of low electron density is found along the projected axis of a σ bond, a π-hole is located perpendicular to a π-bond. π-holes have been observed in carbonyl groups (**Figure 4.1A**), as well as other substituents such as nitro groups (**Figure 4.1B**).[10,11] Like σ-holes, π-hole are not always associated with a positively charged hole, and a region of lower electron density with a diminished local negative charge may also be referred to as a π-hole. Indeed, positively charged π-holes are typically only associated with sp^2-hybridised frameworks bound to strongly electron-withdrawing groups such as the examples shown in **Figure 4.1** below.

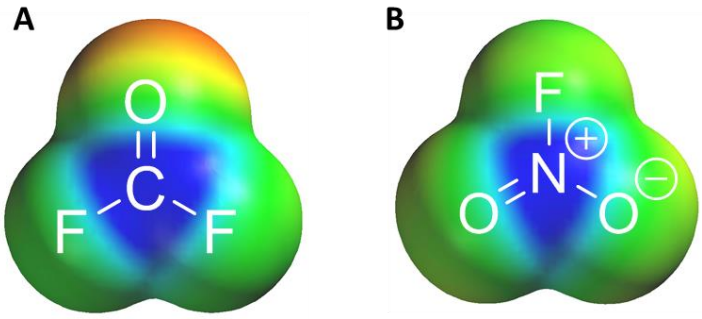

Figure 4.1 Electrostatic potentials (ESPs) of a (A) carbonyl group and (B) nitro group, where areas of blue represent a positive potential. Calculated using Spartan '14 DFT/B3LYP/6-311G*.

Ronald Raines has been at the forefront of investigating the nature of π-hole interactions, specifically focusing on the impact of such interactions in biologically relevant molecules, such as collagen.[12,13] An extensive crystal database search

performed by Raines *et al*. found that many proteins, particularly when adopting a α-helix structure, had interatomic distances between carbonyls of <3.20 Å that fall within the van der Waal radii.[14] Of proteins containing short interatomic distances between carbonyls, the interaction angle was around 100°, nearing the Bürgi-Dunitz angle of 107°, which is the most favourable interacting geometry.[15] When interatomic distances were greater than 3.20 Å, the interatomic angle between interacting carbonyls varied greatly, suggesting significantly less importance in determining the 3D structure. Raines and co-workers proposed that n→π* electron delocalisation was possible when any interatomic distance between the carbonyl groups was <3.20 Å with an interaction geometry lying between 99° and 119° (**Figure 4.2**). According to these criteria many of the ~2000 protein structures investigated were classified as containing at least a small proportion of potential n→π* interactions, while as much as 80% of all of the carbonyl interactions in eight protein structures were suggested to involve n→π* interactions. However, such geometric classifications are clearly arbitrary and provide no quantitative insight into the nature of carbonyl···carbonyl interactions.

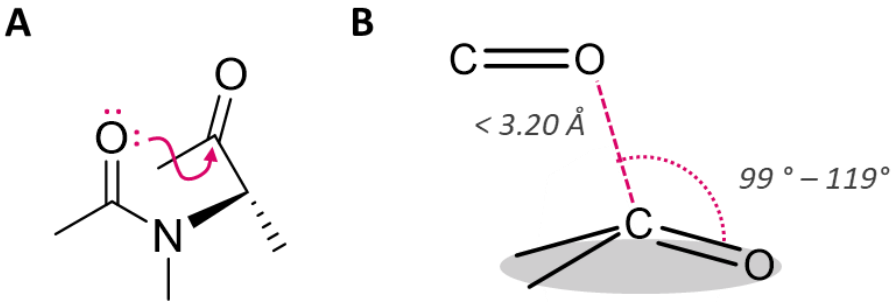

Figure 4.2 (A) Geometry of α-helices containing an n→π* electron delocalisation. (B) Geometry of carbonyl-carbonyl interactions within proteins that fulfil Raines' criteria for an n→π* electron delocalisation governed interaction.

The n→π* electron delocalisation corresponds to the stabilisation of the lone pair of the carbonyl donor into the antibonding π* C=O bond of the acceptor (**Figure 4.3**).

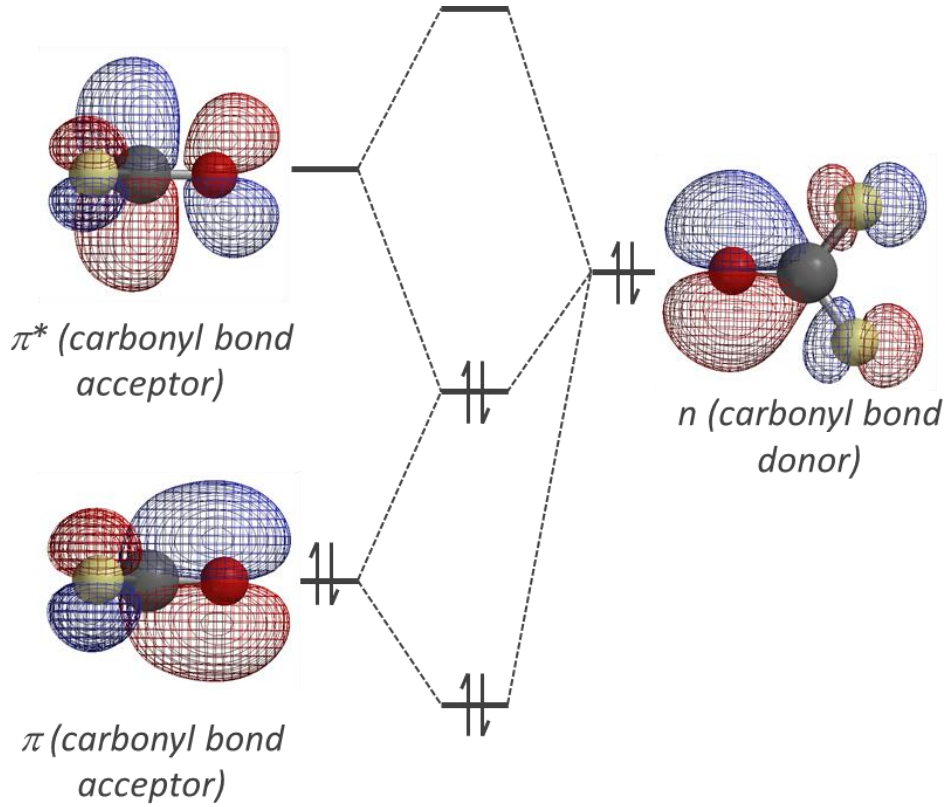

Figure 4.3 Molecular orbital diagram showing the proposed n→π* interaction, stabilising the donor lone pair (n).

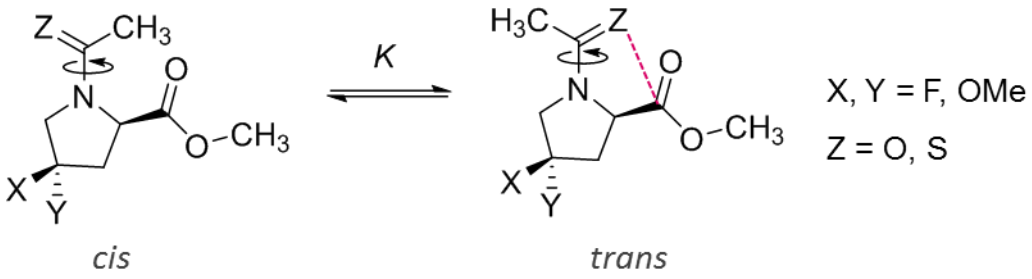

Figure 4.4 Structures of proline-based molecular balances used by Raines and co-workers to investigate the energetic significance and nature of carbonyl···carbonyl interactions.

Further to crystal database searches, Raines and co-workers have presented a molecular balance model system based on the amino acid proline to mimic the interaction observed in proteins (**Figure 4.4**).[16] Raines and co-workers used this

balance to explore the possibility of dipole-dipole, charge-charge and n→π* delocalisation using experimental equilibrium constants $K_{trans/cis}$ measured using NMR spectroscopy. Substitution of the amide with a thioamide was used to probe the nature of the interaction. The introduction of sulfur lead to an increased ratio of *trans*:*cis* conformations, which they suggested to be consistent with electron delocalisation since a sulfur atom was expected to be able to more easily donates its lone pair.[17] Furthermore, sulfur is less electronegative (and thus less polarised) than oxygen, therefore the increase in conformer ratio is the opposite of what would be expected if an electrostatic interaction was responsible for carbonyl···carbonyl interactions. The combined experimental and computational analysis of Raines and co-workers led to the conclusion that carbonyl-carbonyl interactions were dominated by an n→π* interaction,[16] a finding which has been supported by other similar systems.[18,19] The data showed that the interactions can have a large impact on conformational control, with conformational free energies of up to –5 kJ mol^{-1}. The presence of an n→π* delocalisation interaction was confirmed through NBO analysis. The energetic significance of the n→π* delocalisation was predicted to be worth around 6 kJ mol^{-1}.[16] Raines provided further evidence of electron delocalisation from the pyrimidalisation of the carbonyl acceptor group seen in X-ray crystal structures (**Figure 4.2B**). As an orbital interaction is formed, the carbonyl group goes from planar to pyramidal in shape as the sp^2 centre gains sp^3 character, which implies significant covalent character.

A number of other investigation by Raines have come to the same conclusion using similar techniques, particularly by using NBO to demonstrate the n→π* delocalisation present in carbonyl···carbonyl interactions.[20–22]

Meanwhile, Diederich and co-workers have used a molecular balance based on Wilcox's original design[23] (as shown in **Chapter 2**) to probe the nature of the carbonyl···carbonyl interactions[24] (**Figure 4.5**) using a design derived from their earlier investigation of F···carbonyl interactions.[25] A double mutant cycle was used to dissect out the energetic significance of carbonyl···carbonyl interactions.[26] The interaction was found to be the strongest in C_6D_6 at –2.7 kJ mol^{-1}, while the conformational free energy was disturbed when using chlorinated solvents, such as

$CDCl_3$ (–1.5 kJ mol^{-1}) and CD_2Cl_2 (–1.2 kJ mol^{-1}). They proposed that the interaction must therefore be driven by dipoles, as chlorinated solvents have a high dipole moment, and therefore will outcompete the interaction between carbonyl groups and shift the equilibrium towards the unfolded conformer. Diederich's findings have been supported by energy decomposition analyses showing that electrostatics are the governing force in carbonyl···carbonyl interactions.[27]

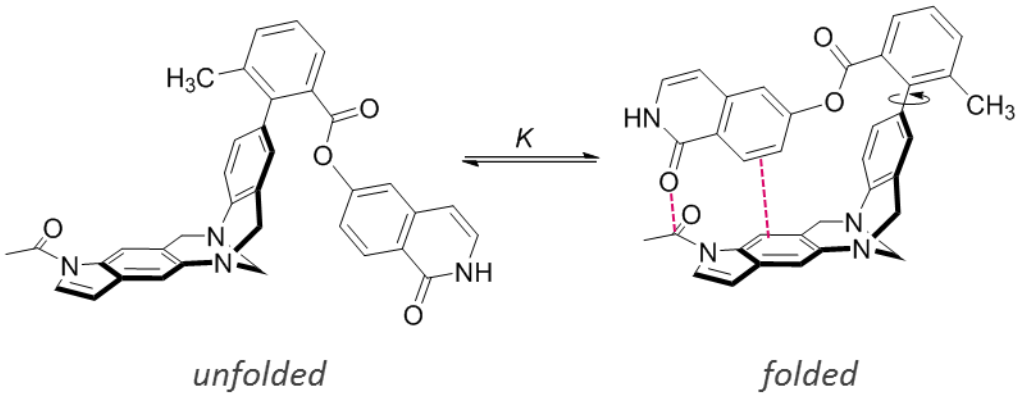

Figure 4.5 Structure of the Wilcox molecular balance used by Diederich and co-workers to investigate carbonyl···carbonyl interactions.

4.1 Aims

Raines and Diederich attributed different underlying physicochemical causes to the origin of carbonyl···carbonyl interactions, either an n→π* electron delocalisation or electrostatics have been proposed respectively. This chapter aims to explore the reasons for this difference and to reconcile the conclusions drawn. Additional theoretical investigation into the nature of these interactions will be performed using a series of molecular balances previously synthesised within the Cockroft group. A combined analysis of these three classes of molecular balances will examine similarities and differences to try and determine the energetic significance of n→π* electron delocalisation in carbonyl···carbonyl interactions.

4.2 Results and discussion

All experimental results in this chapter were obtained by Dr Kamila Muchowska.[28] The molecular balances that she used to measure the energetic significance of carbonyl···carbonyl interactions in solution are related to the designs introduced in **Chapters 2** and **3** have been (**Figure 4.6**).

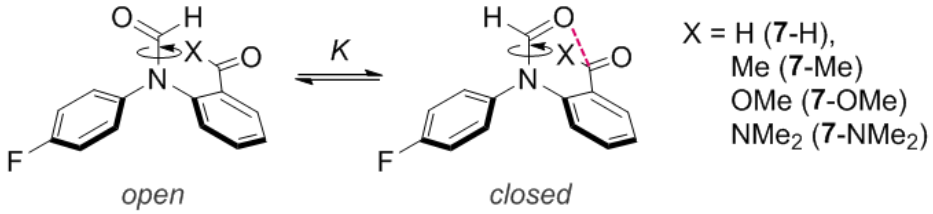

Figure 4.6 Structures of molecular balances used in this study.

Conformational free energies were measured in a range of solvents (a selection is shown in **Figure 4.7**). As was seen in chalcogen bonding in **Chapter 2**, the interaction showed a surprising insensitivity to solvent, with the exception of methanol-d_4, which could be a sign of a significant electron delocalisation interaction.[29] The result in methanol-d_4 most likely arises from its strong H-bond donor properties, which mean that carbonyl···DO solvent interactions compete strongly with the carbonyl···carbonyl interactions.

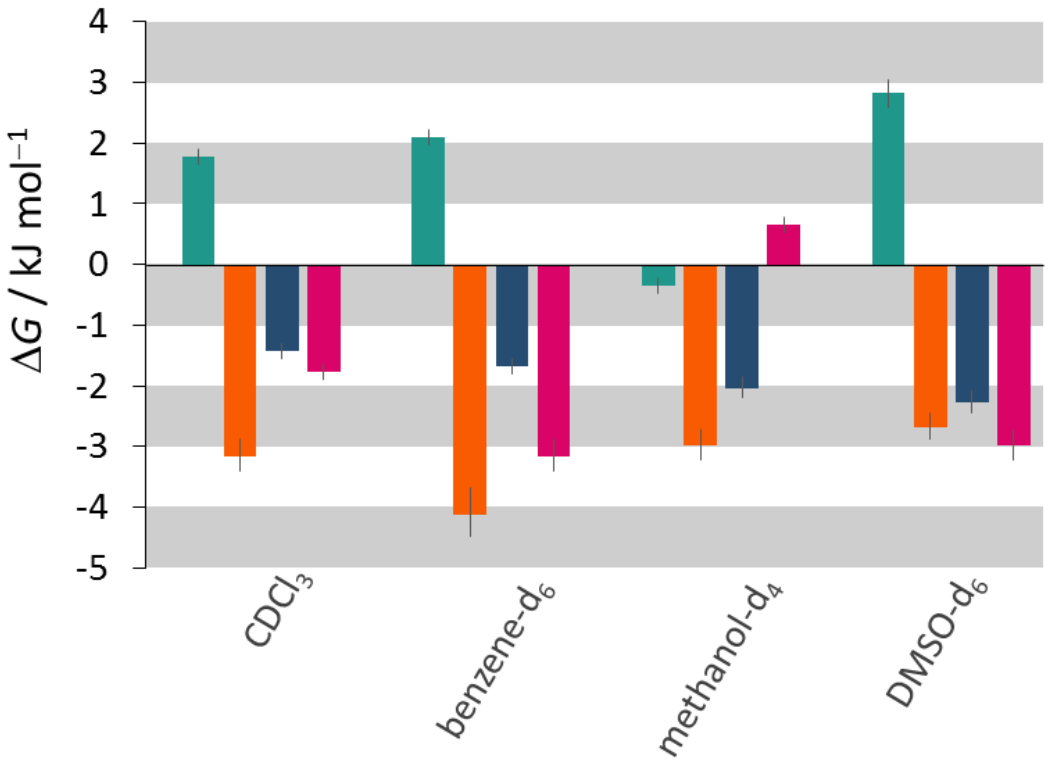

Figure 4.7 Experimentally measured conformational free energies in a select range of solvents for molecular balance **7**-H (teal), **7**-Me (orange), **7**-OMe (blue) and **7**-NMe_2 (pink).

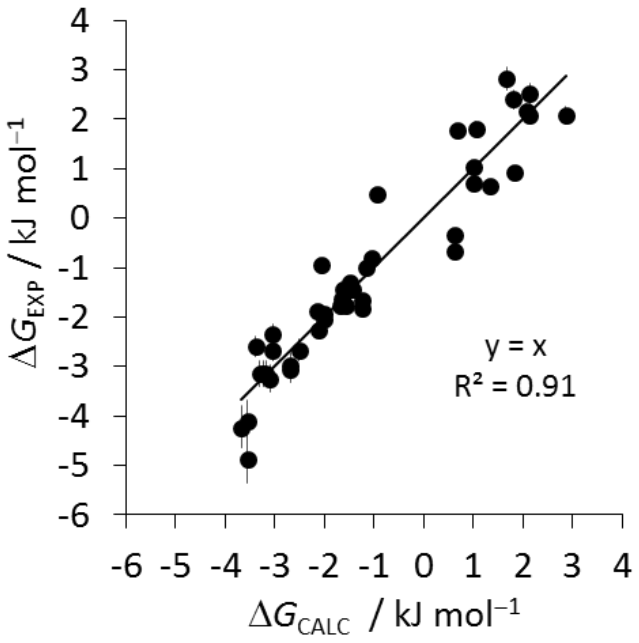

Figure 4.8 Calculated conformational free energies using the Hunter solvation model shown in **Equation 4.1** versus experimentally measured conformational free energies measured by $^{19}F\{^{1}H\}$ NMR (376.5 MHz, 298 K) in a range of solvents for all molecular balances.

The conformational free energies were well-predicted well by the simple empirical electrostatic solvation model used in **Chapter 3** (**Equation 4.1**) giving a y = x fit (**Figure 4.8**).

$$\Delta G_{calc} = \Delta\alpha\beta_s + \Delta\beta\alpha_s + \Delta E \qquad \textbf{(4.1)}$$

Such an electrostatically based prediction was unexpected given the previous report of electron delocalisation within carbonyl···carbonyl interactions.

The observation of solvent independence *versus* the ability to predict conformational free energies using an electrostatic solvation model appear in conflict regarding the underlying nature of the interaction. Thus, computational chemistry was employed to seek an explanation for these apparently contradictory characteristics.

Previous research in the Cockroft group has found the B3LYP methodology gave good predictions of the conformational free energies of formamide molecular balances irrespective of the underlying origin of the interaction, as was shown in

Chapters 2 and **3**. Accordingly, structures of the molecular balances were minimised using B3LYP/6-31G* before performing Natural Bond Orbital (NBO) analysis. Surprisingly, no orbital interaction was observed between the formyl oxygen and the *ortho*-carbonyl acceptor that might be consistent with the proposed n→π* electron delocalisation. To further investigate the possibility of the involvement of electron delocalisation, crystal structures of molecular balances **7**-H and **7**-Me were also examined using the NBO approach. This time, the NBO analysis suggested that electron delocalisation *did* occur between the formyl lone pairs and the π* antibonding orbital of the *ortho*-carbonyl in molecular balance **7**-Me (**Figure 4.9**) with an overall energetic contribution of around 6.5 kJ mol^{-1}, whereas no such electron delocalisation was found in the crystal structure of molecular balance **7**-H.

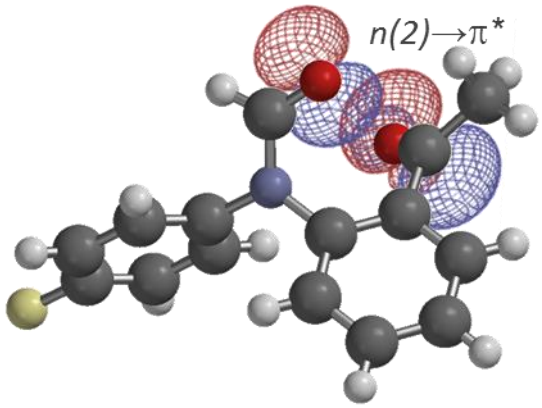

Figure 4.9 Diagram of predicted electron delocalisation from the lone pair of the oxygen formyl into the antibonding π* bond of the C=O group of compound **7**-Me. Calculated from the crystal structure geometry using a single point energy using Gaussian '09 and NBO 6.0.

Clearly, there were important differences between the computationally minimised (B3LYP/6-31G*) structures and the crystal structure of compound **7**-Me. Therefore, further geometry minimisations were performed using the ωB97X-D methodology to include a dispersion correction. The choice of functionals was made based on previous calculations performed in the group to ensure the values were comparable. While both functionals appeared to perform well, it is important to consider that not only

dispersion is altered in this change, moving from a short-ranged (B3LYP) to a long range (ωB97X-D) functional. In future investigations, the B3LYP-D3 functional, for example, may be more appropriate to ensure consistency between a DFT to DFT-D result to make the comparisons more meaningful. The new minimised structures displayed marginally reduced distances between the formyl and carbonyl groups compared to the B3LYP methodology, and more closely reflected the crystal structure (**Figure 4.10**).

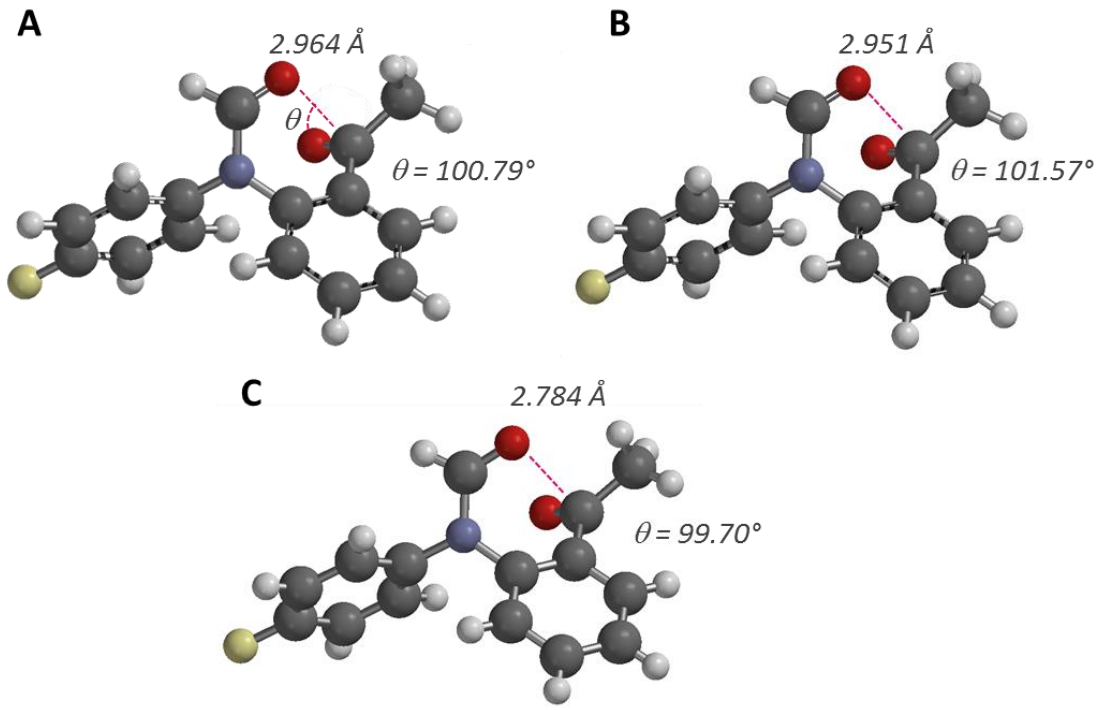

Figure 4.10 Structures of molecular balance **7**-Me (A) minimised using DFT/B3LYP/6-31G*, (B) minimised using DFT/ωB97X-D/6-31G* and (C) crystal structure. Angle θ is defined as the O···C=O angle.

NBO analysis on ωB97X-D minimised structures of all balances only revealed n→π* electron delocalisation to occur **7**-Me worth 6.3 kJ mol^{-1}. Given the findings in previous chapters, second-order perturbation energies do not translate into equivalent changes in the conformational free energies, meaning that this n→π* delocalisation is likely to play a fairly minor role in determining the experimental behaviour.

The limited role of electron delocalisation was further confirmed through a molecular orbital analysis, using the same methodology as seen in **Chapters 2** and **3**. Upon plotting the visually matched molecular orbitals of truncated molecular balance systems (in which the 4-fluorophenyl moiety was replaced with a proton), no molecular orbitals that obviously represented n→π* delocalisation were found. No other molecular orbitals were found to stabilise the closed conformer over the open conformer, as demonstrated by the good fit of all the orbitals to a y = x graph (**Figure 4.11**). This linear relationship confirmed that the carbonyl···carbonyl interactions observed in these molecular balances are not governed by an n→π* electron delocalisation (**Figure 4.11**).

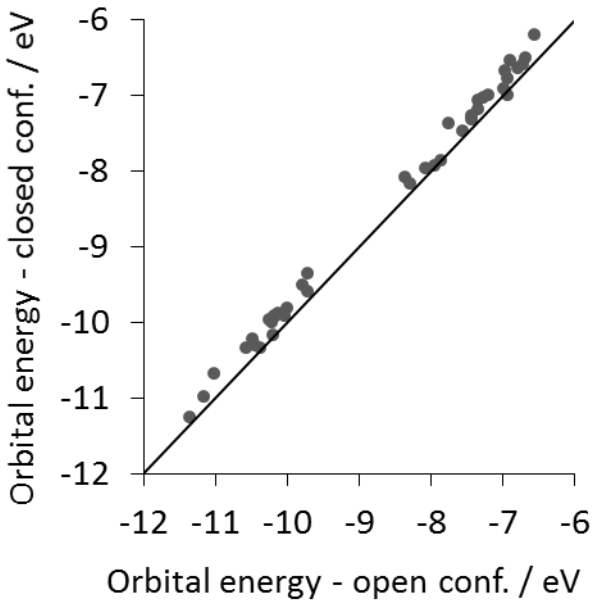

Figure 4.11 Molecular orbital energies in the closed *versus* the open conformer. A straight line of y = x shows no molecular orbitals offer extra stabilisation in the closed compared to the open conformer. Molecular orbital energies calculated using Spartan '14 DFT/B3LYP/6-31G*.

The occurrence of pyramidalisation of the carbonyl acceptor groups was studied in both the crystal structures (where available) and the minimised structures. As previously noted, such pyramidalisation of the carbonyl would provide evidence of a

potential n→π* electron delocalisation. No pyramidalisation of the carbonyl was observed in any of the molecular balances, further suggesting an n→π* electron delocalisation model may not be appropriate to describe carbonyl···carbonyl interactions in this system.

A fiSAPT analysis was used to investigate the components of the interaction in each molecular balance. The basis set used in the fiSAPT calculations was varied to try and improve the accuracy of the calculation. To keep computational costs low, all structures were first minimised using the B3LYP method with 6-31G* basis set. The first, and computationally cheapest, fiSAPT analysis (**Figure 4.12A**) used the SAPT(0) methodology with 6-31G* basis set. Results obtained using the 6-31G* basis set gave reasonable predictions of the experimentally observed trend (**Figure 4.12A**). However, different basis sets were explored due to known inaccuracies of the 6-31G*basis set.[30]

The basis set jun-cc-pvdz was used as an alternative basis set to 6-31G*. jun-cc-pvdz is another double-ζ basis set, but has a number of improvements over 6-31G* that may impact the SAPT0 model predictions at only moderate computational cost (**Figure 4.12B**). The introduction of core correlation ("cc" part of jun-cc-pvdz) accounts for more electron interactions, and therefore improves prediction compared to the Pople functions of 6-31G* (that accounts for fewer interactions between electrons). Despite the more accurate basis set, no improvement was seen in the overall prediction of the total SAPT interaction energy *versus* experimental data (**Figure 4.12B**). The individual components also seemed largely unaffected using the larger basis set, with only minor changes from the 6-31G* basis set.

The much larger, quadruple-ζ aug-cc-pvqz basis set was subsequently used, which also includes *f* and *g* electron shells (**Figure 4.12C**). Using this basis set is computationally expensive, but the accuracy should be improved. However, the choice of basis set does not allow direct comparison as both the ζ value and the further polarisation functions moving from jun- to aug- means there is not only one direct change to compare. A more appropriate change would be to the basis set jun-cc-pvqz. This large basis set increased the prediction of the overall SAPT interaction energy primarily due to the increase in the contribution from van der Waals dispersion forces.

Inaccuracies in the fiSAPT decomposition probably arise from the limit of the SAPT0 method. Unfortunately, SAPT0 is the only available method for intramolecular interactions within the PSI4 software. An extensive review of SAPT methodologies and basis sets revealed that the larger and more complicated the basis set does not always equal greater accuracy.[32] Therefore, a more accurate, but smaller basis set could exist for this specific system. However, it is unrealistic to study all basis sets, and the most efficient computational method found here was the simple 6-31G* basis set, given that higher levels of theory yielded only small improvement, but with much higher computational costs.

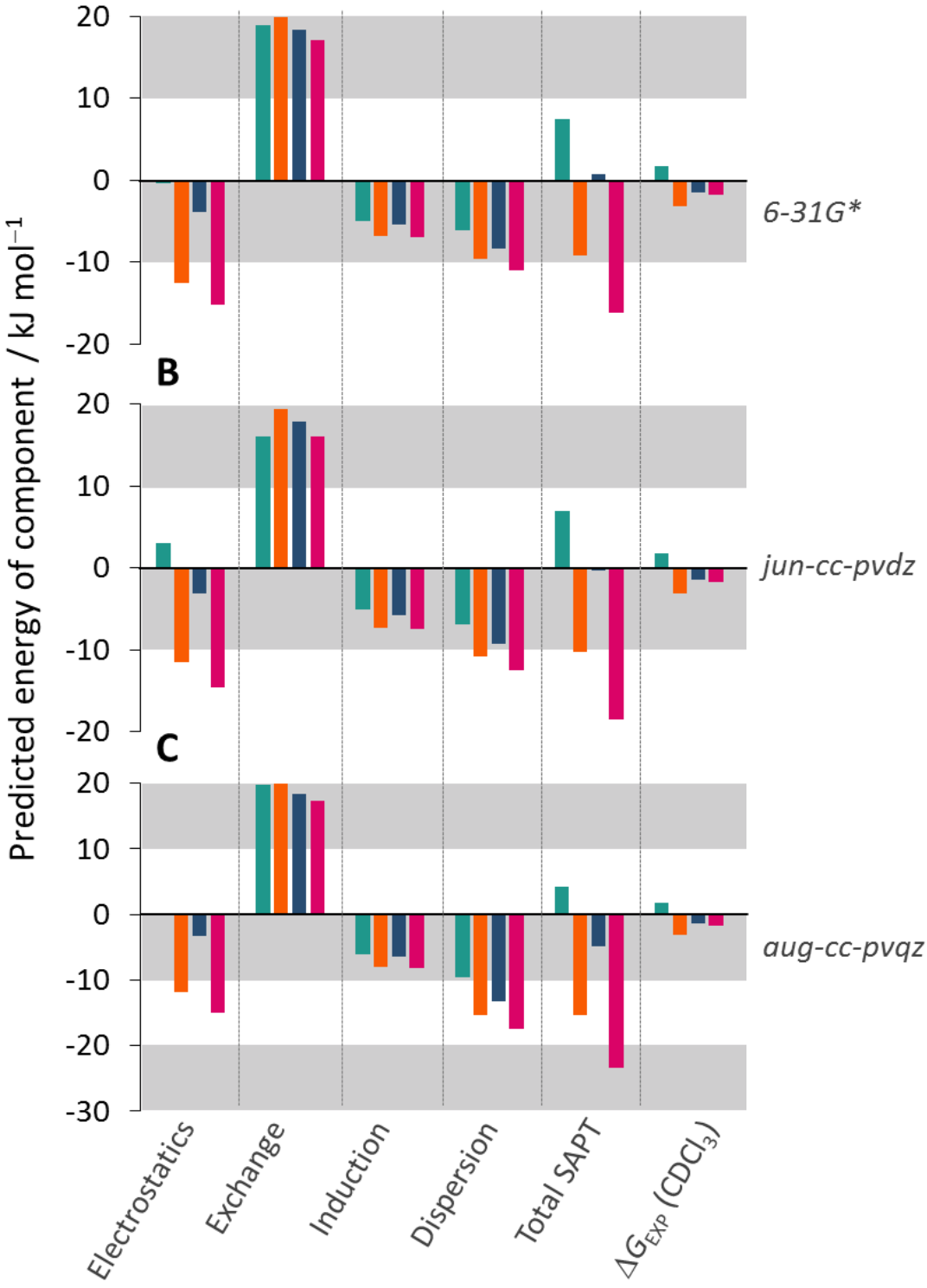

Figure 4.12 Predicted fiSAPT contributions for molecular balances **7**-H (teal), **7**-Me (orange), **7**-OMe (blue) and **7**-NMe_2 (pink) using DFT/B3LYP/6-31G* minimised geometries. Calculated using the methodology SAPT0 and basis set (A) 6-31G*, (B) jun-cc-pvdz and (C) aug-cc-pvqz.

Since different NBOs were observed in molecular balances that were minimised with or without dispersion corrections, a further fiSAPT analysis was performed on the ωB97X-D/6-31G* minimised structures that included dispersion correction. This resulted in minor changes to the components and total SAPT interaction energy compared to the B3LYP-minimised structures (**Figure 4.13**).

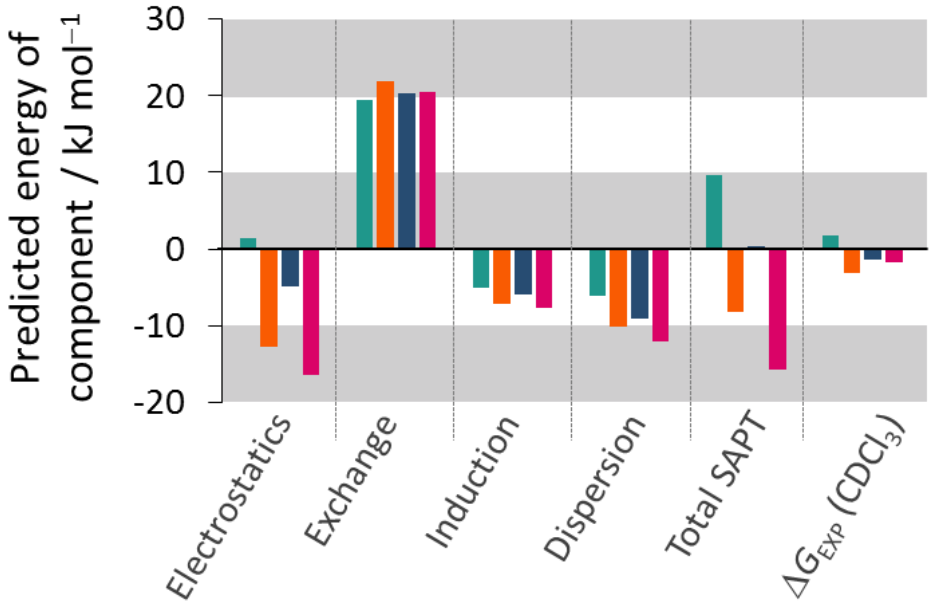

Figure 4.13 Predicted fiSAPT contributions for molecular balances **7**-H (teal), **7**-Me (orange), **7**-OMe (blue) and **7**-NMe_2 (pink) using DFT/ωB97X-D/6-31G* minimised geometries. Calculated using PSI4 SAPT0/6-31G*.

Of each of the four energy components, the pattern in the electrostatic energies most closely resembled the pattern in the experimental behaviour (**Figure 4.13** left *versus* right). Across all basis sets and geometries, the electrostatic component of the system was found to vary significantly depending on the geometry. In molecular balance **7**-H, where the *o*-CHO substituent is flipped (**Figure 4.14A**) compared to the other molecular balances in series **7** (**Figure 4.14B**, **C** and **D**) the electrostatic component of the interaction is actually repulsive, since the local dipoles of the interacting carbonyl groups point in the same direction. Conversely, all other molecular balances have an attractive electrostatic component and the local dipoles are aligned in an anti-parallel

arrangement (**Figure 4.13**). The other attractive components favouring the closed conformation in molecular balances **7**-Me, **7**-OMe and **7**-NMe_2 come from induction and dispersion (**Figure 4.12**). The dispersion component appears to be the next largest contributor to the attractive part of the interaction, particularly when predicted using larger basis sets. Induction was near constant across all geometries and basis sets. The exchange (repulsive) term was the largest, outcompeting electrostatics in all molecular balances (**Figures 4.12** and **4.13**).

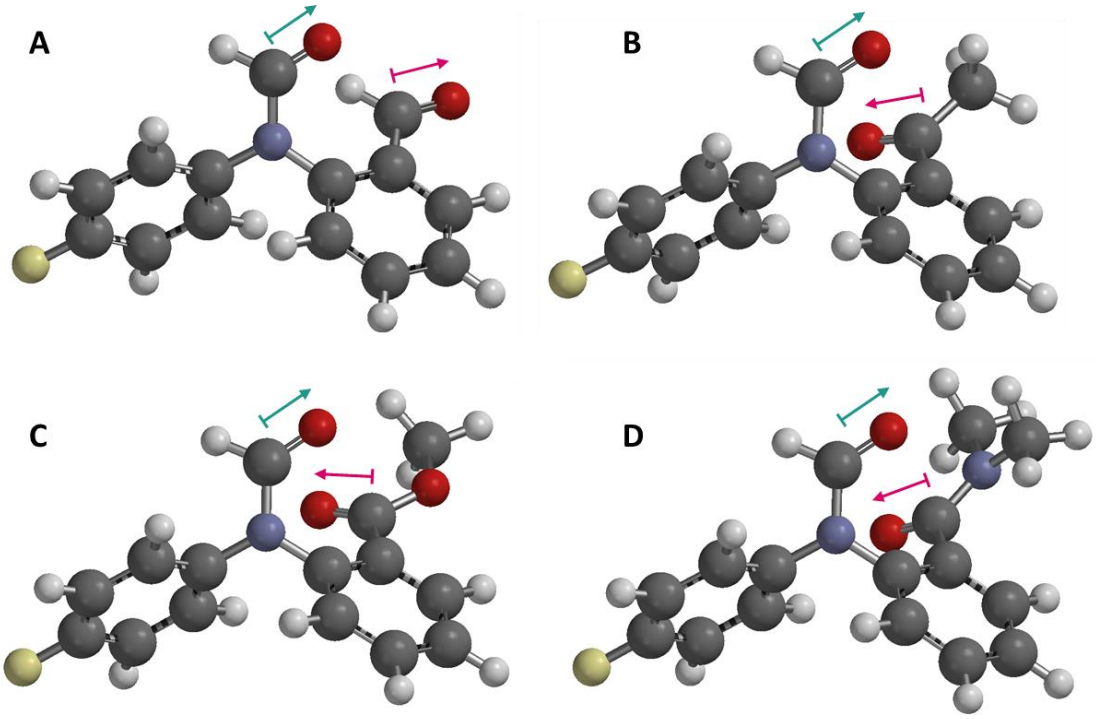

Figure 4.14 Minimised structures of molecular balances (A) **7**-H, (B) **7**-Me, (C) **7**-OMe and (D) **7**-NMe_2. Dipoles are shown for the donor (teal) and acceptor (pink). The orientation of the *ortho*-carbonyl acceptor group is different in **7**-H (A) than the other molecular balances resulting in repulsive dipoles. Minimised using Spartan '14 DFT/B3LYP/6-31G*.

The combination of NBO and fiSAPT calculations suggest that electrostatics are the governing factor in the carbonyl···carbonyl interactions in these formamide-based molecular balances, agreeing with the findings derived by Diederich from his unrelated balance system.[33] For compound **7**-Me, which possessed the most favourable

carbonyl···carbonyl interactions, orbital delocalisation may also play an additional role, but not all of the methods employed suggested this. The prediction of conformational free energies using an empirical electrostatic solvation model showed that the interactions could be accurately predicted using electrostatic terms (H-bond donor and acceptor abilities). The lack of electron delocalisation as seen by NBO and MO analyses of molecular balances, and the larger contribution from electrostatics predicted by fiSAPT further support a predominantly electrostatic origin of the carbonyl interactions in these systems.

A SAPT analysis of a simplified dimer version of Diederich's Wilcox molecular balance system **10** (**Figure 15A**) agreed with the data obtained for the formyl molecular balances. The full molecular balance structure was first minimised, then the geometry of the two carbonyl groups was used to investigate the components of the interaction between the two (**Figure 15B**). The results demonstrated the interaction was dominated by electrostatics with smaller contributions from induction and dispersion to form the overall favourable interaction.[33]

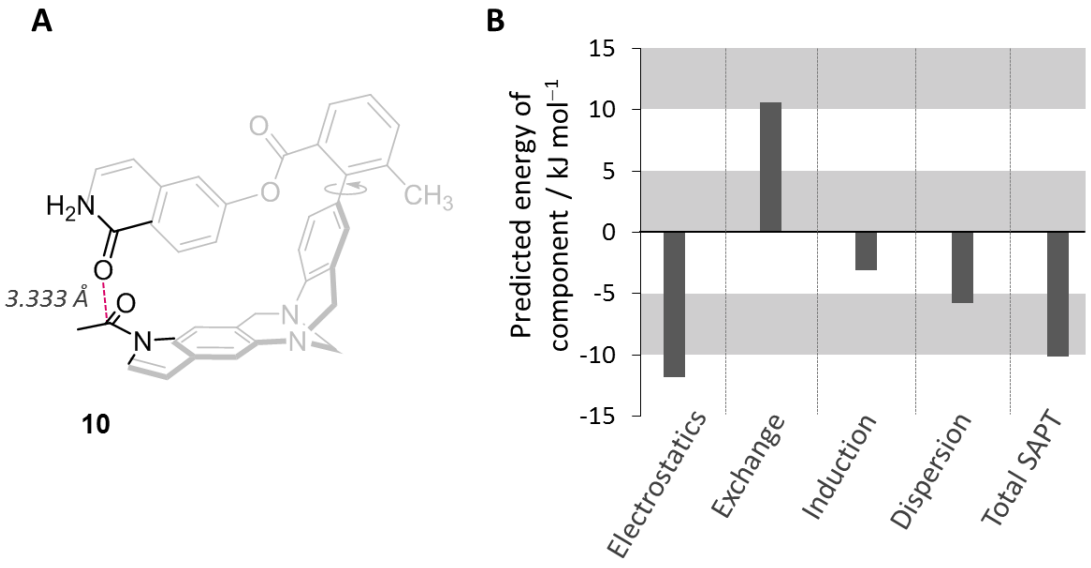

Figure 4.15 (A) Structure of the two interacting dimers (**10**) used in the SAPT analysis of carbonyl···carbonyl interactions in Diederich's Wilcox molecular balance. (B) The energetic contributions of each component of the carbonyl··carbonyl interaction shown in (A). Calculated using SAPT0/6-31G*.

4.3 Proline-based molecular balances to probe carbonyl···carbonyl interactions

The same computational analysis as performed on the Cockroft group balances was applied to Raines' proline-based balances (**Figure 4.16**). Raines has supported an n→π* electron delocalisation model as being important in carbonyl···carbonyl interactions over the last decade.[34] However, only qualitative evidence of such delocalisation has been demonstrated to date (for example, the use of arbitrary geometric descriptors, as discussed above[14]).

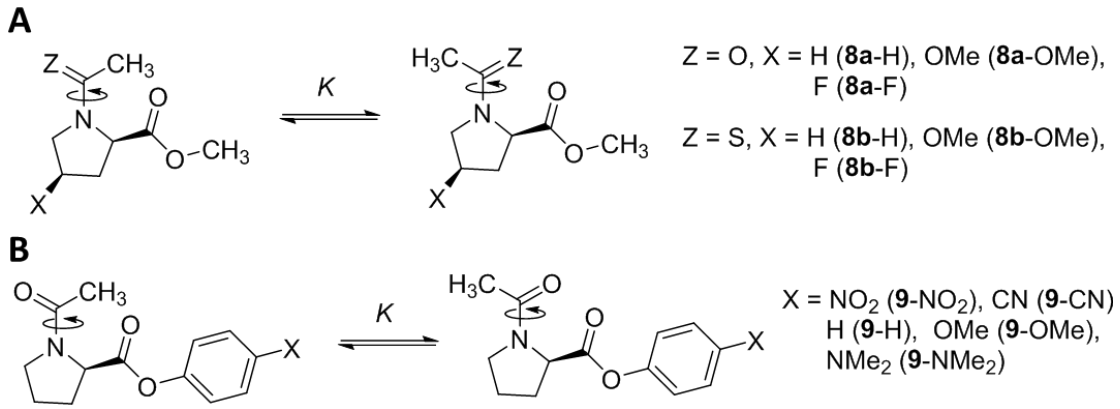

Figure 4.16 Molecular balance structures of series (A) **8** that vary electronics of the proline ring and (B) **9** that vary the electronics of the carbonyl acceptor studied in this section.

Conformational equilibrium constants for series **8** have previously been measured in D_2O,[35] while those for series **9** has been measured in $CDCl_3$.[34] As these solvents have very different properties, the two series will be considered separately. Molecular balances from series **8** (**Figure 4.16A**) were minimised using the B3LYP methodology and 6-31G* basis set to provide a direct comparison to those studied in the previous section. NBO analysis showed n→π* electron delocalisation in all molecular balances from series **8**, with second-order perturbation energy calculations suggesting that they were worth between 8 and 11 kJ mol^{-1} (**Figure 4.17**). The predicted energetic significance of this n→π* delocalisation increased on changing from an oxygen (amide) (**Figure 4.17**, solid) donor to a sulfur (thioamide) donor (**Figure 4.17**, dashed).

Unfortunately, these values showed no correlation to the experimentally measured conformational free energies.

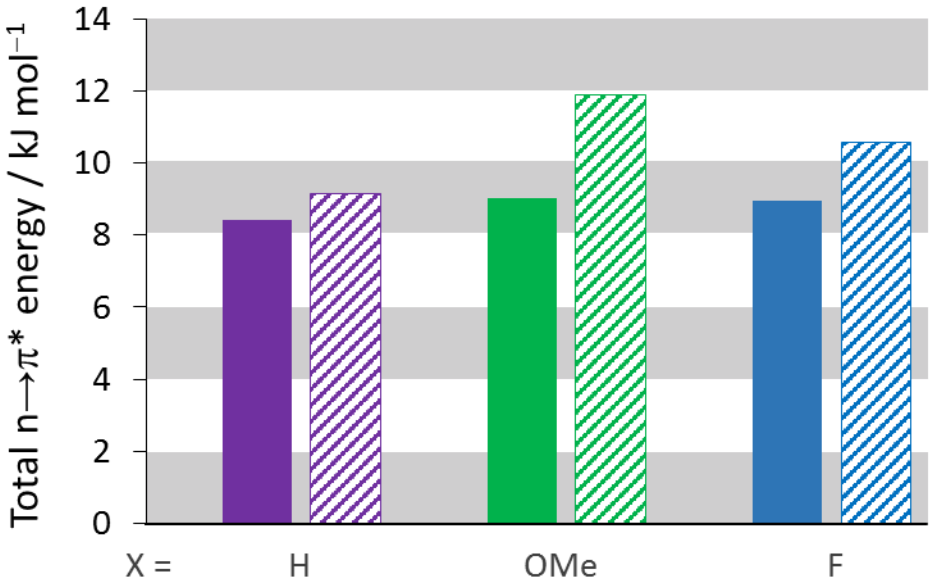

Figure 4.17 Predicted stabilisation energies of the n→π* electron delocalisations in Raines' proline molecular balances. Amide donors are shown as solid and thioamide donors are shown as dashed. NBO calculations performed using Gaussian '09 and NBO 6.0 B3LYP/6-31G*.

A fiSAPT decomposition was performed on the molecular balances in series **8**. The relative contributions from each component appeared to be very different from the formyl molecular balances used to study carbonyl···carbonyl interactions in the Cockroft group (**Figure 4.13** *vs.* **Figure 4.18**). Surprisingly, the SAPT0 methodology predicted the electrostatic component to be strongly repulsive. Only the induction and dispersion components were predicted to be favourable, with the induction term being the largest favourable contributor to the interaction (**Figure 4.18**). The same trends were noted in the thioamide-containing molecular balances of series **8b**, only with more extreme energetic contributions (**Figure 4.18**, dashed). The overall total SAPT energies of the carbonyl···carbonyl interactions are consistent with intramolecular strain. However, no meaningful correlation could be found with the experimental data.

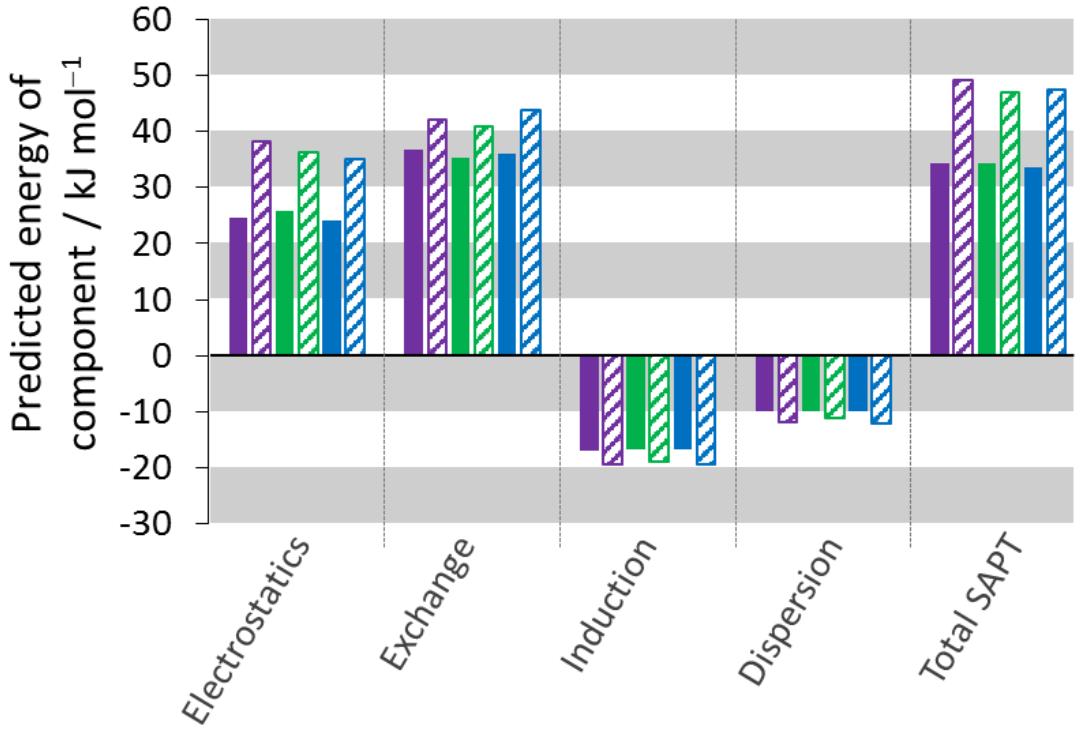

Figure 4.18 Predicted fiSAPT contributions in molecular balances **8a**-H (solid purple), **8b**-H (dashed purple), **8a**-OMe (solid green), **8b**-OMe (dashed green), **8a**-F (solid blue) and **8b**-F (dashed blue). fiSAPT contributions calculated using PSI4 SAPT0/6-31G*.

Finally, a molecular orbital analysis was performed visually matching the MOs between the *cis* and *trans* conformations. The analysis of molecular orbitals showed that no molecular orbitals offered greater stabilisation in the *trans* conformer, with no orbitals falling below the 1:1 correlation (**Figure 4.19**).

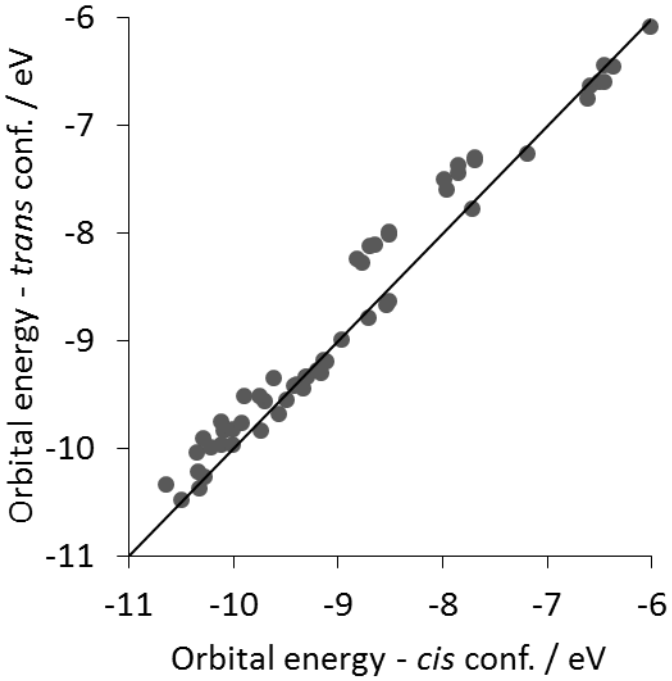

Figure 4.19 Correlation of all molecular orbital energies between HOMO and HOMO{-9} in the open versus closed conformer of simplified molecular balances. No points are seen below the grey line, showing no molecular orbitals stabilised in the *trans* conformer compared to the *cis*. Molecular orbital energies calculated using Spartan '14 DFT/B3LYP/6-31G*.

The balances in series **9** (**Figure 4.16B**) were analysed in the same manner as the series **8** balances. Raines has proposed that these molecular balances are governed by an n→π* electron delocalisation. However, Raines' analysis found that there was a linear correlation with the experimentally measured conformational free energies and Hammett constants of the *para* position (**Figure 4.20**).[34]

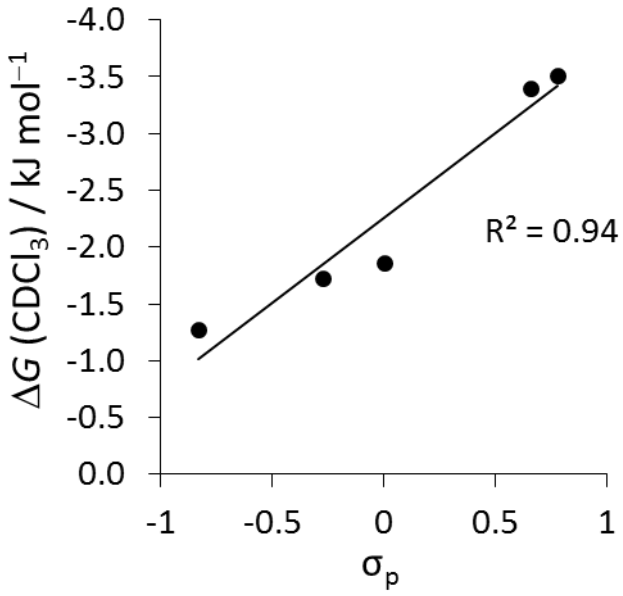

Figure 4.20 Plot of experimentally measured conformational free energies by ^{1}H NMR spectroscopy ($CDCl_3$, 400 MHz, 298 K) *versus* the *para* Hammett constant value, σ_p. Values taken from reference 33.

Despite the initial indications of an electrostatically controlled interaction, NBO analysis of minimised structures from the series **9** all contained n→π* electron delocalisation. The energetic significance of this electron delocalisation varied much more for series **9** than series **8**, ranging from 2.6 and 16.6 kJ mol^{-1} from both lone pairs of the amide donor (**Figure 4.21A** and **B**). The amount of stabilisation provided by the electron delocalisation seemed to follow the expected trend of compounds bearing electron-withdrawing groups on the acceptor side of the molecule having larger stabilising effects (X = NO_2, CN) than those that contained electron-donating groups (X = OMe, NMe_2).

The total predicted energies of the n→π* electron delocalisation gave a surprisingly good correlation with the experimental results (**Figure 4.21C**), suggesting that the n→π* electron delocalisation could indeed be responsible the behaviour of these interactions. However, it is very important to note that the known transferability of substituent effects may mean that both orbital energies and electrostatic factors both scale with each other, making it impossible to definitively determine whether orbital

delocalisation or electrostatics dominate a particular interaction through simple correlation alone.

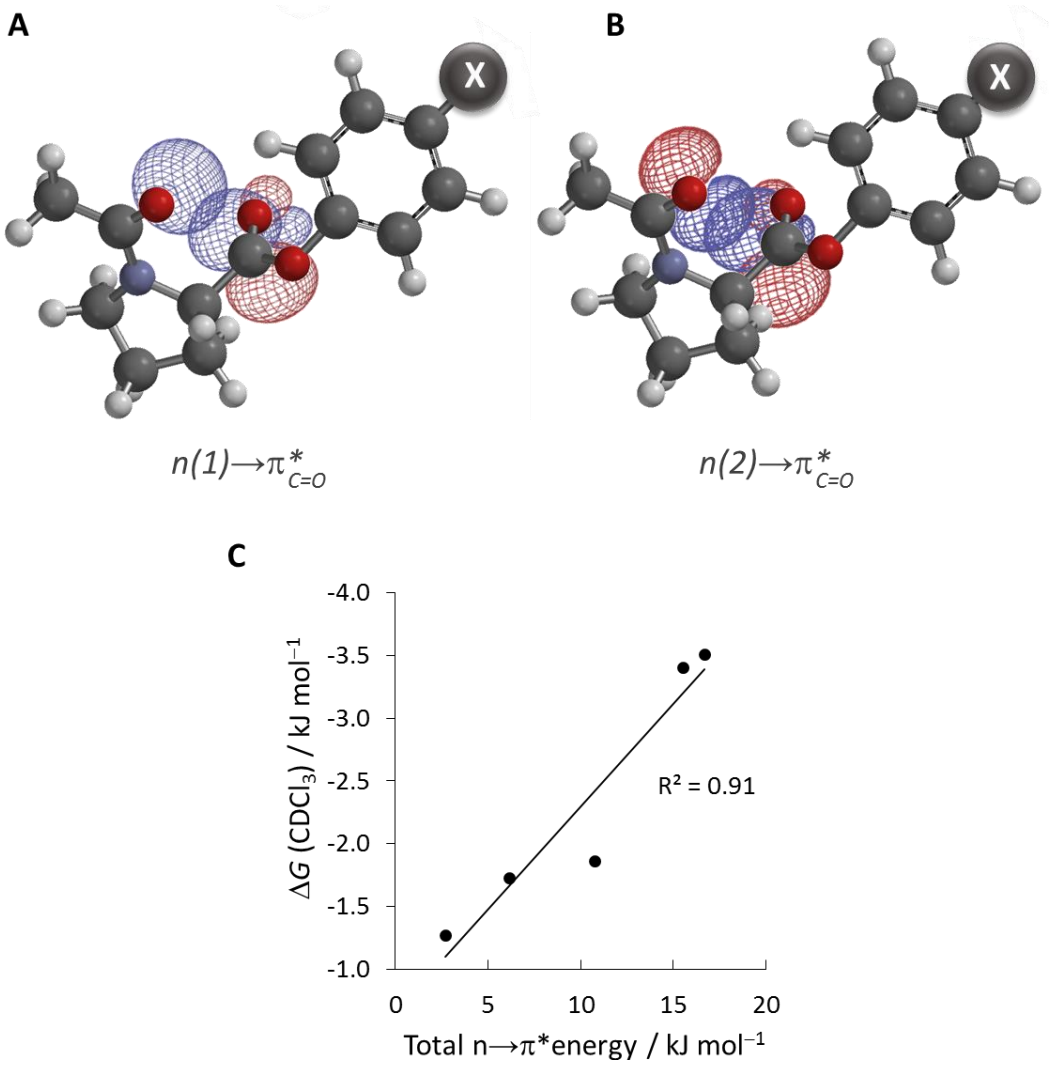

Figure 4.21 (A) and (B) NBOs corresponding to n→π* electron delocalisation from both lone pairs of the amide donor in molecular balances from series **9**. (C) Plot of predicted stabilisation energies from NBO second-order energy perturbations from n→π* electron delocalisation against experimentally measured conformational free energy difference determined by ^{1}H NMR spectroscopy ($CDCl_3$, 400 MHz, 298 K). Experimental values taken from reference 33. NBO calculations performed using Gaussian '09 and NBO 6.0 B3LYP/6-31G*.

fiSAPT analysis was used to further analyse Raines' systems to dissecting out the components of the interaction. The fiSAPT decomposition appeared very similar to the results seen in series **8** (**Figure 4.18**), with only dispersion and induction contributing favourably to the interaction (**Figure 4.22**). Again, the overall interaction was predicted to be unfavourable, consistent with intramolecular strain.

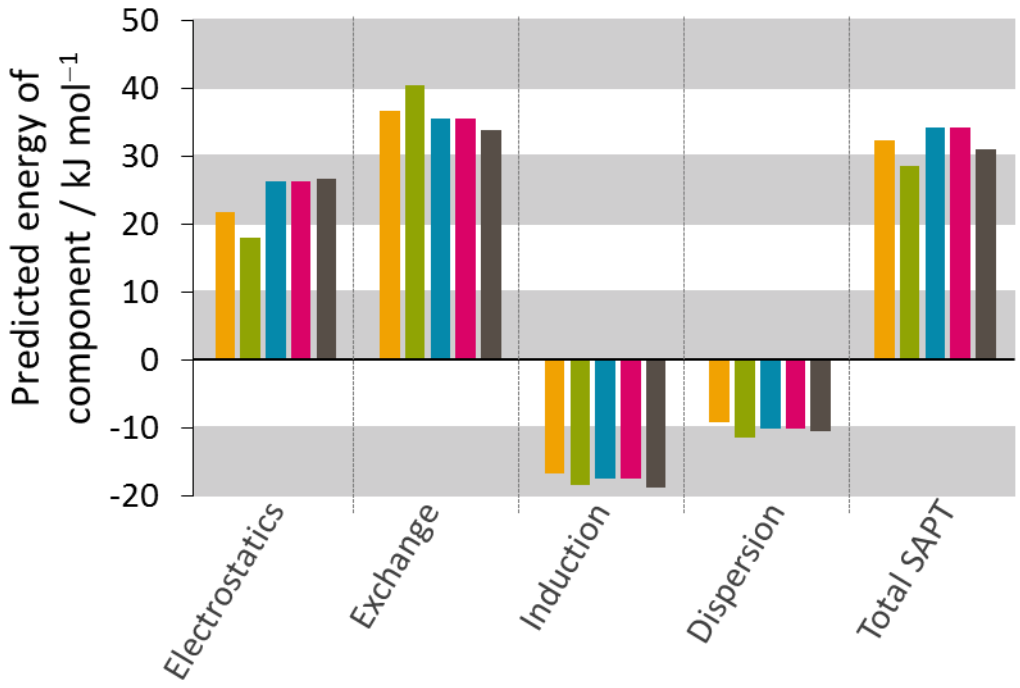

Figure 4.22 fiSAPT energy contributions for molecular balances **9**-NO_2 (yellow), **9**-CN (green), **9**-H (blue), **9**-OMe (pink) and **9**-NMe_2 (grey). Calculated using PSI4 SAPT0/6-31G*.

Finally, a molecular orbital analysis was performed using the same visual matching technique between the *cis* and the *trans* conformations. As was seen in chalcogen bonding in **Chapter 2** and H-bonding in **Chapter 3**, two subsets fell below the line (**Figure 4.23**). These subsets represent molecular orbitals that are lower in energy (more stable) in the *trans* compared to the *cis* conformer.

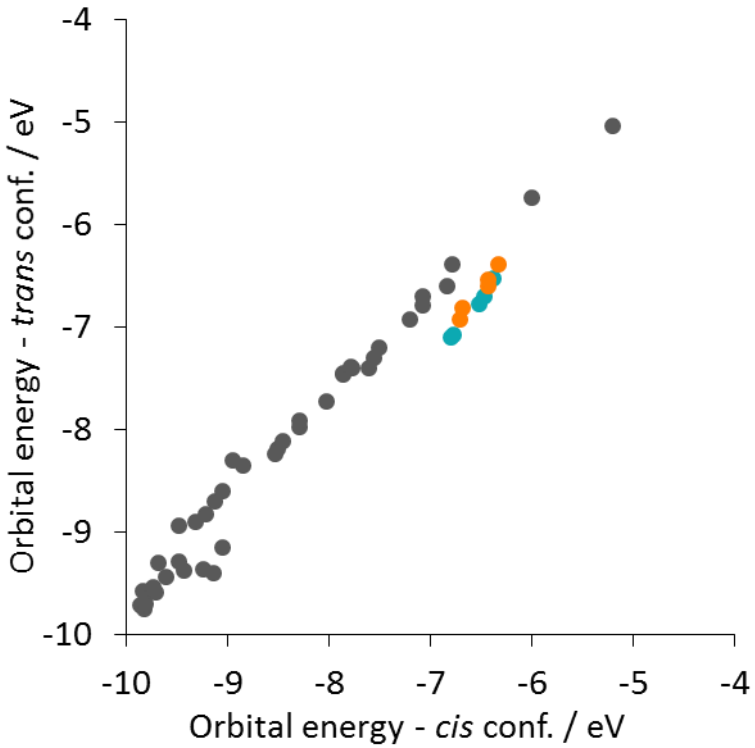

Figure 4.23 Correlation of all molecular orbital energies from HOMO to HOMO{-9} in *cis* versus *trans* conformers of simplified molecular balances. Points below the grey line are stabilised in the *trans* conformer. Teal points represent one lone pair of the amide donor being stabilised and orange corresponds to the orthogonal lone pair. Molecular orbital energies calculated using Spartan '14 DFT/B3LYP/6-31G*.

These data subsets represented orbitals in which both lone pairs from the amide donor were stabilised by delocalisation into the π* orbitals of the C=O bond of the acceptor (**Figure 4.24**). Unlike NBO diagrams, where overlaps are shown between interacting orbitals, molecular orbitals will not show an overlap due to repulsion, and can therefore can cancel out nearby lobes. This may be the explanation for the smaller than expected acceptor orbital.

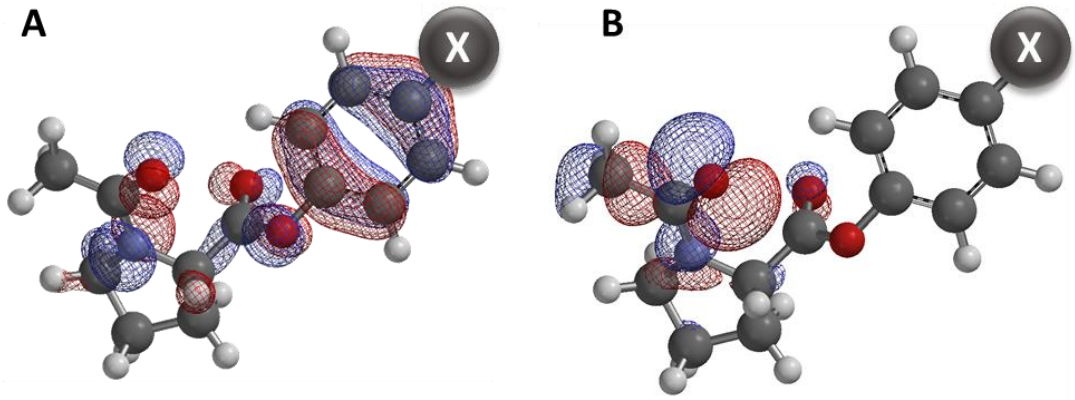

Figure 4.24 Molecular orbitals corresponding to (A) orange points and (B) teal points on **Figure 4.23**.

When plotting the energy of both molecular orbitals against the experimentally determined conformational free energies a good correlation was observed for both sets of orbitals (**Figure 4.25**), providing support for the occurrence of stabilising n→π* electron delocalisation. This correlation of energies with the n→π* electron delocalisation provides the first quantitative evidence of the interactions in Raines' systems.

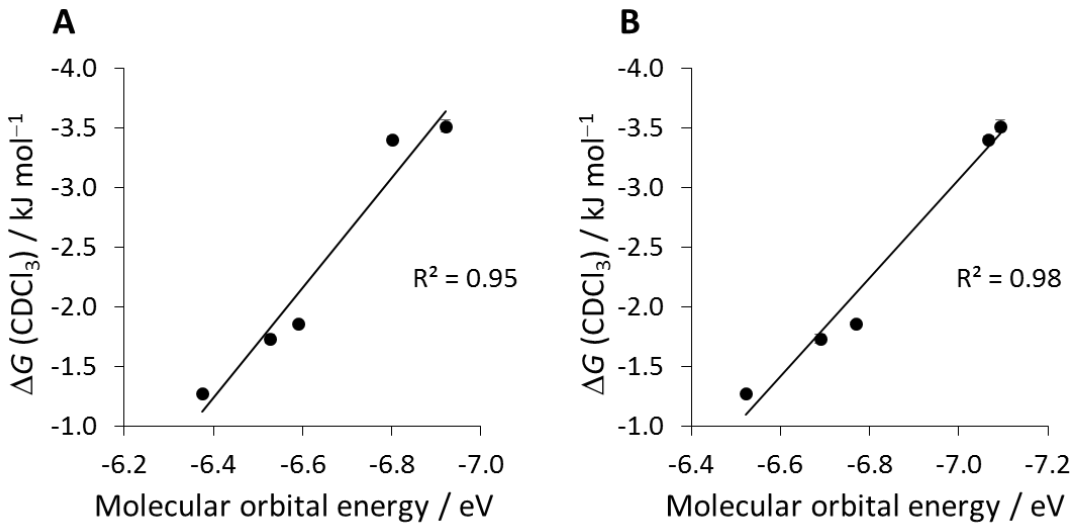

Figure 4.25 Plot of experimentally determined conformational free energies by ^{1}H NMR ($CDCl_3$, 400 MHz, 298 K) versus molecular orbital energy of (A) orange points in **Figure 4.23** and (B) teal points in **Figure 4.23**. Experimental data taken from reference 34.

4.4 Comparison between formyl and proline molecular balances

Experimental and computational results show that the interactions in the Cockroft group's balances and Diederich's Wilcox molecular balance (**Figure 4.7**) differs in nature from some of Raines' proline balances (**Figure 16B**). Structurally, the carbonyl groups in the proline molecular balance sit closer in space than those in the formyl molecular balances (with one atom difference in the connectivity). On average, the intermolecular distance between the carbonyl groups is around 0.2 Å less in the proline molecular balances than the formyl molecular balances (full carbonyl···carbonyl distances, interaction angles and minimised structures can be found in the **Appendix C**, **Figure C.5**). Interestingly, Raines' closely related series **8** do not show convincing evidence for an n→π* electron delocalisation, possibly due to the puckering that addition of substituents onto the proline ring can cause,[35] increasing the intermolecular distance of the interaction. Similarly, Diederich's Wilcox balance also has a longer interaction distance than seen in Raines' series 8 molecular balances, which also contains no electron delocalisation between the two carbonyl groups. These subtle geometric differences suggest that the intermolecular distance in Raines' series **8**,

Diederich's Wilcox balance and the Cockroft formyl balances are too long for significant orbital overlap, resulting in electrostatically controlled interactions, which has a greater intermolecular distance range. Together, the results demonstrate that the nature of carbonyl interactions are very sensitive to the geometry of the system.

4.5 Conclusions and outlook

The molecular balance system used in the Cockroft group (**Figure 4.7**) to investigate the nature of carbonyl···carbonyl interactions found greater agreement with previously reported electrostatic nature proposed by Diederich. Only one molecular balance contained n→π* electron delocalisation that was not predicted to be particularly energetically significant by NBO analysis. A further fiSAPT analysis revealed the most attractive component of these carbonyl···carbonyl interactions arose from electrostatics. The proline-based molecular balance used by Raines had a more significant n→π* electron delocalisation in series **9** (**Figure 4.21**), but not in series **8**, where the electronics of the proline ring is changed. Unlike the formyl-based molecular balances, the electrostatic component was a source of *repulsion*, and the most favourable component originated from induction, which includes the electron delocalisation component (**Figure 4.19**). The molecular orbital analysis shows for the first time a quantitative link between an n→π* electron delocalisation and experimentally determined conformational equilibria in series **9** (**Figure 4.25B**). The proline-based molecular balances will give a better representation of carbonyl···carbonyl interactions in biological systems, such as protein structure given that it is based on an amino acid. However, beyond the relatively restricted structures present in proteins, carbonyl···carbonyl interactions *can still be favourable*. Therefore, it is important to recognise that carbonyl groups at larger distances can still form favourable and significant interactions. Interactions at larger intermolecular distances will become dominated by electrostatics rather than an electron delocalisation, as seen in the formyl molecular balances studied in this chapter. It appears the nature of this interaction is very sensitive to the geometry of the system. While evidence of an n→π* interaction can be found in both the proline and formyl-based molecular balances, their behaviours are not universally dominated by electron delocalisation. However, a minor

change in geometry, as illustrated by the difference between the Raines' systems can alter the nature entirely, becoming dominated by an n→π* delocalisation.

Further work on the formyl molecular balances used in the Cockroft group could involve substituting the amide to a thioamide, which may alter the nature of the interaction to have a greater electron delocalisation component due to a closer contact and therefore a better orbital overlap.

4.6 References

1. Maccallum, P. H.; Poet, R.; James Milner-White, E. Coulombic Attractions between Partially Chargedmain-Chain Atoms Stabilise the Right-Handed Twist Found in Most β-Strands. *J. Mol. Biol.* **1995**, *248* (2), 374–384.

2. Deane, C. M.; Allen, F. H.; Taylor, R.; Blundell, T. L. Carbonyl–carbonyl Interactions Stabilize the Partially Allowed Ramachandran Conformations of Asparagine and Aspartic Acid. *Protein Eng. Des. Sel.* **1999**, *12* (12), 1025–1028.

3. Paulini, R.; Müller, K.; Diederich, F. Orthogonal Multipolar Interactions in Structural Chemistry and Biology. *Angew. Chem. Int. Ed.* **2005**, *44* (12), 1788–1805.

4. Jeffrey, G. A.; Saenger, W. *Hydrogen Bonding in Biological Structures*; Springer Berlin Heidelberg, **1991**.

5. Siebler, C.; Erdmann, R. S.; Wennemers, H. Switchable Proline Derivatives: Tuning the Conformational Stability of the Collagen Triple Helix by pH Changes. *Angew. Chem. Int. Ed.* **2014**, *53* (39), 10340–10344.

6. Rahim, A.; Saha, P.; Jha, K. K.; Sukumar, N.; Sarma, B. K. Reciprocal Carbonyl–carbonyl Interactions in Small Molecules and Proteins. *Nat. Commun.* **2017**, *8* (1), 78.

7. Bartuschat, A. L.; Wicht, K.; Heinrich, M. R. Switching and Conformational Fixation of Amides Through Proximate Positive Charges. *Angew. Chem. Int. Ed.* **2015**, *54* (35), 10294–10298.

8. Murray, J. S.; Lane, P.; Clark, T.; Riley, K. E.; Politzer, P. σ-Holes, π-Holes and Electrostatically-Driven Interactions. *J. Mol. Model.* **2012**, *18* (2), 541–548.

9. Bauzá, A.; Mooibroek, T. J.; Frontera, A. The Bright Future of Unconventional Σ/π-Hole Interactions. *ChemPhysChem* **2015**, *16* (12), 2496–2517.

10. Bauzá, A.; Mooibroek, T. J.; Frontera, A. Directionality of π-Holes in Nitro Compounds. *Chem. Commun.* **2015**, *51* (8), 1491–1493.

11. Báuza, A.; Frontera, A.; Mooibroek, T. J. π-Hole Interactions Involving Nitro Compounds: Directionality of Nitrate Esters. *Cryst. Growth Des.* **2016**, *16* (9), 5520–5524.

12. Bretscher, L. E.; Jenkins, C. L.; Taylor, K. M.; DeRider, M. L.; Raines, R. T. Conformational Stability of Collagen Relies on a Stereoelectronic Effect. *J. Am. Chem. Soc.* **2001**, *123* (4), 777–778.

13. DeRider, M. L.; Wilkens, S. J.; Waddell, M. J.; Bretscher, L. E.; Weinhold, F.; Raines, R. T.; Markley, J. L. Collagen Stability: Insights from NMR Spectroscopic and Hybrid Density Functional Computational Investigations of the Effect of Electronegative Substituents on Prolyl Ring Conformations. *J. Am. Chem. Soc.* **2002**, *124* (11), 2497–2505.

14. Bartlett, G. J.; Choudhary, A.; Raines, R. T.; Woolfson, D. N. N→π* Interactions in Proteins. *Nat. Chem. Biol.* **2010**, *6* (8), 615–620.

15. B:urgi, H. B.; Dunitz, J. D.; Lehn, J. M.; Wipff, G. Stereochemistry of Reaction Paths at Carbonyl Centres. *Tetrahedron* **1974**, *30* (12), 1563–1572.

16. Choudhary, A.; Gandla, D.; Krow, G. R.; Raines, R. T. Nature of Amide Carbonyl−Carbonyl Interactions in Proteins. *J. Am. Chem. Soc.* **2009**, *131* (21), 7244–7246.

17. Pau, J. K.; Ruggera, M. B.; Kim, J. K.; Caserio, M. C. On the Electron-Donating Properties of Oxygen vs. Sulfur. A Study of the Gas-Phase Ion Chemistry of Methoxymethylthioalkanes. *J. Am. Chem. Soc.* **1978**, *100* (13), 4242–4248.

18. Gorske, B. C.; Stringer, J. R.; Bastian, B. L.; Fowler, S. A.; Blackwell, H. E. New Strategies for the Design of Folded Peptoids Revealed by a Survey of Noncovalent Interactions in Model Systems. *J. Am. Chem. Soc.* **2009**, *131* (45), 16555–16567.

19. Pollock, S. B.; Kent, S. B. H. An Investigation into the Origin of the Dramatically Reduced Reactivity of Peptide-Prolyl-Thioesters in Native Chemical Ligation. *Chem. Commun.* **2011**, *47* (8), 2342–2344.

20. Kamer, K. J.; Choudhary, A.; Raines, R. T. Intimate Interactions with Carbonyl Groups: Dipole–Dipole or N →π*? *J. Org. Chem.* **2013**, *78* (5), 2099–2103.

21. Bartlett, G. J.; Newberry, R. W.; VanVeller, B.; Raines, R. T.; Woolfson, D. N. Interplay of Hydrogen Bonds and N →π* Interactions in Proteins. *J. Am. Chem. Soc.* **2013**, *135* (49), 18682–18688.

22. Newberry, R. W.; VanVeller, B.; Guzei, I. A.; Raines, R. T. N →π* Interactions of Amides and Thioamides: Implications for Protein Stability. *J. Am. Chem. Soc.* **2013**, *135* (21), 7843–7846.

23. Paliwal, S.; Geib, S.; Wilcox, C. S. Molecular Torsion Balance for Weak Molecular Recognition Forces. Effects of "Tilted-T" Edge-to-Face Aromatic Interactions on Conformational Selection and Solid-State Structure. *J. Am. Chem. Soc.* **1994**, *116* (10), 4497–4498.

24. Fischer, F. R.; Wood, P. A.; Allen, F. H.; Diederich, F. Orthogonal Dipolar Interactions between Amide Carbonyl Groups. *Proc. Natl. Acad. Sci.* **2008**, *105* (45), 17290–17294.

25. Hof, F.; Scofield, D. M.; Schweizer, W. B.; Diederich, F. A Weak Attractive

Interaction between Organic Fluorine and an Amide Group. *Angew. Chem. Int. Ed.* **2004**, *43* (38), 5056–5059.

26. Cockroft, S. L.; Hunter, C. A. Chemical Double-Mutant Cycles: Dissecting Non-Covalent Interactions. *Chem. Soc. Rev.* **2007**, *36* (2), 172–188.

27. Allen, F. H.; Baalham, C. A.; Lommerse, J. P. M.; Raithby, P. R. Carbonyl–Carbonyl Interactions Can Be Competitive with Hydrogen Bonds. *Acta Crystallogr. Sect. B Struct. Sci.* **1998**, *54* (3), 320–329.

28. Muchowska, K. B. Molecular Balances, **2015**, University of Edinburgh.

29. Pascoe, D. J.; Ling, K. B.; Cockroft, S. L. The Origin of Chalcogen-Bonding Interactions. *J. Am. Chem. Soc.* **2017**, *139* (42), 15160–15167.

30. Moran, D.; Simmonett, A. C.; Leach, F. E.; Allen, W. D.; Schleyer, P. V. R.; Schaefer, H. F. Popular Theoretical Methods Predict Benzene and Arenes To Be Nonplanar. *J. Am. Chem. Soc.* **2006**, *128* (29), 9342–9343.

31. Papajak, E.; Zheng, J.; Xu, X.; Leverentz, H. R.; Truhlar, D. G. Perspectives on Basis Sets Beautiful: Seasonal Plantings of Diffuse Basis Functions. *J. Chem. Theory Comput.* **2011**, *7* (10), 3027–3034.

32. Parker, T. M.; Burns, L. A.; Parrish, R. M.; Ryno, A. G.; Sherrill, C. D. Levels of Symmetry Adapted Perturbation Theory (SAPT). I. Efficiency and Performance for Interaction Energies. *J. Chem. Phys.* **2014**, *140* (9), 94106.

33. Fischer, F. R.; Wood, P. A.; Allen, F. H.; Diederich, F. Orthogonal Dipolar Interactions between Amide Carbonyl Groups. *Proc. Natl. Acad. Sci.* **2008**, *105* (45), 17290–17294.

34. Hodges, J. A.; Raines, R. T. Energetics of an n→ π * Interaction That Impacts Protein Structure. *Org. Lett.* **2006**, *8* (21), 4695–4697.

35. Choudhary, A.; Gandla, D.; Krow, G. R.; Raines, R. T. Nature of Amide Carbonyl−Carbonyl Interactions in Proteins. *J. Am. Chem. Soc.* **2009**, *131* (21), 7244–7246.

Chapter 5
Overall Conclusions

In order to fully exploit molecular interactions and incorporate them into rationally designed systems, it is crucial to develop a detailed molecular-level understanding of the interactions in question. However, determining the underlying physiochemical origin of interactions is very challenging. This thesis has presented a fundamental investigation into the defining characteristics of chalcogen-bonding, H-bonding and carbonyl···carbonyl intramolecular interactions using a range of experimental and computational techniques.

One particular challenge that this thesis has looked to address is the lack of experimental justification for theoretical bonding models. The need for a combination of both computational and experimental techniques has been highlighted throughout. Many previously published investigations into the nature of interactions are limited being either purely computational, or experimental approaches. Computation, therefore, often lacks experimental validation, while experiments often lack a detailed examination of theoretical models to explain bonding modes. The research presented in this thesis has tried to bridge this gap; explaining molecular interactions using a combined computational and experimental approach.

While argument over the validity of specific bonding models to describe real systems will always be a contentious discussion, this thesis has demonstrated that there is an unmet need for general models to describe molecular interactions. The simple molecular orbital plots that have been used within this thesis to easily identify stabilised molecular orbitals presents a simple and easily-applicable general technique. The application of the molecular orbital approach has been demonstrated across three very different systems to identify potential electron delocalisations, and quantitative justification of the approach has been demonstrated in two systems (chalcogen and carbonyl···carbonyl interactions). It is hoped that the molecular orbital approach presented here will find widespread use in other systems in the future, where it may provide new insight into the nature of diverse and important interactions.

In the case of chalcogen bonding, an experimental system was designed (in keeping with a motif supplied by *Syngenta*). While, unfortunately, the use of chalcogen bonds was demonstrated to be inappropriate to use in the development of adaptomers (molecules that can change their physical properties to suit their environment), the work lead to the development of a molecular balance system which provided a detailed experimental investigation of the strength and behaviour of chalcogen bonding in solution. Chalcogen bonding interactions were shown to have significance in solution, regularly being as strong a traditional H-bonds! Crucially, and unlike hydrogen bonds, chalcogen bonds displayed a surprising solvent independence. The solvent independence, and lack of correlation of conformational free energy differences with electrostatic properties, led to an important question: What is the nature of chalcogen bonds? The predominant explanation in literature, to date, having been that chalcogen bonding was electrostatic in nature. For the first time, we presented a molecular orbital analysis of chalcogen bonding, which demonstrated a quantitative link between experimentally determined conformational free energies and the molecular orbital energy containing an n→σ*electron delocalisation.

The computational model employed for the investigation of chalcogen bonding were subsequently applied to other systems to further the understanding of other interactions. Experimental data previously obtained within the Cockroft group on H-bonds and carbonyl···carbonyl interactions was re-examined using the molecular orbital approach, as well as other computational methods.

The hydrogen bonding interactions between amine/amide donors and amide acceptors were demonstrated to be electrostatic in nature, in good agreement with the traditionally accepted view of hydrogen bonding in the literature. However, when part of a cooperative chain, a partial covalent model of hydrogen bonding became more appropriate for the terminal H-bond. Unfortunately, no quantitative link could be found between partially covalent model parameters and experimental data, highlighting the importance of both an electrostatic and electron delocalisation model in H-bonding.

The nature of carbonyl interactions were shown to be exceptionally sensitive to the geometry of the interaction. A quantitative link was determined between molecular

orbital energies containing n→π* electron delocalisation and experimental conformational free energies from the literature. A small change in the interaction distance or angle was shown to change the governing nature of the interaction. A further examination of published experimental data of a proline-based molecular balance from the Raines group indicated an interaction governed by an n→π* electron delocalisation. Although another related proline molecular balance appeared to show the dominance of electrostatics in carbonyl···carbonyl interactions. However, analysis of the formyl molecular balances used in the Cockroft group did not support such an electron delocalisation, and was instead consistent with an electrostatically controlled interaction. The differences in the physiochemical origin of the interaction within these systems was attributed to subtle differences in the geometry. A slight increase in the interaction distance resulted in a geometry incompatible with electron delocalisation, and so electrostatics were found to dominate the interaction at greater distances. Importantly, the research highlights the importance of these interactions outside the confines of rigid protein structure, encouraging the consideration of the significant electrostatic interaction that carbonyls may form at greater distances. This finding was further supported by experimental data on a Wilcox molecular balance containing carbonyl contacts by Diederich and co-workers. The interactions in Diederich's system had the largest interaction distance of all four systems investigated, but still formed favourable interactions that were predicted to be dominated by electrostatics.

This thesis has also demonstrated the challenges of finding quantitative relationships between bonding models and experimental data, and the flaws of some computational techniques have been highlighted. The reliance of models on theoretical constructs rather than physically measurable properties accounts for a significant source of inaccuracy. For example, a commonly used energy decomposition technique, symmetry adapted perturbation theory (SAPT) could not accurately predict interaction strength. As well as demonstrating the limitation of such energy decomposition techniques, this inaccuracy served to highlight the need for experimental justification to be used in connection with computational studies. Furthermore, the quantitative links established between the molecular orbital model provided here and real experimental data demonstrates the validity of the approach.

Ultimately, it is hoped that this research will be of immediate interest, not only to those who investigate molecular interactions, but also to the wider chemistry community who regularly exploit these interactions in applications such as drug design and catalysis. The deeper understanding of the interactions presented here should encourage the thoughtful design of future systems, allowing such interactions to be exploited to their fullest potential.

Appendix A: Experimental and Computational Data for Chapter 2

6.1.1 Synthetic procedures and standard characterisation data

All synthetic starting materials were obtained from commercial sources and used as received. All reactions were carried out, under a nitrogen atmosphere and using dry solvents unless stated otherwise. Analytical TLC was carried out on Merck aluminium sheets coated with silica gel 60F and visualized using UV light (254 nm). Preparatory TLC was carried out on Analtech 20 x 20 cm glass mounted plates on 2000 micron silica and flash chromatography was carried out on silica gel Geduran 60 (40 – 63 μm). Solvent ratios have been indicated in brackets. Mass spectrometry was performed by the University of Edinburgh technician-supported mass spectrometry service, using a ThermoElectron MAT XP spectrometer for EI-HRMS and ESI-HRMS. Melting points were measured in a Gallenkamp melting point apparatus. ^{1}H and ^{13}C NMR spectra were recorded on either 400 or 500 MHz Bruker Avance III spectrometer. ^{19}F NMR spectra were recorded on a 400 MHz Bruker Avance III spectrometer. NMR chemical shifts (δ) are reported in parts per million (ppm) relative to trimethylsilane (δ = 0 ppm) or DMSO (^{1}H δ = 2.50 ppm and ^{13}C δ = 39.52 ppm) as an internal reference. ^{13}C and ^{19}F spectra were ^{1}H decoupled. Coupling constants, *J*, are reported in Hertz (Hz). All minor conformer peaks are denoted *.

6.1.2 General procedure for the copper-mediated coupling of halo-aromatics to aryl-amides

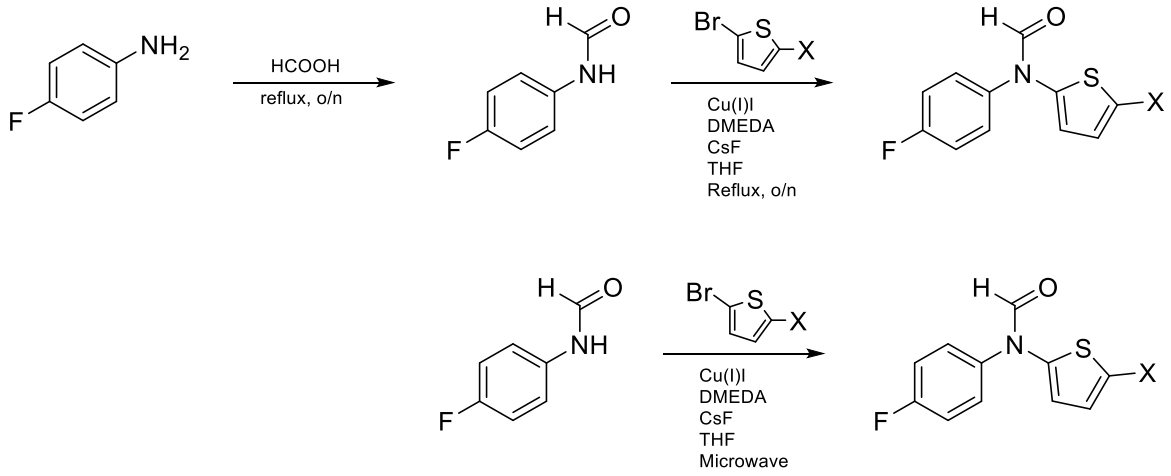

All the balances were cross-coupled with copper (I) iodide catalyst under the same general conditions, unless stated otherwise. The amide, aryl halide, catalyst and base (CsF) were added to an oven dried flask which was sealed before evacuating and back filling with nitrogen three times. Dry solvent (THF) and ligand *N,N'*-dimethylethylenediamine (DMEDA) were added *via* syringe and the system was evacuated and back filled with nitrogen twice more. The suspension was heated at reflux overnight (**thermal procedure**), or heated to 100 ^{o}C for 40 min in the microwave (**microwave procedure**), and then cooled to ambient temperature and diluted with EtOAc. The aqueous phase was extracted with organic solvent and the combined organic phases were washed with brine, dried over $MgSO_4$ and concentrated *in vacuo*. The resulting products were further purified by chromatography.

6.1.3 General procedure for Lawesson's reagent reaction

The amide (1 eq) and Lawesson's reagent (1 eq) were dissolved in 1,4-dioxane and heated to reflux overnight. The reaction was cooled to room temperature and extracted with ethyl acetate and washed with water. The organics were collected, dried over anhydrous $MgSO_4$, filtered and concentrated before being purified by silica gel chromatography.

***N*-(4-fluorophenyl)-*N*-(2-thienyl)formamide (1a-H)**

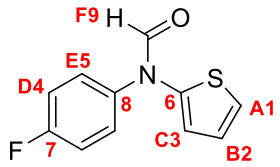

Prepared using the general coupling procedure (thermal). 2-Bromothiophene (1.0 g, 6.13 mmol), *N*-formyl-4-fluoroaniline (853 mg, 6.13 mmol), CsF (1.39 g, 9.15 mmol), Cu(I)I (233 mg, 1.23 mmol), DMEDA (162 mg, 1.84 mmol) and THF (20 ml). Purification with silica gel chromatography (ethyl acetate/hexane, 1:4) yielded **1a**-H as an off-white solid (280 mg, 1.27 mmol, 20%). MP: 65 – 67 °C, ^{1}H NMR (500 MHz, DMSO-d_6) δ 8.66 (s, 1H*), 8.46 (s, 1H), 7.60 – 7.53 (m, 2H), 7.46 – 7.36 (m, 3H*), 7.30 (t, J = 8.8 Hz, 1H*), 7.26 – 7.20 (m, 1H), 7.20 – 7.15 (m, 1H*), 7.02 (dd, J = 5.5, 3.7 Hz, 1H*), 6.88 (dt, J = 9.5, 4.8 Hz, 1H), 6.40 (dd, J = 3.8, 1.4 Hz, 1H). ^{13}C NMR (126 MHz, DMSO-d_6) δ 162.41* (s), 162.17 (d, $^{1}J_{C\text{-}F}$ = 245.8 Hz), 160.99 (s), 144.50* (s), 141.76 (s), 136.71* (d, $^{4}J_{C\text{-}F}$ = 2.3 Hz), 136.58 (d, $^{4}J_{C\text{-}F}$ J = 2.8 Hz), 130.11 (d, $^{3}J_{C\text{-}F}$ = 9.0 Hz), 128.50* (d, $^{3}J_{C\text{-}F}$ = 8.8 Hz), 126.71* (s), 124.68* (s), 124.61 (s), 122.93* (s), 120.61 (s), 117.29 (d, $^{2}J_{C\text{-}F}$ = 22.9 Hz), 116.57* (d, $^{12}J_{C\text{-}F}$ = 22.8 Hz), 116.25 (s). ^{19}F NMR (376 MHz, DMSO-d_6) δ -112.92 (s), -114.52* (s). HRMS EI m/z (M^+) = 221.03052 (expected 221.03106).

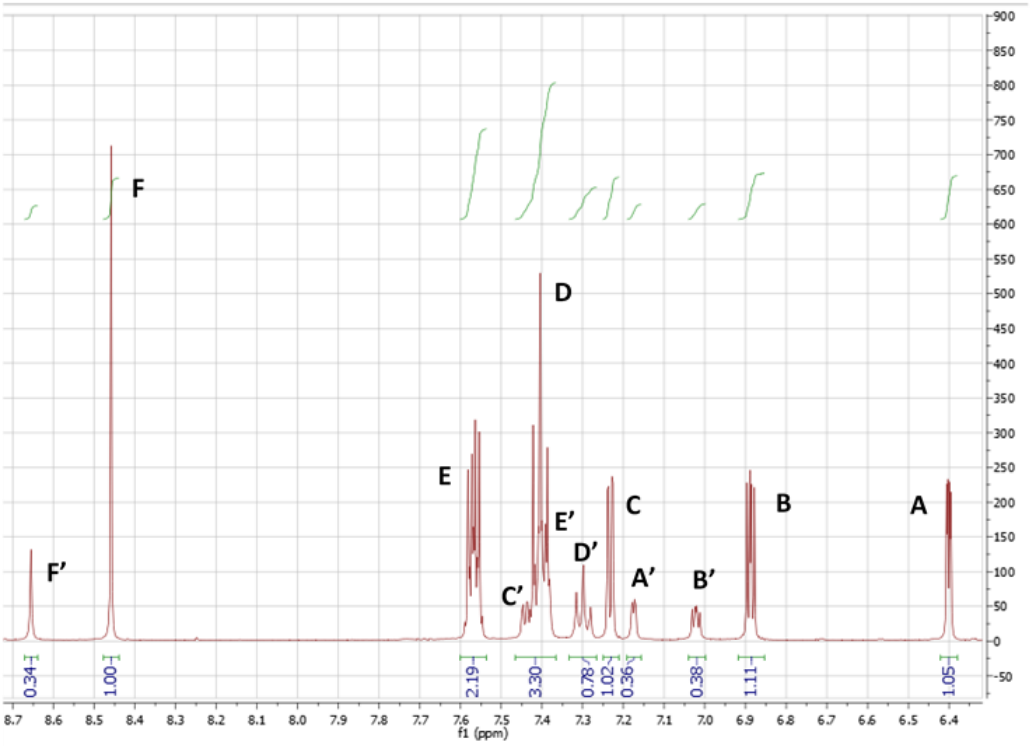

_N_-(4-fluorophenyl)-_N_-(5-methyl-2-thienyl)formamide (1a-Me)

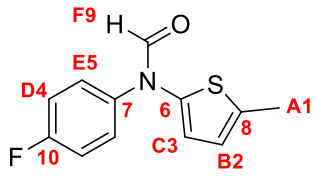

Prepared using general coupling procedure (microwave). 2-Bromo-5-methylthiophene (500 mg, 2.82 mmol), _N_-formyl-4-fluoroaniline (392 mg, 2.82 mmol), CsF (643 mg, 4.23 mmol), Cu(I)I (107 mg, 0.56 mmol), DMEDA (75 mg, 0.85 mmol) and THF (3 ml). Purification with silica gel chromatography (ethyl acetate/hexane, 1:4) yielded **1a**-Me as a pale pink solid (180 mg, 1.27 mmol, 30%). MP: 45 – 47 ºC. ^{1}H NMR (500 MHz, DMSO-d_6) δ 8.59 (s, 1H*), 8.42 (s, 1H), 7.55 – 7.48 (m, 2H), 7.41 – 7.34 (m, 3H*), 7.28 (t, J = 8.8 Hz, 1H*), 6.99 (d, J = 3.5 Hz, 1H*), 6.71 (d, J = 2.5 Hz, 1H*), 6.59 – 6.57 (m, 1H), 6.25 (d, J = 3.7 Hz, 1H), 2.39 (s, 1H*), 2.39 (s, 1H). ^{13}C NMR (126 MHz, DMSO-d_6) δ 162.41 (d, $^{1}J_{C\text{-}F}$ = 135.9 Hz), 162.37* (s), 160.96 (s), 141.38* (s), 138.99 (s), 136.69 (d, $^{4}J_{C\text{-}F}$ = 2.6 Hz), 133.98 (s), 129.59 (d, $^{3}J_{C\text{-}F}$ = 9.0 Hz), 128.08* (d, $^{3}J_{C\text{-}F}$ = 8.7 Hz), 124.57* (s), 123.88* (s), 122.69 (s), 117.17 (d, $^{2}J_{C\text{-}F}$ = 22.9 Hz), 117.04 (s), 116.45* (d, $^{2}J_{C\text{-}F}$ = 22.8 Hz), 15.69* (s), 15.08 (s). ^{19}F NMR (376 MHz, DMSO-d_6) δ -113.35 (s), -114.82* (s). HRMS EI m/z (M^{+}) = 235.04617 (expected 235.04671).

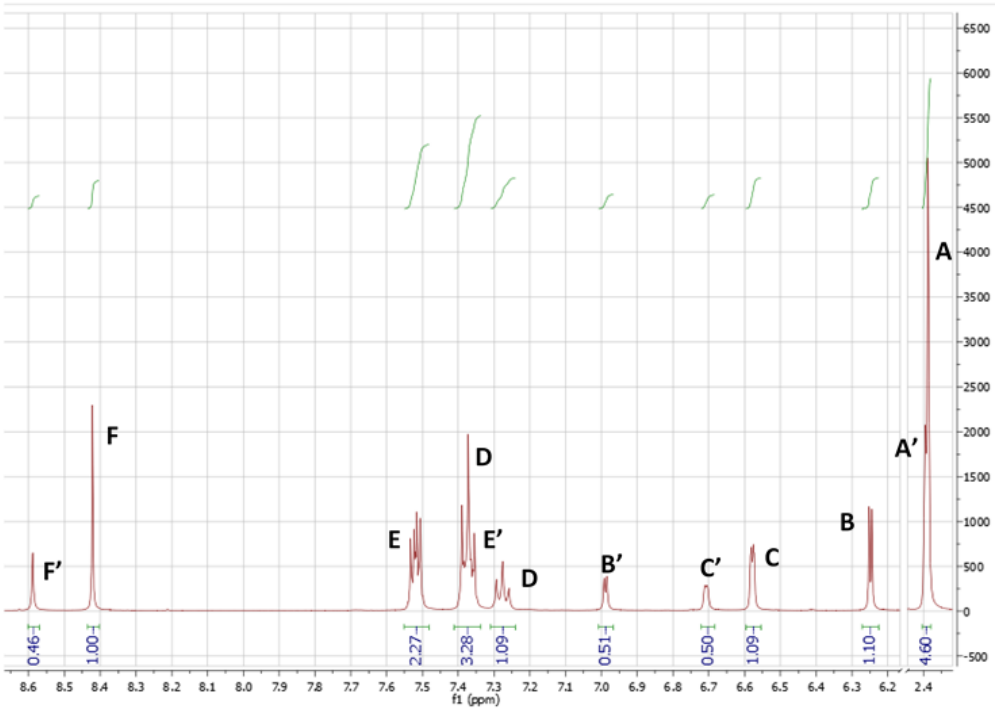

_N_-(5-chloro-2-thienyl)-_N_-(4-fluorophenyl)formamide (1a-Cl)

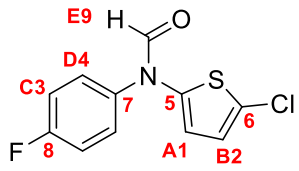

Prepared using general coupling procedure (microwave). 2-Bromo-5-chlorothiophene (1.0 g, 5.06 mmol), *N*-formyl-4-fluoroaniline (704 mg, 5.06 mmol), CsF (1.15 g, 7.59 mmol), Cu(I)I (193 mg, 1.01 mmol), DMEDA (134 mg, 1.52 mmol) and THF (3 ml). Purification with silica gel chromatography (ethyl acetate/hexane, 1:4) yielded **1a**-Cl as a colourless solid (360 mg, 1.41 mmol, 28%). MP: 111 – 113 °C, ^{1}H NMR (500 MHz, DMSO-d_6) δ 8.63 (s, 1H*), 8.44 (s, 1H), 7.65 – 7.58 (m, 2H), 7.47 – 7.39 (m, 3H*), 7.31 (t, J = 8.7 Hz, 1H*), 7.10 (dt, J = 17.6, 4.9 Hz, 1H*), 6.90 (d, J = 4.3 Hz, 1H), 6.08 (d, J = 4.3 Hz, 1H). ^{13}C NMR (126 MHz, DMSO-d_6) δ 162.53 (d, $^{1}J_{C-F}$ = 246.6 Hz), 162.45* (s), 161.06 (s), 139.15 (s), 134.80 (d, $^{4}J_{C-F}$ = 2.9 Hz), 130.81 (d, $^{3}J_{C-F}$ = 9.1 Hz), 128.53* (d, $^{3}J_{C-F}$ = 9.1 Hz), 126.47* (s), 123.65 (s), 123.55* (s), 122.34 (s), 117.47 (d, $^{2}J_{C-F}$ = 23.0 Hz), 116.67* (d, $^{2}J_{C-F}$ = 23.2 Hz), 113.43 (s).^{19}F NMR (376 MHz, DMSO-d_6) δ -112.07 (s), -114.15* (s). HRMS EI (M^{+}) = 254.99154 (expected 254.99209).

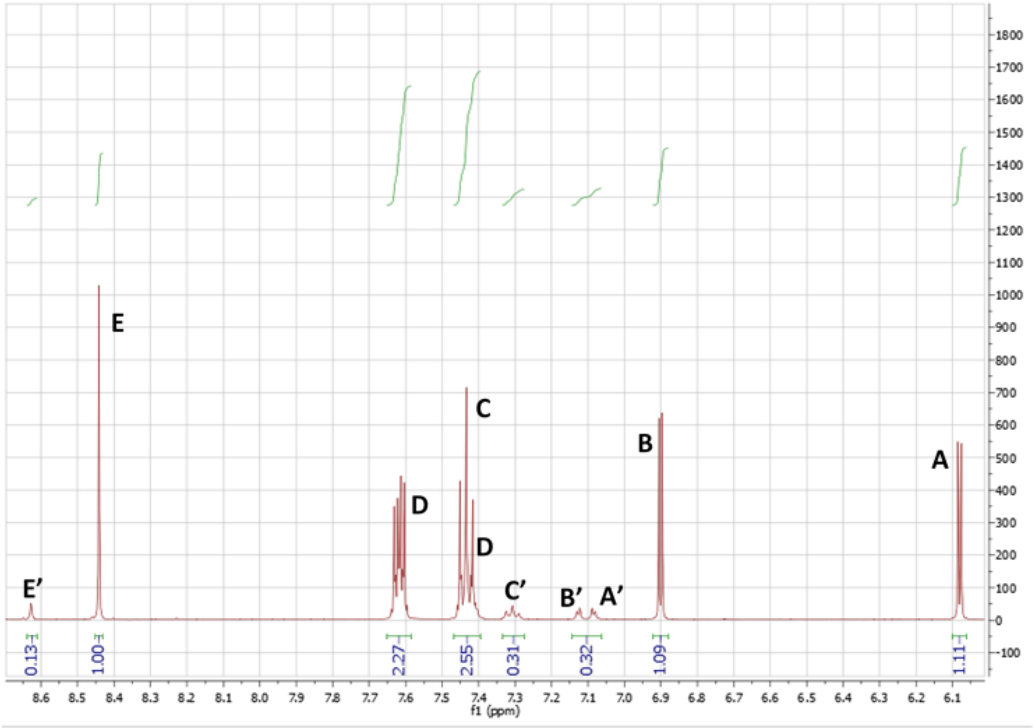

_N_-(5-acetyl-2-thienyl)-_N_-(4-fluorophenyl)formamide (1a-COMe**)**

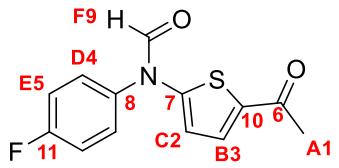

Prepared using general coupling procedure (microwave) 2-Acetyl-5-bromothiophene (300 mg, 1.46 mmol), _N_-formyl-4-fluoroaniline (203 mg, 1.46 mmol), CsF (333 mg, 2.19 mmol), Cu(I)I (55 mg, 0.29 mmol), DMEDA (39 mg, 0.44 mmol) and THF (3 ml). Purification with silica gel chromatography (ethyl acetate/hexane, 3:7) yielded **1a**-COMe as a pale brown solid (40 mg, 0.15 mmol, 10%). MP: 129 – 131 ºC, ^{1}H NMR (500 MHz, DMSO-d_6) δ 8.96 (s, 1H*), 8.53 (s, 1H), 7.70 (d, J = 4.3 Hz, 1H), 7.67 – 7.63 (m, 1H), 7.49 – 7.44 (m, 1H), 6.29 (d, J = 4.3 Hz, 1H), 2.47 (s, 1H). ^{13}C NMR (126 MHz, DMSO-d_6) δ 191.60 (s), 162.70 (d, $^{1}J_{C\text{-}F}$ = 246.8 Hz), 161.59 (s), 148.90 (s), 135.88 (s), 135.08 (d, $^{4}J_{C\text{-}F}$ = 2.9 Hz), 132.11 (s), 131.17 (d, $^{3}J_{C\text{-}F}$ = 9.2 Hz), 117.58 (d, $^{2}J_{C\text{-}F}$ = 23.0 Hz), 115.12 (s), 26.58 (s). ^{19}F NMR (376 MHz, DMSO-d_6) δ -111.69 (s), -112.83* (s). HRMS EI (M^{+}) = 263.04108 (expected 263.04163).

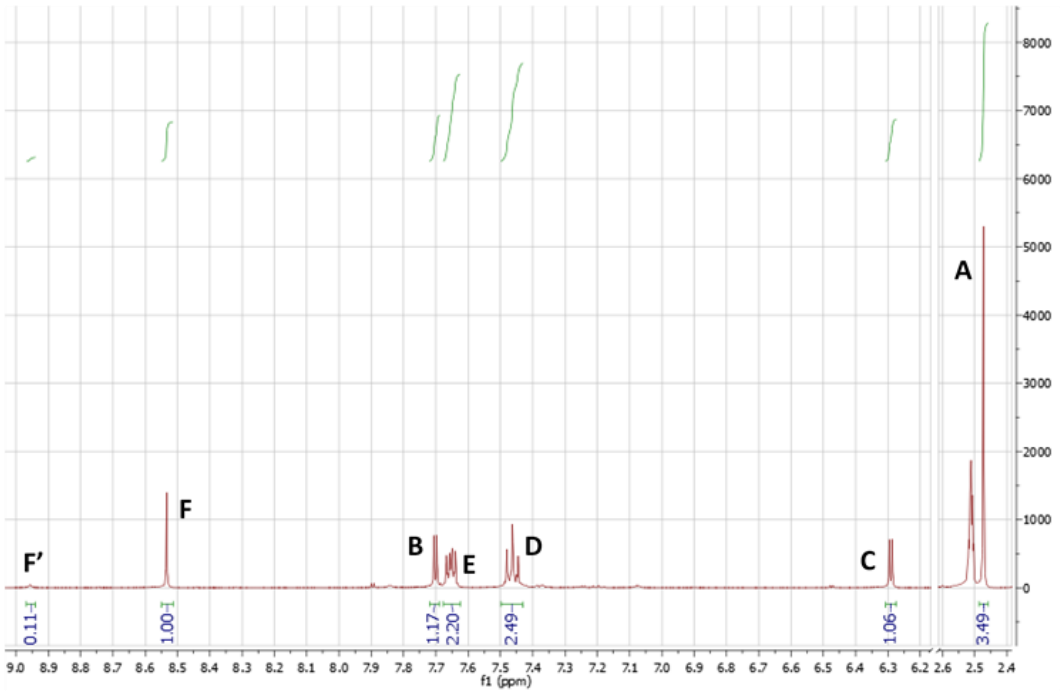

***N*-(4-fluorophenyl)-*N*-(5-formyl-2-thienyl)formamide (1a**-CHO)

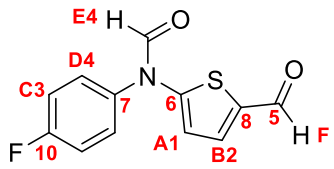

Prepared using general coupling procedure (microwave). 5-Bromo-2-thiophenecarboxyaldehyde (500 mg, 2.62 mmol), *N*-formyl-4-fluoroaniline (364 mg, 2.62 mmol), CsF (597 mg, 3.93 mmol), Cu(I)I (100 mg, 0.52 mmol), DMEDA (69 mg, 0.79 mmol) and THF (3 ml). Purification with silica gel chromatography (ethyl acetate/hexane, 3:7) yielded **1a**-CHO as a pale brown solid (70 mg, 0.28 mmol, 11%). MP: 130 – 132 °C. ^{1}H NMR (500 MHz, DMSO-d_6) δ 9.86 (s, 1H), 8.57 (s, 1H), 7.78 (t, J = 3.7 Hz, 1H), 7.71 – 7.65 (m, 2H), 7.51 – 7.43 (m, 2H), 6.36 (d, J = 4.3 Hz, 1H). ^{13}C NMR (126 MHz, DMSO-d_6) δ 185.11 (s), 162.78 (d, $^{1}J_{C\text{-}F}$ = 247.0 Hz), 161.85 (s), 149.96 (s), 136.47 (s), 135.35 (s), 134.95 (d, $^{4}J_{C\text{-}F}$ = 2.9 Hz), 131.27 (d, $^{3}J_{C\text{-}F}$ = 9.2 Hz), 117.62 (d, $^{2}J_{C\text{-}F}$ = 23.1 Hz), 115.22 (s). ^{19}F NMR (376 MHz, DMSO-d_6) δ -111.49 (s), -112.48 (s). HRMS EI (M^+) = 249.02543 (expected 249.02598).

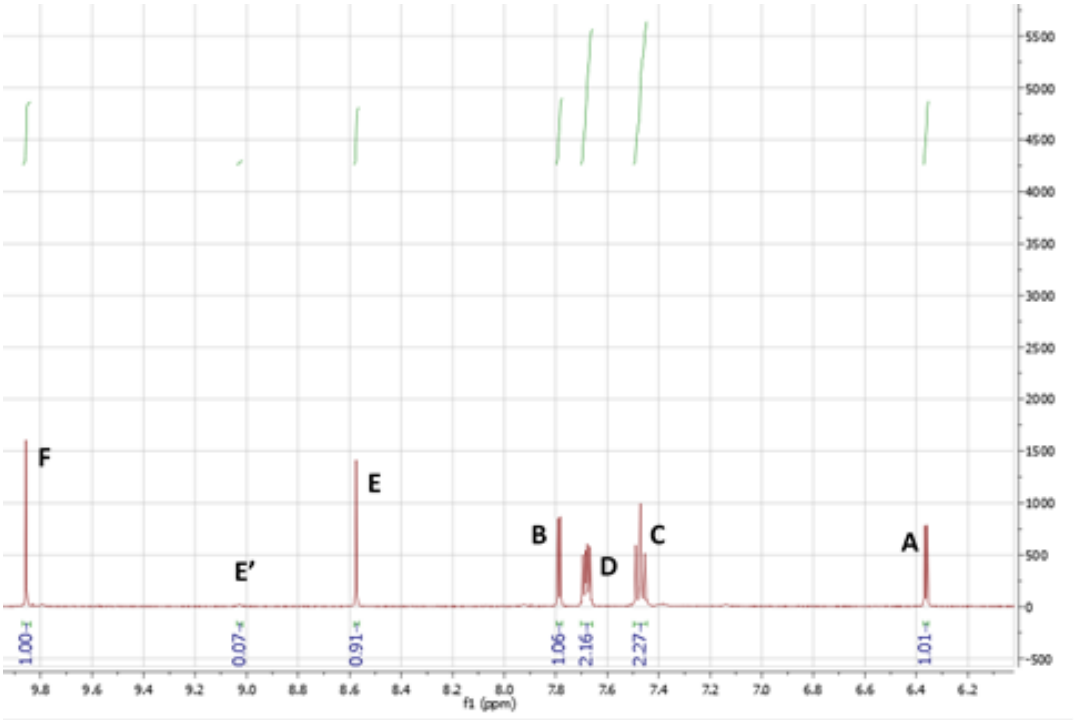

Methyl 5-bromothiophene-2-carboxylate

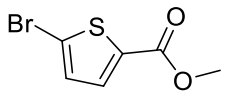

5-Bromo-2-thiophene carboxylic acid (500 mg, 2.41 mg) was dissolved in methanol (10 ml) and 10 drops of concentrated H_2SO_4 were added. The reaction was heated to 75 ^oC under reflux overnight. The reaction was allowed to cool before being extracted with ethyl acetate and washed with saturated $NaHCO_3$ and brine. The organics were collected, dried over anhydrous $MgSO_4$, filtered and concentrated to give a pale yellow solid (410 mg, 77%). The product was used without any further purification.

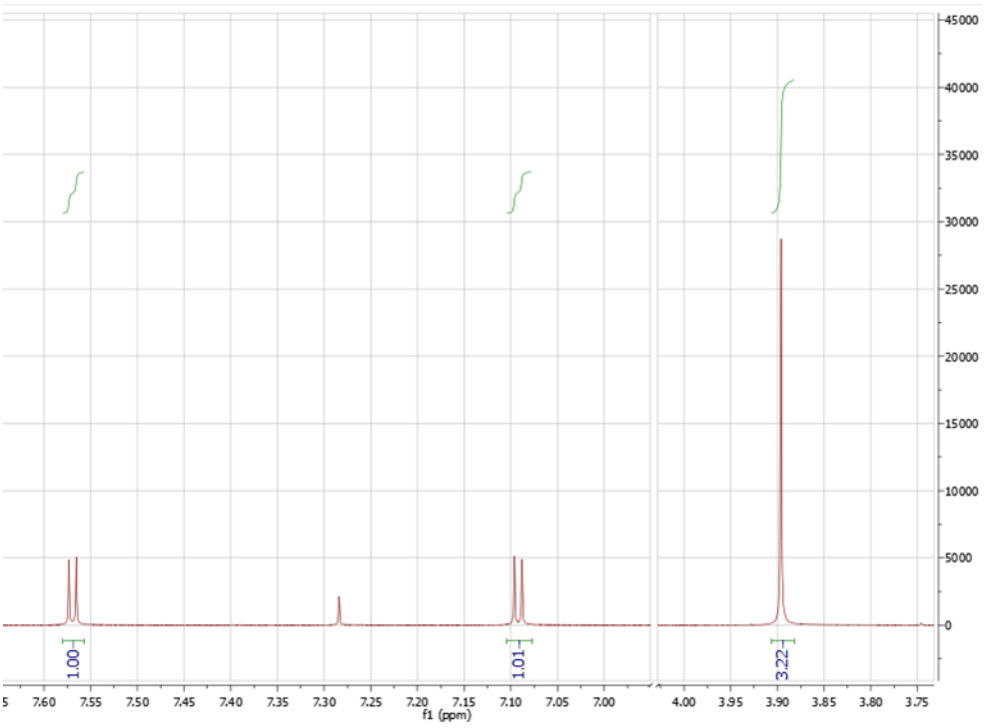

Methyl 5-(4-fluoro-*N*-formyl-anilino)thiophene-2-carboxylate (1a-COOMe**)**

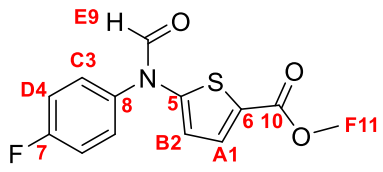

Prepared using general coupling procedure (microwave).

Methyl 5-bromothiophene-2-carboxylate (410 mg, 1.85 mmol), *N*-formyl-4-fluoroaniline (258 mg, 1.85 mmol), CsF (422 mg, 2.78 mmol), Cu(I)I (69 mg, 0.36 mmol), DMEDA (48 mg, 0.55 mmol) and THF (3 ml). Purification with silica gel chromatography (ethyl acetate/hexane, 1:4) yielded **1a**-COOMe as a colourless solid (60 mg, 0.21 mmol, 11%). MP: 95 – 97 °C. ^{1}H NMR (500 MHz, DMSO-d_6) δ 8.53 (s, 1H), 7.69 – 7.63 (m, 2H), 7.58 (d, J = 4.3 Hz, 1H), 7.49 – 7.43 (m, 2H), 6.25 (d, J = 4.3 Hz, 1H), 3.81 (s, 3H). ^{13}C NMR (126 MHz, DMSO-d_6) δ 162.89 (s), 162.72 (d, $^{1}J_{C\text{-}F}$ = 246.7 Hz), 161.53 (s), 147.38 (s), 134.92 (d, $^{4}J_{C\text{-}F}$ = 2.8 Hz), 131.67 (s), 131.20 (d, $^{3}J_{C\text{-}F}$ = 9.2 Hz), 124.35 (s), 117.58 (d, $^{2}J_{C\text{-}F}$ = 23.0 Hz), 114.63 (s), 52.47 (s). ^{19}F NMR (376 MHz, DMSO-d_6) δ -111.63 (s), -112.91 (s). HRMS EI m/z (M^{+}) = 279.03463 (expected 279.03654).

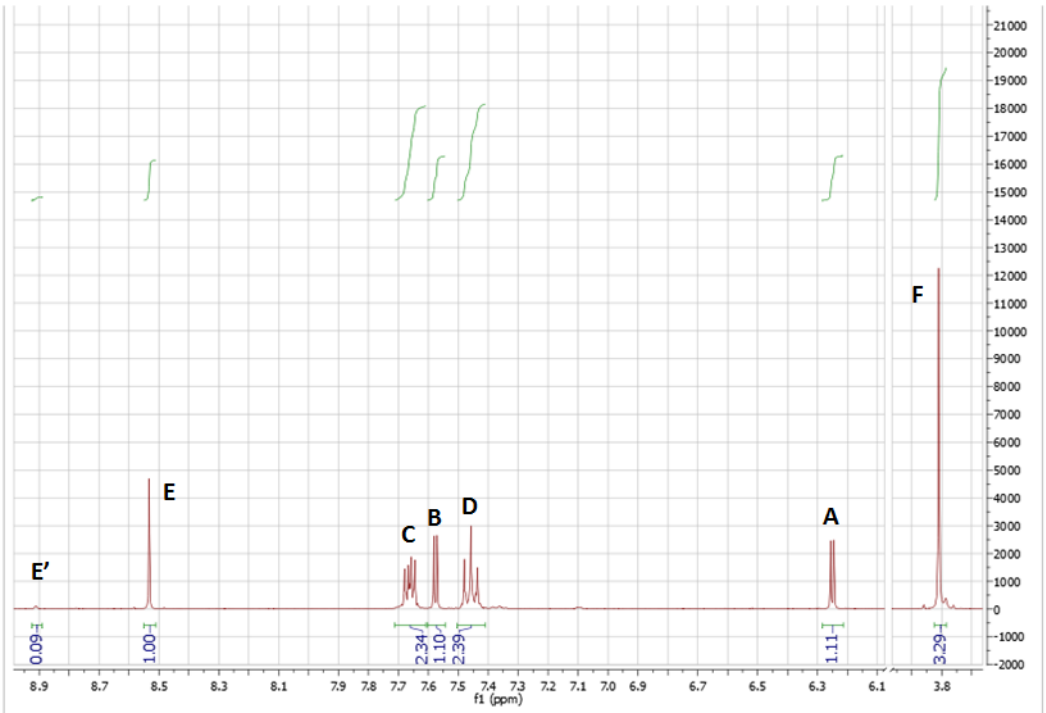

_N_-(4-fluorophenyl)-_N_-(3-thienyl)formamide (1b-H)

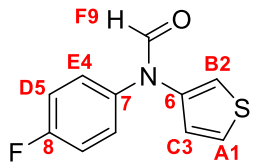

Prepared using general coupling procedure (microwave). 3-Bromothiophene (500 mg, 3.07 mmol), *N*-formyl-4-fluoroaniline (427 mg, 3.07 mmol), CsF (699 mg, 4.61 mmol), Cu(I)I (117 mg, 0.61 mmol), DMEDA (81 mg, 0.92 mmol) and THF (3 ml). Purification with silica gel chromatography (ethyl acetate/hexane, 1:4) yielded **1b**-H as a pale brown solid (150 mg, 0.68 mmol, 22%). MP: 53 – 55 ºC, ^{1}H NMR (500 MHz, DMSO-d_6) δ 8.73 (s, 1H*), 8.48 (s, 1H), 7.63 (dt, J = 8.8, 4.4 Hz, 1H*), 7.55 (dt, J = 9.0, 4.5 Hz, 1H), 7.42 (tdt, J = 4.6, 3.2, 2.5 Hz, 4H*), 7.37 – 7.26 (m, 7H*), 7.00 (ddd, J = 8.2, 5.2, 1.4 Hz, 2H*).^{13}C NMR (126 MHz, DMSO-d_6) δ 162.21 (d, $^{2}J_{C\text{-}F}$ = 70.0 Hz), 162.16 (s), 161.86 (s)*, 160.27* (d, $^{2}J_{C\text{-}F}$ = 69.4 Hz), 140.67* (s), 138.47 (s), 137.88* (d, J = 2.8 Hz), 136.16 (d, $^{4}J_{C\text{-}F}$ = 2.8 Hz), 128.80* (d, $^{3}J_{C\text{-}F}$ = 8.7 Hz), 128.65 (d, J = 8.8 Hz), 127.77* (s), 125.97 (s), 124.14 (s), 123.83* (s), 117.02 (d, J = 22.9 Hz), 116.65* (s), 116.51* (d, J = 22.8 Hz), 116.35 (s). ^{19}F NMR (376 MHz, DMSO-d_6) δ -114.58 (s), -114.99 (s). HRMS EI m/z (M^{+}) = 221.03127 (expected 221.03106).

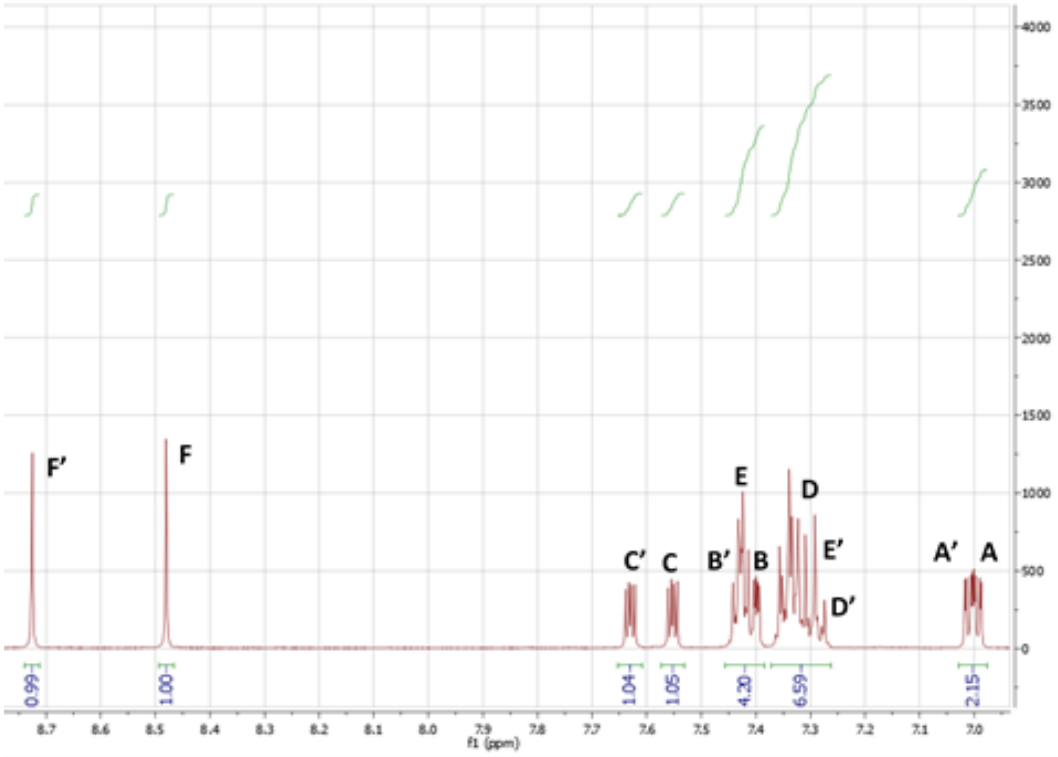

***N*-(4-fluorophenyl)-*N*-(5-methyl-3-thienyl)formamide (1b-Me)**

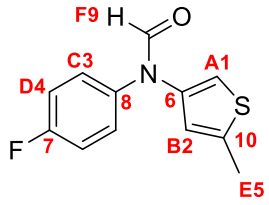

Prepared using general coupling procedure (microwave).

4-Bromo-2-methylthiophene (500 mg, 2.82 mmol), *N*-formyl-4-fluoroaniline (393 mg, 2.82 mmol), CsF (643 mg, 4.23 mmol), Cu(I)I (107 mg, 0.56 mmol), DMEDA (70 mg, 0.85 mmol) and THF (3 ml). Purification with silica gel chromatography (ethyl acetate/hexane, 1:4) yielded **1b**-Me as a pale yellow oil (120 mg, 0.51 mmol, 18%). ^{1}H NMR (500 MHz, DMSO-d_6) δ 8.67 (s, 1H), 8.44 (s, 1H*), 7.43 – 7.38 (m, 2H), 7.36 – 7.25 (m, 6H*), 7.15 (d, J = 1.4 Hz, 2H*), 6.70 (s, 2H*), 2.40 (s, 6H*). ^{13}C NMR (126 MHz, DMSO-d_6) δ 161.99 (s), 161.78* (s), 161.48 (d, $^{1}J_{C\text{-}F}$ = 244.6 Hz), 160.92* (d, $^{1}J_{C\text{-}F}$ = 243.9 Hz), 140.75 (s), 139.68* (s), 138.83* (s), 137.81* (d, $^{4}J_{C\text{-}F}$ = 2.8 Hz), 137.58 (s), 136.03 (d, $^{4}J_{C\text{-}F}$ = 2.8 Hz), 128.70 (d, $^{3}J_{C\text{-}F}$ = 8.7 Hz), 128.60* (d, $^{3}J_{C\text{-}F}$ = 8.9 Hz), 122.49* (s), 122.16 (s), 116.97* (d, $^{2}J_{C\text{-}F}$ = 22.8 Hz), 116.47 (d, $^{2}J_{C\text{-}F}$ = 22.7 Hz), 114.31* (s), 114.03 (s), 15.70 (s), 15.57* (s). ^{19}F NMR (376 MHz, DMSO-d_6) δ -114.66 (s), -115.06 (s). HRMS EI m/z (M^{+}) = 235.04979 (expected 235.04671).

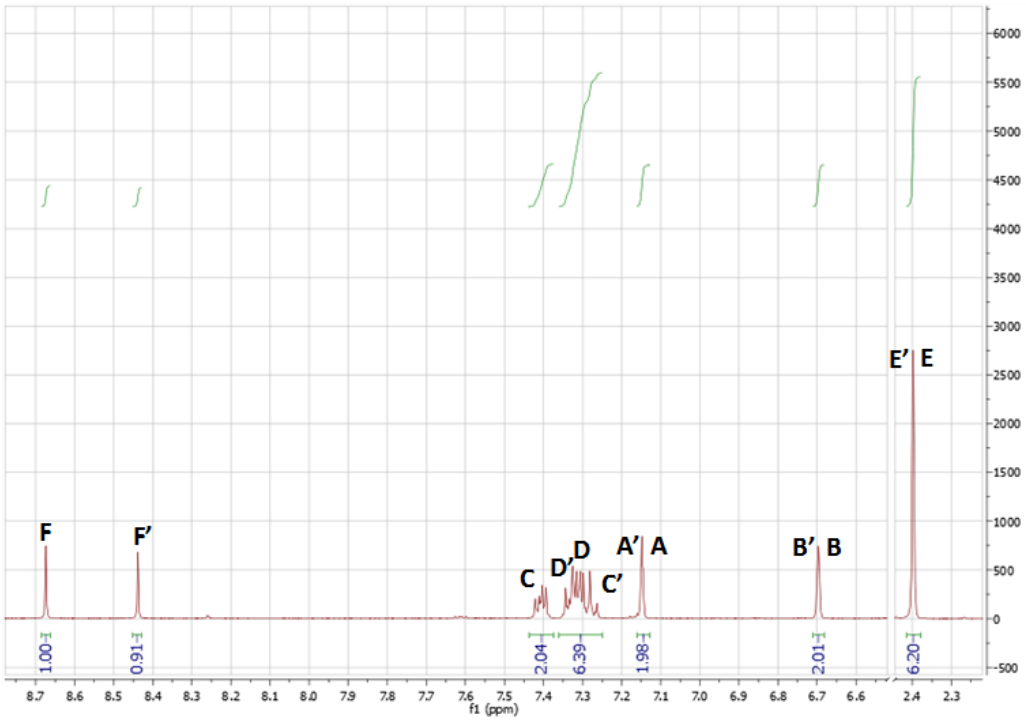

***N*-(4-fluorophenyl)-*N*-(5-formyl-3-thienyl)formamide (1b-CHO)**

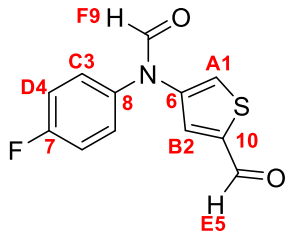

Prepared using the general coupling procedure (microwave).

4-Bromo-2-thiophenecarboxaldehyde (500 mg, 2.62 mmol), *N*-formyl-4-fluoroaniline (393 mg, 2.62 mmol), CsF (597 mg, 3.93 mmol), Cu(I)I (100 mg, 0.52 mmol), DMEDA (70 mg, 0.77 mmol) and THF (3 ml). Purification with silica gel chromatography (ethyl acetate/hexane, 3:7) yielded **1b**-CHO as a brown oil (170 mg, 0.68 mmol, 26%). ^{1}H NMR (500 MHz, DMSO-*d*$_6$) δ 9.90 (d, *J* = 1.2 Hz, 1H), 9.87 (d, *J* = 1.1 Hz, 1H*), 8.79 (s, 1H*), 8.51 (s, 1H), 7.96 (dd, *J* = 2.9, 1.5 Hz, 1H*), 7.94 (d, *J* = 1.6 Hz, 1H), 7.91 (d, *J* = 1.6 Hz, 1H*), 7.53 – 7.48 (m, 2H), 7.41 – 7.35 (m, 3H*), 7.35 – 7.30 (m, 1H*). ^{13}C NMR (126 MHz, DMSO-*d*$_6$) δ 184.96 (s), 184.71* (s), 162.14 (s), 162.12* (s), 161.83 (d, $^{1}J_{C\text{-}F}$ = 245.2 Hz), 161.28* (d, $^{1}J_{C\text{-}F}$ = 244.5 Hz), 143.19 (s), 141.97* (s), 141.72* (s), 139.41 (s), 137.10 (d, $^{4}J_{C\text{-}F}$ = 2.8 Hz), 135.59* (d, $^{4}J_{C\text{-}F}$ = 2.9 Hz), 133.34 (s), 132.90* (s), 129.28* (d, $^{3}J_{C\text{-}F}$ = 8.8 Hz), 129.18 (d, $^{3}J_{C\text{-}F}$ = 8.9 Hz), 125.79 (s), 124.97* (s), 117.25 (d, $^{2}J_{C\text{-}F}$ = 22.9 Hz), 116.77* (d, $^{2}J_{C\text{-}F}$ = 22.7 Hz). ^{19}F NMR (376 MHz, DMSO-*d*$_6$) δ -113.91 (s), -114.39 (s). HRMS EI m/z (M^{+}) = 249.02411 (expected 249.02598).

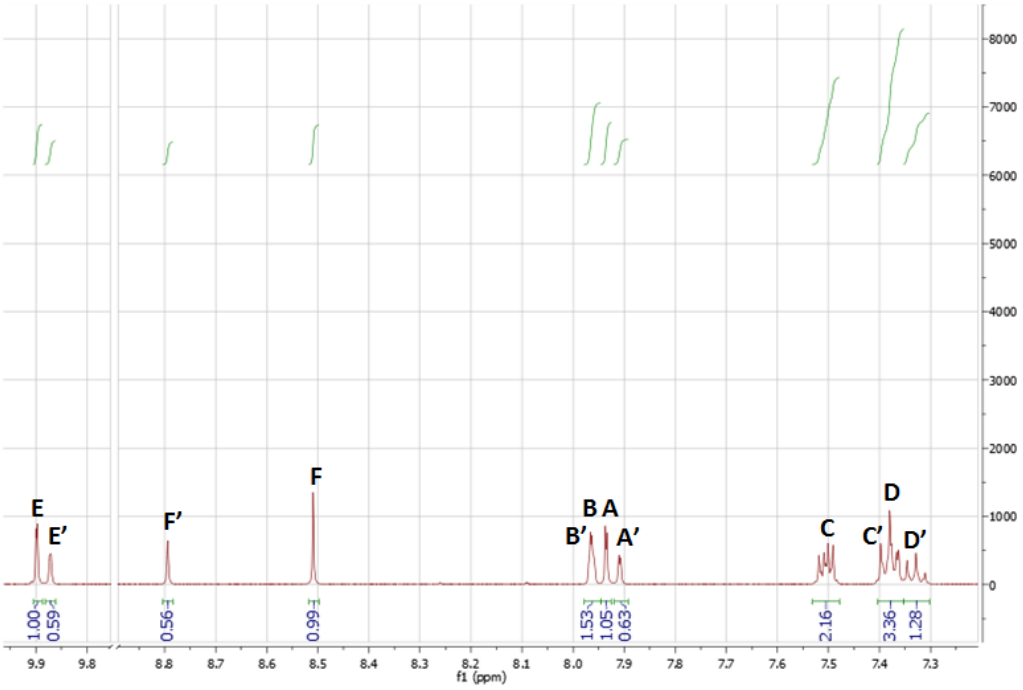

***N*-(4-fluorophenyl)-*N*-selenophen-2-yl-formamide (1c)**

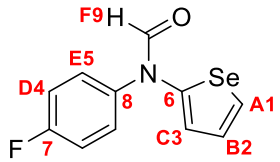

Synthetic precursor, 2-bromoselenophene was prepared using a procedure based on the literature.[2] In brief, a solution of selenophene (884 mg, 6.75 mmol) in DCM/Acetic acid (7:3, 40 ml) was cooled to 0 °C. *N*-Bromosuccinimide (1.2 g, 6.75 mmol) was added and the reaction was allowed to warm to room temperature and was allowed to stir overnight. The reaction was cooled and diluted with an equal volume of DCM and washed with saturated $NaHCO_3$. The organics were collected, dried over $MgSO_4$, filtered and concentrated to give a brown oil. The crude product was used directly in the next step to minimize oxidation. Next, the title compound was synthesized using the general procedure (thermal). 2-Bromoselenophene (1.04 g, 4.95 mmol), *N*-formyl-4-fluoroaniline (689 mg, 4.95 mmol), CsF (1.13 g, 7.43 mmol), Cu(I)I (189 mg, 0.99 mmol), DMEDA (131 mg, 1.49 mmol) and THF (10 ml). Purification with silica gel chromatography (ethyl acetate/hexane, 1:4) yielded **1c** as a pale brown solid (60 mg, 0.22 mmol, 4%). MP: 108 – 110 °C, ^{1}H NMR (500 MHz, DMSO-*d*$_6$) δ 8.46 (s, 1H), 7.77 (dd, *J* = 6.1, 1.2 Hz, 1H), 7.62 – 7.59 (m, 2H), 7.46 – 7.42 (m, 2H), 7.06 (dd, *J* = 6.1, 4.1 Hz, 1H), 6.28 (dd, *J* = 4.1, 1.2 Hz, 1H). ^{13}C NMR (126 MHz, DMSO-*d*$_6$) δ 162.48 (d, $^{1}J_{C\text{-}F}$ = 246.3 Hz), 160.63 (s), 143.77 (s), 135.89 (d, $^{4}J_{C\text{-}F}$ = 2.9 Hz), 131.01 (d, $^{3}J_{C\text{-}F}$ = 9.1 Hz), 126.02 (s), 125.32 (s), 117.42 (d, $^{2}J_{C\text{-}F}$ = 22.9 Hz), 114.69 (s). ^{19}F NMR (376 MHz, DMSO-*d*$_6$) δ -112.20 (s), -114.22 (s). HRMS EI (M^+) = 268.97531 (expected 268.97551).

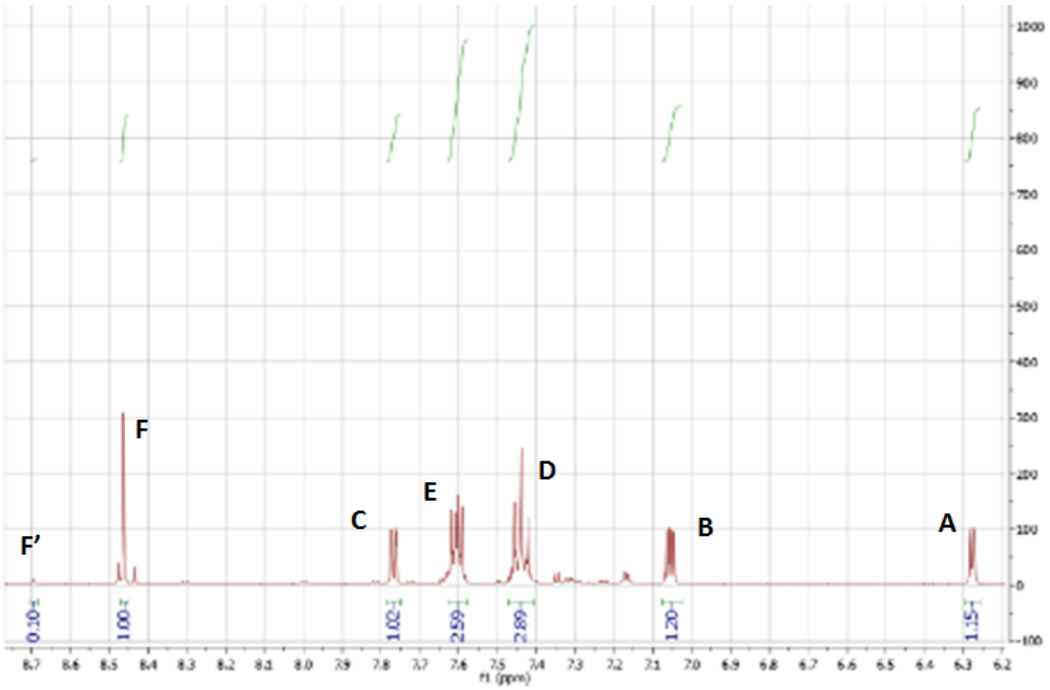
F
F'
C
E
D
B
A
0.10
1.00
1.02
2.59
2.89
1.20
1.15
f1 (ppm)

N-(4-fluorophenyl)-*N*-(2-thienyl)thioformamide (2a-H)

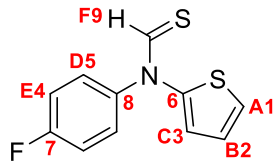

Prepared using the general Lawesson's reaction procedure. **1a**-H (190 mg, 0.86 mmol) and Lawesson's reagent (348 mg, 0.86 mmol) in dioxane (10 ml). Purification with silica gel chromatography (ethyl acetate/hexane, 1:4) yielded **2a**-H as a dark green solid (140 mg, 0.59 mmol, 68%). MP: 40 – 42 °C, ^{1}H NMR (500 MHz, DMSO-d_6) δ 10.12 (s, 1H*), 9.84 (s, 1H), 7.53 (ddd, J = 9.8, 5.0, 2.6 Hz, 2H*), 7.48 – 7.44 (m, 3H*), 7.42 – 7.35 (m, 5H*), 7.12 (dd, J = 3.8, 1.4 Hz, 1H*), 7.00 (ddd, J = 12.1, 5.5, 3.9 Hz, 2H*), 6.82 (dd, J = 3.9, 1.4 Hz, 1H). ^{13}C NMR (126 MHz, DMSO-d_6) δ 191.94* (s), 190.68 (s), 162.10 (d, $^{1}J_{C\text{-}F}$ = 246.3 Hz), 161.86* (d, $^{1}J_{C\text{-}F}$ = 245.9 Hz), 148.70* (s), 143.11 (s), 142.21* (d, $^{4}J_{C\text{-}F}$ = 2.9 Hz), 138.65 (d, $^{4}J_{C\text{-}F}$ = 3.1 Hz), 130.24* (d, $^{3}J_{C\text{-}F}$ = 9.1 Hz), 127.43 (d, $^{3}J_{C\text{-}F}$ = 9.0 Hz), 126.92* (s), 125.19 (s), 123.65 (s), 123.25 (s), 123.07* (s), 118.52* (s), 117.34* (d, $^{2}J_{C\text{-}F}$ = 23.0 Hz), 117.18 (d, $^{2}J_{C\text{-}F}$ = 23.1 Hz). ^{19}F NMR (376 MHz, DMSO-d_6) δ -112.31 (s), -113.16 (s). HRMS EI m/z (M^+) = 237.00780 (expected 237.00822).

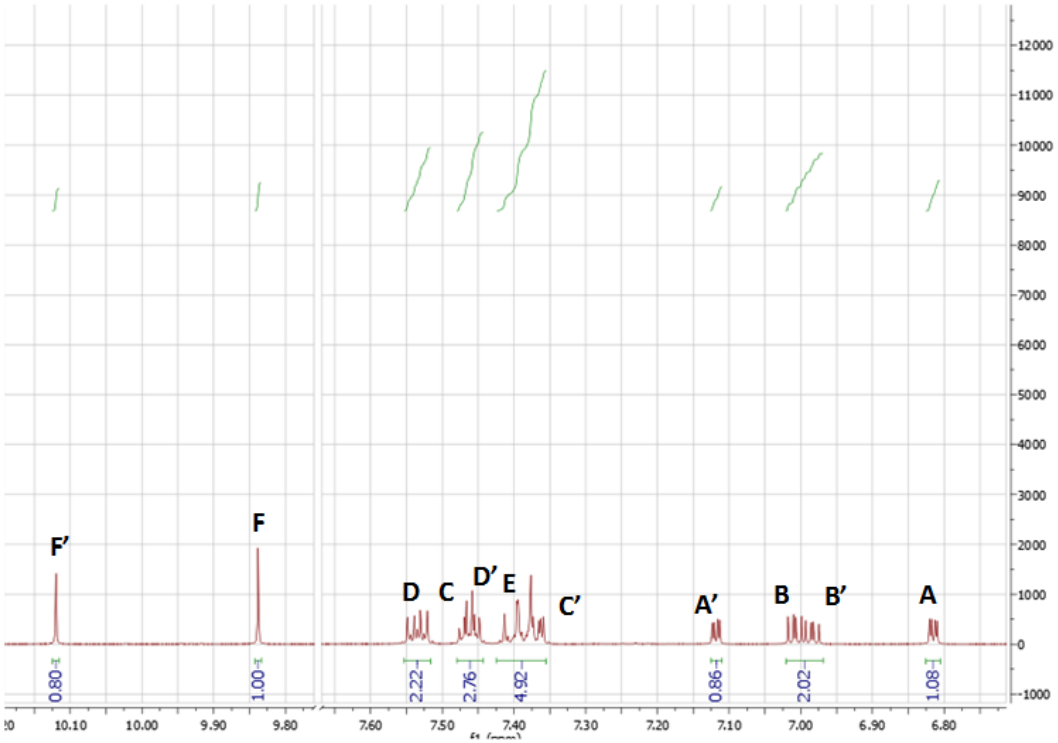

***N*-(4-fluorophenyl)-*N*-(5-methyl-2-thienyl)thioformamide (2a-Me)**

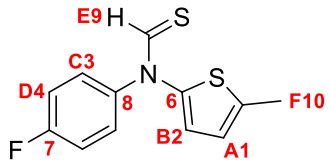

Prepared using the general Lawesson's reaction procedure. **1a**-Me (80 mg, 0.34 mmol) and Lawesson's reagent (138 mg, 0.34 mmol) in dioxane (10 ml). Purification with silica gel chromatography (ethyl acetate/hexane, 1:4) yielded **2a**-Me as a dark green oil (40 mg, 0.16 mmol, 47%).^{1}H NMR (500 MHz, DMSO-*d*$_6$) δ 10.01 (s, 1H*), 9.79 (s, 1H), 7.54 – 7.47 (m, 2H), 7.46 – 7.40 (m, 1H*), 7.40 – 7.31 (m, 4H*), 6.91 (d, *J* = 3.7 Hz, 1H*), 6.70 (dt, *J* = 3.5, 1.1 Hz, 1H), 6.68 – 6.65 (m, 1H*), 6.62 (d, *J* = 3.8 Hz, 1H), 2.43 (d, *J* = 1.1 Hz, 3H), 2.36 (d, *J* = 1.1 Hz, 2H*). ^{13}C NMR (126 MHz, DMSO-*d*$_6$) δ 191.61 (s), 190.45* (s), 140.28 (s), 137.03 (s), 136.73 (s), 130.07 (d, $^{3}J_{C\text{-}F}$ = 9.1 Hz), 127.13 (d, $^{3}J_{C\text{-}F}$ = 9.0 Hz), 124.78 (s), 123.51 (s), 123.34 (s), 118.93 (s), 117.24 (d, $^{2}J_{C\text{-}F}$ = 23.1 Hz), 117.09 (d, $^{2}J_{C\text{-}F}$ = 23.1 Hz). ^{19}F NMR (376 MHz, DMSO-*d*$_6$) δ -112.49 (s), -113.43 (s). HRMS EI m/z (M^{+}) = 251.02236 (expected 251.02387).

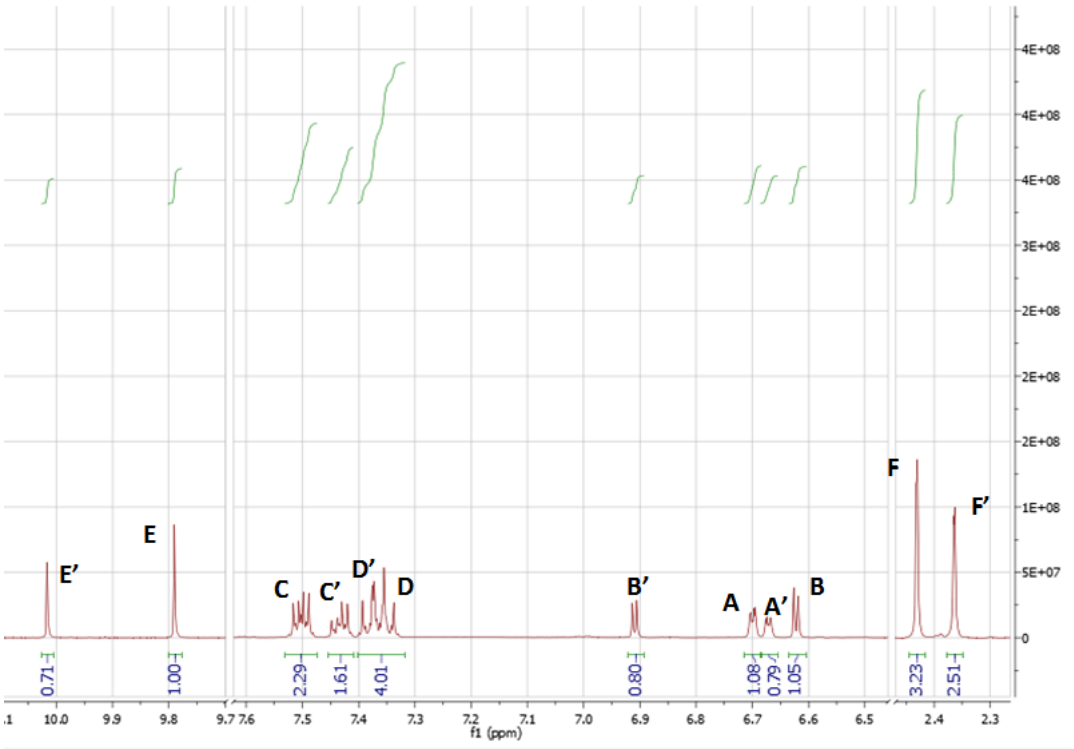

***N*-(5-chloro-2-thienyl)-*N*-(4-fluorophenyl)thioformamide (2a-Cl)**

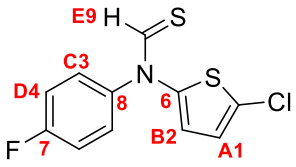

Prepared using the general Lawesson's reaction procedure. **1a**-Cl (80 mg, 0.31 mmol) and Lawesson's reagent (127 mg, 0.31 mmol) in dioxane (10 ml). Purification with silica gel chromatography (ethyl acetate/hexane, 1:4) yielded **2a**-Cl as a dark green oil (60 mg, 0.22 mmol, 71%).^{1}H NMR (500 MHz, DMSO-d_6) δ 10.10 (s, 1H), 9.71 (s, 1H*), 7.64 – 7.58 (m, 2H), 7.50 – 7.45 (m, 2H*), 7.45 – 7.38 (m, 3H*), 7.05 (q, J = 4.2 Hz, 1H*), 7.01 (d, J = 4.4 Hz, 1H*), 6.44 (d, J = 4.4 Hz, 1H*). ^{13}C NMR (126 MHz, DMSO-d_6) δ 192.46* (s), 188.75 (s), 162.39* (d, $^{1}J_{C\text{-}F}$ = 246.8 Hz), 162.24 (d, $^{1}J_{C\text{-}F}$ = 246.6 Hz), 146.26* (s), 140.68 (d, $^{4}J_{C\text{-}F}$ = 3.0 Hz), 130.28* (d, $^{3}J_{C\text{-}F}$ = 9.1 Hz), 128.85 (d, $^{3}J_{C\text{-}F}$ = 9.1 Hz), 126.72* (s), 124.12 (s), 123.65 (s), 120.40 (s), 118.50* (s), 117.45 (d, $^{2}J_{C\text{-}F}$ = 23.2 Hz). HRMS EI m/z (M^{+}) = 270.96783 (expected 270.96925).

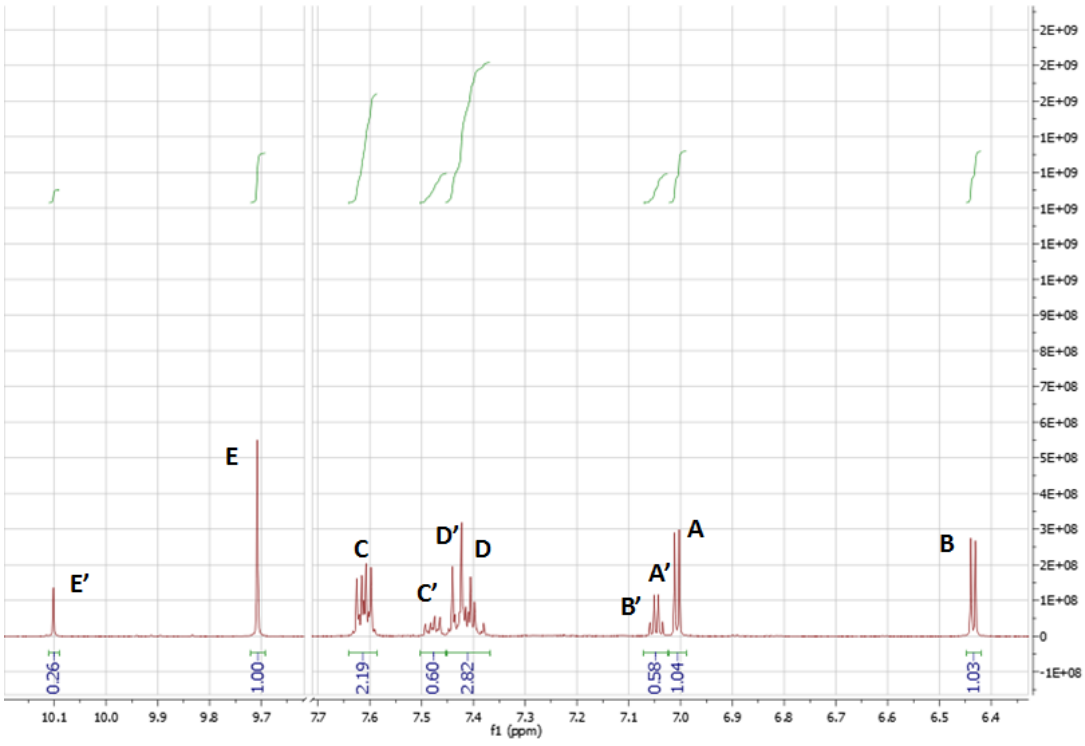

N-(4-fluorophenyl)-*N*-(3-thienyl)thioformamide (2b)

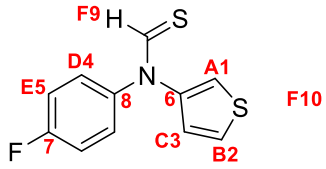

Prepared using the general Lawesson's reaction procedure. **1b**-H (40 mg, 0.18 mmol) and Lawesson's reagent (73 mg, 0.18 mmol) in dioxane (10 ml). Purification with silica gel chromatography (ethyl acetate/hexane, 1:4) yielded **2b** as a dark green oil (20 mg, 0.08 mmol, 40%). ^{1}H NMR (500 MHz, DMSO-*d*$_6$) δ 10.19 (s, 1H), 9.93 (s, 1H*), 7.70 (dd, *J* = 3.1, 1.4 Hz, 1H*), 7.66 (dd, *J* = 5.1, 3.1 Hz, 1H*), 7.63 (dd, *J* = 5.3, 3.2 Hz, 1H), 7.42 – 7.36 (m, 5H*), 7.33 – 7.27 (m, 1H*), 7.20 (dd, *J* = 3.2, 1.6 Hz, 1H), 7.16 (dd, *J* = 5.3, 1.5 Hz, 1H), 7.14 (dd, *J* = 5.1, 1.4 Hz, 1H*). ^{13}C NMR (126 MHz, DMSO-*d*$_6$) δ 191.95* (s), 191.38 (s), 161.90 (d, $^{1}J_{C\text{-}F}$ = 245.6 Hz), 144.45 (s), 139.61* (s), 138.16 (d, $^{4}J_{C\text{-}F}$ = 3.0 Hz), 130.36 (d, $^{3}J_{C\text{-}F}$ = 9.0 Hz), 128.01 (s), 126.84* (s), 126.09* (s), 125.67* (d, $^{3}J_{C\text{-}F}$ = 8.7 Hz), 122.61* (s), 121.75 (s), 117.24 (d, $^{2}J_{C\text{-}F}$ = 23.0 Hz), 116.83* (d, $^{2}J_{C\text{-}F}$ = 23.0 Hz), 114.21 (s). HRMS EI (M^{+}) = 237.00823 (expected 237.00822).

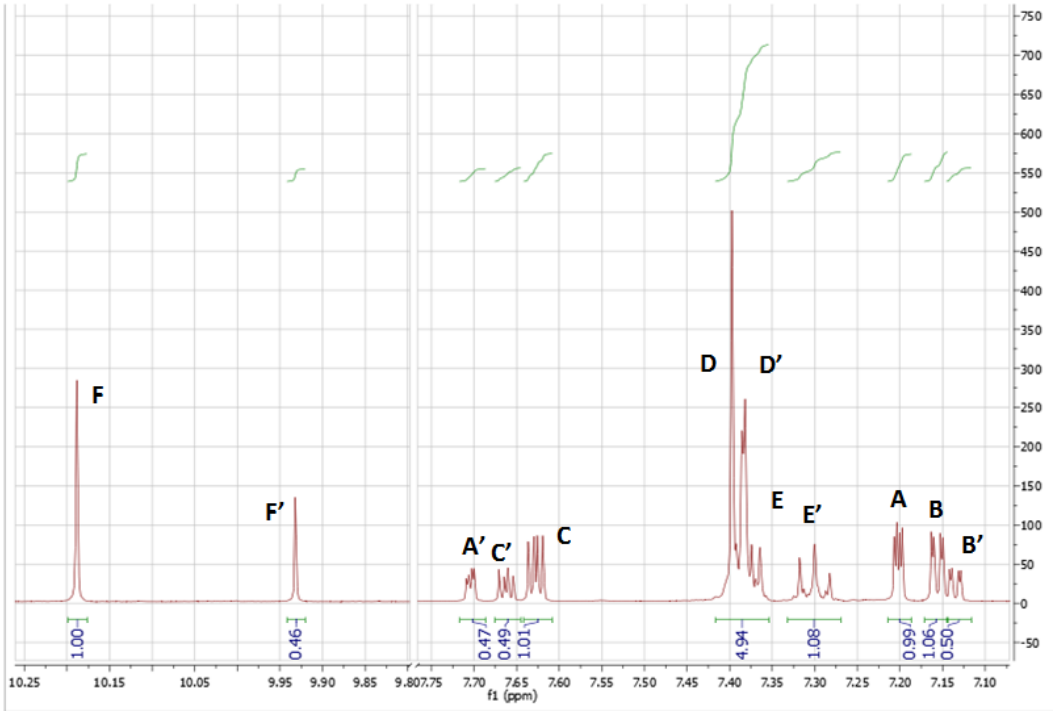

Conformational Free Energies

The following tables present the experimental conformational free energies and associated errors of molecular balances seen in **Chapter 2** (**Figure 2.18**). Conformational free energies below −7.4 kJ mol^{-1} were considered inaccurate, and therefore have been capped at −7.4 kJ mol^{-1}.

Table A.1 Experimental conformational free energy differences of molecular balance **1a**-Me, ΔG_{EXP} measured in various solvents at 298 K.

1a-Me			
		Error	
	ΔG / kJ mol^{-1}	-	+
Benzene-d_6	-2.0	0.17	0.16
CS_2	-1.0	0.12	0.12
Diethyl ether	-1.2	0.12	0.12
Chloroform-d	-1.0	0.12	0.12
Ethyl acetate	-1.7	0.15	0.14
THF	-1.6	0.15	0.14
DCM	-1.3	0.13	0.12
Acetone-d_6	-1.6	0.14	0.14
Ethanol	-1.1	0.12	0.12
Methanol-d_4	-1.1	0.12	0.12
Acetonitrile-d_3	-1.6	0.15	0.14
DMSO-d_6	-2.0	0.17	0.16
C_4F_9OH	-0.2	0.12	0.12

Table A.2 Experimental conformational free energy differences of molecular balance **1a**-H, ΔG_{EXP} measured in various solvents at 298 K.

1a-H			
		Error	
	ΔG / kJ mol^{-1}	-	+
Benzene-d$_6$	-3.2	0.28	0.25
CS$_2$	-2.3	0.19	0.18
Diethyl ether	-2.7	0.24	0.22
Chloroform-d	-2.0	0.17	0.16
Ethyl acetate	-2.5	0.22	0.20
THF	-2.7	0.23	0.21
DCM	-2.3	0.19	0.18
Acetone-d$_6$	-2.7	0.23	0.21
Ethanol	-2.1	0.18	0.17
Methanol-d$_4$	-2.1	0.18	0.17
Acetonitrile-d$_3$	-2.5	0.21	0.19
DMSO-d$_6$	-2.8	0.24	0.22
C$_4$F$_9$OH	-0.9	0.12	0.12

Table A.3 Experimental conformational free energy differences of molecular balance **1a**-Cl, ΔG_{EXP} measured in various solvents at 298 K.

1a-Cl			
		Error	
	ΔG / kJ mol^{-1}	-	+
Benzene-d$_6$	-5.5	0.79	0.60
CS$_2$	-5.1	0.65	0.51
Diethyl ether	-3.1	0.27	0.24
Chloroform-d	-4.1	0.43	0.36
Ethyl acetate	-5.5	0.79	0.60
THF	-5.7	0.88	0.65
DCM	-4.7	0.55	0.45
Acetone-d$_6$	-5.5	0.79	0.60
Ethanol	-5.1	0.65	0.51
Methanol-d$_4$	-5.1	0.65	0.51
Acetonitrile-d$_3$	-5.1	0.65	0.51
DMSO-d$_6$	-5.3	0.71	0.55
C$_4$F$_9$OH	-2.2	0.19	0.17

Table A.4 Experimental conformational free energy differences of molecular balance **1a**-COOMe, ΔG_{EXP} measured in various solvents at 298 K.

1a-COOMe			
		Error	
	ΔG / kJ mol^{-1}	-	+
Benzene-d_6	-7.0	1.72	1.00
CS_2	-6.0	1.00	0.71
Diethyl ether	-6.6	1.39	0.88
Chloroform-d	-5.7	0.88	0.65
Ethyl acetate	-7.0	1.72	1.00
THF	-7.4	2.29	1.14
DCM	-6.3	1.16	0.79
Acetone-d_6	-7.0	1.72	1.00
Ethanol	-7.0	1.72	1.00
Methanol-d_4	-6.3	1.16	0.79
Acetonitrile-d_3	-6.0	1.00	0.71
DMSO-d_6	-6.6	1.39	0.88
C_4F_9OH	-3.2	0.29	0.26

Table A.5 Experimental conformational free energy differences of molecular balance **1a**-COMe, ΔG_{EXP} measured in various solvents at 298 K.

1a-COMe			
		Error	
	ΔG / kJ mol^{-1}	-	+
Benzene-d_6	-6.3	1.16	0.79
CS_2	< -7.4	-	-
Diethyl ether	-7.0	1.72	1.00
Chloroform-d	-5.5	0.79	0.60
Ethyl acetate	-6.3	1.16	0.79
THF	-6.6	1.39	0.88
DCM	-5.7	0.88	0.65
Acetone-d_6	-6.3	1.16	0.79
Ethanol	< -7.4	-	-
Methanol-d_4	< -7.4	-	-
Acetonitrile-d_3	-5.5	0.79	0.60
DMSO-d_6	-5.7	0.88	0.65
C_4F_9OH	-3.3	0.30	0.27

Table A.6 Experimental conformational free energy differences of molecular balance **1a**-CHO, ΔG_{EXP} measured in various solvents at 298 K.

1a-CHO			
		Error	
	ΔG / kJ mol^{-1}	-	+
Benzene-d$_6$	< -7.4	-	-
CS$_2$	< -7.4	-	-
Diethyl ether	< -7.4	-	-
Chloroform-d	-6.3	1.16	0.79
Ethyl acetate	-6.3	1.16	0.79
THF	< -7.4	-	-
DCM	< -7.4	-	-
Acetone-d$_6$	-6.3	1.16	0.79
Ethanol	< -7.4	-	-
Methanol-d$_4$	< -7.4	-	-
Acetonitrile-d$_3$	-5.7	0.88	0.65
DMSO-d$_6$	-6.6	1.39	0.88
C$_4$F$_9$OH	-6.3	1.16	0.79

Table A.7 Experimental conformational free energy differences of molecular balance **1c**, ΔG_{EXP} measured in various solvents at 298 K.

1c			
		Error	
	ΔG / kJ mol^{-1}	-	+
Benzene-d$_6$	-7.4	-	-
CS$_2$	-	-	-
Diethyl ether	-	-	-
Chloroform-d	-6.3	1.16	0.79
Ethyl acetate	-	-	-
THF	-	-	-
DCM	-	-	-
Acetone-d$_6$	-7.4	2.29	1.14
Ethanol	-	-	-
Methanol-d$_4$	-6.3	1.16	0.79
Acetonitrile-d$_3$	-7.0	1.72	1.00
DMSO-d$_6$	-7.4	2.29	1.14
C$_4$F$_9$OH	-	-	-

Table A.8 Experimental conformational free energy differences of molecular balance **1b**-Me, ΔG_{EXP} measured in various solvents at 298 K.

1b-Me			
		Error	
	ΔG / kJ mol^{-1}	-	+
Benzene-d$_6$	0.8	0.12	0.12
CS$_2$	0.9	0.12	0.12
Diethyl ether	0.6	0.12	0.12
Chloroform-d	0.4	0.12	0.12
Ethyl acetate	0.4	0.12	0.12
THF	0.4	0.12	0.12
DCM	0.3	0.12	0.12
Acetone-d$_6$	0.1	0.12	0.12
Ethanol	0.0	0.12	0.12
Methanol-d$_4$	0.1	0.12	0.12
Acetonitrile-d$_3$	0.0	0.12	0.12
DMSO-d$_6$	0.2	0.12	0.12
C$_4$F$_9$OH	0.1	0.12	0.12

Table A.9 Experimental conformational free energy differences of molecular balance **1b**-H, ΔG_{EXP} measured in various solvents at 298 K.

1b-H			
		Error	
	ΔG / kJ mol^{-1}	-	+
Benzene-d$_6$	-1.5	0.14	0.13
CS$_2$	-1.4	0.14	0.13
Diethyl ether	-1.2	0.12	0.12
Chloroform-d	-0.8	0.12	0.12
Ethyl acetate	-0.9	0.12	0.12
THF	-0.7	0.12	0.12
DCM	-1.0	0.12	0.12
Acetone-d$_6$	-0.6	0.12	0.12
Ethanol	-1.0	0.12	0.12
Methanol-d$_4$	-0.3	0.12	0.12
Acetonitrile-d$_3$	-0.4	0.12	0.12
DMSO-d$_6$	-0.1	0.12	0.12
C$_4$F$_9$OH	-0.3	0.12	0.12

Table A.10 Experimental conformational free energy differences of molecular balance **1a**-CHO, ΔG_{EXP} measured in various solvents at 298 K.

1b-CHO			
		Error	
	ΔG / kJ mol^{-1}	-	+
Benzene-d_6	-3.2	0.28	0.25
CS_2	-4.4	0.48	0.40
Diethyl ether	-3.8	0.36	0.32
Chloroform-d	-3.8	0.36	0.32
Ethyl acetate	-2.7	0.24	0.22
THF	-2.8	0.24	0.22
DCM	-3.3	0.30	0.27
Acetone-d_6	-2.3	0.20	0.18
Ethanol	-2.1	0.18	0.17
Methanol-d_4	-2.0	0.17	0.16
Acetonitrile-d_3	-2.0	0.17	0.16
DMSO-d_6	-1.4	0.13	0.13
C_4F_9OH	-3.8	0.36	0.32

Table A.11 Experimental conformational free energy differences of molecular balance **2b**, ΔG_{EXP} measured in various solvents at 298 K.

2b			
		Error	
	ΔG / kJ mol^{-1}	-	+
Benzene-d_6	1.1	0.12	0.12
CS_2	1.0	0.12	0.12
Diethyl ether	1.4	0.12	0.12
Chloroform-d	1.5	0.12	0.12
Ethyl acetate	1.6	0.12	0.12
THF	1.7	0.12	0.12
DCM	1.8	0.12	0.12
Acetone-d_6	1.8	0.12	0.12
Ethanol	1.5	0.12	0.12
Methanol-d_4	1.6	0.12	0.12
Acetonitrile-d_3	1.5	0.12	0.12
DMSO-d_6	2.5	0.12	0.12
C_4F_9OH	1.0	0.12	0.12

Table A.12 Experimental conformational free energy differences of molecular balance **2a**-Me, ΔG_{EXP} measured in various solvents at 298 K.

2a-Me			
		Error	
	ΔG / kJ mol^{-1}	-	+
Benzene-d_6	1.3	0.12	0.12
CS_2	0.5	0.12	0.12
Diethyl ether	0.7	0.12	0.12
Chloroform-d	0.3	0.12	0.12
Ethyl acetate	0.8	0.12	0.12
THF	0.8	0.12	0.12
DCM	0.4	0.12	0.12
Acetone-d_6	0.6	0.12	0.12
Ethanol	0.5	0.12	0.12
Methanol-d_4	0.4	0.12	0.12
Acetonitrile-d_3	0.5	0.12	0.12
DMSO-d_6	0.6	0.12	0.12
C_4F_9OH	0.1	0.12	0.12

Table A.13 Experimental conformational free energy differences of molecular balance **2a**-H, ΔG_{EXP} measured in various solvents at 298 K.

2a-H			
		Error	
	ΔG / kJ mol^{-1}	-	+
Benzene-d_6	-1.3	0.13	0.12
CS_2	-0.7	0.12	0.12
Diethyl ether	-0.7	0.12	0.12
Chloroform-d	-0.4	0.12	0.12
Ethyl acetate	-1.1	0.12	0.12
THF	-0.9	0.12	0.12
DCM	-0.3	0.12	0.12
Acetone-d_6	-0.6	0.12	0.12
Ethanol	-0.5	0.12	0.12
Methanol-d_4	-0.4	0.12	0.12
Acetonitrile-d_3	-0.5	0.12	0.12
DMSO-d_6	-0.6	0.12	0.12
C_4F_9OH	-0.3	0.12	0.12

Table A.14 Experimental conformational free energy differences of molecular balance **2a**-Cl, ΔG_{EXP} measured in various solvents at 298 K.

2a-Cl			
		Error	
	ΔG / kJ mol^{-1}	-	+
Benzene-d_6	-4.1	0.43	0.36
CS_2	-3.8	0.36	0.32
Diethyl ether	-4.1	0.43	0.36
Chloroform-d	-3.1	0.27	0.24
Ethyl acetate	-3.9	0.38	0.33
THF	-4.2	0.45	0.38
DCM	-3.2	0.29	0.26
Acetone-d_6	-3.8	0.36	0.32
Ethanol	-3.8	0.36	0.32
Methanol-d_4	-3.3	0.30	0.27
Acetonitrile-d_3	-3.3	0.30	0.27
DMSO-d_6	-3.2	0.28	0.25
C_4F_9OH	-0.9	0.12	0.12

The conformational free energies were measured at a range of concentrations to investigate if the interaction was concentration dependent (**Chapter 2, Figure 2.19**).

Table A.15 Free energies of balance **1a**-Cl at varying concentrations in three different solvents.

Concentration/ mM	$CDCl_3$ ΔG/ kJmol^{-1}	Benxene-d_6 ΔG/ kJmol^{-1}	DMSO-d_6 ΔG /kJmol^{-1}
200	-4.39	-5.25	-5.25
100	-4.39	-5.25	-5.25
50	-4.39	-5.25	-5.25
10	-4.39	-5.25	-5.25
1	-4.39	-5.25	-5.25

Calculated conformational free energies

The absolute energy differences between the two conformers was measured to give ΔE_{CALC} using different methods, which was then used to plot against experimentally measured conformational free energies (**Figures 2.23-2.25**).

Table A.16 Calculated conformational energy differences of full balance series **1** and **2** calculated using B3LYP/6-311G*. Data in final column calculated at B3LYP/6-31G* using the implicit solvent model SM8 for chloroform in Spartan '14.[a] Not supported by basis set.

Compound	Closed conformer E/ kJ mol^{-1}	Open conformer E / kJ mol^{-1}	ΔE_{CALC}/ kJ mol^{-1}	ΔE_{CALC} (SM8 $CHCl_3$)/ kJ mol^{-1}
1a-H	-2762427.95	-2762426.92	-1.03	-3.13
1a-Me	-2865679.57	-2865680.05	0.48	-1.76
1a-Cl	-3969155.51	-3969150.82	-4.69	-7.74
1a-COMe	-3163316.09	-3163308.97	-7.12	-11.25
1a-CHO	-3060052.79	-3060043.91	-8.88	-11.05
1a-COOMe	-3360890.81	-3360883.45	-7.36	-12.38
1b-H	-2762431.96	-2762430.56	-1.40	-1.6
1b-Me	-2865683.85	-2865683.75	-0.10	-0.87
1b-CHO	-3060050.77	-3060044.91	-5.86	-3.91
1c	-8022174.03	-8022164.72	-9.31	-[a]
2a-H	-3610348.76	-3610347.33	-1.43	-3
2a-Me	-3713601.88	-3713603.75	1.87	0.42
2a-Cl	-4817073.79	-4817070.38	-3.41	-6.23
2b	-3610354.73	-3610355.92	1.19	0.9

Table A.17: Calculated conformational energy differences of full balance series **1** and **2** calculated using M06-2X/6-311G*.

Compound	Closed conformer *E*/ kJ mol^{-1}	Open conformer *E* / kJ mol^{-1}	ΔE_{CALC}/ kJ mol^{-1}
1a-H	-2761693.57	-2761689.26	-4.31
1a-Me	-2864891.03	-2864891.98	0.95
1a-Cl	-3968359.91	-3968356.00	-3.91
1a-COMe	-3162422.68	-3162416.43	-6.25
1a-CHO	-3059208.79	-3059201.05	-7.74
1a-COOMe	-3359937.63	-3359931.31	-6.32
1b-H	-2761699.73	-2761698.01	-1.72
1b-Me	-2864897.62	-2864897.10	-0.52
1b-CHO	-3059208.76	-3059203.78	-4.98
1c	-8021528.88	-8021520.70	-8.18
2a-H	-3609598.50	-3609596.87	-1.63
2a-Me	-3712797.32	-3712799.05	1.73
2a-Cl	-4816262.08	-4816259.10	-2.98
2b	-3609606.19	-3609607.14	0.95

Table A.18 Calculated conformational energy differences of full balance series **1** and **2** calculated using ωB97X-D/6-311G*.

Compound	Closed conformer *E*/ kJ mol^{-1}	Open conformer *E* / kJ mol^{-1}	ΔE_{CALC}/ kJ mol^{-1}
1a-H	-2761801.71	-2761801.18	-0.53
1a-Me	-2865021.03	-2865022.49	1.46
1a-Cl	-3968487.29	-3968483.33	-3.96
1a-COMe	-3162557.83	-3162551.61	-6.22
1a-CHO	-3059323.21	-3059315.07	-8.14
1a-COOMe	-3360070.44	-3360064.08	-6.36
1b-H	-2761809.20	-2761807.20	-2.00
1b-Me	-2865029.30	-2865028.56	-0.74
1b-CHO	-3059325.11	-3059319.29	-5.82
1c	-8021667.76	-8021658.69	-9.07
2a-H	-3609730.05	-3609727.86	-2.19
2a-Me	-3712951.17	-3712952.56	1.39
2a-Cl	-4816412.32	-4816409.06	-3.26
2b	-3609738.14	-3609739.65	1.51

Further molecular balances were used to further validate the molecular orbital plot seen in **Figure 2.33**.

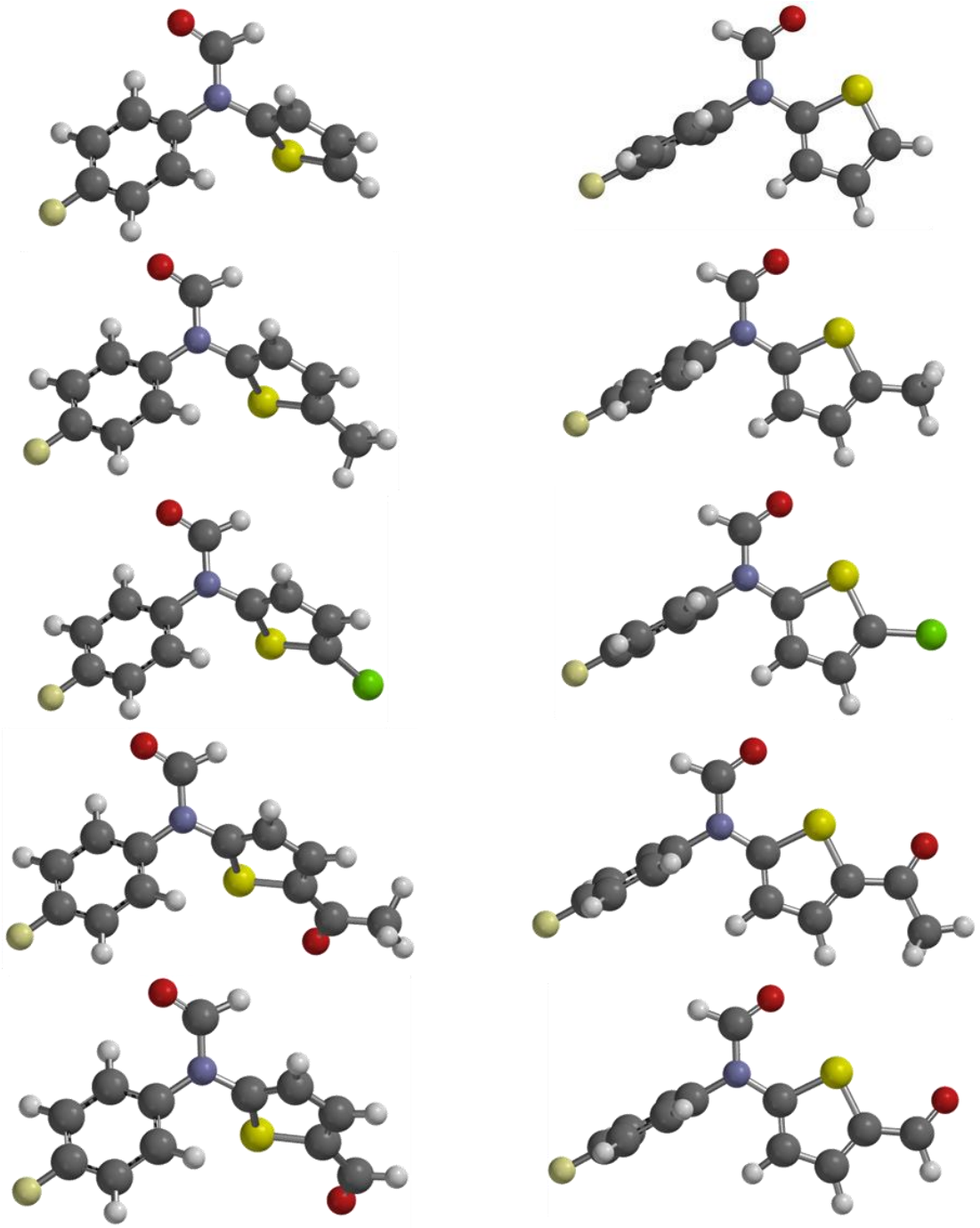

Figure A.1 Minimised structures of molecular balances in series **1**. Minimised using Spartan ’14 DFT/B3LYP/6-311G*.

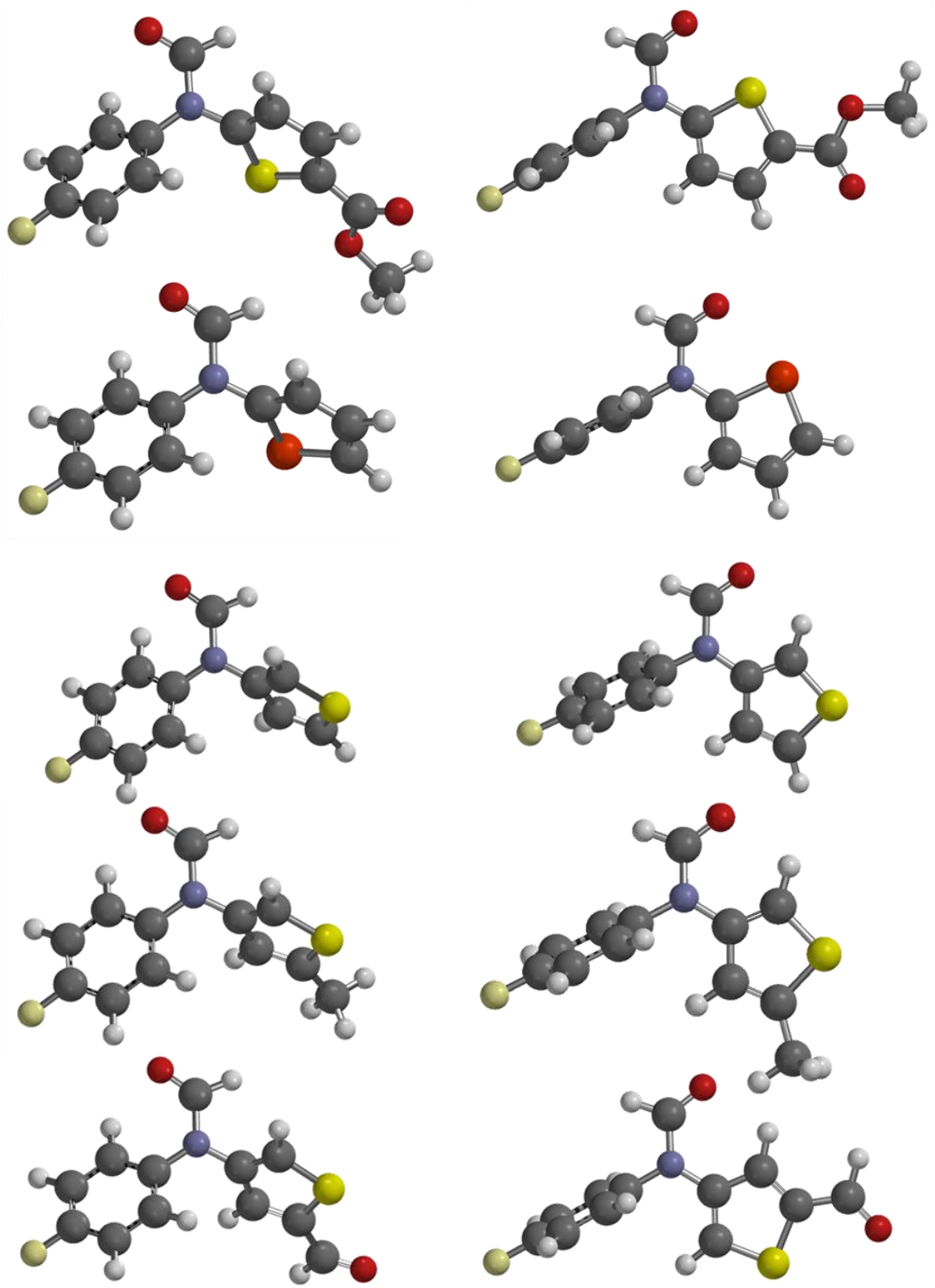

Figure A.2 Minimised structures of molecular balances in series **1**. Minimised using Spartan ’14 DFT/B3LYP/6-311G*.

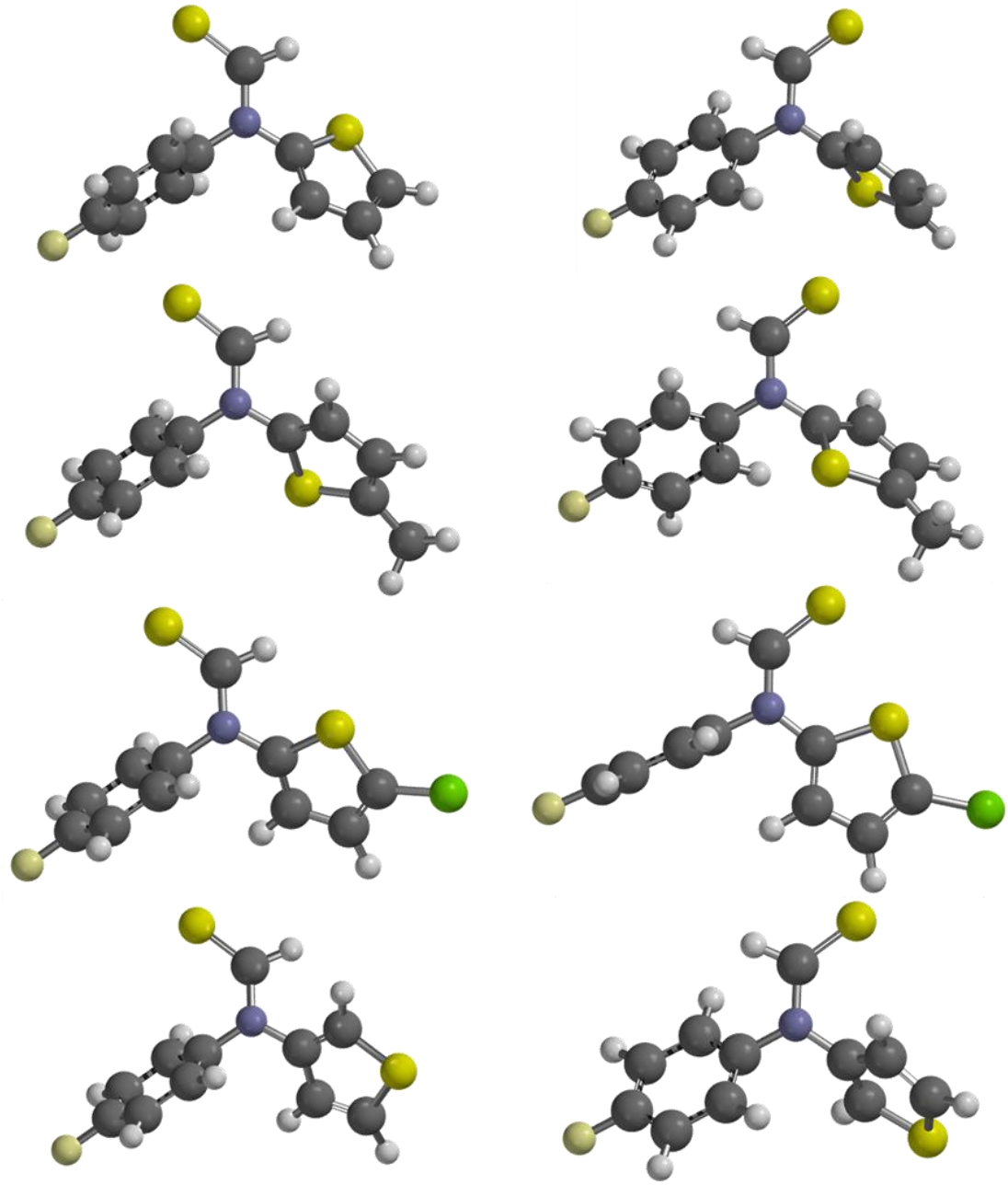

Figure A.3 Minimised structures of molecular balances from series **2**. Minimised using Spartan '14 DFT/B3LYP/6-311G*.

Table A.19 Calculated conformational energy differences of full balances used for comparative validation versus simplified balances. Data calculated using B3LYP/6-311G* (top), M06-2X/6-311G* (middle) and ωB97X-D/6-311G* (bottom).

Compound	Closed conformer *E*/ kJ mol^{-1}	Open conformer *E* / kJ mol^{-1}	ΔE_{CALC}/ kJ mol^{-1}
1a-NO_2	-3299489.79	-3299476.28	-13.51
1a-NMe_2	-3114228.16	-3114233.89	5.73
1a-F	-3023021.23	-3023020.01	-1.22
1a-CF_3	-3647589.83	-3647581.83	-8.00
1a-SF_5	-5117071.38	-5117058.54	-12.84
1a-SMe	-3911179.69	-3911175.54	-4.15
1a-CN	-3004677.60	-3004665.54	-12.06

Compound	Closed conformer *E*/ kJ mol^{-1}	Open conformer *E* / kJ mol^{-1}	ΔE_{CALC}/ kJ mol^{-1}
1a-NO_2	-3298558.05	-3298545.84	-12.21
1a-NMe_2	-3113339.41	-3113344.82	5.41
1a-F	-3022215.35	-3022214.83	-0.52
1a-CF_3	-3646603.38	-3646595.99	-7.39
1a-SF_5	-5115863.70	-5115852.74	-10.96
1a-SMe	-3910312.55	-3910309.70	-2.85
1a-CN	-3003866.37	-3003855.38	-10.99

Compound	Closed conformer *E*/ kJ mol^{-1}	Open conformer *E* / kJ mol^{-1}	ΔE_{CALC}/ kJ mol^{-1}
1a-NO_2	-3298685.85	-3298673.37	-12.48
1a-NMe_2	-3113494.85	-3113501.61	6.76
1a-F	-3022325.92	-3022325.36	-0.56
1a-CF_3	-3646730.18	-3646722.73	-7.45
1a-SF_5	-5116048.73	-5116037.33	-11.40
1a-SMe	-3910470.66	-3910467.51	-3.15
1a-CN	-3003952.84	-3003941.64	-11.20

The predicted conformation free energies, ΔE_{CALC}, were then calculated for the simplified molecular balances (**Figure A.4**). A ‘ denotes the simplified molecular orbital.

Table A.20 Calculated conformational energy differences of simplified balances in the **1’** and **2’** series determined using B3LYP/6-311G*.

Compound	Closed conformer E/ kJ mol^{-1}	Open conformer E / kJ mol^{-1}	ΔE_{CALC}/ kJ mol^{-1}
1’a-H	-1895074.91	-1895067.94	-6.97
1’a-Me	-1998326.54	-1998320.92	-5.62
1’a-Cl	-3101801.51	-3101793.11	-8.40
1’a-COMe	-2295963.17	-2295953.58	-9.59
1’a-CHO	-2192699.74	-2192688.89	-10.85
1’a-COOMe	-2493537.78	-2493526.92	-10.86
1’b-H	-1895081.29	-1895070.16	-11.13
1’b-Me	-1998332.60	-1998322.55	-10.05
1’b-CHO	-2192698.79	-2192686.17	-12.62
1’c	-7154820.66	-7154806.12	-14.54
1’a-NO_2	-2432135.60	-2432121.87	-13.73
1’a-NMe_2	-2246873.78	-2246874.00	0.22
1’a-F	-2155666.79	-2155660.92	-5.87
1’a-CF_3	-2780235.77	-2780224.90	-10.87
1’a-SF_5	-4249715.63	-4249701.44	-14.19
1’a-SMe	-3043826.42	-3043818.31	-8.11
1’a-CN	-2137323.58	-2137310.12	-13.46
2’a-H	-2742990.33	-2743000.86	10.53
2’a-Me	-2846243.53	-2846256.01	12.48
2’a-Cl	-3949725.36	-3949723.39	-1.97
2b’	-2742996.37	-2743008.11	11.74

Table A.21 Calculated conformational energy differences for simplified balances in the **1'** and **2'** series determined using M06-2X/6-311G*.

Compound	Closed conformer *E*/ kJ mol^{-1}	Open conformer *E* / kJ mol^{-1}	ΔE_{CALC}/ kJ mol^{-1}
1'a-H	-1894646.79	-1894636.76	-10.03
1'a-Me	-1997845.01	-1997839.47	-5.54
1'a-Cl	-3101313.34	-3101304.23	-9.11
1'a-COMe	-2295376.95	-2295366.80	-10.15
1'a-CHO	-2192162.99	-2192151.85	-11.14
1'a-COOMe	-2492891.73	-2492880.95	-10.78
1'b-H	-1894655.34	-1894643.61	-11.73
1'b-Me	-1997850.76	-1997842.71	-8.05
1'b-CHO	-2192162.69	-2192150.99	-11.70
1'c	-7154482.82	-7154468.15	-14.67
1'a-NO_2	-2431511.49	-2431496.57	-14.92
1'a-NMe_2	-2246291.19	-2246290.97	-0.22
1'a-F	-2155168.50	-2155162.43	-6.07
1'a-CF_3	-2779556.93	-2779545.28	-11.65
1'a-SF_5	-4248815.93	-4248802.16	-13.77
1'a-SMe	-3043266.81	-3043258.50	-8.31
1'a-CN	-2136819.95	-2136806.09	-13.86
2'a-H	-2742554.21	-2742547.00	-7.21
2'a-Me	-2845745.42	-2845754.24	8.82
2'a-Cl	-3949219.17	-3949216.03	-3.14
2b'	-2742554.72	-2742561.91	7.19

Table A.22 Calculated conformational energy differences of simplified balances in the **1'** and **2'** series determined using ωB97X-D/6-311G*.

Compound	Closed conformer *E*/ kJ mol^{-1}	Open conformer *E* / kJ mol^{-1}	ΔE_{CALC}/ kJ mol^{-1}
1'a-H	-1894725.04	-1894721.36	-3.68
1'a-Me	-1997944.15	-1997942.23	-1.92
1'a-Cl	-3101409.63	-3101403.83	-5.80
1'a-COMe	-2295481.07	-2295474.21	-6.86
1'a-CHO	-2192246.42	-2192238.24	-8.18
1'a-COOMe	-2492993.61	-2492985.68	-7.93
1'b-H	-1894734.43	-1894724.96	-9.47
1'b-Me	-1997954.02	-1997945.74	-8.28
1'b-CHO	-2192249.83	-2192237.92	-11.91
1'c	-7154590.54	-7154578.18	-12.36
1'a-NO_2	-2431608.08	-2431596.36	-11.72
1'a-NMe_2	-2246416.64	-2246419.62	2.98
1'a-F	-2155247.93	-2155245.47	-2.46
1'a-CF_3	-2779652.62	-2779644.25	-8.37
1'a-SF_5	-4248970.01	-4248958.71	-11.30
1'a-SMe	-3043393.83	-3043388.30	-5.53
1'a-CN	-2136875.34	-2136864.27	-11.07
2'a-H	-2742649.38	-2742655.88	6.50
2'a-Me	-2845870.20	-2845876.76	6.56
2'a-Cl	-3949331.77	-3949336.77	5.00
2b'	-2742656.83	-2742665.97	9.14

Calculated Molecular Orbital Energies

A detailed molecular orbital analysis was performed in this study in which the orbital energies of open and closed conformers of the molecular balances were compared. To enable identification and pairing of molecular orbitals found in the open and closed conformers (**Figure 2.32**) it was necessary to avoid orbital splitting arising from the canonical resonance forms of the aromatic electrons (that were not involved in the interactions of interest). The minimised full molecular balance structures were subsequently used to generate simplified balance structures of the type shown in **Figure A.4**, in which the 4-fluorophenyl moiety was replaced with a proton with a N-H bond length of 1.012 Å.

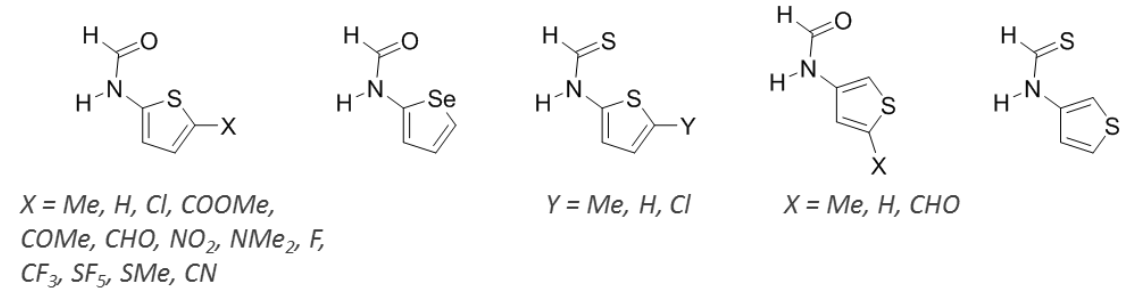

Figure A.4 Structures of simplified molecular balances used for molecular orbital analyses.

Table A.23 Molecular orbital energies of balance **1'a**-H in the open and closed conformers. The 6-311G* basis set was used with the indicated levels of theory.

Molecular orbital	1'a-H Molecular orbital energy (eV)					
	Open conformer			Closed conformer		
	B3LYP	M06-2X	ωB97X-D	B3LYP	M06-2X	ωB97X-D
HOMO	-6.75	-8.22	-8.77	-5.92	-7.25	-7.90
HOMO {-1}	-7.34	-8.72	-9.40	-6.93	-8.28	-8.97
HOMO {-2}	-7.45	-9.35	-9.64	-7.58	-9.49	-9.76
HOMO {-3}	-7.95	-9.49	-10.13	-8.75	-10.43	-11.00
HOMO {-4}	-9.92	-11.46	-12.10	-9.51	-11.11	-11.70
HOMO {-5}	-10.71	-12.55	-13.08	-10.38	-12.16	-12.81
HOMO {-6}	-10.83	-12.64	-13.21	-10.62	-12.32	-12.82
HOMO {-7}	-11.39	-13.02	-13.62	-11.08	-12.70	-13.30
HOMO {-8}	-11.65	-13.61	-13.95	-11.77	-13.62	-14.05
HOMO {-9}	-11.96	-13.89	-14.34	-12.12	-14.22	-14.59

Table A.24 Molecular orbital energies of balance **1'a**-Me in the open and closed conformers. The 6-311G* basis set was used with the indicated levels of theory.

Molecular orbital	1'a-Me Molecular orbital energy (eV)					
	Open conformer			Closed conformer		
	B3LYP	M062X	ωB97X-D	B3LYP	M062X	ωB97X-D
HOMO	-6.50	-7.85	-8.49	-5.69	-7.00	-7.65
HOMO {-1}	-7.22	-8.60	-9.28	-6.82	-8.20	-8.87
HOMO {-2}	-7.36	-9.28	-9.57	-7.48	-9.38	-9.67
HOMO {-3}	-7.80	-9.48	-9.97	-8.52	-10.20	-10.74
HOMO {-4}	-9.66	-11.18	-11.83	-9.29	-10.89	-11.49
HOMO {-5}	-10.29	-12.11	-12.68	-10.08	-11.78	-12.41
HOMO {-6}	-10.52	-12.16	-12.75	-10.24	-11.96	-12.47
HOMO {-7}	-10.74	-12.40	-12.96	-10.46	-12.00	-12.62
HOMO {-8}	-11.48	-13.26	-13.75	-11.32	-13.01	-13.55
HOMO {-9}	-11.71	-13.71	-14.06	-11.59	-13.45	-13.95

Table A.25 Molecular orbital energies of balance **1'a**-Cl in the open and closed conformers. The 6-311G* basis set was used with the indicated levels of theory.

Molecular orbital	1'a-Cl Molecular orbital energy (eV)					
	Open conformer			Closed conformer		
	B3LYP	M06-2X	ωB97X-D	B3LYP	M06-2X	ωB97X-D
HOMO	-6.73	-8.11	-8.75	-6.00	-7.30	-7.95
HOMO {-1}	-7.58	-9.08	-9.72	-7.28	-8.67	-9.33
HOMO {-2}	-7.73	-9.55	-9.86	-7.80	-9.68	-9.98
HOMO {-3}	-8.12	-9.74	-10.25	-8.56	-10.21	-10.76
HOMO {-4}	-9.24	-10.87	-11.42	-8.88	-10.56	-11.07
HOMO {-5}	-9.78	-11.53	-12.08	-9.78	-11.58	-12.09
HOMO {-6}	-10.37	-11.96	-12.58	-9.98	-11.60	-12.19
HOMO {-7}	-11.16	-12.97	-13.46	-11.05	-12.70	-13.34
HOMO {-8}	-11.55	-13.50	-14.01	-11.15	-13.03	-13.52
HOMO {-9}	-11.88	-13.71	-14.19	-11.69	-13.36	-13.94

Table A.26 Molecular orbital energies of balance **1'a**-COMe in the open and closed conformers. The 6-311G* basis set was used with the indicated levels of theory.

Molecular orbital	1'a-COMe Molecular orbital energy (eV)					
	Open conformer			Closed conformer		
	B3LYP	M06-2X	ωB97X-D	B3LYP	M06-2X	ωB97X-D
HOMO	-6.87	-8.22	-8.86	-6.30	-7.56	-8.21
HOMO {-1}	-7.33	-8.99	-9.58	-6.90	-8.63	-9.15
HOMO {-2}	-7.59	-9.32	-9.65	-7.27	-8.88	-9.31
HOMO {-3}	-7.76	-9.65	-9.92	-7.87	-9.76	-10.04
HOMO {-4}	-8.48	-10.06	-10.59	-8.92	-10.61	-11.13
HOMO {-5}	-10.13	-11.72	-12.34	-9.77	-11.41	-11.99
HOMO {-6}	-10.16	-12.00	-12.48	-9.91	-11.75	-12.21
HOMO {-7}	-10.94	-12.67	-13.20	-10.64	-12.30	-12.88
HOMO {-8}	-11.09	-12.94	-13.46	-10.77	-12.64	-13.16
HOMO {-9}	-11.22	-12.98	-13.52	-10.90	-14.57	-13.16

Table A.27 Molecular orbital energies of balance **1'a**-CHO in the open and closed conformers. The 6-311G* basis set was used with the indicated levels of theory.

Molecular orbital	1'a-CHO Molecular orbital energy (eV)					
	Open conformer			Closed conformer		
	B3LYP	M06-2X	ωB97X	B3LYP	M06-2X	ωB97X-D
HOMO	-6.99	-8.31	-8.95	-6.44	-7.69	-8.34
HOMO {-1}	-7.47	-9.15	-9.75	-7.02	-8.79	-9.29
HOMO {-2}	-7.74	-9.49	-9.81	-7.43	-9.04	-9.46
HOMO {-3}	-7.91	-9.79	-10.05	-8.01	-9.89	-10.17
HOMO {-4}	-8.65	-10.24	-10.78	-9.06	-10.74	-11.27
HOMO {-5}	-10.34	-11.90	-12.53	-9.96	-11.58	-12.17
HOMO {-6}	-10.61	-12.53	-13.02	-10.39	-12.32	-12.77
HOMO {-7}	-11.30	-13.04	-13.58	-11.10	-12.69	-13.32
HOMO {-8}	-11.65	-13.49	-13.96	-11.28	-13.27	-13.72
HOMO {-9}	-11.77	-13.75	-14.22	-11.42	-13.31	-13.75

Table A.28 Molecular orbital energies of balance **1'a**-COOMe in the open and closed conformers. The 6-311G* basis set was used with the indicated levels of theory.

Molecular orbital	1'a-COOMe Molecular orbital energy (eV)					
	Open conformer			Closed conformer		
	B3LYP	M06-2X	ωB97X-D	B3LYP	M06-2X	ωB97X-D
HOMO	-6.84	-8.16	-8.84	-6.24	-7.52	-8.17
HOMO {-1}	-7.55	-8.96	-9.62	-7.22	-8.59	-9.25
HOMO {-2}	-7.70	-9.61	-9.86	-7.57	-9.59	-9.82
HOMO {-3}	-8.00	-9.96	-10.25	-7.90	-9.87	-10.11
HOMO {-4}	-8.42	-10.21	-10.58	-8.32	-10.22	-10.58
HOMO {-5}	-8.69	-10.57	-10.96	-8.95	-10.65	-11.17
HOMO {-6}	-9.95	-11.63	-12.17	-9.60	-11.32	-11.82
HOMO {-7}	-10.44	-12.27	-12.71	-10.08	-11.93	-12.34
HOMO {-8}	-10.64	-12.54	-13.03	-10.43	-12.34	-12.80
HOMO {-9}	-11.15	-12.93	-13.42	-10.98	-12.59	-13.19

Table A.29 Molecular orbital energies of balance **1'c** in the open and closed conformers. The 6-311G* basis set was used with the indicated levels of theory.

Molecular orbital	1'c Molecular orbital energy (eV)					
	Open conformer			Closed conformer		
	B3LYP	M062X	ωB97X-D	B3LYP	M062X	ωB97X-D
HOMO	-6.61	-7.91	-8.61	-5.88	-7.22	-7.86
HOMO {-1}	-7.00	-8.33	-9.00	-6.52	-7.87	-8.52
HOMO {-2}	-7.42	-9.39	-9.62	-7.61	-9.47	-9.78
HOMO {-3}	-7.96	-9.74	-10.15	-8.65	-10.37	-10.91
HOMO {-4}	-9.52	-11.01	-11.66	-9.11	-10.70	-11.27
HOMO {-5}	-10.31	-12.16	-12.75	-10.08	-11.61	-12.26
HOMO {-6}	-10.49	-12.26	-12.77	-10.09	-12.02	-12.51
HOMO {-7}	-11.29	-12.97	-13.53	-11.01	-12.65	-13.21
HOMO {-8}	-11.66	-13.62	-13.94	-11.73	-13.53	-14.00
HOMO {-9}	-11.91	-13.91	-14.29	-12.10	-14.22	-14.58

Table A.30 Molecular orbital energies of balance **1'a**-NO_2 in the open and closed conformers. The 6-311G* basis set was used with the indicated levels of theory.

Molecular orbital	1'a-NO_2 Molecular orbital energy (eV)					
	Open conformer			Closed conformer		
	B3LYP	M06-2X	ωB97X-D	B3LYP	M06-2X	ωB97X-D
HOMO	-7.26	-8.63	-9.31	-6.81	-8.10	-8.74
HOMO {-1}	-8.03	-9.55	-10.13	-7.78	-9.18	-9.83
HOMO {-2}	-8.22	-10.05	-10.32	-7.98	-10.13	-10.34
HOMO {-3}	-8.43	-10.65	-10.82	-8.24	-10.28	-10.45
HOMO {-4}	-8.88	-10.68	-11.18	-8.47	-10.34	-10.76
HOMO {-5}	-8.89	-10.83	-11.20	-8.57	-10.71	-10.92
HOMO {-6}	-9.16	-11.05	-11.29	-9.53	-11.23	-11.74
HOMO {-7}	-10.88	-12.51	-13.10	-10.50	-12.15	-12.71
HOMO {-8}	-11.43	-13.38	-13.86	-11.16	-13.10	-13.57
HOMO {-9}	-11.85	-13.60	-14.12	-11.65	-13.27	-13.87

Table A.31 Molecular orbital energies of balance **1'a**-NMe_2 in the open and closed conformers. The 6-311G* basis set was used with the indicated levels of theory.

Molecular orbital	1'a-NMe_2 Molecular orbital energy (eV)					
	Open conformer			Closed conformer		
	B3LYP	M06-2X	ωB97X-D	B3LYP	M06-2X	ωB97X-D
HOMO	-5.43	-6.79	-7.39	-4.91	-6.27	-6.86
HOMO {-1}	-7.05	-8.48	-9.14	-6.70	-8.11	-8.76
HOMO {-2}	-7.19	-9.00	-9.40	-7.13	-8.74	-9.27
HOMO {-3}	-7.41	-9.22	-9.55	-7.37	-9.31	-9.58
HOMO {-4}	-8.17	-9.84	-10.36	-8.67	-10.38	-10.92
HOMO {-5}	-9.51	-11.06	-11.69	-9.22	-10.83	-11.42
HOMO {-6}	-10.41	-12.19	-12.77	-10.12	-11.89	-12.51
HOMO {-7}	-10.51	-12.30	-12.83	-10.38	-12.05	-12.60
HOMO {-8}	-10.94	-12.53	-13.10	-10.57	-12.16	-12.73
HOMO {-9}	-10.98	-12.74	-13.26	-10.85	-12.49	-13.06

Table A.32 Molecular orbital energies of balance **1'a**-F in the open and closed conformers. The 6-311G* basis set was used with the indicated levels of theory.

Molecular orbital	1'a-F Molecular orbital energy (eV)					
	Open conformer			Closed conformer		
	B3LYP	M06-2X	ωB97X-D	B3LYP	M06-2X	ωB97X-D
HOMO	-6.74	-8.10	-8.77	-5.93	-7.27	-7.90
HOMO {-1}	-7.54	-9.05	-9.69	-7.24	-8.63	-9.29
HOMO {-2}	-7.69	-9.54	-9.81	-7.74	-9.67	-9.93
HOMO {-3}	-8.07	-9.79	-10.24	-8.77	-10.50	-11.01
HOMO {-4}	-10.23	-11.84	-12.43	-9.85	-11.50	-12.06
HOMO {-5}	-10.63	-12.58	-13.03	-10.38	-12.22	-12.70
HOMO {-6}	-10.78	-12.60	-13.07	-10.48	-12.36	-12.80
HOMO {-7}	-11.38	-13.29	-13.71	-11.56	-12.36	-13.79
HOMO {-8}	-11.86	-13.90	-14.18	-12.05	-14.14	-14.38
HOMO {-9}	-12.42	-14.41	-14.75	-12.25	-14.39	-14.72

Table A.33 Molecular orbital energies of balance **1'a**-CF_3 in the open and closed conformers. The 6-311G* basis set was used with the indicated levels of theory.

Molecular orbital	1'a-CF_3 Molecular orbital energy (eV)					
	Open conformer			Closed conformer		
	B3LYP	M06-2X	ωB97X-D	B3LYP	M06-2X	ωB97X-D
HOMO	-7.14	-8.48	-9.17	-6.49	-7.82	-8.45
HOMO {-1}	-7.75	-9.23	-9.86	-7.46	-8.84	-9.50
HOMO {-2}	-7.92	-9.80	-10.04	-8.00	-9.92	-10.17
HOMO {-3}	-8.60	-10.30	-10.75	-9.22	-10.95	-11.45
HOMO {-4}	-10.44	-12.03	-12.63	-10.05	-11.69	-12.25
HOMO {-5}	-11.04	-12.92	-13.31	-10.75	-12.56	-12.97
HOMO {-6}	-11.14	-13.11	-13.57	-10.81	-12.80	-13.23
HOMO {-7}	-11.42	-13.32	-13.78	-11.05	-12.99	-13.48
HOMO {-8}	-11.49	-13.86	-13.86	-11.26	-13.74	-13.51
HOMO {-9}	-11.83	-14.10	-14.15	-11.60	-13.74	-13.94

Table A.34 Molecular orbital energies of balance **1'a**-SF_5 in the open and closed conformers. The 6-311G* basis set was used with the indicated levels of theory.

Molecular orbital	1'a-SF_5 Molecular orbital energy (eV)					
	Open conformer			Closed conformer		
	B3LYP	M06-2X	ωB97X-D	B3LYP	M06-2X	ωB97X-D
HOMO	-7.36	-8.69	-9.40	-6.84	-8.13	-8.77
HOMO {-1}	-7.99	-9.53	-10.10	-7.80	-9.16	-9.82
HOMO {-2}	-8.23	-10.01	-10.29	-8.27	-10.15	-10.41
HOMO {-3}	-9.00	-10.65	-11.07	-9.52	-11.22	-11.73
HOMO {-4}	-10.78	-12.35	-12.93	-10.40	-12.01	-12.57
HOMO {-5}	-11.31	-13.17	-13.60	-11.04	-12.85	-13.33
HOMO {-6}	-11.44	-13.39	-13.80	-11.14	-13.08	-13.45
HOMO {-7}	-11.56	-13.62	-14.01	-11.21	-13.28	-13.65
HOMO {-8}	-11.67	-14.07	-14.03	-11.33	-13.88	-13.68
HOMO {-9}	-11.81	-14.30	-14.16	-11.46	-13.96	-13.89

Table A.35 Molecular orbital energies of balance **1'a**-SMe in the open and closed conformers. The 6-311G* basis set was used with the indicated levels of theory.

Molecular orbital	1'a-SMe Molecular orbital energy (eV)					
	Open conformer			Closed conformer		
	B3LYP	M06-2X	ωB97X-D	B3LYP	M06-2X	ωB97X-D
HOMO	-6.60	-7.89	-8.64	-6.00	-7.27	-7.96
HOMO {-1}	-6.86	-8.28	-8.92	-6.44	-7.88	-8.52
HOMO {-2}	-7.43	-8.83	-9.51	-7.08	-8.45	-9.13
HOMO {-3}	-7.60	-9.55	-9.78	-7.74	-9.65	-9.93
HOMO {-4}	-8.18	-9.85	-10.31	-8.59	-10.18	-10.77
HOMO {-5}	-9.40	-10.93	-11.58	-9.26	-10.87	-11.46
HOMO {-6}	-10.05	-11.63	-12.26	-9.71	-11.32	-11.92
HOMO {-7}	-10.59	-12.27	-12.88	-10.33	-11.97	-12.60
HOMO {-8}	-11.14	-12.89	-13.44	-10.87	-12.56	-13.16
HOMO {-9}	-11.37	-13.09	-13.71	-11.08	-12.77	-13.37

Table A.36 Molecular orbital energies of balance **1'a**-CN in the open and closed conformers. The 6-311G* basis set was used with the indicated levels of theory.

Molecular orbital	1'a-CN Molecular orbital energy (eV)					
	Open conformer			Closed conformer		
	B3LYP	M06-2X	ωB97X-D	B3LYP	M06-2X	ωB97X-D
HOMO	-7.10	-8.40	-9.11	-6.52	-7.81	-8.45
HOMO {-1}	-7.92	-9.44	-10.06	-7.68	-9.06	-9.74
HOMO {-2}	-8.13	-9.96	-10.24	-8.15	-10.04	-10.33
HOMO {-3}	-8.68	-10.35	-10.81	-8.97	-10.66	-11.20
HOMO {-4}	-9.61	-11.33	-11.88	-9.23	-11.01	-11.52
HOMO {-5}	-10.17	-11.98	-12.51	-9.92	-11.93	-12.31
HOMO {-6}	-10.31	-12.31	-12.71	-10.11	-11.95	-12.45
HOMO {-7}	-10.76	-12.48	-13.00	-10.37	-12.08	-12.60
HOMO {-8}	-11.58	-13.48	-13.93	-11.35	-13.26	-13.82
HOMO {-9}	-11.87	-13.76	-14.32	-11.63	-13.33	-13.87

Table A.37 Molecular orbital energies of balance **1'b**-H in the open and closed conformers. The 6-311G* basis set was used with the indicated levels of theory.

Molecular orbital	1'b-H Molecular orbital energy (eV)					
	Open conformer			Closed conformer		
	B3LYP	M06-2X	ωB97X-D	B3LYP	M06-2X	ωB97X-D
HOMO	-6.71	-8.04	-8.68	-6.15	-7.47	-8.13
HOMO {-1}	-7.16	-8.59	-9.23	-6.88	-8.26	-8.92
HOMO {-2}	-7.33	-9.28	-9.54	-7.43	-9.39	-9.64
HOMO {-3}	-8.15	-9.81	-10.37	-8.68	-10.37	-10.91
HOMO {-4}	-10.01	-11.53	-12.18	-9.66	-11.17	-11.82
HOMO {-5}	-10.73	-12.63	-13.12	-10.48	-12.40	-12.91
HOMO {-6}	-10.92	-12.72	-13.29	-10.88	-12.43	-13.07
HOMO {-7}	-11.37	-13.08	-13.64	-11.19	-12.86	-13.42
HOMO {-8}	-11.65	-13.55	-13.95	-11.78	-13.63	-14.07
HOMO {-9}	-11.95	-13.89	-14.31	-11.89	-14.01	-14.37

Table A.38 Molecular orbital energies of balance **1'b**-Me in the open and closed conformers. The 6-311G* basis set was used with the indicated levels of theory.

Molecular orbital	1'b-Me Molecular orbital energy (eV)					
	Open conformer			Closed conformer		
	B3LYP	M06-2X	ωB97X-D	B3LYP	M06-2X	ωB97X-D
HOMO	-6.51	-7.77	-8.46	-5.97	-7.28	-7.93
HOMO {-1}	-7.01	-8.38	-9.04	-6.69	-8.07	-8.73
HOMO {-2}	-7.23	-9.23	-9.46	-7.38	-9.32	-9.56
HOMO {-3}	-7.97	-9.72	-10.22	-8.53	-10.11	-10.72
HOMO {-4}	-9.73	-11.24	-11.89	-9.40	-10.91	-11.56
HOMO {-5}	-10.36	-12.17	-12.75	-10.17	-11.92	-12.49
HOMO {-6}	-10.66	-12.24	-12.86	-10.43	-11.97	-12.58
HOMO {-7}	-10.72	-12.45	-12.98	-10.61	-12.29	-12.89
HOMO {-8}	-11.44	-13.28	-13.75	-11.41	-13.11	-13.67
HOMO {-9}	-11.56	-13.56	-13.90	-11.63	-13.61	-14.04

Table A.39 Molecular orbital energies of balance **1'b**-CHO in the open and closed conformers. The 6-311G* basis set was used with the indicated levels of theory.

Molecular orbital	1'b-CHO Molecular orbital energy (eV)					
	Open conformer			Closed conformer		
	B3LYP	M06-2X	ωB97X-D	B3LYP	M06-2X	ωB97X-D
HOMO	-7.06	-8.31	-9.01	-6.60	-7.85	-8.52
HOMO {-1}	-7.53	-9.06	-9.67	-7.29	-8.76	-9.44
HOMO {-2}	-7.62	-9.54	-9.82	-7.42	-9.39	-9.64
HOMO {-3}	-7.79	-9.68	-9.94	-7.80	-9.71	-9.97
HOMO {-4}	-8.56	-10.23	-10.75	-9.02	-10.65	-11.25
HOMO {-5}	-10.41	-11.95	-12.59	-10.08	-11.60	-12.24
HOMO {-6}	-10.70	-12.61	-13.09	-10.49	-12.38	-12.86
HOMO {-7}	-11.33	-13.24	-13.67	-11.44	-13.03	-13.62
HOMO {-8}	-11.64	-13.31	-13.89	-11.47	-13.29	-13.89
HOMO {-9}	-11.84	-13.83	-14.25	-11.59	-13.54	-13.96

Table A.40 Molecular orbital energies of balance **2'a**-H in the open and closed conformers. The 6-311G* basis set was used with the indicated levels of theory.

Molecular orbital	2'a-H Molecular orbital energy (eV)					
	Open conformer			Closed conformer		
	B3LYP	M06-2X	ωB97X-D	B3LYP	M06-2X	ωB97X-D
HOMO	-6.18	-7.47	-8.26	-5.94	-7.37	-8.01
HOMO {-1}	-6.34	-7.67	-8.29	-6.55	-7.87	-8.59
HOMO {-2}	-7.53	-8.88	-9.58	-7.09	-8.45	-9.11
HOMO {-3}	-7.66	-9.18	-9.76	-7.33	-8.69	-9.36
HOMO {-4}	-10.04	-11.55	-12.23	-9.69	-11.25	-11.89
HOMO {-5}	-10.20	-11.94	-12.48	-10.04	-11.63	-12.25
HOMO {-6}	-10.46	-12.13	-12.71	-10.34	-11.89	-12.53
HOMO {-7}	-11.13	-12.81	-13.45	-10.66	-12.51	-13.09
HOMO {-8}	-11.62	-13.22	-13.84	-11.31	-12.91	-13.52
HOMO {-9}	-12.03	-14.00	-14.43	-11.82	-13.63	-14.15

Table A.41 Molecular orbital energies of balance **2'a**-Me in the open and closed conformers. The 6-311G* basis set was used with the indicated levels of theory.

Molecular orbital	2'a-Me Molecular orbital energy (eV)					
	Open conformer			Closed conformer		
	B3LYP	M06-2X	ωB97X-D	B3LYP	M06-2X	ωB97X-D
HOMO	-6.09	-7.47	-8.07	-5.86	-7.30	-7.92
HOMO {-1}	-6.27	-7.58	-8.20	-6.38	-7.75	-8.41
HOMO {-2}	-7.36	-8.78	-9.47	-6.93	-8.23	-8.93
HOMO {-3}	-7.44	-8.79	-9.53	-7.17	-8.51	-9.21
HOMO {-4}	-9.78	-11.34	-11.98	-9.53	-11.05	-11.72
HOMO {-5}	-9.96	-11.56	-12.28	-9.76	-11.32	-11.98
HOMO {-6}	-10.25	-11.88	-12.51	-10.19	-11.81	-12.44
HOMO {-7}	-10.79	-12.40	-12.89	-10.29	-11.96	-12.56
HOMO {-8}	-10.84	-12.46	-13.17	-10.61	-12.18	-12.79
HOMO {-9}	-11.69	-13.42	-14.01	-11.46	-13.13	-13.72

Table A.42 Molecular orbital energies of balance **2'a**-Cl in the open and closed conformers. The 6-311G* basis set was used with the indicated levels of theory.

Molecular orbital	2'a-Cl Molecular orbital energy (eV)					
	Open conformer			Closed conformer		
	B3LYP	M06-2X	ωB97X-D	B3LYP	M06-2X	ωB97X-D
HOMO	-6.34	-7.53	-8.41	-6.09	-7.31	-8.16
HOMO {-1}	-6.41	-7.83	-8.43	-6.33	-7.76	-8.66
HOMO {-2}	-7.66	-9.16	-9.64	-7.42	-8.79	-9.19
HOMO {-3}	-7.85	-9.23	-9.92	-7.77	-9.20	-9.65
HOMO {-4}	-9.32	-10.93	-11.50	-9.01	-10.64	-11.29
HOMO {-5}	-9.70	-11.39	-12.03	-9.36	-11.08	-11.88
HOMO {-6}	-10.44	-11.97	-12.63	-10.18	-11.75	-12.22
HOMO {-7}	-10.52	-12.21	-12.69	-10.66	-12.21	-12.72
HOMO {-8}	-11.04	-12.89	-13.24	-10.96	-12.87	-12.80
HOMO {-9}	-11.74	-13.45	-14.15	-11.37	-12.92	-13.92

Table A.43 Molecular orbital energies of balance **2'b** in the open and closed conformers. The 6-311G* basis set was used with the indicated levels of theory.

Molecular orbital	2'b Molecular orbital energy (eV)					
	Open conformer			Closed conformer		
	B3LYP	M06-2X	ωB97X-D	B3LYP	M06-2X	ωB97X-D
HOMO	-6.06	-7.50	-8.15	-5.90	-7.34	-7.97
HOMO {-1}	-6.42	-7.65	-8.34	-6.48	-7.69	-8.45
HOMO {-2}	-7.34	-8.74	-9.42	-6.98	-8.41	-9.05
HOMO {-3}	-7.79	-9.18	-9.88	-7.49	-8.90	-9.55
HOMO {-4}	-10.08	-11.62	-12.28	-9.71	-11.26	-11.89
HOMO {-5}	-10.14	-11.72	-12.37	-10.18	-11.81	-12.44
HOMO {-6}	-10.50	-12.21	-12.82	-10.29	-11.94	-12.50
HOMO {-7}	-11.23	-12.93	-13.56	-10.79	-12.59	-13.18
HOMO {-8}	-11.71	-13.34	-13.97	-11.38	-13.00	-13.63
HOMO {-9}	-12.06	-13.89	-14.41	-11.88	-13.67	-14.19

The same molecular orbital plot as seen in **Chapter 2** (**Figure 2.33**) can be performed for molecular orbital energies calculated using the M06-2X or ωB97X-D theory level.

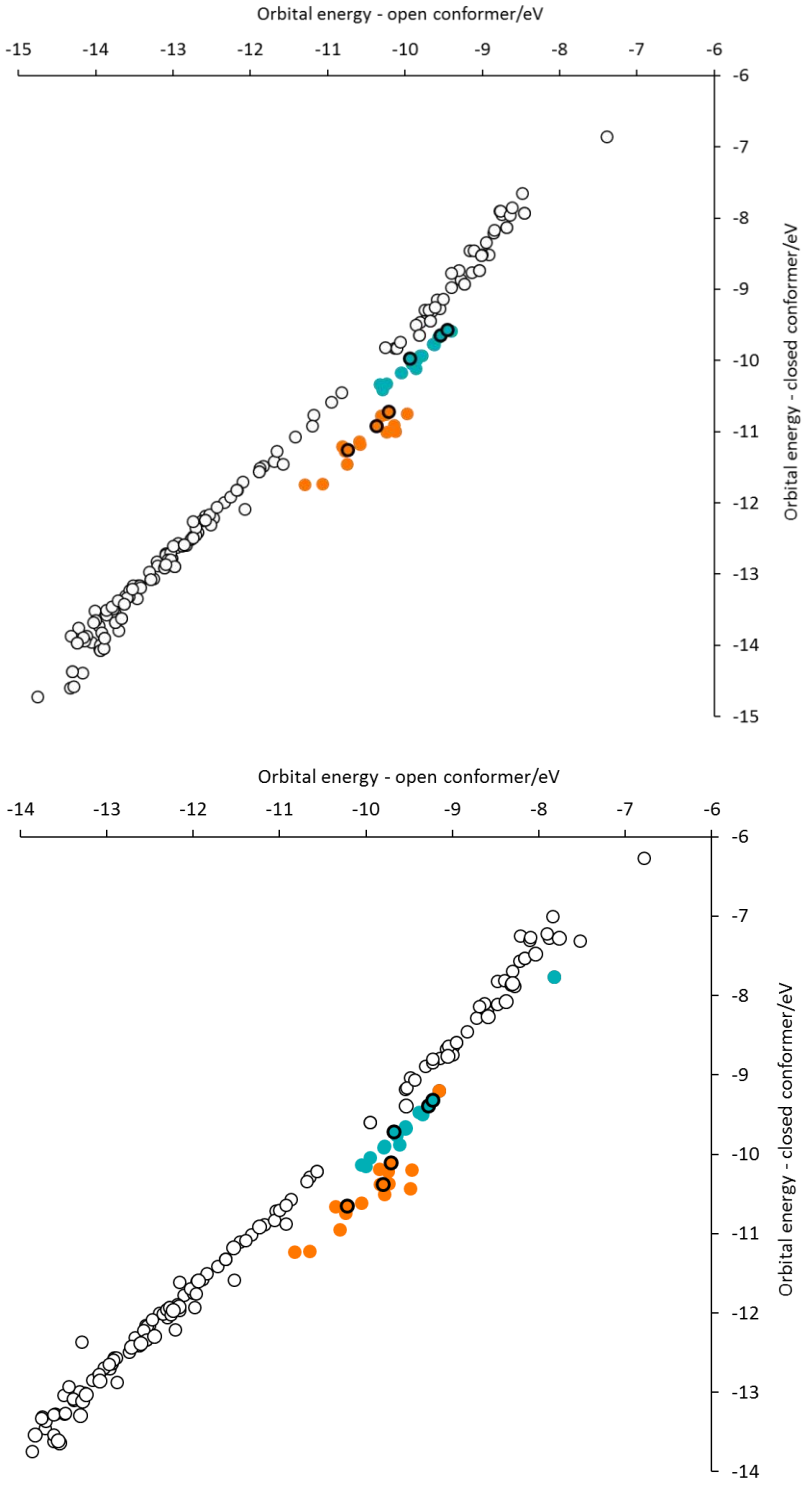

Figure A.5 A plot of orbital energies in the open conformer vs. those in the closed conformer calculated at ωB97X-D/6-311G* (top), M06-2X/6-311G* (bottom). A version of this figure calculated using B3LYP/6-311G* data is provided in **Chapter 2**, **Figure 2.33**.

Molecular orbitals energies corresponding to n→σ* electron delocalisation (teal points, **Figure 2.33**) and a through bond resonance delocalisation (orange points, **Figure 2.33**) were plotted against experimentally measured conformational free energies in $CDCl_3$, including the selenium **1c'** outlier (**Figure A.6**).

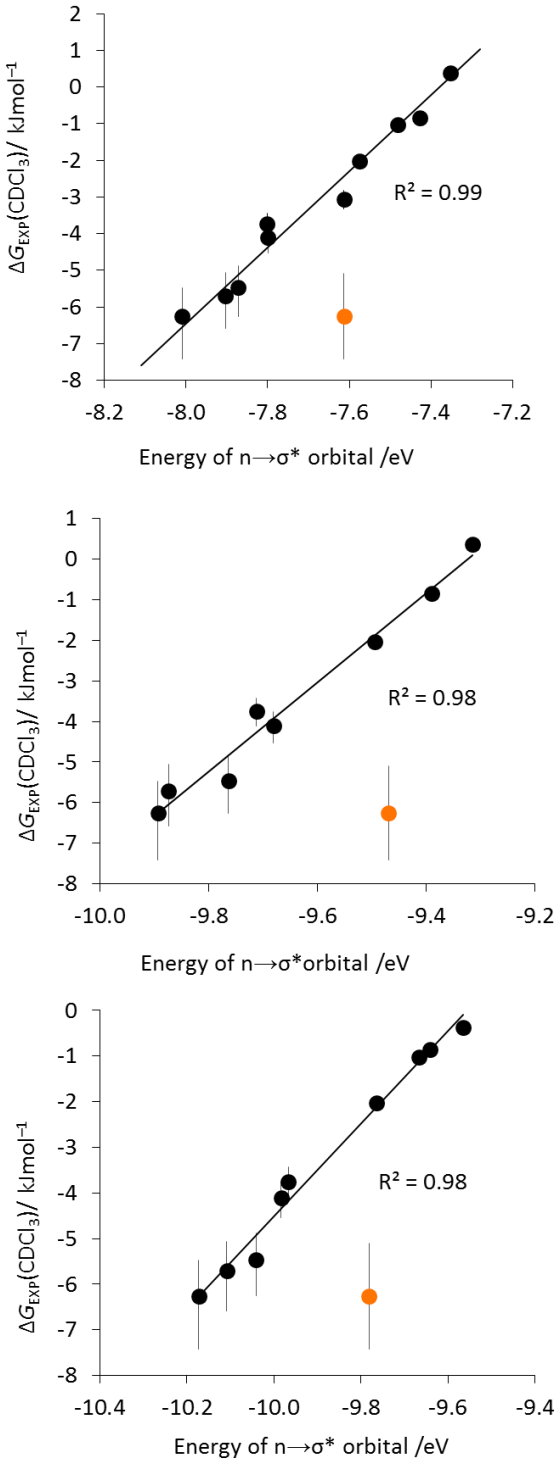

Figure A.6 Plots of the orbital energies for those containing n→σ* (S-C) and n→σ* (H-C) delocalization against experimental conformational free energies measured in $CDCl_3$ at 298 K. Data were calculated using B3LYP/6-311G* (top), M06-2X/6-311G* (middle), and ωB97X-D/6-311G* (bottom). The outlying orange point corresponds to the selenium-containing compound **1c**.

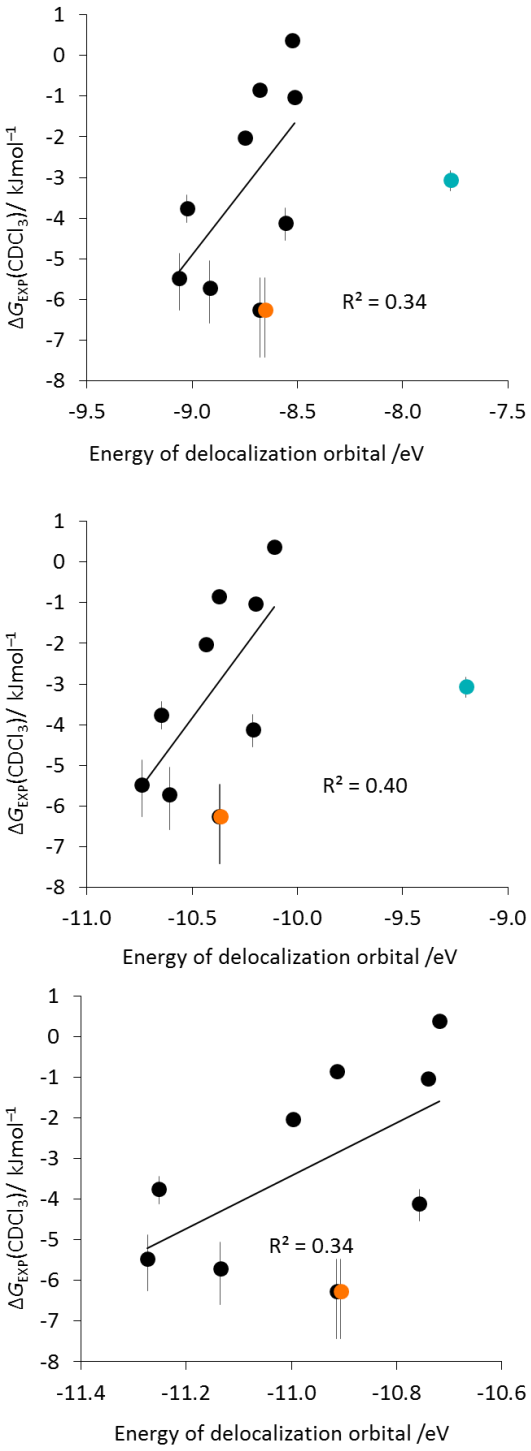

Figure A.7 A plot of orbital energies of the delocalization orbital calculated at B3LYP/6-311G* (top), M06-2X/6-311G* (middle), and ωB97X-D/6-311G* (bottom) against experimental free energies measured in $CDCl_3$. Se balance **1c** data shown in orange and **2a**-Cl in teal.

Calculated Natural Bond Orbital Energies

Natural bond orbital (NBO) analyses were performed using a single point energy calculation using Gaussian 09 Revision E.01[1] at DFT/B3LYP/6-311G* using the geometry from the already minimised full molecular balance from Spartan '14 to generate an NBO output. The NBO output was then inputted to NBO 6.0[2] to obtain second-order perturbation theory output energies, images created using JmolNbo Visualization Helper Version 2.0 and Jmol.

Table A.44 NBO second-order perturbation energies. Orbital delocalization was seen from both lone pairs orbitals on the formyl oxygen. The sum total lone pair n→σ* interaction energy is also given. [a]Corresponds to the n(1)→σ*(S/Se-C) NBO (**Figure 2.27A**), [b]Corresponds to the n(2)→σ*(S/Se-C) NBO (**Figure 2.27B**) [c]Corresponds to the n→σ*(C-S) NBO (Figure **Figure 2.27C**), [d]Corresponds to the n→σ*(H-C) NBO (**Figure 2.27D**), [e]Corresponds to the n→σ*(C-C) NBO (**Figure 2.27D**).

Compound	LP (1) → σ* / kJ mol^{-1}	LP (2) → σ* / kJ mol^{-1}	Combined interaction strength / kJ mol^{-1}
1a-H	3.22[a]	8.62[b]	11.84
1a-Me	3.22 [a]	8.37[b]	11.59
1a-Cl	3.77 [a]	10.13[b]	13.89
1a-COMe	3.35 [a]	8.66[b]	12.01
1a-CHO	3.47 [a]	8.91[b]	12.38
1a-COOMe	3.56 [a]	9.12[b]	12.68
1b-H	-	3.31[c]	3.31
1b-Me	-	3.89[c]	3.89
1b-CHO	3.05[d]	2.13[e]	5.19
1c	5.82[a]	14.81[b]	20.63
2a-Cl	3.72[a]	18.95[b]	22.68

References

1. Frisch, M. J.; Trucks, G. W.; Schlegel, H. B.; Scuseria, G. E.; Robb, M. A.; Cheeseman, J. R.; Scalmani, G.; Barone, V.; Mennucci, B.; Petersson, G. A.; *et al*. Gaussian 09, Revision E.01. Gaussian, Inc: Wallingford CT 2013.

2. Glendening, E. D.; Badenhoop, J. K.; Reed, A. E.; Carpenter, J. E.; Bohmann, J. A.; Morales, C. M.; Landis, C. R.; Weinhold, F. NBO 6.0. Theoretical Chemistry Institute, University of Wisconsin: Madison, WI 2013.

Appendix B: Experimental and Computational Data for Chapter 3

Experimental Data

Below is the experimental data used for comparison to computational results. All experimental data was measured by Nicole Meredith or Nicholas Dominelli Whitely.

Solvent independent values, ΔE, calculated from **Equation 3.4** were compared to computational results for series **3** and **4**.

Table B.1 Solvent independent ΔE values calculated from **Equation 3.4** for molecular balance series **3** and **4**. Calculated by NM.

		Error	
	ΔE / kJ mol^{-1}	-	+
3a	-12.7	2.1	2.1
3b-OMe	-8.7	0.4	0.4
3b-CN	-10.6	0.7	0.7
3b-H	-13.1	2.3	2.3
4a-Me	-15.7	1.9	1.9
4a-CF_3	-16.2	1.2	1.2
4a-^{t}Bu	-13.9	2.6	2.6
4b-H	-14.7	2.1	2.1
4b-OMe	-14.7	2.1	2.1
4c-H	-7.0	0.5	0.5
4c-F	-7.6	0.6	0.6

A solvent screen was used to investigate the nature of H-bonds in series **5**. Experimental conformational free energies were measured across a range of solvents.

Table B.2 Experimental conformational free energy differences of molecular balance **5**-1H, ΔG_{EXP} measured in various solvents at 298 K. Measured by NDW and NM.

5-1H			
		Error	
	ΔG / kJ mol^{-1}	-	+
Chloroform-d	-4.2	0.5	0.4
Acetone	0.4	0.1	0.1
Acetonitrile-d_3	-0.5	0.1	0.1
Ethyl acetate	0.7	0.1	0.1
Tetrahydrofuran	1.5	0.1	0.1
Dichloromethane	-3.9	0.1	0.1
Ethanol	1.2	0.1	0.1
Methanol-d_4	0.5	0.1	0.1
DMSO-d_6	0.5	0.1	0.1

Table B.3 Experimental conformational free energy differences of molecular balance **5**-2H, ΔG_{EXP} measured in various solvents at 298 K. Measured by NDW and NM.

5-2H			
		Error	
	ΔG / kJ mol^{-1}	-	+
Chloroform-d	-8.0	3.4	1.4
Acetone	0.8	0.1	0.1
Acetonitrile-d_3	-0.5	0.1	0.1
Ethyl acetate	0.6	0.1	0.1
Tetrahydrofuran	2.0	0.2	0.2
Dichloromethane	-7.0	0.1	0.1
Ethanol	-	-	-
Methanol-d_4	0.7	0.1	0.1
DMSO-d_6	0.6	0.1	0.1

Table B.4 Experimental conformational free energy differences of molecular balance **5**-3H, ΔG_{EXP} measured in various solvents at 298 K. Measured by NDW and NM.

5-3H			
		Error	
	ΔG / kJ mol^{-1}	-	+
Chloroform-d	-7.4	2.3	1.2
Acetone	1.4	0.1	0.1
Acetonitrile-d$_3$	0.0	0.1	0.1
Ethyl acetate	1.3	0.1	0.1
Tetrahydrofuran	2.7	0.2	0.2
Dichloromethane	-6.3	0.1	0.1
Ethanol	1.9	0.2	0.2
Methanol-d$_4$	1.0	0.1	0.1
DMSO-d$_6$	1.1	0.1	0.1

Molecular balances from series **6** were measured in $CDCl_3$ for comparison to computational results.

Table B.5 Experimental conformational free energy differences of molecular balances from series **6**, ΔG_{EXP} measured in $CDCl_3$ at 298 K. Measured by NDW.

		Error	
	ΔG / kJ mol^{-1}	-	+
6-*p*F	-5.0	0.7	0.5
6-*p*NO$_2$	-7.8	3.4	1.4
6-*p*CF$_3$	-6.5	1.2	0.8
6-*m*Me	-4.0	0.4	0.3
6-*m*OH	-5.1	0.7	0.5

Minimised Geometries

Full molecular balance structures shown in **Figures 3.4** and **3.16** minimised in both the open and closed conformations using the B3LYP method and basis sets 6-311G* in Spartan '14. Frequency calculations were performed on all minimised structures, which confirmed no imaginary frequencies. The resulting gas-phase energies and corresponding energy differences, ΔE_{CALC} in each conformer

Table B.6 Calculated conformational energy differences of full balance series **3** and **4** calculated using B3LYP/6-311G*.

Compound	**Closed conformer *E*/ kJ mol^{-1}**	**Open conformer *E* / kJ mol^{-1}**	**ΔE_{CALC}/ kJ mol^{-1}**
3a	-2168868.53	-2168893.03	-24.50
3b-OMe	-3076368.25	-3076379.73	-11.48
3b-CN	-3017857.74	-3017874.83	-17.09
3b-H	-2775603.24	-2775633.46	-30.22
4a-Me	-2569776.85	-2569809.82	-32.97
4a-CF_3	-3351660.16	-3351690.81	-30.65
4a-^{t}Bu	-2879492.57	-2879522.49	-29.92
4a-NH_2	-2611934.42	-2611972.18	-37.76
4b-H	-3073288.02	-3073315.73	-27.71
4b-OMe	-3374048.10	-3374074.59	-26.49
4c-H	-3115432.81	-3115441.48	-8.67
4c-F	-3376045.61	-3376057.86	-12.25

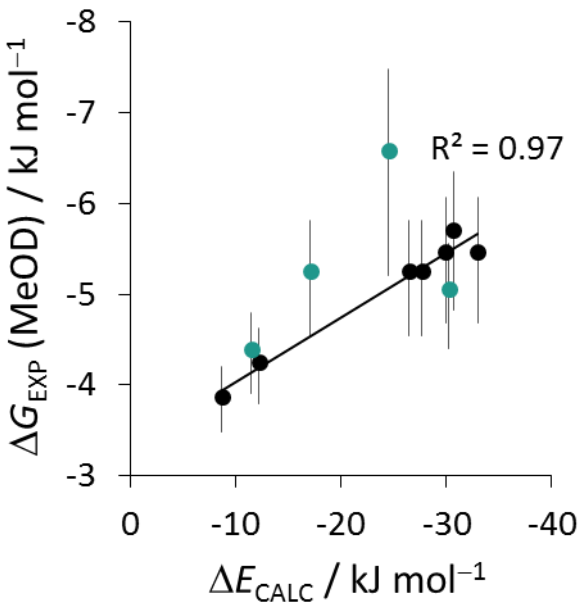

Figure B.1 Plot of experimental conformational free energies (ΔG_{EXP}) measured in methanol-d_4 at 298 K versus calculated conformational energy differences (ΔE_{CALC}). Series **3** is shown in teal and series **4** is shown in black. Series **4** gives a good correlation with experimentally determined free energies ($R^2 = 0.97$).

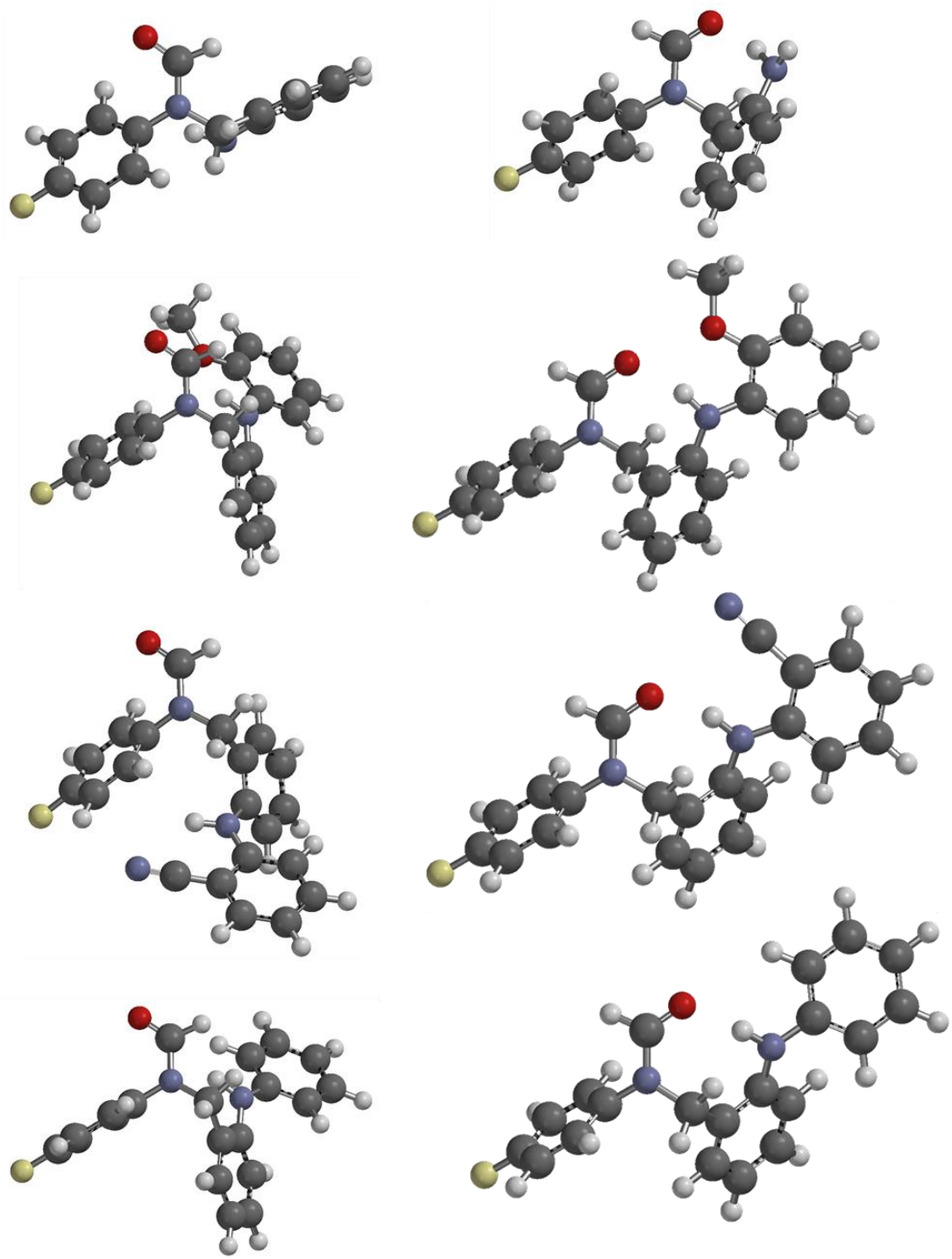

Figure B.2 Minimised geometries of molecular balances in series **3**.Minimised using Spartan ’14 DFT/B3LYP/6-311G*.

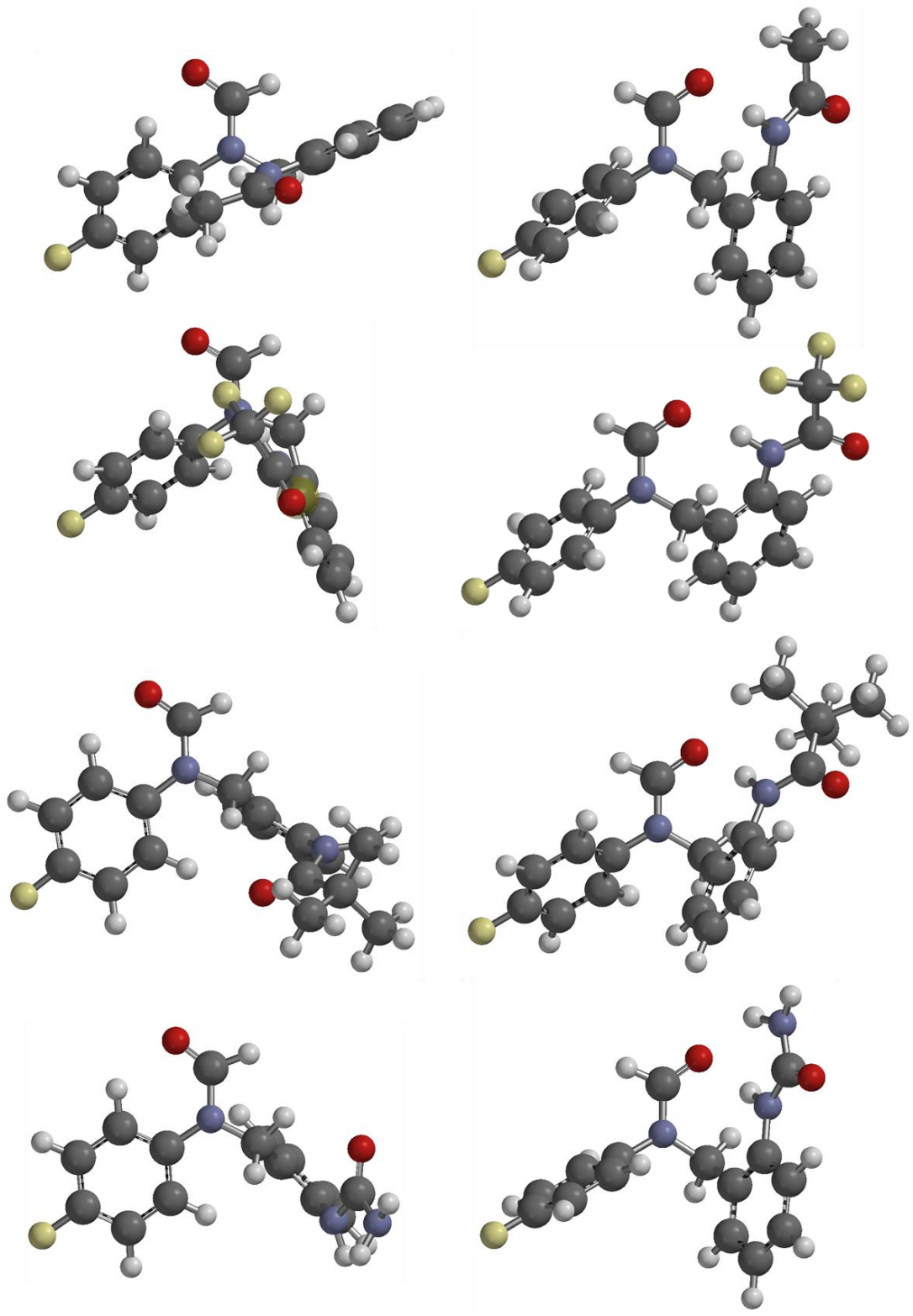

Figure B.3 Minimised geometries of molecular balances in series **4a**.Minimised using Spartan ’14 DFT/B3LYP/6-311G*.

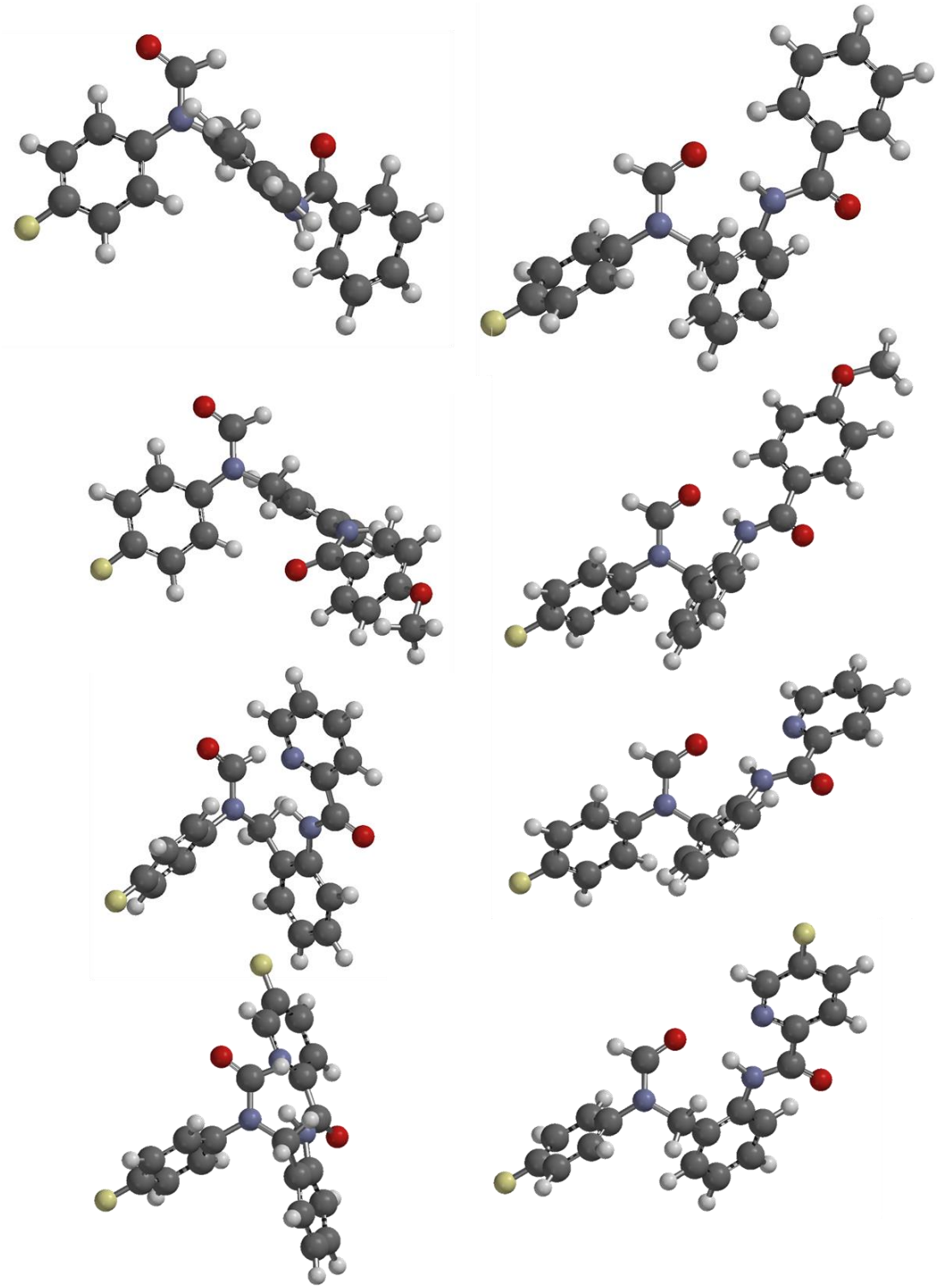

Figure B.4 Minimised geometries of molecular balances in series **4b**.Minimised using Spartan ’14 DFT/B3LYP/6-311G*.

Table B.7 Calculated conformational energy differences of full balance series **5** and **6** calculated using B3LYP/6-311G*.

Compound	Closed conformer *E*/ kJ mol^{-1}	Open conformer *E* / kJ mol^{-1}	ΔE_{CALC}/ kJ mol^{-1}
5-1H	-2117808.66	-2117820.12	-11.46
5-2H	-2315350.27	-2315370.97	-20.70
5-3H	-2512893.32	-2512913.27	-19.95
6-*p*F	-2378429.42	-2378441.72	-12.30
6-*p*NO_2	-2654864.71	-2654884.44	-19.73
6-*p*CF_3	-3002967.70	-3002983.05	-15.35
6-*m*Me	-2221056.46	-2221067.12	-10.66
6-*m*OH	-2315338.61	-2315351.59	-12.98

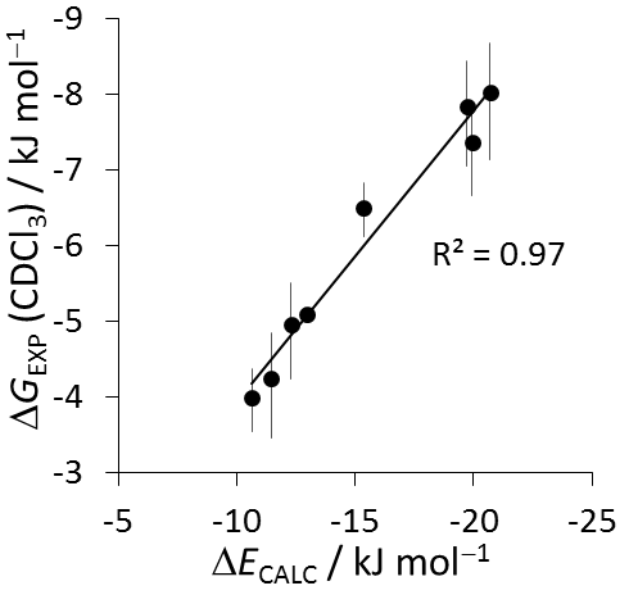

Figure B.5 Plot of experimental conformational free energies (ΔG_{EXP}) measured in chloroform-d at 298 K versus calculated conformational energy differences (ΔE_{CALC}) for series **5** and **6**. Calculated using B3LYP/6-311G*.

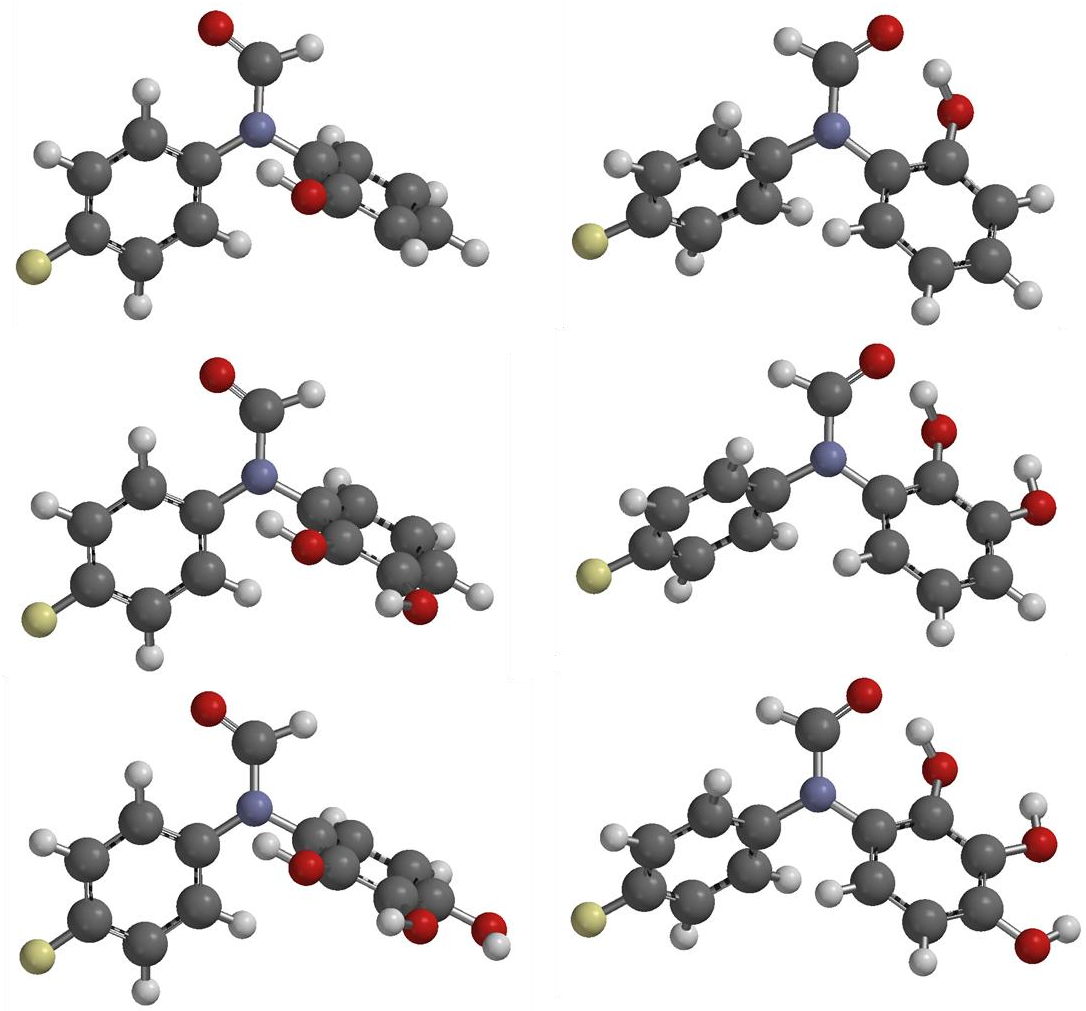

Figure B.6 Minimised geometries of molecular balances in series **5**.Minimised using Spartan ’14 DFT/B3LYP/6-311G*.

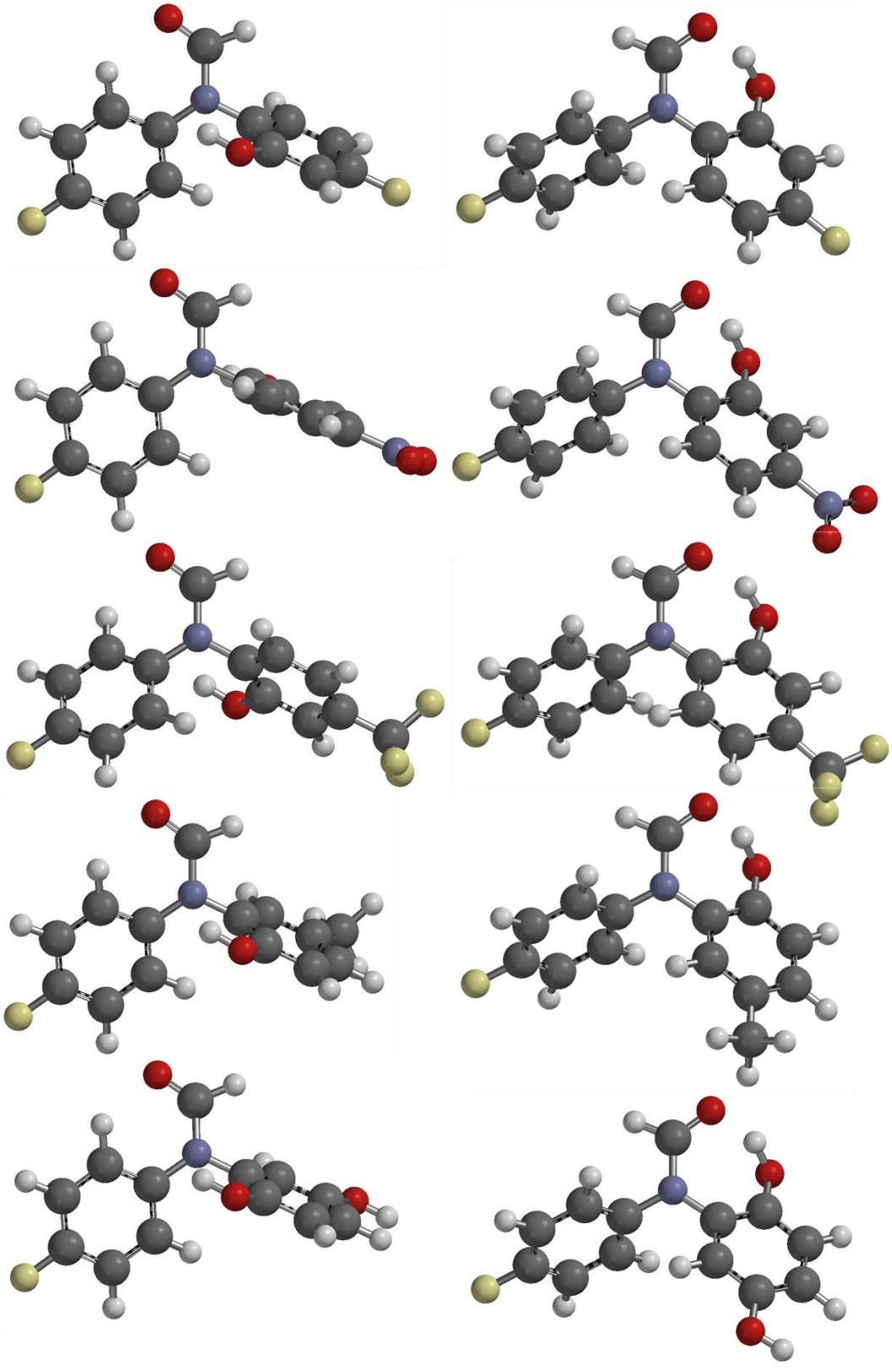

Figure B.7 Minimised geometries of molecular balances in series **6**.Minimised using Spartan ’14 DFT/B3LYP/6-311G*.

Calculated Natural Bond Orbital Energies

Natural bond orbital (NBO) analyses were performed using a single point energy calculation using Gaussian 09 Revision E.01[1] at DFT/B3LYP/6-311G* using the geometry from the already minimised full molecular balance from Spartan '14 to generate an NBO output. The NBO output was then inputted to NBO 6.0[2] to obtain second-order perturbation theory output energies, images created using JmolNbo Visualization Helper Version 2.0 and Jmol.

Table B.8 NBO second-order perturbation energies. Orbital delocalization was seen from both lone pairs orbitals on the formyl oxygen. The sum total lone pair n→σ* interaction energy is also given. Lone pair n→σ* interactions were seen (**Figure 3.8**). A further lone pair n→σ* orbital delocalisation was seen from the N of the pyridine into the N-H antibonding orbital (**Figure 3.9**).

Compound	LP (1) → σ* / kJ mol^{-1}	LP (2) → σ* / kJ mol^{-1}	LP(N) →σ* / kJ mol^{-1}	Combined interaction strength / kJ mol^{-1}
3a	11.96	22.21		34.18
3b-OMe	12.76	19.91		32.67
3b-CN	20.12	26.94		47.06
3b-H	16.40	29.74		46.14
4a-Me	11.63	23.72		35.35
4a-CF_3	22.96	37.81		60.78
4a-^{t}Bu	17.86	29.62		47.48
4a-NH_2	11.21	24.39		35.60
4b-H	17.15	29.11		46.26
4b-OMe	16.06	27.73		43.80
4c-H	15.39	20.79	10.88	47.06
4c-F	15.94	22.84	10.00	48.77

Table B.9 NBO second-order perturbation energies. Orbital delocalization was seen from both lone pairs orbitals on the formyl oxygen. The sum total lone pair n→σ* interaction energy is also given. Lone pair n→σ* interactions were seen (**Figure 3.19**). A further lone pair n→σ* orbital delocalisation was seen in subsequent H-bonds in molecular balances **5**-2H and **5**-3H from the O of the hydroxy group into the O-H antibonding orbital (**Figure 3.19**).

Compound	LP (1) → σ* / kJ mol^{-1}	LP (2) → σ* / kJ mol^{-1}	LP (1) → σ* / kJ mol^{-1}	LP (2) → σ* / kJ mol^{-1}	LP (1) → σ* / kJ mol^{-1}	Combined interaction strength / kJ mol^{-1}
5-1H	16.53	30.63				47.15
5-2H	20.17	36.57	6.82	2.97		66.53
5-3H	21.21	39.50	5.06	2.34	2.76	70.88
6-*p*F	17.99	35.02				53.01
6-*p*NO_2	19.29	35.61				54.89
6-*p*CF_3	18.79	34.81				53.60
6-*m*Me	16.48	30.12				46.61
6-*m*OH	15.65	27.45				43.10

Calculated Molecular Orbital Energies

A detailed molecular orbital analysis was performed in this study in which the orbital energies of open and closed conformers of the molecular balances were compared. To enable identification and pairing of molecular orbitals found in the open and closed conformers it was necessary to avoid orbital splitting arising from the canonical resonance forms of the aromatic electrons (that were not involved in the interactions of interest). The minimised full molecular balance structures were subsequently used to generate simplified balance structures of the type shown in **Figure B.8**, in which the 4-fluorophenyl moiety was replaced with a proton with a N-H bond length of 1.012 Å.

Single point energy calculations were then performed on each structure to generate both conformation energy differences and the orbitals used for the detailed orbital analysis study. The simplified system was verified, where the calculated conformational energy difference between the open and closed conformers for the full balances (**Figures 3.4 and 3.16**) were compared with those of the simplified balances (**Figure B.8**) and found to correlate well within each series of balances (**Figures B.9** and **B.10)**. These correlations verified that the simplified balances provided reasonable models of the electronic trends governing the conformational preferences of the balances.

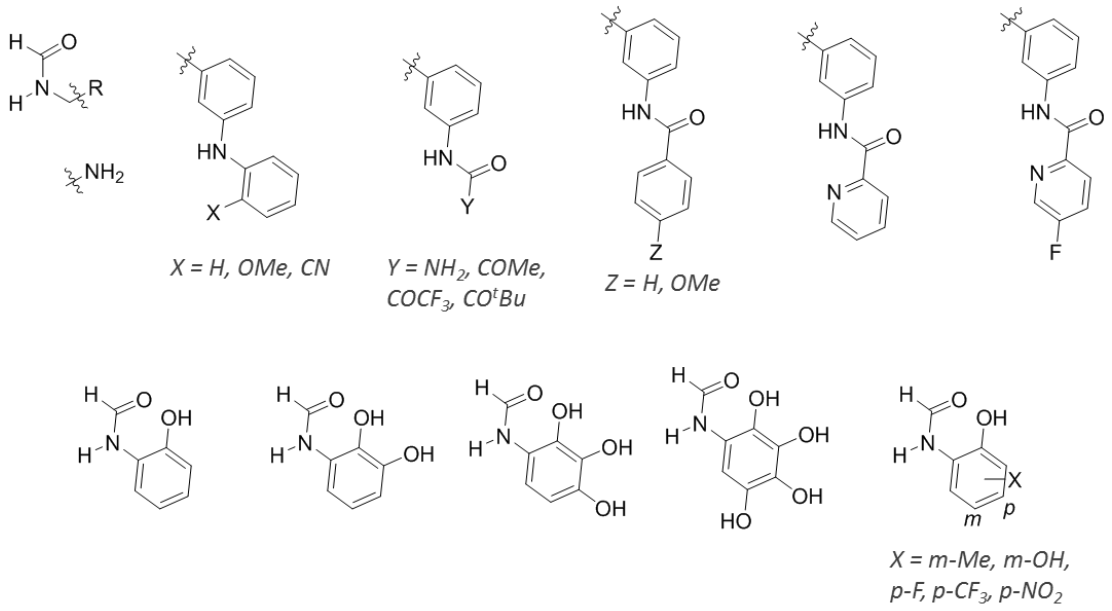

Figure B.8 Structures of simplified molecular balances used for molecular orbital analyses.

Table B.10 Calculated conformational energy differences of simple balance series **3'** and **4'** (**Figure B.8**) calculated using B3LYP/6-311G*.

Compound	Closed conformer *E*/ kJ mol^{-1}	Open conformer *E* / kJ mol^{-1}	ΔE_{CALC}/ kJ mol^{-1}
3a'	-1301510.93	-1301537.06	-26.13
3b'-OMe	-2209017.92	-2209023.24	-5.32
3b'-CN	-2150496.97	-2150517.84	-20.87
3b'-H	-1908257.04	-1908277.70	-20.66
4a'-Me	-1702418.25	-1702454.18	-35.93
4a'-CF_3	-2484308.69	-2484334.05	-25.36
4a'-^{t}Bu	-2012124.16	-2012166.64	-42.48
4a'-NH_2	-1744570.25	-1744616.15	-45.90
4b'-H	-2205924.16	-2205959.65	-35.49
4b'-OMe	-2506679.71	-2506718.40	-38.69
4c'-H	-2248081.21	-2248083.85	-2.64
4c'-F	-2508696.75	-2508700.71	-3.96

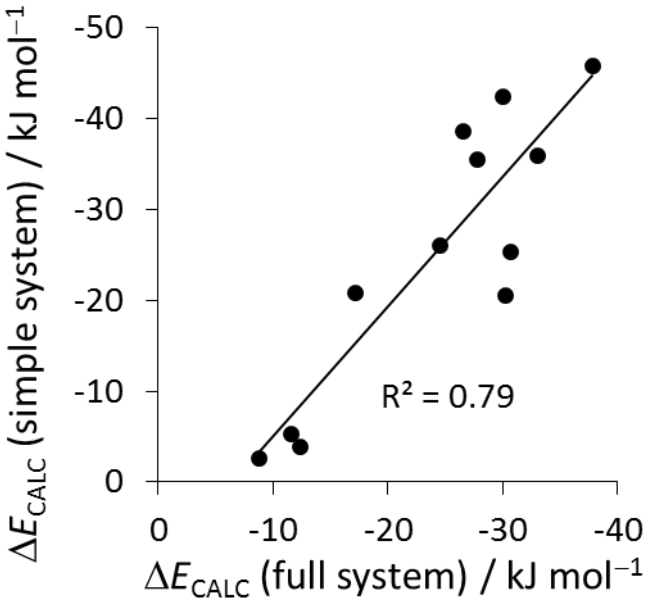

Figure B.9 Plot of conformational energy differences between full molecular balances and simplified molecular balances of series **3** and **4**. Calculated using B3LYP/6-311G*

Table B.11 Calculated conformational energy differences of simple balance series **5'** and **6'** (**Figure B.8**) calculated using B3LYP/6-311G*.

Compound	Closed conformer *E*/ kJ mol^{-1}	Open conformer *E* / kJ mol^{-1}	ΔE_{CALC}/ kJ mol^{-1}
5'-1H	-1250447.47	-1250467.99	-20.52
5'-2H	-1447987.51	-1448019.59	-32.08
5'-3H	-1645531.52	-1645561.52	-30.00
6'-*p*F	-1511068.18	-1511090.26	-22.08
6'-*p*NO_2	-1787504.70	-1787533.12	-28.42
6'-*p*CF_3	-2135607.49	-2135631.62	-24.13
6'-*m*Me	-1353694.30	-1353715.70	-21.40
6'-*m*OH	-1447976.83	-1448000.33	-23.50

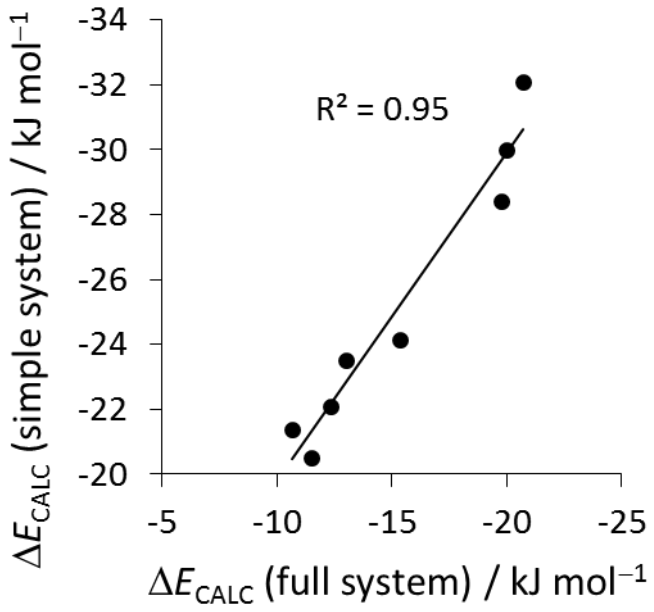

Figure B.10 Plot of conformational energy differences between full molecular balances and simplified molecular balances of series **5** and **6**. Calculated using B3LYP/6-311G*.

Table B.12 Molecular orbital energies of balances **3a**', **3b**'-OMe and **3b**'-CN in the open and closed conformers. Calculated at B3LYP/6-311G*

Molecular orbital	**3a'**		**3b'-OMe**		**3b'-CN**	
	Molecular Orbital Energies / eV					
	open	*closed*	*open*	*closed*	*open*	*closed*
HOMO	-5.90	-5.44	-5.27	-4.93	-6.16	-5.60
HOMO {-1}	-6.73	-6.73	-6.41	-6.09	-7.09	-7.03
HOMO {-2}	-7.25	-7.47	-6.92	-6.73	-7.18	-7.12
HOMO {-3}	-7.38	-7.61	-7.07	-6.84	-7.50	-7.32
HOMO {-4}	-8.72	-8.35	-7.36	-7.41	-7.69	-7.61
HOMO {-5}	-9.62	-9.37	-7.40	-7.56	-7.72	-7.77
HOMO {-6}	-9.89	-9.61	-8.79	-8.45	-9.28	-8.72
HOMO {-7}	-10.41	-10.23	-8.93	-8.60	-9.46	-8.89
HOMO {-8}	-10.70	-10.76	-9.22	-8.88	-9.85	-9.26
HOMO {-9}	-11.18	-10.90	-9.68	-9.42	-10.05	-9.44

Table B.13 Molecular orbital energies of balances **3b**'-H, **4a**'-Me and **4a**'-CF_3 in the open and closed conformers. Calculated at B3LYP/6-311G*

Molecular orbital	**3b'-H**		**4a'-Me**		**4a'-CF_3**	
	Molecular Orbital Energies / eV					
	open	*closed*	*open*	*closed*	*open*	*closed*
HOMO	-5.57	-5.14	-6.41	-6.06	-6.84	-6.61
HOMO {-1}	-7.00	-6.71	-6.97	-6.78	-7.40	-7.23
HOMO {-2}	-7.05	-6.82	-7.22	-6.97	-7.79	-7.56
HOMO {-3}	-7.20	-6.91	-7.55	-7.88	-7.85	-7.96
HOMO {-4}	-7.43	-7.66	-7.64	-8.01	-8.08	-8.14
HOMO {-5}	-7.47	-7.79	-8.64	-8.35	-9.19	-8.66
HOMO {-6}	-8.87	-8.59	-9.88	-9.64	-10.22	-10.03
HOMO {-7}	-9.58	-9.23	-10.04	-9.70	-10.51	-10.18
HOMO {-8}	-9.75	-9.42	-10.15	-9.88	-10.65	-10.38
HOMO {-9}	-9.95	-9.68	-10.76	-10.67	-11.17	-11.07

Table B.14 Molecular orbital energies of balances **4a**'-^{t}Bu, **4a**'-NH_2 and **4b**'-H in the open and closed conformers. Calculated at B3LYP/6-311G*

Molecular orbital	**4a'-^{t}Bu**		**4a'-NH_2**		**4b'-H**	
	Molecular Orbital Energies / eV					
	open	*closed*	*open*	*closed*	*open*	*closed*
HOMO	-6.74	-6.07	-6.59	-5.85	-6.67	-6.10
HOMO {-1}	-6.96	-6.59	-6.90	-6.89	-6.91	-6.70
HOMO {-2}	-7.08	-6.99	-6.94	-6.94	-6.99	-6.89
HOMO {-3}	-7.19	-7.87	-7.18	-7.32	-7.21	-6.96
HOMO {-4}	-7.30	-8.02	-7.60	-7.99	-7.34	-7.08
HOMO {-5}	-8.17	-8.17	-8.11	-8.13	-7.54	-7.85
HOMO {-6}	-9.47	-8.84	-8.41	-8.42	-7.68	-8.02
HOMO {-7}	-9.53	-8.87	-9.84	-9.60	-8.39	-8.21
HOMO {-8}	-9.90	-9.52	-9.96	-9.83	-9.83	-9.33
HOMO {-9}	-9.93	-9.67	-10.08	-10.14	-9.97	-9.66

Table B.15 Molecular orbital energies of balances **4b**'-OMe, **4c**'-H and **4c**'-F in the open and closed conformers. Calculated at B3LYP/6-311G*

Molecular orbital	**4b'-OMe**		**4c'-H**		**4c'-F**	
	Molecular Orbital Energies / eV					
	open	*closed*	*open*	*closed*	*open*	*closed*
HOMO	-6.49	-5.92	-6.22	-6.05	-6.29	-6.13
HOMO {-1}	-6.73	-6.21	-6.98	-6.67	-7.05	-6.79
HOMO {-2}	-6.89	-6.68	-7.11	-6.89	-7.26	-7.00
HOMO {-3}	-7.02	-6.93	-7.39	-7.30	-7.46	-7.31
HOMO {-4}	-7.11	-6.99	-7.46	-7.42	-7.55	-7.50
HOMO {-5}	-7.42	-7.79	-7.59	-7.50	-7.60	-7.64
HOMO {-6}	-7.53	-7.95	-7.99	-7.70	-8.25	-7.87
HOMO {-7}	-8.21	-8.10	-8.37	-8.07	-8.56	-8.19
HOMO {-8}	-9.22	-8.74	-8.62	-8.13	-8.73	-8.35
HOMO {-9}	-9.46	-8.94	-9.76	-9.58	-9.84	-9.65

Table B.16 Molecular orbital energies of balances **5**'-1H, **5**'-2H and **5**'-3H in the open and closed conformers. Calculated at B3LYP/6-311G*

Molecular orbital	**5-1H**		**5-2H**		**5-3H**	
	Molecular Orbital Energies / eV					
	open	*closed*	*open*	*closed*	*open*	*closed*
HOMO	-6.56	-6.30	-6.26	-6.03	-6.21	-5.87
HOMO {-1}	-7.28	-6.91	-6.98	-6.59	-6.47	-6.24
HOMO {-2}	-7.46	-7.90	-7.49	-8.05	-7.45	-8.01
HOMO {-3}	-8.10	-8.42	-8.00	-8.40	-7.88	-8.12
HOMO {-4}	-9.69	-8.96	-9.51	-9.23	-9.17	-9.21
HOMO {-5}	-9.92	-9.72	-10.11	-9.54	-10.18	-9.55
HOMO {-6}	-10.57	-10.25	-10.43	-9.95	-10.31	-9.96
HOMO {-7}	-11.13	-10.46	-10.53	-10.42	-10.52	-10.13
HOMO {-8}	-11.31	-11.38	-10.99	-10.78	-11.04	-10.65
HOMO {-9}	-11.61	-11.82	-11.55	-11.07	-11.11	-11.01

Table B.17 Molecular orbital energies of balances **6**'-*p*F, **6**'-*p*NO_2 and **6**'-*p*CF_3 in the open and closed conformers. Calculated at B3LYP/6-311G*

Molecular orbital	**6'-*p*F**		**6'-*p*NO_2**		**6'-*p*CF_3**	
	Molecular Orbital Energies / eV					
	open	*closed*	*open*	*closed*	*open*	*closed*
HOMO	-6.81	-6.46	-7.34	-6.99	-7.01	-6.74
HOMO {-1}	-7.39	-7.04	-8.20	-7.68	-7.72	-7.43
HOMO {-2}	-7.59	-8.06	-8.40	-8.16	-7.77	-8.25
HOMO {-3}	-8.16	-8.52	-7.88	-8.44	-8.58	-8.89
HOMO {-4}	-9.74	-9.27	-8.53	-8.61	-10.15	-9.41
HOMO {-5}	-10.27	-9.87	-8.85	-8.67	-10.34	-10.18
HOMO {-6}	-10.74	-10.19	-8.92	-9.18	-10.83	-10.58
HOMO {-7}	-11.29	-11.26	-10.43	-9.70	-11.30	-10.76
HOMO {-8}	-11.64	-11.57	-10.79	-10.48	-11.51	-11.12
HOMO {-9}	-11.76	-11.68	-11.55	-11.05	-11.60	-11.55

Table B.18 Molecular orbital energies of balances **6**'-*m*Me and **6**'-*m*OH in the open and closed conformers. Calculated at B3LYP/6-311G*

Molecular orbital	**6-*m*Me**		**6-*m*OH**	
	Molecular Orbital Energies / eV			
	open	*closed*	*open*	*closed*
HOMO	-6.35	-6.09	-6.01	-5.83
HOMO {-1}	-7.27	-6.84	-7.27	-6.91
HOMO {-2}	-7.41	-7.85	-7.42	-7.85
HOMO {-3}	-7.93	-8.27	-8.07	-8.10
HOMO {-4}	-9.34	-8.87	-8.91	-8.84
HOMO {-5}	-9.77	-9.48	-9.89	-9.26
HOMO {-6}	-10.31	-9.96	-10.50	-9.92
HOMO {-7}	-10.56	-10.18	-11.01	-10.90
HOMO {-8}	-11.23	-10.89	-11.11	-10.97
HOMO {-9}	-11.34	-11.20	-11.31	-11.25

Functional Group Intramolecular Symmetry Adapted Perturbation Theory (fiSAPT)

The PSI4 software[3] was used to perform fiSAPT calculations using the SAPT0 methodology (explained in **Chapter 1**, **Equation 1.3**). Geometries from minimisations performed in Spartan '14 were used as an input for fiSAPT calculations. In **Chapter 3** the 6-311G* basis set was used for all calculations. The output gave the energetic contributions of electrostatics, induction, exchange-repulsion and dispersion to give a total SAPT interaction energy prediction. These values are presented in **Chapter 3** (**Figures 3.14** and **3.24**).

Table B.19 Energetic contributions of the H-bonds seen in molecular balance series **3** and **4**. The interaction is decomposed into electrostatics, exchange-repulsion, induction and dispersion to give a total SAPT predicted interaction energy. Calculated using PSI4 SAPT0/6-311G*.

Compound	Electrostatics / kJ mol^{-1}	Exchange / kJ mol^{-1}	Induction / kJ mol^{-1}	Dispersion / kJ mol^{-1}	Total SAPT / kJ mol^{-1}
3a	-31.19	42.04	-10.96	-6.78	-6.78
3b-OMe	-17.76	36.12	-10.37	-9.82	-1.83
3b-CN	-24.27	45.28	-14.46	-10.56	-4.01
3b-H	-37.11	49.05	-14.24	-9.97	-12.27
4a-Me	-41.24	48.55	-13.74	-10.64	-17.06
4a-CF_3	-42.82	48.05	-16.36	-9.50	-20.63
4a-^{t}Bu	-44.77	51.36	-16.27	-13.41	-23.09
4a-NH_2	-58.37	60.03	-15.89	-12.16	-26.39
4b-H	-47.51	49.19	-16.31	-12.24	-26.88
4b-OMe	-47.04	48.63	-16.14	-12.24	-26.78
4c-H	-18.87	29.37	-9.39	-8.74	-7.62
4c-F	-21.08	31.47	-10.12	-9.16	-8.88

Table B.20 Energetic contributions of the H-bonds seen in molecular balance series **5** and **6**. The interaction is decomposed into electrostatics, exchange-repulsion, induction and dispersion to give a total SAPT predicted interaction energy. Calculated using PSI4 SAPT0/6-311G*.

Compound	Electrostatics / kJ mol^{-1}	Exchange / kJ mol^{-1}	Induction / kJ mol^{-1}	Dispersion / kJ mol^{-1}	Total SAPT / kJ mol^{-1}
5-1H	-57.6531	69.39517	-24.1448	-10.4594	-22.8621
5-2H	-63.2576	74.86267	-27.0989	-10.965	-26.4589
5-3H	-64.971	76.49647	-28.0263	-10.978	-27.4789
6-*p*F	-60.6461	72.55042	-25.5636	-10.6356	-24.2949
6-*p*NO_2	-62.9858	74.98801	-26.4445	-11.0236	-25.466
6-*p*CF_3	-62.0572	73.81003	-26.1713	-10.9142	-25.3327
6-*m*Me	-57.5809	68.25706	-24.1788	-10.4615	-23.9641
6-*m*OH	-56.0242	66.20123	-23.0399	-10.3219	-23.1848

References

1. Frisch, M. J.; Trucks, G. W.; Schlegel, H. B.; Scuseria, G. E.; Robb, M. A.; Cheeseman, J. R.; Scalmani, G.; Barone, V.; Mennucci, B.; Petersson, G. A.; *et al*. Gaussian 09, Revision E.01. Gaussian, Inc: Wallingford CT 2013.

2. Glendening, E. D.; Badenhoop, J. K.; Reed, A. E.; Carpenter, J. E.; Bohmann, J. A.; Morales, C. M.; Landis, C. R.; Weinhold, F. NBO 6.0. Theoretical Chemistry Institute, University of Wisconsin: Madison, WI 2013.

3. Parrish, R. M.; Burns, L. A.; Smith, D. G. A.; Simmonett, A. C.; DePrince, A. E.; Hohenstein, E. G.; Bozkaya, U.; Sokolov, A. Y.; Di Remigio, R.; Richard, R. M.; *et al*. Psi4 1.1: An Open-Source Electronic Structure Program Emphasizing Automation, Advanced Libraries, and Interoperability. *J. Chem. Theory Comput.* **2017**, *13* (7), 3185–3197.

Appendix C: Experimental and Computational Data for Chapter 4

Experimental Data

Below is the experimental data used for comparison to computational results. All experimental data has been measured by Kamila Muchowska.

Table C.1 Experimental conformational free energy differences of molecular balance **7**-CHO, ΔG_{EXP} measured in various solvents at 298 K. Measured by KM.

7-H			
		Error	
	ΔG / kJ mol^{-1}	-	+
Chloroform-d	1.8	0.13	0.13
Acetone	2.5	0.20	0.22
Acetonitrile-d_3	2.4	0.19	0.20
Benzene-d_6	2.1	0.13	0.13
Ethyl acetate	2.1	0.17	0.18
Hexane	0.9	0.13	0.13
THF	2.1	0.17	0.18
DCM	1.8	0.13	0.13
Ethanol	-0.7	0.13	0.13
Methanol	-0.3	0.13	0.13
DMSO-d_6	2.8	0.22	0.24

Table C.2 Experimental conformational free energy differences of molecular balance **7**-COMe, ΔG_{EXP} measured in various solvents at 298 K. Measured by KM.

7-Me			
		Error	
	ΔG / kJ mol^{-1}	-	+
Chloroform-d	-3.2	0.28	0.25
Acetone	-2.7	0.23	0.21
Acetonitrile-d_3	-2.3	0.20	0.18
Benzene-d_6	-4.1	0.43	0.36
Ethyl acetate	-3.2	0.29	0.26
Hexane	-4.2	0.45	0.38
THF	-3.2	0.28	0.25
DCM	-2.6	0.22	0.20
Ethanol	-3.1	0.27	0.24
Methanol	-3.0	0.26	0.24
DMSO-d_6	-2.7	0.23	0.21

Table C.3 Experimental conformational free energy differences of molecular balance **7**-COOMe, ΔG_{EXP} measured in various solvents at 298 K. Measured by KM.

7-OMe			
		Error	
	ΔG / kJ mol^{-1}	-	+
Chloroform-d	-1.4	0.13	0.13
Acetone	-1.6	0.13	0.13
Acetonitrile-d_3	-1.8	0.13	0.13
Benzene-d_6	-1.7	0.13	0.13
Ethyl acetate	-1.4	0.13	0.13
Hexane	-1.0	0.13	0.13
THF	-1.3	0.13	0.13
DCM	-1.4	0.13	0.13
Ethanol	-1.9	0.13	0.13
Methanol	-2.0	0.17	0.16
DMSO-d_6	-2.3	0.19	0.18

Table C.4 Experimental conformational free energy differences of molecular balance **7**-$CONMe_2$, ΔG_{EXP} measured in various solvents at 298 K. Measured by KM.

7-NMe_2			
		Error	
	ΔG / kJ mol^{-1}	-	+
Chloroform-d	-1.8	0.13	0.13
Acetone	-0.8	0.13	0.13
Acetonitrile-d_3	0.5	0.13	0.13
Benzene-d_6	-3.2	0.28	0.25
Ethyl acetate	-1.8	0.13	0.13
Hexane	-4.9	0.60	0.48
THF	-1.9	0.13	0.13
DCM	-1.0	0.13	0.13
Ethanol	1.0	0.13	0.13
Methanol	0.7	0.13	0.13
DMSO-d_6	0.6	0.13	0.13

Minimised Geometries

Full molecular balance structures shown in **Figures 4.6** and **4.16** minimised in both the open and closed conformations using either the B3LYP or M06-2X methods and basis sets 6-31G* in Spartan '14. Frequency calculations were performed on all minimised structures, which confirmed no imaginary frequencies. The resulting gas-phase energies and corresponding energy differences, ΔE_{CALC} in each conformer are reported.

Table C.5 Distance and interaction angles between carbonyl donor and acceptor groups for molecular balances in series 7, 8 and 9 (**Chapter 4, Figures 4.6** and **4.16**). Calculated using Spartan '14 DFT/B3LYP/6-31G*.

Compound	Carbonyl···carbonyl distance/ Å	Interaction angle/ °
7-H	3.062	130.2
7-Me	2.964	100.8
7-OMe	3.022	90.0
7-NMe_2	3.070	110.71
8a-H	2.794	100.4
8a-F	2.788	101.34
8a-OMe	2.792	101.44
8b-H	3.182	101.4
8b-F	3.158	101.5
8b-OMe	3.251	101.9
9-NO_2	2.687	99.8
9-CN	2.702	99.8
9-H	2.741	99.8
9-OMe	2.851	100.1
9-NMe_2	3.010	97.4
10	3.333	109.3

Table C.6 Calculated conformational energy differences of full balance series **7** calculated using B3LYP/6-31G*.

Compound	Closed conformer *E*/ kJ mol^{-1}	Open conformer *E* / kJ mol^{-1}	ΔE_{CALC}/ kJ mol^{-1}
7-H	-2217335.71	-2217335.29	0.42
7-Me	-2320569.35	-2320577.52	-8.17
7-OMe	-2518095.02	-2518097.55	-2.53
7-NMe_2	-2569138.45	-2569152.16	-13.71

Table C.7 Calculated conformational energy differences of full balance series **7** calculated using ωB97X-D/6-311G*.

Compound	Closed conformer *E*/ kJ mol^{-1}	Open conformer *E* / kJ mol^{-1}	ΔE_{CALC}/ kJ mol^{-1}
7-H	-2216627.37	-2216627.31	0.06
7-Me	-2319841.55	-2319847.04	-5.49
7-OMe	-2517304.40	-2517306.31	-1.91
7-NMe_2	-2568342.41	-2568356.72	-14.31

Table C.8 Calculated conformational energy differences of full balance series **8** and **9** calculated using B3LYP/6-311G*.

Compound	Closed conformer *E*/ kJ mol^{-1}	Open conformer *E* / kJ mol^{-1}	ΔE_{CALC}/ kJ mol^{-1}
8a-H	-1557249.10	-1557255.15	-6.05
8a-F	-1817781.01	-1817786.50	-5.49
8a-OMe	-1754709.92	-1754713.42	-3.50
8b-H	-2405168.93	-2405174.27	-5.34
8b-F	-2665699.77	-2665703.90	-4.13
8b-OMe	-2705818.22	-2705824.53	-6.31
9-NO_2	-2597571.40	-2597585.53	-14.13
9-CN	-2302837.28	-2302851.00	-13.72
9-H	-2060654.88	-2060663.74	-8.86
9-OMe	-2361336.11	-2361341.90	-5.79
9-NMe_2	-2412387.57	-2412392.48	-4.91

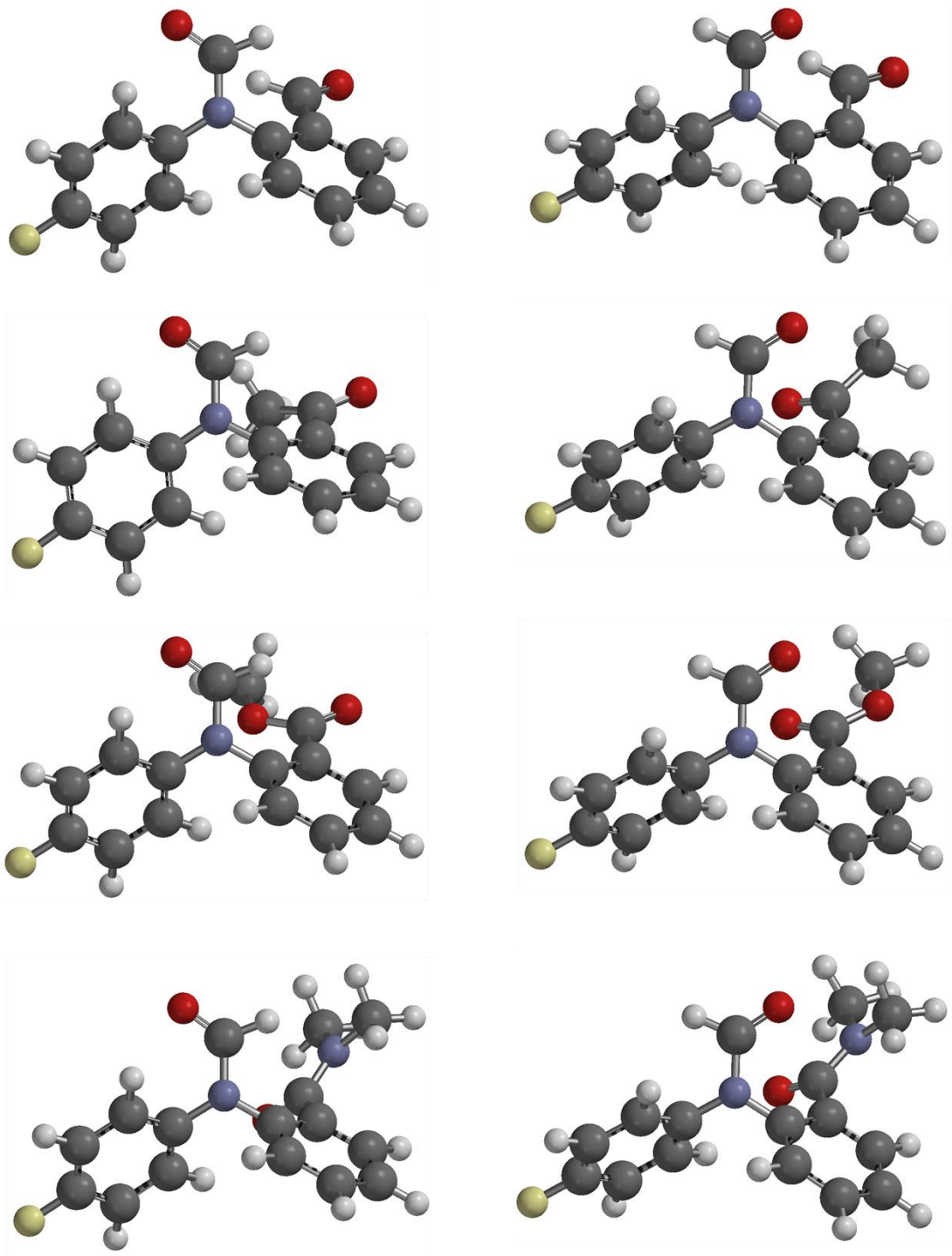

Figure C.1 Minimised geometries of molecular balances in series **7**.Minimised using Spartan ’14 DFT/B3LYP/6-31G*.

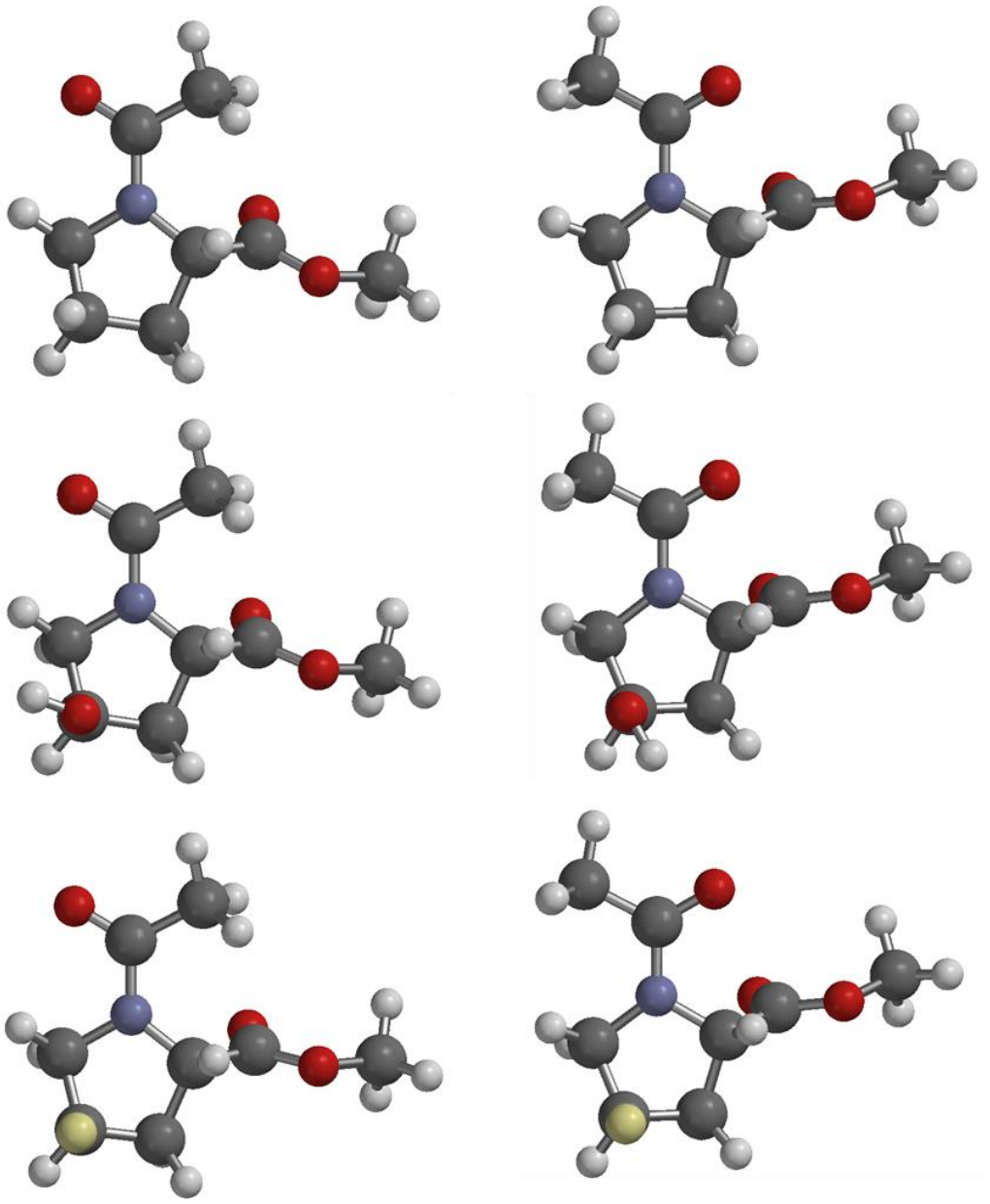

Figure C.2 Minimised geometries of molecular balances in series **8a**.Minimised using Spartan ’14 DFT/B3LYP/6-31G*.

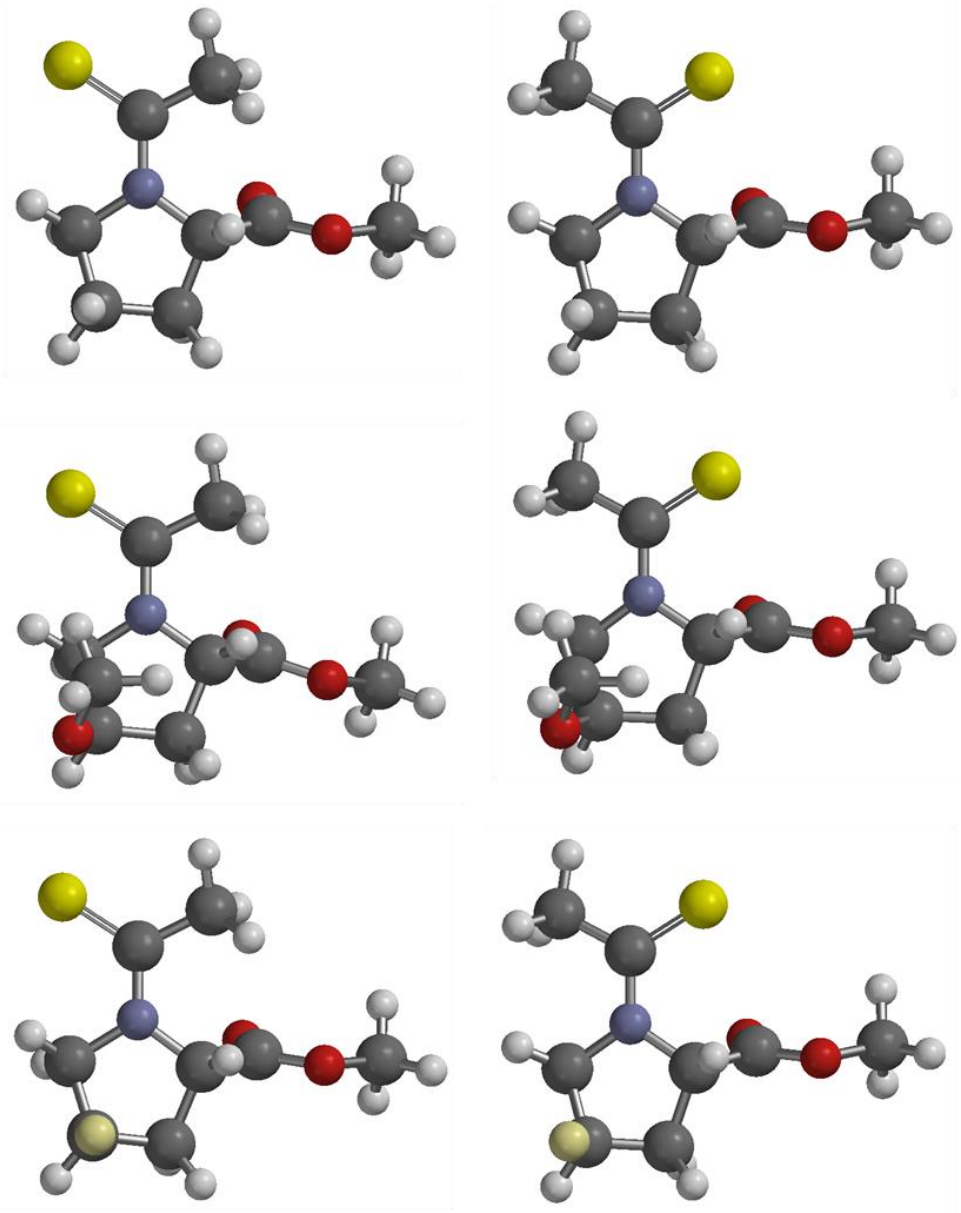

Figure C.3 Minimised geometries of molecular balances in series **8b**.Minimised using Spartan ’14 DFT/B3LYP/6-31G*.

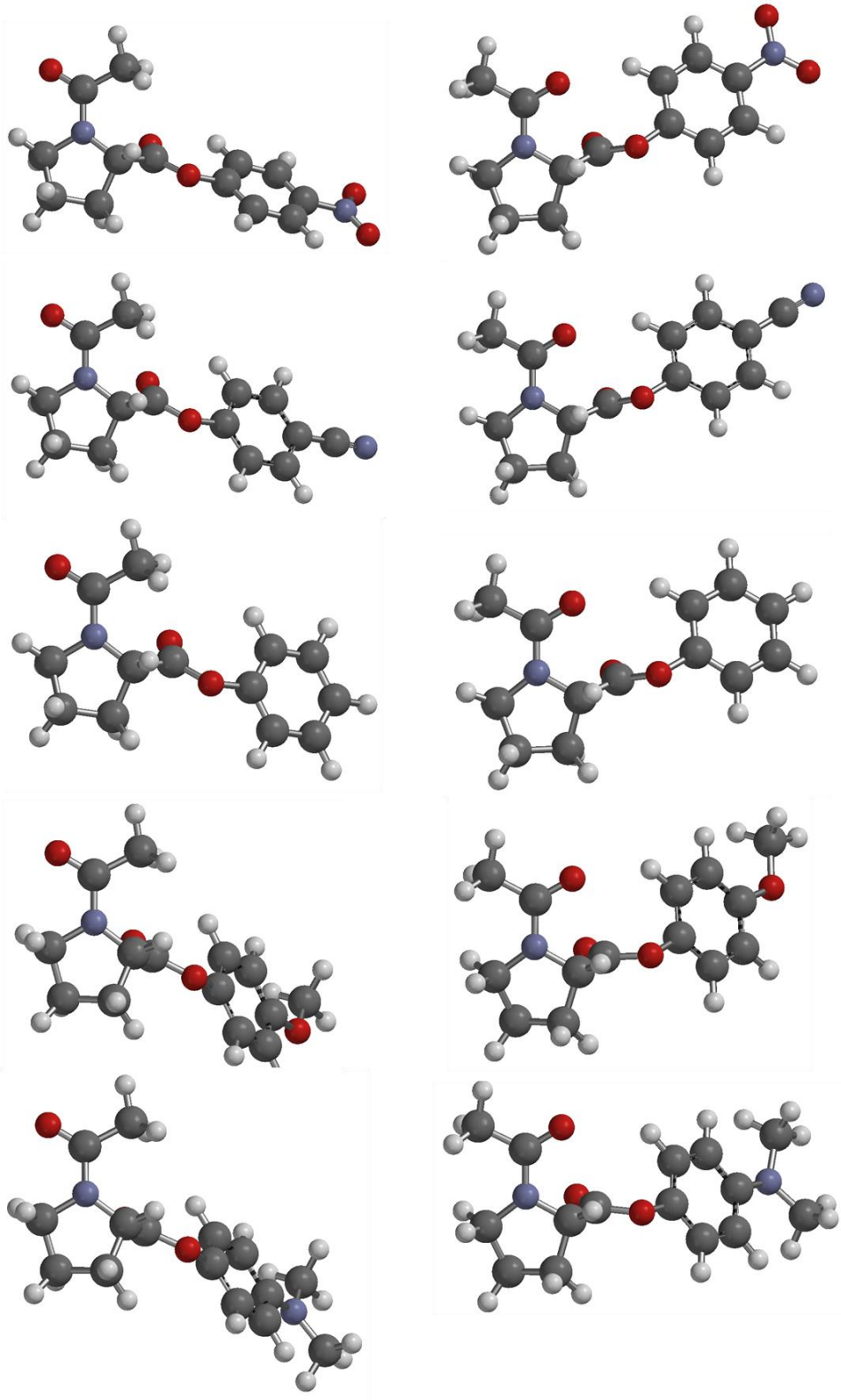

Figure C.4 Minimised geometries of molecular balances in series **9**.Minimised using Spartan ’14 DFT/B3LYP/6-31G*.

Calculated Molecular Orbital Energies

A detailed molecular orbital analysis was performed in this study in which the orbital energies of open and closed conformers of the molecular balances were compared. To enable identification and pairing of molecular orbitals found in the open and closed conformers it was necessary to avoid orbital splitting arising from the canonical resonance forms of the aromatic electrons (that were not involved in the interactions of interest). The minimised full molecular balance structures were subsequently used to generate simplified balance structures from series **7** of the type shown in **Figure C.5**, in which the 4-fluorophenyl moiety was replaced with a proton with a N-H bond length of 1.012 Å. For molecular balances from series **8** and **9**, full molecular balance structures were used for the molecular orbital analyses.

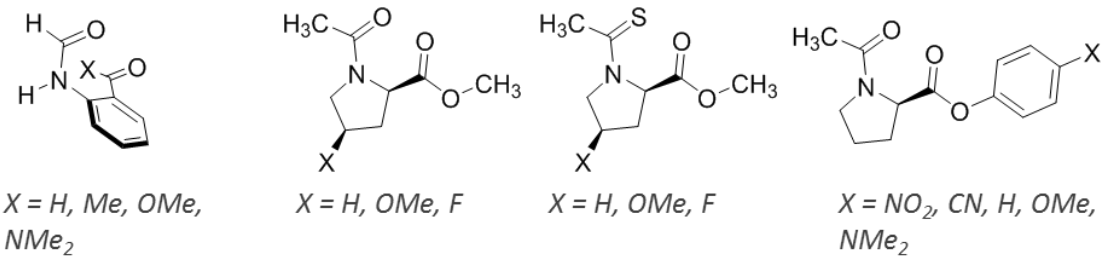

Figure C.5 Structures of molecular balances used for the molecular orbital analyses.

Table C.9 Calculated conformational energy differences of simplified balance series **7** (**Figure 6.2C**) calculated using B3LYP/6-31G*.

Compound	**Closed conformer *E*/ kJ mol^{-1}**	**Open conformer *E* / kJ mol^{-1}**	**ΔE_{CALC}/ kJ mol^{-1}**
7-H	-1350179.59	-1350179.95	-0.36
7-Me	-1453410.34	-1453415.90	-5.56
7-OMe	-1650936.57	-1650937.51	-0.94
7-NMe$_2$	-1701976.19	-1701988.18	-11.99

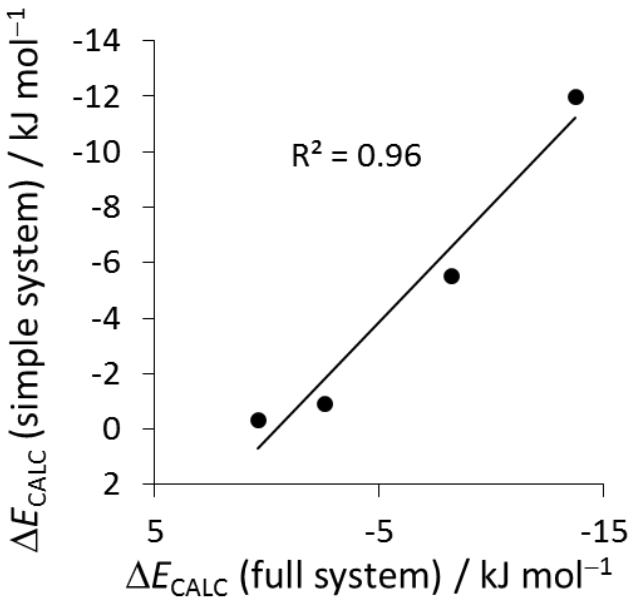

Figure A.19 Plot of conformational energy differences between full molecular balances and simplified molecular balances of series **7**. Calculated using B3LYP/6-311G*.

Table C.10 Molecular orbital energies of balances **7**'-CHO, **7**'-COMe and **7**'-COOMe in the open and closed conformers. Calculated at B3LYP/6-311G*

Molecular orbital	**7'-H**		**7'-Me**		**7'-OMe**	
	Molecular Orbital Energies / eV					
	open	*closed*	*open*	*closed*	*open*	*closed*
HOMO	-6.94	-6.78	-6.90	-6.21	-6.73	-6.58
HOMO {-1}	-7.21	-6.99	-6.98	-6.50	-6.99	-6.92
HOMO {-2}	-7.35	-7.18	-7.27	-6.64	-7.35	-7.06
HOMO {-3}	-7.57	-7.47	-7.44	-6.99	-7.75	-7.37
HOMO {-4}	-8.29	-8.16	-8.09	-7.26	-7.96	-7.93
HOMO {-5}	-10.19	-9.92	-9.72	-7.86	-8.36	-8.08
HOMO {-6}	-10.22	-9.99	-10.05	-9.50	-9.72	-9.59
HOMO {-7}	-10.57	-10.34	-10.21	-9.81	-10.13	-9.87
HOMO {-8}	-11.17	-10.98	-10.46	-9.97	-10.18	-9.92
HOMO {-9}	-11.36	-11.25	-11.01	-10.22	-10.39	-10.34

Table C.11 Molecular orbital energies of balances **7**'-$CONMe_2$, **8a**'-H and **8a**'-OMe in the open and closed conformers. Calculated at B3LYP/6-311G*

Molecular orbital	**7'-NMe_2**		**8a'-H**		**8a'-OMe**	
	Molecular Orbital Energies / eV					
	open	*closed*	*open*	*closed*	*open*	*closed*
HOMO	-6.90	-6.54	-6.37	-6.44	-6.46	-6.43
HOMO {-1}	-6.98	-6.67	-6.46	-6.59	-6.51	-6.58
HOMO {-2}	-7.27	-7.03	-7.70	-7.29	-7.70	-7.31
HOMO {-3}	-7.44	-7.32	-8.52	-7.98	-7.73	-7.77
HOMO {-4}	-8.09	-7.96	-9.17	-9.29	-8.51	-8.00
HOMO {-5}	-9.72	-9.35	-9.62	-9.34	-9.12	-9.18
HOMO {-6}	-10.05	-9.90	-9.71	-9.55	-9.43	-9.41
HOMO {-7}	-10.21	-10.16	-9.74	-9.82	-9.91	-9.50
HOMO {-8}	-10.46	-10.30	-10.10	-9.83	-10.12	-9.95
HOMO {-9}	-11.01	-10.67	-10.34	-10.36	-10.29	-10.26

Table C.12 Molecular orbital energies of balances **8a**'-F, **8b**'-H and **8b**'-OMe in the open and closed conformers. Calculated at B3LYP/6-311G*

Molecular orbital	**8a'-F**		**8b'-H**		**8b'-OMe**	
	Molecular Orbital Energies / eV					
	open	*closed*	*open*	*closed*	*open*	*closed*
HOMO	-6.60	-6.62	-5.27	-5.40	-5.37	-5.49
HOMO {-1}	-6.62	-6.74	-5.88	-5.94	-5.98	-6.03
HOMO {-2}	-7.86	-7.43	-7.86	-7.36	-7.19	-7.26
HOMO {-3}	-8.65	-8.10	-8.54	-8.11	-7.97	-7.59
HOMO {-4}	-9.15	-9.17	-8.70	-8.66	-8.52	-8.26
HOMO {-5}	-9.32	-9.32	-9.20	-9.27	-8.78	-8.62
HOMO {-6}	-9.50	-9.54	-9.75	-9.50	-8.97	-8.98
HOMO {-7}	-10.12	-9.75	-9.93	-9.76	-9.34	-9.43
HOMO {-8}	-10.34	-10.20	-10.01	-9.95	-10.01	-9.81
HOMO {-9}	-10.51	-10.47	-10.36	-10.03	-10.23	-9.98

Table C.13 Molecular orbital energies of balances **8b**'-F, **9**-NO_2 and **9**'-CN in the open and closed conformers. Calculated at B3LYP/6-311G*

Molecular orbital	**8b'-F**		**9'-NO_2**		**9'-CN**	
	Molecular Orbital Energies / eV					
	open	*closed*	*open*	*closed*	*open*	*closed*
HOMO	-5.41	-5.52	-6.72	-6.92	-6.69	-6.80
HOMO {-1}	-6.02	-6.08	-6.80	-7.09	-6.77	-6.92
HOMO {-2}	-8.00	-7.49	-7.51	-7.19	-7.21	-7.07
HOMO {-3}	-8.72	-8.23	-7.86	-7.44	-7.79	-7.38
HOMO {-4}	-8.83	-8.78	-8.02	-7.71	-8.30	-7.90
HOMO {-5}	-9.31	-9.33	-8.30	-7.97	-9.13	-8.69
HOMO {-6}	-9.40	-9.40	-8.51	-8.18	-9.22	-8.82
HOMO {-7}	-9.58	-9.68	-8.54	-8.24	-9.48	-9.29
HOMO {-8}	-10.29	-9.90	-9.49	-8.94	-9.84	-9.57
HOMO {-9}	-10.66	-10.33	-9.83	-9.74	-9.87	-9.71

Table C.14 Molecular orbital energies of balances **9**-H, **9**-OMe and **9**'-NMe_2 in the open and closed conformers. Calculated at B3LYP/6-311G*

Molecular orbital	**9'-H**		**9'-OMe**		**9'-NMe_2**	
	Molecular Orbital Energies / eV					
	open	*closed*	*open*	*closed*	*open*	*closed*
HOMO	-6.44	-6.37	-6.01	-5.72	-5.20	-5.03
HOMO {-1}	-6.52	-6.59	-6.44	-6.53	-6.34	-6.38
HOMO {-2}	-6.80	-6.70	-6.47	-6.69	-6.38	-6.52
HOMO {-3}	-7.08	-6.77	-7.08	-6.77	-6.83	-6.60
HOMO {-4}	-7.87	-7.46	-7.78	-7.39	-7.56	-7.29
HOMO {-5}	-8.96	-8.30	-8.46	-8.10	-7.61	-7.39
HOMO {-6}	-9.24	-9.30	-9.06	-8.60	-8.85	-8.34
HOMO {-7}	-9.68	-9.36	-9.14	-8.89	-9.06	-9.15
HOMO {-8}	-9.73	-9.53	-9.32	-9.40	-9.44	-9.38
HOMO {-9}	-9.81	-9.69	-9.71	-9.58	-9.61	-9.44

Functional Group Intramolecular Symmetry Adapted Perturbation Theory (fiSAPT)

The PSI4 software[1] was used to perform fiSAPT calculations using the SAPT0 methodology (explained in **Chapter 1**, **Equation 1.3**). Geometries from minimisations performed in Spartan '14 were used as an input for fiSAPT calculations. In **Chapter 4** either the 6-31G*, jun-cc-pvdz or aug-cc-pvqz basis sets were used, which are highlighted in the main text. The output gave the energetic contributions of electrostatics, induction, exchange-repulsion and dispersion to give a total SAPT interaction energy prediction. These values are presented in **Chapter 4** (**Figures 4.12**, **4.13**, **4.18**, **4.15** and **4.22**).

Table C.15 Energetic contributions of the H-bonds seen in molecular balance series **7** and molecular balance **10**. The interaction is decomposed into electrostatics, exchange-repulsion, induction and dispersion to give a total SAPT predicted interaction energy. Calculated using PSI4 SAPT0/6-31G* using geometry minimised balaces from Spartan '14 DFT/B3LYP/6-31G*.

Compound	Electrostatics / kJ mol^{-1}	Exchange / kJ mol^{-1}	Induction / kJ mol^{-1}	Dispersion / kJ mol^{-1}	Total SAPT / kJ mol^{-1}
7-H	-0.42	18.91	-4.99	-6.04	7.45
7-Me	-12.60	19.90	-6.78	-9.63	-9.12
7-OMe	-3.88	18.39	-5.44	-8.32	0.76
7-NMe_2	-15.23	17.13	-6.99	-11.04	-16.12
10	-11.81	10.58	-3.07	-5.81	-10.12

Table C.16 Energetic contributions of the H-bonds seen in molecular balance series **7**. The interaction is decomposed into electrostatics, exchange-repulsion, induction and dispersion to give a total SAPT predicted interaction energy. Calculated using PSI4 SAPT0/jun-cc-pvdz using geometry minimised balaces from Spartan '14 DFT/B3LYP/6-31G*.

Compound	Electrostatics / kJ mol^{-1}	Exchange / kJ mol^{-1}	Induction / kJ mol^{-1}	Dispersion / kJ mol^{-1}	Total SAPT / kJ mol^{-1}
7-H	3.05	15.97	-5.12	-6.95	6.94
7-Me	-11.45	19.42	-7.36	-10.81	-10.19
7-OMe	-3.10	17.78	-5.79	-9.23	-0.34
7-NMe_2	-14.52	16.07	-7.47	-12.51	-18.43

Table C.17 Energetic contributions of the H-bonds seen in molecular balance series **7**. The interaction is decomposed into electrostatics, exchange-repulsion, induction and dispersion to give a total SAPT predicted interaction energy. Calculated using PSI4 SAPT0/aug-cc-pvqz using geometry minimised balaces from Spartan '14 DFT/B3LYP/6-31G*.

Compound	Electrostatics / kJ mol^{-1}	Exchange / kJ mol^{-1}	Induction / kJ mol^{-1}	Dispersion / kJ mol^{-1}	Total SAPT / kJ mol^{-1}
7-H	0.10	19.78	-6.04	-9.64	4.21
7-Me	-11.90	19.86	-8.00	-15.29	-15.33
7-OMe	-3.35	18.31	-6.47	-13.30	-4.81
7-NMe_2	-15.04	17.34	-8.22	-17.41	-23.33

Table C.18 Energetic contributions of the H-bonds seen in molecular balance series **7**. The interaction is decomposed into electrostatics, exchange-repulsion, induction and dispersion to give a total SAPT predicted interaction energy. Calculated using PSI4 SAPT0/6-31G* using geometry minimised balaces from Spartan '14 DFT/ωB97X-D/6-31G*.

Compound	Electrostatics / kJ mol^{-1}	Exchange / kJ mol^{-1}	Induction / kJ mol^{-1}	Dispersion / kJ mol^{-1}	Total SAPT / kJ mol^{-1}
7-H	1.34	19.38	-4.99	-6.14	9.60
7-Me	-12.80	21.86	-7.20	-10.09	-8.23
7-OMe	-4.94	20.31	-5.94	-9.04	0.39
7-NMe_2	-16.48	20.55	-7.64	-12.15	-15.72

Table C.19 Energetic contributions of the H-bonds seen in molecular balance series **8**. The interaction is decomposed into electrostatics, exchange-repulsion, induction and dispersion to give a total SAPT predicted interaction energy. Calculated using PSI4 SAPT0/6-31G* using geometry minimised balaces from Spartan '14 DFT/B3LYP/6-31G*.

Compound	Electrostatics / kJ mol^{-1}	Exchange / kJ mol^{-1}	Induction / kJ mol^{-1}	Dispersion / kJ mol^{-1}	Total SAPT / kJ mol^{-1}
8a-H	24.50	36.73	-16.95	-9.92	34.37
8a-OMe	25.79	35.18	-16.76	-9.83	34.38
8a-F	24.12	35.99	-16.68	-9.92	33.52
8b-H	38.18	42.06	-19.25	-11.81	49.18
8b-OMe	36.19	40.81	-18.82	-11.16	47.03
8b-F	35.00	43.86	-19.36	-12.13	47.37

Table C.20 Energetic contributions of the H-bonds seen in molecular balance series **9**. The interaction is decomposed into electrostatics, exchange-repulsion, induction and dispersion to give a total SAPT predicted interaction energy. Calculated using PSI4 SAPT0/6-31G* using geometry minimised balaces from Spartan '14 DFT/B3LYP/6-31G*.

Compound	Electrostatics / kJ mol^{-1}	Exchange / kJ mol^{-1}	Induction / kJ mol^{-1}	Dispersion / kJ mol^{-1}	Total SAPT / kJ mol^{-1}
9-NO_2	26.68	33.89	-18.87	-10.63	31.07
9-CN	17.98	43.11	-20.90	-13.73	26.46
9-H	26.30	35.50	-17.43	-10.17	34.19
9-OMe	17.97	40.53	-18.50	-11.41	28.58
8b-NMe_2	21.67	36.59	-16.72	-9.27	32.27

References

1. Parrish, R. M.; Burns, L. A.; Smith, D. G. A.; Simmonett, A. C.; DePrince, A. E.; Hohenstein, E. G.; Bozkaya, U.; Sokolov, A. Y.; Di Remigio, R.; Richard, R. M.; *et al*. Psi4 1.1: An Open-Source Electronic Structure Program Emphasizing Automation, Advanced Libraries, and Interoperability. *J. Chem. Theory Comput.* **2017**, *13* (7), 3185–3197.

JACS
JOURNAL OF THE AMERICAN CHEMICAL SOCIETY
Article
Cite This: J. Am. Chem. Soc. XXXX, XXX, XXX-XXX
pubs.acs.org/JACS

The Origin of Chalcogen-Bonding Interactions

Dominic J. Pascoe,[†] Kenneth B. Ling,[‡] and Scott L. Cockroft*[,†]

[†]EaStCHEM School of Chemistry, University of Edinburgh, Joseph Black Building, David Brewster Road, Edinburgh EH9 3FJ, U.K.
[‡]Syngenta, Jealott's Hill International Research Centre, Bracknell, Berkshire RG42 6EY, U.K.

Supporting Information

ABSTRACT: Favorable molecular interactions between group 16 elements have been implicated in catalysis, biological processes, and materials and medicinal chemistry. Such interactions have since become known as chalcogen bonds by analogy to hydrogen and halogen bonds. Although the prevalence and applications of chalcogen-bonding interactions continues to develop, debate still surrounds the energetic significance and physicochemical origins of this class of σ-hole interaction. Here, synthetic molecular balances were used to perform a quantitative experimental investigation of chalcogen-bonding interactions. Over 160 experimental conformational free energies were measured in 13 different solvents to examine the energetics of O···S, O···Se, S···S, O···HC, and S···HC contacts and the associated substituent and solvent effects. The strongest chalcogen-bonding interactions were found to be at least as strong as conventional H-bonds, but unlike H-bonds, surprisingly independent of the solvent. The independence of the conformational free energies on solvent polarity, polarizability, and H-bonding characteristics showed that electrostatic, solvophobic, and van der Waals dispersion forces did not account for the observed experimental trends. Instead, a quantitative relationship between the experimental conformational free energies and computed molecular orbital energies was consistent with the chalcogen-bonding interactions being dominated by n → σ* orbital delocalization between a lone pair (n) of a (thio)amide donor and the antibonding σ* orbital of an acceptor thiophene or selenophene. Interestingly, stabilization was manifested through the same acceptor molecular orbital irrespective of whether a direct chalcogen···chalcogen or chalcogen···H−C contact was made. Our results underline the importance of often-overlooked orbital delocalization effects in conformational control and molecular recognition phenomena.

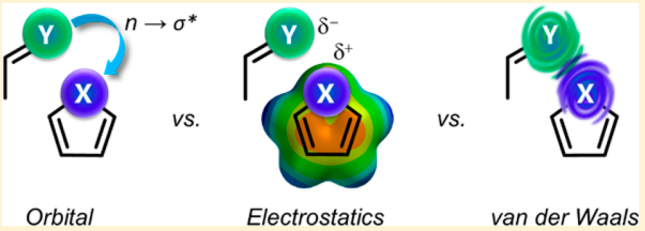

INTRODUCTION

It is reasonable to expect that electron-rich group 16 (chalcogen) elements such as oxygen, sulfur, and selenium may not form particularly favorable contacts with each other. However, chalcogen−chalcogen contacts are so commonly observed in X-ray crystal structures that they have become known as chalcogen-bonding interactions.[1−3] Chalcogen-bonding interactions have been invoked in such diverse areas as catalytic,[4,5] synthetic,[6,7] materials,[8,9] biological,[10] medicinal,[1,11] and supramolecular chemistry.[12−14] Chalcogen-bonding interactions are themselves considered to be a subclass of "σ-hole interactions",[15] which are most well-known for their association with halogen-bonding interactions (group 17).[16−18] Alongside the halogens and chalcogens, tetrel elements (group 14),[19] pnictogens (group 15),[20,21] and even aerogens (group 18)[22] have been identified as being able to engage in σ-hole interactions. Despite the undoubted prevalence of σ-hole interactions, their energetic significance in solution, and the underlying physicochemical origins are the subject of debate.[23−30] σ-Holes were originally defined as being associated with a region of positive electrostatic potential that projects along the Z-axis opposite to a σ bond.[15] In line with the original definition, some experimental characteristics of σ-hole interactions can be qualitatively, and sometimes quantitatively, correlated with electrostatic potentials.[30−32] However, other studies have suggested that dispersion and orbital delocalization effects may also make important contributions.[17,24,29,33−37] For example, X-ray crystallographic data have revealed the striking directional dependency of some σ-hole interactions, which is consistent with geometry dependent orbital effects.[38−41]

Due to the difficulty associated with the measurement of weak interactions in solution, there remains a paucity of quantitative experimental investigations of chalcogen-bonding interactions.[31,36] Furthermore, developing a quantitative understanding of the nature of these interactions is further complicated by the challenges associated with dissecting multiple competing influences and solvent effects, which are both hard to predict, and may dominate the experimental behavior.[42−45]

Here we have used synthetic molecular balances (Figure 1) to perform a quantitative experimental investigation of chalcogen-bonding interactions. Experimental conformational free energies were compared with theory to examine the empirical significance of solvent-mediated electrostatic and solvophobic effects (Figure 2), van der Waals dispersion (Figures 2 and 3), and orbital delocalization (Figures 4−7).

Received: August 10, 2017
Published: October 6, 2017

DOI: 10.1021/jacs.7b08511
J. Am. Chem. Soc. XXXX, XXX, XXX−XXX

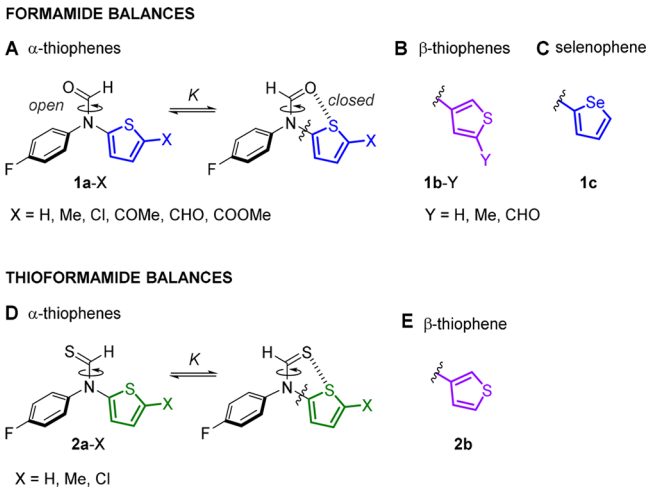

Figure 1. Molecular balances used in the present investigation to investigate chalcogen-bonding interactions.

EXPERIMENTAL EVALUATION OF CHALCOGEN-BONDING INTERACTIONS

We used molecular balances[46] for our quantitative experimental investigation of chalcogen-bonding interactions (Figure 1). Molecular balances provide useful tools for the quantification of interactions, since the position of a conformational equilibrium depends on the magnitude of intramolecular interactions and the competing solvent effects (Figure 1A).[42,43,47,48] Accordingly, molecular balances have been used to measure a wide range of interaction classes including those involving fluorine,[49−51] arenes,[52−61] and carbonyl groups.[62−67] More specifically, the molecular balances shown in Figure 1 are derived from previous investigations of solvent effects and hydrogen bonding interactions.[42,47,68] The new designs in Figure 1 host chalcogen-bonding interactions in the closed conformers (Figure 1A,D, right) that are absent in the open conformation (Figure 1A,D, left). Since rotation about the (thio)formamide is slow on the NMR time scale at room temperature, integration of the discrete ^{19}F NMR resonances corresponding to each conformer provides direct access to the conformational equilibrium constant K and, therefore, the conformational free energy difference, $\Delta G_{EXP} = -RT \ln K$.

The compounds shown in Figure 1 containing a range of potential O, S, and Se contacts were synthesized (see the SI). An X-ray crystal structure of balance **1a**-Cl (CSD deposition no. 1563020) and density functional theory (DFT) calculations confirmed that most of the α-substituted **1a** and **2a** series of molecular balances accommodated chalcogen···chalcogen contacts in the closed conformation (Figure 2 and Figures S10−S12). In addition, balances containing β-substituted thiophenes that were incapable of forming direct chalcogen···chalcogen contacts in the closed conformer were synthesized with the intention of serving as controls (**1b** series and **2b**, Figure 1B,E). Conformers were assigned using HMBC/NOESY NMR spectroscopy and by the comparison of experimental and computed conformational ratios (see the SI and below). The conformational free energy differences between the open and closed conformers were measured for each balance in 13 different solvents (Figure 2).

All of the compounds in series **1a** and **1c** preferred the closed conformers in which O···S, or O···Se contacts were formed (<−7.4 to −1 kJ mol^{-1}). Such conformational preferences are comparable to those of OH to O═C H-bonds measured in structurally related molecular balances.[68] Varying the thiophene substituent had a substantial influence on the preference for O···S contacts, following the trend Me < H < Cl < COOMe < COMe < CHO (Figure 2, left). Interestingly, the O···Se contact in compound **1c** was slightly more favorable than the O···S contact in compound **1a**-CHO, despite the increased steric bulk and the lack of an electron-withdrawing group on the selenophene ring. β-Thiophene compounds **1b**-H and **1b**-CHO, which could not form O···S contacts, had a weaker preference for the closed conformer compared to the corresponding α-thiophenes **1a**-H and **1a**-CHO that could form direct O···S contacts. Thioformamide balances **2a**-Me, **2a**-H, and **2a**-Cl that could potentially host S···S contacts had ∼1.5 kJ mol^{-1} decreased preference for the closed conformer compared to the equivalently substituted **1a** balances that hosted O···S contacts. Indeed, while balances in series **1a** and **1c** had minimized structures containing planar O···S or O···Se contacts, such a planar structure and corresponding S···S contact was only seen in balance **2a**-Cl. Similarly, β-thiophenes in the **1b** series were calculated to have planar structures, hosting C═O···HC contacts, while the equivalent β-substituted thioformamide **2b** did not, and instead adopted a propeller-like conformation. Consistent with previous studies,[1] there was little difference in the energies of secondary conformers in which X/Y-carbonyl substituents were flipped, suggesting that no significant secondary chalcogen···chalcogen interactions were present in the X/Y-carbonyl substituted compounds.[69]

EVALUATION OF SOLVENT-MEDIATED ELECTROSTATIC AND SOLVOPHOBIC CONTRIBUTIONS

Solvents are known to exert both electrostatic (including H-bonding interactions) and solvophobic influences on the conformational preferences of molecular balances.[42−45,47,48,60,70] The conformational free energy differences in Figure 2 show striking solvent independence for balances that preferred the closed conformation. For example, conformational free energies across compound series **1** were similar in solvophobic H-bonding solvents such as methanol-d_4 and dimethyl sulfoxide-d_6 compared to very apolar solvents, such as carbon disulfide and benzene-d_6. The only significant changes in conformational free energies were seen when the very strong H-bond donor perfluoro-*tert*-butyl alcohol was used as the solvent. Conformational free energies in this solvent were found to be driven toward the open conformer by ∼2 kJ mol^{-1} compared to the other solvents due to its ability to form strong competitive H-bonding interactions with formyl carbonyl groups (Figure 2, bottom). There have been previous reports of very weak solvent effects on some other σ-hole interactions,[29,33,34,71,72] but such observations are not universal.[31] The lack of solvent dependence in the present investigation is particularly surprising considering that the conformational free energies of similar formamide molecular balances hosting H-bonding and aromatic interactions were found to be strongly dependent on the H-bond donor and acceptor abilities of the solvent.[42,68] These findings indicate that the chalcogen-bonding interactions in the present investigation do not have a substantial solvophobic, electrostatic or dipolar origin (Table S18). Although, the balances in the present investigation were not soluble in water, given the apparent universality of the observed solvent independence, it might be

DOI: 10.1021/jacs.7b08511
J. Am. Chem. Soc. XXXX, XXX, XXX−XXX

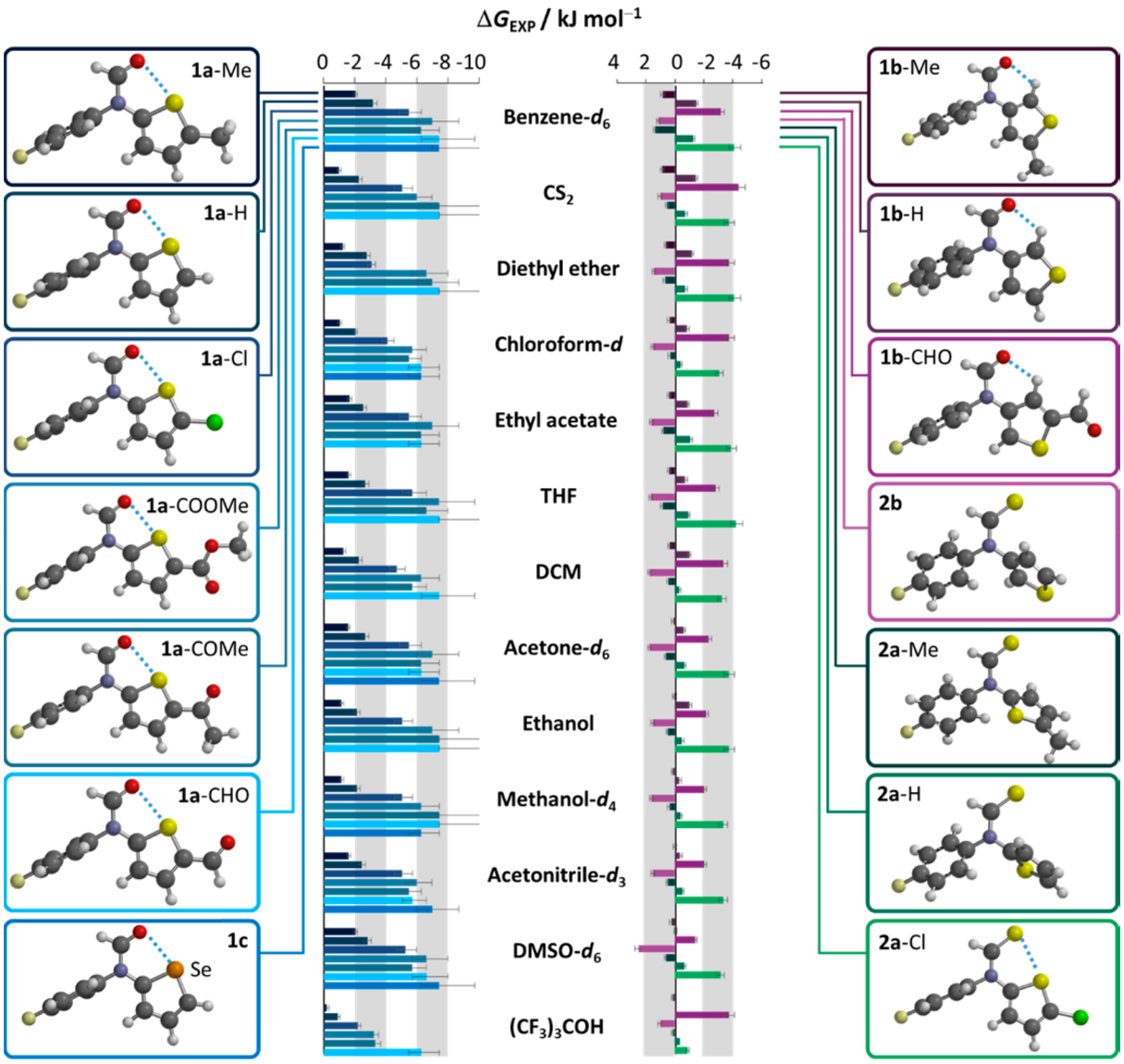

Figure 2. Experimental conformational free energies (ΔG_{EXP}) measured in 13 different solvents at 298 K. Corresponding minimized structures of each of the molecular balances calculated in the gas phase using B3LYP/6-311G* are shown. Colors correspond to those used in structures shown in Figure 1. Where the conformational equilibrium constant, $K > 20$, conformational energies are plotted at −7.4 kJ mol^{-1} with error bars truncated beyond −10.0 kJ mol^{-1}. All data and errors are tabulated in the SI.

reasonable to expect similar conformational preferences in aqueous solution.

EVALUATION OF VAN DER WAALS DISPERSION CONTRIBUTIONS

Having ruled out substantial solvophobic and electrostatic contributions to chalcogen-bonding interactions in our investigation, we then set out to consider van der Waals dispersion forces. Bulk solvent polarizability has been shown to describe the extent to which the solvent competes with, and attenuates dispersion forces between functional groups.[43,73] Solvents with low bulk polarizability would be expected to favor closed conformers that accommodate chalcogen···chalcogen interactions involving polarizable S and Se atoms, while highly polarizable solvents would be expected to favor the open conformer to expose polarizable groups to the solvent. However, Figure 2 shows that there is a negligible difference between the conformational free energies measured in the highly polarizable solvent carbon disulfide, compared to methanol-d_4, which has a low bulk polarizability.[43] The solvent with the lowest bulk polarizability in our investigation is perfluoro-*tert*-butyl alcohol, which should favor the closed conformer if contributions from dispersion forces in the chalcogen···chalcogen contacts are significant. Instead, the conformational free energies in perfluoro-*tert*-butyl alcohol are driven toward the open conformer compared to all of the other solvents. This indicates that solvation of the formyl oxygen atoms by hydrogen bonding is more energetically significant than any contribution from residual differences in dispersion forces in the solution phase. Furthermore, the experimental conformational free energies were compared with those calculated in the gas-phase using DFT methods that both did, and did not, include dispersion corrections (M06-2X and ωB97X-D vs B3LYP). The strongest correlation was found against conformational energies (ΔE_{CALC}) calculated using the non-dispersion corrected B3LYP method (R^2 = 0.94, Figure

DOI: 10.1021/jacs.7b08511
J. Am. Chem. Soc. XXXX, XXX, XXX−XXX

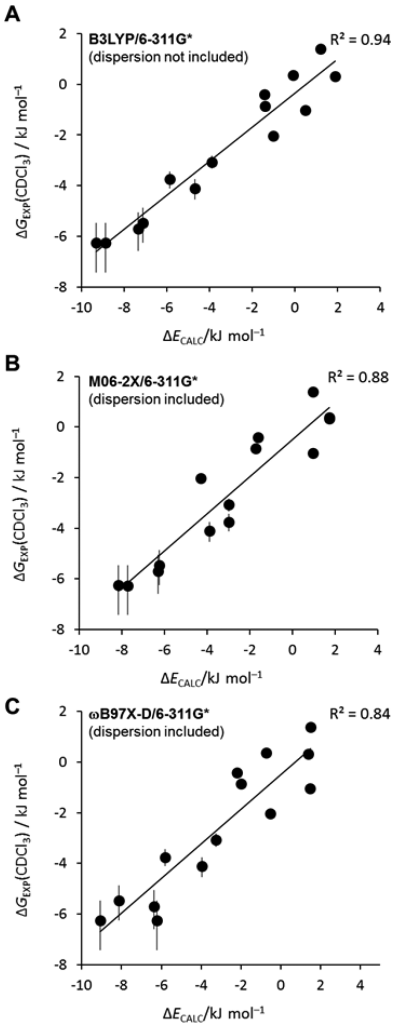

Figure 3. Correlations of experimental conformational free energies measured in $CDCl_3$ at 298 K (ΔG_{EXP}) vs those predicted at the indicated levels of theory in the gas phase (ΔE_{CALC}). An additional correlation using the SM8 implicit solvent model for chloroform showed no improvement in the correlation coefficient (Figure S23).

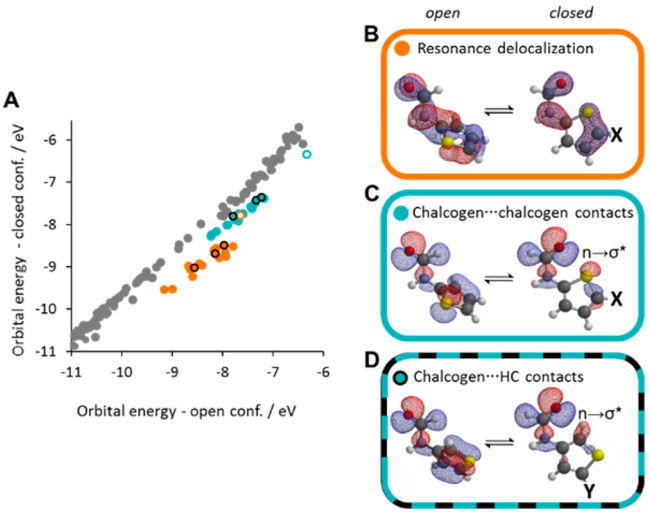

Figure 4. (A) Correlation of calculated orbital energies in the open vs closed molecular balance conformers. Data points that fall below the line formed by the gray points are stabilized in the closed conformer due to (B) resonance delocalization modulated by structural planarization (orange), and n → σ^* orbital delocalization (teal) associated with either (C) direct chalcogen···chalcogen contacts, or (D) chalcogen···H–C contacts. Solid filled points are orbital energies for α-thiophene series **1a**-X and α-selenophene balance **1c**. Points with black outlines are the β-thiophene balances in the **1b**-Y series. Open circles correspond to the only thioformamide balance hosting a favorable S–S contact, **2a**-Cl. Alternative correlations using M06-2X/6-311G* and ωB97X-D/6-311G*, plus a comparison of full vs simplified molecular balance data are provided in the SI.

3A). In contrast, conformational energies calculated using dispersion-corrected (DFT-D) methods formed substantially poorer correlations (R^2 = 0.88 and 0.84, Figures 3B,C). Thus, these correlations, combined with the very limited solvent dependence of the conformational free energies indicate that differences in dispersion forces make negligible contributions to the chalcogen-bonding interactions that govern the observed conformational free energies.

EVALUATION OF ORBITAL DELOCALIZATION CONTRIBUTIONS

So far, we have discounted electrostatic, solvophobic, and dispersion forces as the primary determinants of the chalcogen-bonding interactions in our molecular balances. Others have proposed that orbital delocalization effects may play a role in various classes of σ-hole interactions based on spectroscopic, structural, and computational analyses.[17,24,29,33−41] Delocalization effects are long recognized aspects of bond theory; most chemists are familiar with the concepts of inductive polarization along σ-bonds, resonance involving π-bonds, and hyperconjugation between σ- and π-bonds. However, similar forms of orbital delocalization are commonly overlooked in the context of molecular interactions, which are often considered to be "non-bonding" or "non-covalent". We point out that the terminology used to describe electron delocalization effects in "non-bonded" interactions is often inconsistent: polarization, donor–acceptor interactions, charge transfer, partial covalency, orbital mixing, and orbital interactions, among others, have all been used to describe a broadly similar ground-state phenomenon.[11,32,74−78] Such inconsistencies may arise, at least in part, from the challenge of obtaining systematic, direct experimental measurements of weak interactions in solution, and further establishing causal association with quantum mechanical descriptors.[77]

Nonetheless, n → π^* orbital delocalization from a lone pair (n) into the carbonyl antibonding orbital (π^*) has been proposed to stabilize carbonyl–carbonyl interactions,[62−66] alongside competing dipolar electrostatic explanations.[67] Similarly, n → σ^* delocalization from a lone pair orbital (n) into the antibonding orbital of a σ-bond (σ^*) has been suggested by theory to stabilize interactions involving chalcogens.[24,29,33−41,79] Thus, we set about performing a comprehensive orbital analysis of our molecular balances.

Our orbital analysis began by performing geometry minimizations on the open and closed conformations of molecular balances bearing a range of substituents (all of the compounds shown in Figure 1 and more, see the SI) using both DFT and DFT-D methods. We hypothesized that the energies of particular orbitals in the open and closed conformers could be compared to reveal orbital interactions that specifically stabilized one conformer over the other. To avoid the splitting of the orbitals arising from the canonical resonance forms of the aromatic electrons that were not involved in the chalcogen

DOI: 10.1021/jacs.7b08511
J. Am. Chem. Soc. XXXX, XXX, XXX–XXX

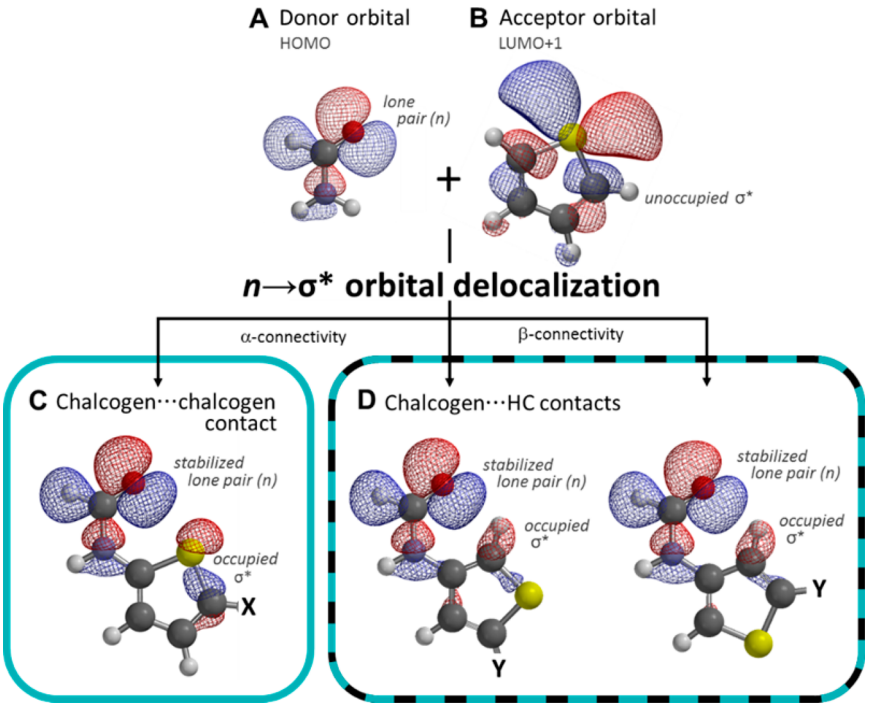

Figure 5. Orbital decomposition analysis illustrating the hypothetical combination of molecular fragments A + B in the three orientations shown. (A) HOMO containing the formyl oxygen lone pair (n) is stabilized in (C) and (D) by the same set of antibonding σ^* orbitals of the (seleno/thio)phene fragment, irrespective of the orientation of the connected ring and the specific intramolecular contacts present. The preferred conformers of the compounds investigated are shown in Figure 2. All orbitals and minimized geometries were calculated using B3LYP/6-311G*.

interactions, the fluorophenyl moiety was replaced with a proton, and a single-point energy calculation was performed on each structure (retaining the geometry of the complete balance). The use of such fragments greatly simplified the task of assigning pairs of open/closed orbitals (see the SI for validation). The resulting comparison of orbital energies for all of the balances with planar structures from Figure 2 is presented in Figure 4. The line formed by the gray points in Figure 4A corresponds to the vast majority of orbitals in which there is little difference in energy between the open and closed conformers. Data points that fall below the gray background line correspond to orbitals that are more stable in the closed than the open conformer. Two sets of data sit below the background line (orange and teal, Figure 4A). Upon inspection of the molecular orbitals, the orange data were found to correspond to through-bond, resonance delocalization of the lone pair orbital that lies above and below the plane of the amide into the coplanar aromatic system (orange, Figure 4B). Such delocalized orbitals were, accordingly, only present in molecular balances that had planar closed conformations. The teal series corresponded to orbitals in which the other, orthogonal lone pair orbital of the amide was delocalized into the S−C (or Se−C) σ-bond of the adjacent thiophene (or selenophene) (Figures 4C,D and 5C,D). Thus, these orbitals were consistent with the occurrence of stabilizing n → σ^* orbital interactions.

We confirmed the identity of these delocalized n → σ^* orbitals by further decomposition of the molecular balance fragments into the constituent (thio)formamide (e.g., Figure 5A) and thiophene (or selenophene) components (e.g., Figure 5B). This hypothetical decomposition analysis indicated that the stabilized, delocalized orbitals of the type shown in Figures 4C,D and 5C,D did indeed result from the hybridization of a high-energy, but occupied, lone-pair orbital (Figure 5A) with an even higher energy, unoccupied, antibonding molecular orbital of the thiophene (or selenophene) (Figure 5B). Interestingly, this decomposition analysis showed that the same molecular orbitals (Figures 5A,B) combine to stabilize the formamide lone pair, irrespective of the α/β-connectivity, or the orientation of the thiophene ring (Figure 5C,D). Furthermore, we used Natural Bond Orbital (NBO)[76] analysis to examine the occurrence and stabilizing character of specific n → σ^* orbital interactions. In simplistic terms, NBOs are theoretical constructs that are intermediate between molecular orbitals (such as those shown in Figure 5) and the constituent atomic orbitals.[80] NBOs reveal orbital delocalization that includes both covalent bonds and orbital interactions that can be considered as having "partial" covalent character. Indeed, NBO analysis has previously been used to analyze putative n → σ^* and n → π^* interactions.[29,33−36,65,66] NBO analysis of our balances revealed the potential for stabilizing n → σ^*_{S-C} and n → σ^*_{Se-C} delocalization where direct chalcogen···chalcogen contacts occurred, while weaker n → σ^*_{C-S}, n → σ^*_{H-C}, and n → σ^*_{C-C} NBOs were present in the β-connected thiophene balances (Figure S23 and Table S45).

The occurrence of such orbital interactions should be indicated by lengthening of the accepting bond in the closed conformer relative to the open conformer of each molecular balance. Computational geometry minimizations revealed lengthening of the bonds aligned with the (thio)amide contact in the closed conformation (blue bonds, Figure 6). The extent of bond lengthening did not correlate with the experimental conformational free energies measured in the molecular balances, since changes in electron density were also modulated by the adjacent X and Y substituents (Figure 1). Consistent with this suggestion, bond lengthening also occurred at electron-accepting substituents (purple bonds, Figure 6).

DOI: 10.1021/jacs.7b08511
J. Am. Chem. Soc. XXXX, XXX, XXX−XXX

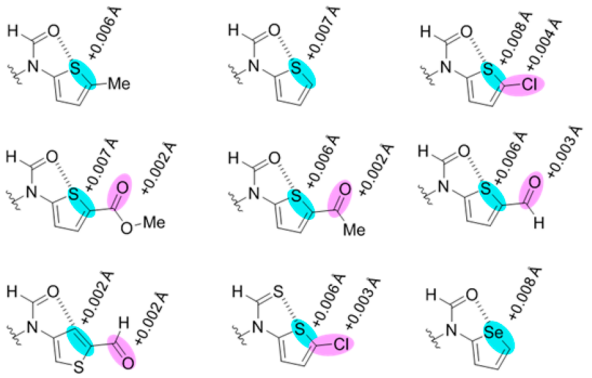

Figure 6. Calculated bond lengthening (B3LYP/6-311G*) in the closed vs open conformers for molecular balances hosting chalcogen−chalcogen contacts. Further bond length differences are provided in Figure S13.

Having confirmed the identity and possible stabilizing nature of n → σ^* orbital contributions to chalcogen-bonding interactions, we sought a quantitative energetic relationship between experiment and theory. Unfortunately, we found no correlation between the experimental conformational free energy differences measured in the molecular balances and the n → σ^* orbital delocalization energies output from the NBO calculations (Figure S22 and Table S45). Indeed, one limitation of NBO analysis is that it can be challenging to ascribe an easily understood physical meaning to NBOs. Instead, we compared the computed energies of physically relevant molecular orbitals with our experimental conformational free energies. A striking correlation was found between the energies of the molecular orbitals identified in Figure 5C,D that contained n → σ^* orbital delocalization (R^2 = 0.99, Figure 7A). The energies relating to balances containing both direct chalcogen···chalcogen and chalcogen···H−C contacts (teal and black outlined points, respectively) were found to fit on the same correlation. This finding was consistent with the involvement of the same σ^* acceptor orbital (Figure 5C,D), irrespective of the orientation or connectivity of the thiophene ring. Contrasting with previous suggestions,[79] the β-connected thiophenes (black outlines in Figure 7A) were weaker lone pair acceptors than the equivalently substituted α-connected variants (filled circles in Figure 7A). However, it is important to note that the relative acceptor abilities may not be general, as they are likely to be influenced by the geometric constraints imposed by our intramolecular system. The single point associated with selenophene balance **1c** was an outlier (Figure S19) indicating the increased favorability of this interaction compared to the O···S and S···S interactions. In comparison, the energies of the resonance delocalized orbitals (Figure 7B), along with other molecular orbitals (Figure S21) did not form good correlations with the same experimental data. Thus, the strong correlation in Figure 7A establishes a quantitative link between the experimentally determined conformational free energies and the theoretically determined energies of n → σ^* delocalized orbitals involved in stabilizing the chalcogen-bonding interactions.

CONCLUSION

We have performed a quantitative, experimental investigation of chalcogen-bonding interactions. Synthetic molecular balances were used to examine solvent and substituent effects on a range of chalcogen···chalcogen and chalcogen···HC contacts (Figure 1). The conformational free energies of balances hosting chalcogen-bonding interactions were found to be surprisingly solvent independent, ruling out substantial contributions from electrostatic and solvophobic effects (Figure 2).[81] This solvent independence combined with comparison against dispersion-corrected calculated conformational energies further indicated that van der Waals dispersion forces did not account for the observed interaction trends (Figure 3). The latter finding was consistent with previous studies that have found substantial attenuation of dispersion forces between functional groups due

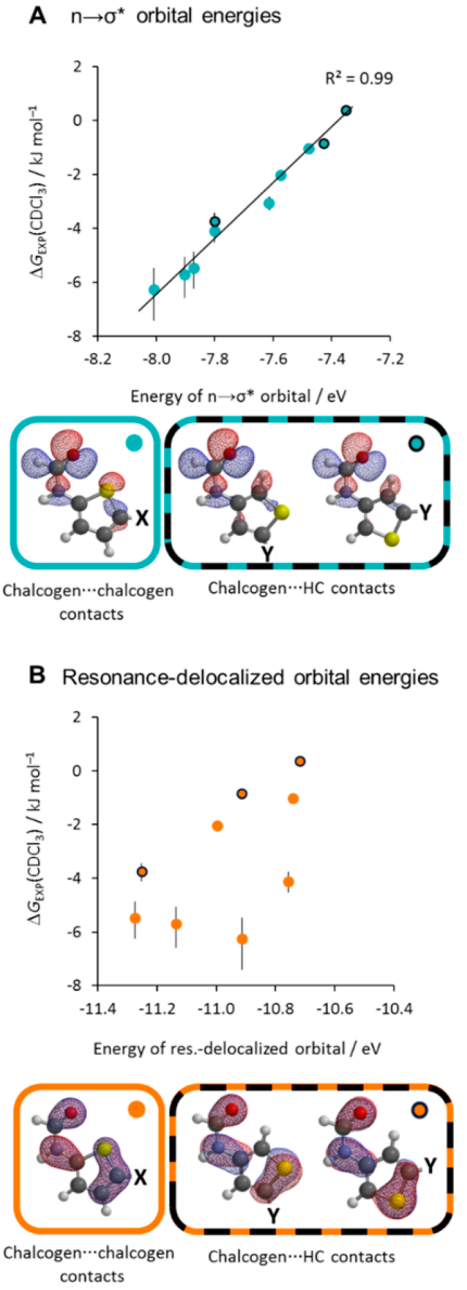

Figure 7. Correlations of the calculated energies of orbitals stabilized by (A) n → σ^* orbital delocalization (teal) and (B) resonance delocalization modulated by planarization (orange). Solid filled points correspond to α-substituted thiophenes, while β-substituted thiophenes are indicated with black outlines. Calculations were performed on structures of the type shown inset using B3LYP/6-311G*. X and Y = substituents as shown in Figure 1. Alternative correlations using DFT-D methods are provided in the SI.

DOI: 10.1021/jacs.7b08511
J. Am. Chem. Soc. XXXX, XXX, XXX−XXX

to competitive dispersion interactions with the surrounding solvent.[43,61,70,73] Instead, computed changes in bond lengths and NBO analysis pointed toward the involvement of stabilizing contributions from n → σ^* orbital delocalization between the lone pair on a (thio)amide donor and the antibonding σ^* orbitals of the adjacent thiophene (or selenophene) acceptor. A quantitative relationship between the energy of the orbital hosting n → σ^* orbital delocalization and the experimental data was seen. Interestingly, thiophene rings were found to accept electrons into the same antibonding molecular orbital in both α- and β-connected thiophenes, either via direct chalcogen···chalcogen or chalcogen···HC contacts. Intriguingly, our quantitative comparison of experimental and computational data reveals empirical behavior most consistent with a dominant contribution from orbital delocalization.[29,33−36] Our results highlight the energetic significance of orbital delocalization in molecular interactions.

■ ASSOCIATED CONTENT

Supporting Information

The Supporting Information is available free of charge on the ACS Publications website at DOI: 10.1021/jacs.7b08511.

Experimental, characterization, and computational data (PDF)

Crystallographic data for compound **1a**-Cl (CIF)

■ AUTHOR INFORMATION

Corresponding Author

*scott.cockroft@ed.ac.uk

ORCID

Scott L. Cockroft: 0000-0001-9321-8997

Author Contributions

The manuscript was written through contributions of all authors.

Notes

The authors declare no competing financial interest.

■ ACKNOWLEDGMENTS

We thank Syngenta and the EPSRC for funding. We thank Dr. Stefan Borsley for helpful feedback.

■ REFERENCES

(1) Beno, B. R.; Yeung, K.-S.; Bartberger, M. D.; Pennington, L. D.; Meanwell, N. A. *J. Med. Chem.* **2015**, *58*, 4383−4438.

(2) Murray, J. S.; Lane, P.; Politzer, P. *Int. J. Quantum Chem.* **2008**, *108*, 2770−2781.

(3) Murray, J. S.; Lane, P.; Clark, T.; Politzer, P. *J. Mol. Model.* **2007**, *13*, 1033−1038.

(4) Benz, S.; López-Andarias, J.; Mareda, J.; Sakai, N.; Matile, S. *Angew. Chem., Int. Ed.* **2017**, *56*, 812−815.

(5) Robinson, E. R. T.; Walden, D. M.; Fallan, C.; Greenhalgh, M. D.; Cheong, P. H.-Y.; Smith, A. D. *Chem. Sci.* **2016**, *7*, 6919−6927.

(6) Shiina, I.; Nakata, K.; Ono, K.; Onda, Y.-s.; Itagaki, M. *J. Am. Chem. Soc.* **2010**, *132*, 11629−11641.

(7) Cox, P. A.; Leach, A. G.; Campbell, A. D.; Lloyd-Jones, G. C. *J. Am. Chem. Soc.* **2016**, *138*, 9145−9157.

(8) Mahmudov, K. T.; Kopylovich, M. N.; Guedes da Silva, M. F. C.; Pombeiro, A. J. L. *Dalton Trans.* **2017**, *46*, 10121−10138.

(9) Werz, D. B.; Gleiter, R.; Rominger, F. *J. Am. Chem. Soc.* **2002**, *124*, 10638−10639.

(10) Fick, R. J.; Kroner, G. M.; Nepal, B.; Magnani, R.; Horowitz, S.; Houtz, R. L.; Scheiner, S.; Trievel, R. C. *ACS Chem. Biol.* **2016**, *11*, 748−754.

(11) Reid, R. C.; Yau, M.-K.; Singh, R.; Lim, J.; Fairlie, D. P. *J. Am. Chem. Soc.* **2014**, *136*, 11914−11917.

(12) Lim, J. Y. C.; Marques, I.; Thompson, A. L.; Christensen, K. E.; Félix, V.; Beer, P. D. *J. Am. Chem. Soc.* **2017**, *139*, 3122−3133.

(13) Gleiter, R.; Werz, D. B.; Rausch, B. J. *Chem. - Eur. J.* **2003**, *9*, 2676−2683.

(14) Robinson, S. W.; Mustoe, C. L.; White, N. G.; Brown, A.; Thompson, A. L.; Kennepohl, P.; Beer, P. D. *J. Am. Chem. Soc.* **2015**, *137*, 499−507.

(15) Murray, J. S.; Lane, P.; Politzer, P. *J. Mol. Model.* **2009**, *15*, 723−729.

(16) Beale, T. M.; Chudzinski, M. G.; Sarwar, M. G.; Taylor, M. S. *Chem. Soc. Rev.* **2013**, *42*, 1667−1680.

(17) Cavallo, G.; Metrangolo, P.; Milani, R.; Pilati, T.; Priimagi, A.; Resnati, G.; Terraneo, G. *Chem. Rev.* **2016**, *116*, 2478−2601.

(18) Clark, T.; Hennemann, M.; Murray, J. S.; Politzer, P. *J. Mol. Model.* **2007**, *13*, 291−296.

(19) Bauzá, A.; Mooibroek, T. J.; Frontera, A. *Angew. Chem., Int. Ed.* **2013**, *52*, 12317−12321.

(20) Murray, J. S.; Lane, P.; Politzer, P. *Int. J. Quantum Chem.* **2007**, *107*, 2286−2292.

(21) Zahn, S.; Frank, R.; Hey-Hawkins, E.; Kirchner, B. *Chem. - Eur. J.* **2011**, *17*, 6034−6038.

(22) Bauzá, A.; Frontera, A. *Angew. Chem., Int. Ed.* **2015**, *54*, 7340−7343.

(23) Burling, F. T.; Goldstein, B. M. *J. Am. Chem. Soc.* **1992**, *114*, 2313−2320.

(24) Bleiholder, C.; Gleiter, R.; Werz, D. B.; Köppel, H. *Inorg. Chem.* **2007**, *46*, 2249−2260.

(25) Cozzolino, A. F.; Vargas-Baca, I.; Mansour, S.; Mahmoudkhani, A. H. *J. Am. Chem. Soc.* **2005**, *127*, 3184−3190.

(26) Esrafili, M. D.; Mohammadian-Sabet, F. *Chem. Phys. Lett.* **2015**, *634*, 210−215.

(27) Murray, J. S.; Lane, P.; Clark, T.; Riley, K. E.; Politzer, P. *J. Mol. Model.* **2012**, *18*, 541−548.

(28) Duarte, D. J. R.; Sosa, G. L.; Peruchena, N. M. *J. Mol. Model.* **2013**, *19*, 2035−2041.

(29) Iwaoka, M.; Komatsu, H.; Katsuda, T.; Tomoda, S. *J. Am. Chem. Soc.* **2004**, *126*, 5309−5317.

(30) Stone, A. J. *J. Am. Chem. Soc.* **2013**, *135*, 7005−7009.

(31) Garrett, G. E.; Gibson, G. L.; Straus, R. N.; Seferos, D. S.; Taylor, M. S. *J. Am. Chem. Soc.* **2015**, *137*, 4126−4133.

(32) Politzer, P.; Murray, J. S.; Clark, T. *Phys. Chem. Chem. Phys.* **2013**, *15*, 11178−11189.

(33) Iwaoka, M.; Komatsu, H.; Katsuda, T.; Tomoda, S. *J. Am. Chem. Soc.* **2002**, *124*, 1902−1909.

(34) Barton, D. H. R.; Hall, M. B.; Lin, Z.; Parekh, S. I.; Reibenspies, J. *J. Am. Chem. Soc.* **1993**, *115*, 5056−5059.

(35) Komatsu, H.; Iwaoka, M.; Tomoda, S. *Chem. Commun.* **1999**, 205−206.

(36) Iwaoka, M.; Tomoda, S. *J. Am. Chem. Soc.* **1996**, *118*, 8077−8084.

(37) Bleiholder, C.; Werz, D. B.; Köppel, H.; Gleiter, R. *J. Am. Chem. Soc.* **2006**, *128*, 2666−2674.

(38) Bauza, A.; Quinonero, D.; Deya, P. M.; Frontera, A. *CrystEngComm* **2013**, *15*, 3137−3144.

(39) Iwaoka, M.; Takemoto, S.; Tomoda, S. *J. Am. Chem. Soc.* **2002**, *124*, 10613−10620.

(40) Rittner, R.; Ducati, L. C.; Tormena, C. F.; Fiorin, B. C.; Braga, C. B. *Spectrochim. Acta, Part A* **2011**, *79*, 1071−1076.

(41) Hudson, B.; Nguyen, E.; Tantillo, D. J. *Org. Biomol. Chem.* **2016**, *14*, 3975−3980.

(42) Mati, I. K.; Adam, C.; Cockroft, S. L. *Chem. Sci.* **2013**, *4*, 3965−3965.

(43) Adam, C.; Yang, L.; Cockroft, S. L. *Angew. Chem., Int. Ed.* **2015**, *54*, 1164−1167.

(44) Cockroft, S. L.; Hunter, C. A. *Chem. Commun.* **2009**, 3961−3963.

DOI: 10.1021/jacs.7b08511
J. Am. Chem. Soc. XXXX, XXX, XXX−XXX

(45) Cockroft, S. L.; Hunter, C. A. *Chem. Commun.* **2006**, 3806−3808.
(46) Mati, I. K.; Cockroft, S. L. *Chem. Soc. Rev.* **2010**, *39*, 4195−4205.
(47) Muchowska, K. B.; Adam, C.; Mati, I. K.; Cockroft, S. L. *J. Am. Chem. Soc.* **2013**, *135*, 9976−9979.
(48) Yang, L.; Adam, C.; Cockroft, S. L. *J. Am. Chem. Soc.* **2015**, *137*, 10084−10087.
(49) Hof, F.; Scofield, D. M.; Schweizer, W. B.; Diederich, F. *Angew. Chem., Int. Ed.* **2004**, *43*, 5056−5059.
(50) Li, P.; Maier, J. M.; Vik, E. C.; Yehl, C. J.; Dial, B. E.; Rickher, A. E.; Smith, M. D.; Pellechia, P. J.; Shimizu, K. D. *Angew. Chem., Int. Ed.* **2017**, *56*, 7209−7212.
(51) Ams, M. R.; Fields, M.; Grabnic, T.; Janesko, B. G.; Zeller, M.; Sheridan, R.; Shay, A. *J. Org. Chem.* **2015**, *80*, 7764−7769.
(52) Maier, J. M.; Li, P.; Hwang, J.; Smith, M. D.; Shimizu, K. D. *J. Am. Chem. Soc.* **2015**, *137*, 8014−8017.
(53) Tatko, C. D.; Waters, M. L. *J. Am. Chem. Soc.* **2002**, *124*, 9372−9373.
(54) Gung, B. W.; Wekesa, F.; Barnes, C. L. *J. Org. Chem.* **2008**, *73*, 1803−1808.
(55) Newcomb, L. F.; Gellman, S. H. *J. Am. Chem. Soc.* **1994**, *116*, 4993−4994.
(56) Kim, E.-i.; Paliwal, S.; Wilcox, C. S. *J. Am. Chem. Soc.* **1998**, *120*, 11192−11193.
(57) Paliwal, S.; Geib, S.; Wilcox, C. S. *J. Am. Chem. Soc.* **1994**, *116*, 4497−4498.
(58) Gardarsson, H.; Schweizer, W. B.; Trapp, N.; Diederich, F. *Chem. - Eur. J.* **2014**, *20*, 4608−4616.
(59) Motherwell, W. B.; Moïse, J.; Aliev, A. E.; Nič, M.; Coles, S. J.; Horton, P. N.; Hursthouse, M. B.; Chessari, G.; Hunter, C. A.; Vinter, J. G. *Angew. Chem., Int. Ed.* **2007**, *46*, 7823−7826.
(60) Emenike, B. U.; Bey, S. N.; Bigelow, B. C.; Chakravartula, S. V. S. *Chem. Sci.* **2016**, *7*, 1401−1407.
(61) Hwang, J.; Dial, B. E.; Li, P.; Kozik, M. E.; Smith, M. D.; Shimizu, K. D. *Chem. Sci.* **2015**, *6*, 4358−4364.
(62) Bartlett, G. J.; Newberry, R. W.; VanVeller, B.; Raines, R. T.; Woolfson, D. N. *J. Am. Chem. Soc.* **2013**, *135*, 18682−18688.
(63) Newberry, R. W.; Orke, S. J.; Raines, R. T. *Org. Lett.* **2016**, *18*, 3614−3617.
(64) Bartlett, G. J.; Choudhary, A.; Raines, R. T.; Woolfson, D. N. *Nat. Chem. Biol.* **2010**, *6*, 615−620.
(65) Newberry, R. W.; VanVeller, B.; Guzei, I. A.; Raines, R. T. *J. Am. Chem. Soc.* **2013**, *135*, 7843−7846.
(66) Choudhary, A.; Gandla, D.; Krow, G. R.; Raines, R. T. *J. Am. Chem. Soc.* **2009**, *131*, 7244−7246.
(67) Fischer, F. R.; Wood, P. A.; Allen, F. H.; Diederich, F. *Proc. Natl. Acad. Sci. U. S. A.* **2008**, *105*, 17290−17294.
(68) Dominelli-Whiteley, N.; Brown, J. J.; Muchowska, K. B.; Mati, I. K.; Adam, C.; Hubbard, T. A.; Elmi, A.; Brown, A. J.; Bell, I. A. W.; Cockroft, S. L. *Angew. Chem., Int. Ed.* **2017**, *56*, 7658−7662.
(69) In addition, NBO calculations revealed no such secondary interactions.
(70) Yang, L.; Adam, C.; Nichol, G. S.; Cockroft, S. L. *Nat. Chem.* **2013**, *5*, 1006−1010.
(71) Sarwar, M. G.; Dragisic, B.; Salsberg, L. J.; Gouliaras, C.; Taylor, M. S. *J. Am. Chem. Soc.* **2010**, *132*, 1646−1653.
(72) Robertson, C. C.; Perutz, R. N.; Brammer, L.; Hunter, C. A. *Chem. Sci.* **2014**, *5*, 4179−4183.
(73) Yang, L.; Brazier, J. B.; Hubbard, T. A.; Rogers, D. M.; Cockroft, S. L. *Angew. Chem., Int. Ed.* **2016**, *55*, 912−916.
(74) Stone, A. J.; Price, S. L. *J. Phys. Chem.* **1988**, *92*, 3325−3335.
(75) Bent, H. A. *Chem. Rev.* **1968**, *68*, 587−648.
(76) Reed, A. E.; Curtiss, L. A.; Weinhold, F. *Chem. Rev.* **1988**, *88*, 899−926.
(77) Gonthier, J. F.; Steinmann, S. N.; Wodrich, M. D.; Corminboeuf, C. *Chem. Soc. Rev.* **2012**, *41*, 4671−4687.
(78) Grabowski, S. J. *Chem. Rev.* **2011**, *111*, 2597−2625.
(79) Alabugin, I. V.; Zeidan, T. A. *J. Am. Chem. Soc.* **2002**, *124*, 3175−3185.
(80) Weinhold, F.; Landis, C. R. *Chem. Educ. Res. Pract.* **2001**, *2*, 91−104.
(81) Our findings rule out a purely electrostatic model for chalcogen-bonding interactions, though they may be, at least qualitatively, compatible with an electrostatic plus polarization model. Murray, J. S.; Politzer, P. *Wiley Interdiscipl. Rev. Comp. Mol. Sci.* **2017**, e1326.

DOI: 10.1021/jacs.7b08511
J. Am. Chem. Soc. XXXX, XXX, XXX−XXX